



HAL
open science

Dynactin1 mutations associated with amyotrophic lateral sclerosis and their effect on axonal transport and neuromuscular junction formation

Valérie Bercier

► **To cite this version:**

Valérie Bercier. Dynactin1 mutations associated with amyotrophic lateral sclerosis and their effect on axonal transport and neuromuscular junction formation. *Neurons and Cognition [q-bio.NC]*. Université Pierre et Marie Curie - Paris VI, 2017. English. NNT : 2017PA066176 . tel-02292543

HAL Id: tel-02292543

<https://theses.hal.science/tel-02292543v1>

Submitted on 20 Sep 2019

HAL is a multi-disciplinary open access archive for the deposit and dissemination of scientific research documents, whether they are published or not. The documents may come from teaching and research institutions in France or abroad, or from public or private research centers.

L'archive ouverte pluridisciplinaire **HAL**, est destinée au dépôt et à la diffusion de documents scientifiques de niveau recherche, publiés ou non, émanant des établissements d'enseignement et de recherche français ou étrangers, des laboratoires publics ou privés.

Université Pierre et Marie Curie

École doctorale Cerveau, cognition, comportement (ED 158)

Institut Curie / Laboratoire développement des circuits neuronaux

Dynactin1 mutations associated with amyotrophic lateral sclerosis and their effect on axonal transport and neuromuscular junction formation

Par Valérie Bercier

Thèse de doctorat en Sciences de la vie, spécialité Neurosciences

Dirigée par Filippo Del Bene

Présentée et soutenue publiquement le 18 septembre 2017

Devant un jury composé de :

Dr DEL BENE, Filippo, DR

Directeur de thèse

Dr JANKE, Carsten, DR

Rapporteur

Dr SCHMID, Bettina, DR

Rapporteur

Dr STEVANIN, Giovanni, DR

Examineur

Dr HAZAN, Jamilé, DR

Examinatrice

Dr ANDRIEUX, Anne, DR

Examinatrice



“It is a mistake to think you can solve any major problems just with potatoes.”

- Douglas Adams, *Life, the Universe and Everything*

Acknowledgements

First of all I would like to thank my supervisor Filippo Del Bene for the opportunity to work in his lab. It was not an easy start and we had to learn a lot to get this project on the way, as well as butt heads a few times, but in the end, we found a phenotype!!!

Thank you to the Del Bene lab for all the help, the teaching moments, the coffee breaks, the picnics and retreats. You were all there during the triumphs and the unfortunate disasters that also sometimes happen. In particular, thank you to Karine, Thomas and Christoph who were the first ones to very patiently answer all my questions, and to Vincenzo, Flavia, Céline, Shahad, Giulia, Noé, Julie, Juliette, Marion, and Gokul. It is true when they say “it takes a village” and you guys were it! Also thank you to the passing members of the lab, namely Federica, Alessio, Anne, Dina, Natalia, and Katrina who all brought a little bit of sunshine to the back corner of the office.

In addition, a special thanks goes out to the animal facility staff (Olivier, Armelle, Tarek and Cédric) and to the awesome Curie administrative staff, who all made my life easier (Isabelle, Virginie and Déborah). Thank you also to the dwellers of the 3rd floor for your camaraderie, in particular ALL THE ITALIANS who seem to appear from nowhere and aggregate like (very loud) prions (Angelo, Roberta, Sara, Ariana, Manu, Edoardo, Magherita, Irene, etc.) Audrey, Daniel, Michel, Antoine and the rest. Also thank you for bringing sweets and leaving them unattended at the coffee machine...

Of course one must not forget the fellowship that provided me with support, both administrative, and emotional, since before I even moved to Paris: the École des Neurosciences de Paris. The help from Yvette, Laura, Deborah, Laetitia, André, Patricia, Laure and Laurent was invaluable. In addition, thank you to the students who, like me, are part of this fellowship. In particular, I would like to thank Malou and Jaime, as well as Hannah and Darinka who not only were great friends, but somehow got roped into being ENP student representatives with me. Thank you also to Heike, Laurianne, Emma, Maja, Damiano, Sabah, Mariana, Jenna, Urs, Alessandra, Ralitsa, Maria Julia, Kasia and the rest. Even though you came from all over the world, you were like a family to me during my time in France.

My gratitude also goes out to Claire Wyart and her team at ICM. Thanks to Kevin and Jeff for tackling the physiology of this project, and to Claire for her sound advice and unfailing enthusiasm.

Finally, thank you to my family for supporting me across an ocean. I'm really grateful for the visits, the skype calls and the packages that brought a bit of home to our apartment. Thank you to my husband, Witek, for his love, care and encouragement, and for going head first into this crazy adventure with me. France has been at times harsh and wonderful to us and I think we will forever keep good memories of it, which brings me to my last acknowledgement: thank you to "croquette" for being my writing partner and for giving me perspective in the end pages of this thesis. Indeed, there are great things still ahead!

Abstract

Amyotrophic lateral sclerosis (ALS) is an adult-onset neurodegenerative disease, which is mainly sporadic in nature. This progressive pathology has an estimated incidence of 1-2 per 100 000 worldwide and generally leads to death within 2-5 years of diagnosis due to muscle wasting and severe motor neuron loss. Over the last years, mutations have been identified in both sporadic and familial ALS patients, interfering with the function of many genes, including *DCTN1*, which encodes for a subunit of the motor protein complex dynactin. The dynactin complex serves as an adaptor for the dynein motor complex, responsible for retrograde axonal transport, and it is believed to regulate dynein activity and the binding capacity for cargo, however its role in ALS pathogenesis is still unknown.

We set out to characterize a mutant zebrafish line for *dynactn1a* (named *mikre oko*^{m632}, *mok*^{m632}), looking specifically at caudal primary motor neurons (CaPs), with regard to axonal development, formation and stability of the neuromuscular junction (NMJ) and the behavioral phenotype produced in embryos, as well as axonal transport metrics.

We observed that homozygous mutant embryos exhibited an abnormal locomotor activity at 48hpf, as assayed by a touch-evoked escape response assay, suggesting a fatiguing phenotype of the neuromuscular junction. These embryos also had an abnormal axonal morphology at 6dpf, with arbors of reduced size and with a lower number of projections. The neuromuscular junction showed defects in structure, with misaligned pre- and postsynaptic sites. However, miniature end-plate currents (mEPC) at the NMJ were normal, suggesting fusion and spontaneous release machinery to be functional in our mutant embryos. Paired-recordings of motor neurons and muscle at 6dpf revealed abnormal firing patterns for both low and high frequency stimulation, where mutant embryos display failures and asynchronous release. Additionally, we found that our mutants have a reduced number of putative synapses, which were also of smaller size and unstable. This instability was postulated to be the cause of the reduced growth in CaPs the NMJ physiological defects, which leads to the behavioral abnormalities. We were able to rescue the mutant CaP morphological phenotype by overexpressing the human Dynactin1-GFP protein, whereas the overexpression had no effect on CaP morphology in wild-type embryos. The human protein was found to localize at synaptic sites, supporting a possible role in synapse stability. Fast axonal transport was quantified in primary motor neurons using the GAL4/UAS bipartite system and fusion protein tracking *in vivo* by confocal time-lapse microscopy. We quantified the transport dynamics of cargoes such as mitochondria and early, late and recycling endosome in the motor neurons of wild-type versus *mok*^{m632} mutant embryos *in vivo*. We did not observe a change in transport states of cargoes (stable, anterograde, retrograde) and while we found few differences in transport behavior, the overall results suggest that dynactin1 is not essential for dynein activity and for axonal transport in general.

We investigated dynactin1's interaction with the cytoskeleton and did not find defects in microtubule growth in arbors, microtubule stability, or at the level of microtubule capture and anchoring at synapses. In addition, we did not find changes in the filopodia dynamics in CaPs, which could indicate defective trophic signaling, since filopodia dynamics were normal, as was the transport of the p75 low-affinity trophic receptor. Overall, we suggest a role for *dynactin1* in synapse stability, where the loss-of-function of this gene leads to growth defects, electrophysiological abnormalities and behavioral deficits. Surprisingly, this role appears to be independent of its known function as a regulator of dynein, its implication in axonal transport, or its regulation of microtubule dynamics.

Résumé

La sclérose latérale amyotrophique (SLA) est une pathologie neurodégénérative progressive se déclarant vers 50-60 ans. Elle est majoritairement de nature sporadique son incidence est estimée à 1-2 par 100 000. La SLA mène à une paralysie progressive et entraîne généralement à la mort des patients de 2 à 5 ans suivant le diagnostic aux suites d'une fonte musculaire importante liée à la perte des neurones moteurs. Au cours des années, plusieurs mutations ont été identifiées autant chez les patients atteints de SLA sporadique que de SLA familiale. Ces mutations interfèrent avec la fonction de gènes variés, tels que *DCTN1*, codant pour la protéine dynactine1, sous-unité du complexe multimoléculaire dynactine. Ce complexe sert d'adaptateur au moteur moléculaire dynéine, chargé du transport axonal rétrograde, où sa fonction permettrait de régir l'activité du complexe moteur et sa capacité à lier divers cargos, mais son rôle dans le développement de la SLA demeure spéculatif. Nous avons donc entrepris la caractérisation d'une lignée de poissons zèbre mutants pour *dynactin1a* (nommés *mikre oko*^{m632}, *mok*^{m632}), plus particulière en terme du développement d'un type de neurone moteur primaire (les CaPs), afin de déterminer l'effet de la perte de fonction de ce gène sur l'axonogenèse, la formation et la stabilisation de la jonction neuromusculaire, sur le comportement de l'embryon, ainsi que sur le transport axonal.

Nous avons observé une activité locomotrice anormale à 48hpf suggérant un phénotype de fatigue de la jonction neuromusculaire. Nous rapportons aussi une morphologie anormale des CaPs chez les embryons homozygotes à 6dpf, qui présentent une arborisation de taille et de complexité réduite. La jonction neuromusculaire a aussi révélé des défauts structuraux, où les sites pré- et post synaptiques sont désalignés. Au niveau fonctionnel toutefois, l'analyse de fusions spontanées de quanta (mEPC) à la jonction neuromusculaire n'a pas révélé d'anomalies, suggérant que les mécanismes de fusion sont fonctionnels chez notre mutant. Des enregistrements couplés neurone moteur-fibre musculaire ont ensuite été effectués à 6dpf, révélant une activité anormale de décharge neuronale suite à des stimulations de haute et basse fréquence, où les embryons mutants démontrent des échecs de réponse au niveau du muscle, ainsi qu'une augmentation de décharges asynchrones. De plus, une étude de la jonction neuromusculaire des embryons mutants a révélé une diminution du nombre de synapses putatives, qui étaient également de taille réduite et à caractère instable. Nous suggérons que cette instabilité mène aux défauts de croissance des CaP, aux anomalies électrophysiologiques, qui engendrent le comportement anormal. Nous avons obtenu le sauvetage du phénotype morphologique des CaPs mutants par surexpression de la protéine humaine Dynactine1-GFP, alors que cette même surexpression n'a eu aucun effet sur la structure des CaPs chez les embryons de type sauvage. La protéine humaine ainsi surexprimée est localisée au niveau des synapses, suggérant un rôle pour dynactin1 dans la stabilité synaptique.

Le transport axonal a été analysé et quantifié chez les neurones moteurs primaires par usage du système bipartite GAL4/UAS et l'expression de protéines de fusion permettant le suivi *in vivo* des cargos par imagerie confocale de type *time-lapse*. Nous avons examiné le transport *in vivo* de cargos tels que les mitochondries, les endosomes précoces, matures et de recyclage au sein des CaPs d'embryons de type sauvage versus mutants pour *mok*^{m632}. Nous n'avons cependant pas distingué de changement dans la cinétique de transport des cargos (stable, antérograde ou rétrograde) et quoique nous ayons noté quelques différences en termes de comportement, la vue d'ensemble des résultats suggère que la dynactine1 n'est pas essentielle à l'activité de la dynéine et au processus de transport axonal. Nous avons ensuite examiné l'interaction de la dynactine1 avec le cytosquelette et n'avons pas observé de défauts au niveau de la croissance

des microtubules au sein de l'arborisation axonale, ni au niveau de la stabilité des microtubules ou de leur capture fin d'ancrage synaptique. De plus, aucun changement n'a été détecté chez les CaPs indiquant un potentiel défaut de traitement des signaux trophiques. En effet, la dynamique des filopodes d'actine s'est avérée normale, ainsi que le transport des récepteurs trophiques de faible affinité p75.

Somme toute, nous suggérons que *dynactin1* favorise la stabilité synaptique, où une perte de fonction de ce gène entraîne des défauts de croissance, des anomalies électrophysiologiques et un comportement anormal. Ce rôle semble être indépendant des fonctions connues de régulateur du moteur dynéine, de son implication dans le transport axonal ou de son action sur la dynamique des microtubules.

List of abbreviations

A.a.: Amino acid

AChR: Acetylcholine receptor

ALS: Amyotrophic lateral sclerosis

AnkB: Ankyrin-B

Arl3: ADP-ribosylation factor-like 3

Bp: Base pairs

BSA: Bovine serum albumin

CaP: Caudal primary motor neuron

CAP-Gly: cytoskeletal-associated protein glycine-rich

CHCHD10: Coiled-coil-helix- coiled-coil-helix domain containing protein 10

CLIP-170: Cytoplasmic linker protein-170

CMT2F: Charcot-Marie-Tooth type 2F

CRISPR/Cas9: Clustered regularly interspaced palindromic repeats/CRISPR-associated protein 9

CSF: Cerebrospinal fluid

DDB: Dynein-dynactin-BicD2 complex

DIC: Dynein intermediate chain

Dpf: Days post-fertilization

DMSO: Dimethyl sulfoxide

EB: End-binding proteins

ENU: N-ethyl-N-nitrosourea

ER: Endoplasmic reticulum

fALS: Familial ALS

FTD: Fronto-temporal dementia

HAP1: Huntingtin-associated protein1

Hpf: Hours post-fertilization

HMN7B: Distal hereditary motor neuropathy type VIIB

HSP: Hereditary spastic paraplegia

ICM: Institut du Cerveau et de la Moelle Épineière, Paris, France

JIP1: C-jun-amino-terminal kinase-interacting protein 1

LC8: Dynein light chain 8

Lis1: Lissencephaly1 or Platelet-activating factor acetylhydrolase IB subunit alpha

MAPs: Microtubule-associated proteins

MiP: Middle primary motor neuron

MND: Motor neuron disease

NGF: Nerve growth factor

NMJ: Neuromuscular junction

ORF: Open reading frame

ORPL1: Oxysterol-binding protein-related protein 1

PI3P: Phosphatidylinositol 3-phosphate

PBS: Phosphate-buffered saline solution

Rab11-FIP3: Rab11 family-interacting protein

RILP: Rab7-interacting lysosomal protein

ROI: Region of interest

RoP: Rostral primary motor neuron

sALS: Sporadic ALS

SBMA: Spinal bulbar muscular atrophy

SNARE: Soluble NSF adaptor proteins (SNAPs) receptors

SNX6: Sorting nexin 6

SOD1: Superoxide dismutase 1

TBCB: Tubulin-binding cofactor B

TEER: Touch-evoked escape response

UAS: Upstream activating sequence

UPR: Unfolded protein response

VNR: Ventral nerve root

Table of contents

Acknowledgements	ii
Abstract	iv
Résumé	v
List of abbreviations	vii
Table of contents	x
Introduction	1
I-ALS	1
I.1-Pathophysiology	3
I.2-The neuromuscular junction (NMJ)	6
II-Dynactin1	7
II.1-The different domains of dynactin1	9
II.2-Disassembly of the dynactin complex from dynein	11
II.3-Axonal transport	12
II.4-The neuronal cytoskeleton	13
II.5-Synapse stability	16
II.6-Alternative splicing: p135 versus p150	18
II.7-Mutations and associations with human disease	18
III-The zebrafish animal model	22
III.1-The zebrafish spinal cord and NMJ	22
III.2-Mutant zebrafish line for <i>dynactin1a</i>	23
III.3-Role of <i>dynactin1b</i>	24
IV-Aim of the thesis	26
Results	28
I-Morphological phenotype of the <i>mikre oko (mok)</i> ^{m632/-} embryos	28
II-Motor behavior at 48hpf	29
III-Axonal morphology and neuromuscular junction structure	30
IV-Axonal morphology at 48hpf and 6dpf	31
V-Neuromuscular junction structure at 48hpf and 6dpf	33
VI-Quantitative RT-PCR profile of 6dpf <i>mok</i> ^{m632/-} embryos	35
VII-Rescue of the axonal morphology phenotype with human DCTN1	36
VII.1- Axonal morphology at 6dpf	37
VII.2-Axonal morphology at 48hpf	38
VIII-Putative synapse number at 48hpf and 6dpf	39
IX- Putative synapse stability at 48hpf	41
X-Spontaneous activity of the CaPs in the spinal cord at 4dpf	42
XI-Neuromuscular junction mEPC at 6dpf	43
XII- Neuromuscular junction paired-recordings at 6dpf	45
XIII- Axonal transport	46
XIII.1-Choice of cargo and method of expression	47
XIII.2-Cargo distribution at 48hpf	48
XIII.3-Cargo behavior and run metrics at 48hpf	50
XIII.4-Caveats of the expression method	57
XIV-Trophic signaling involvement	59
XIV.1- Actin filopodia dynamics from 48hpf	59
XIV.2-p75 receptor axonal transport	61
XV- Microtubule stability at 48hpf and 6dpf	63
XVI- Microtubule growth at 48hpf and 6dpf	64

XVII- Synaptic microtubule capture at 48hpf and 6dpf.....	66
XVIII- Adhesion molecules at the NMJ (N-Cadherin).....	68
XIX- Controls and validation.....	69
XIX.1- <i>dynactin1b</i> CRISPR/Cas9 mutant generation.....	69
XIX.2-Other dynein/dynactin mutant and DN-dynactin1 axonal morphology.....	73
Discussion	74
Conclusion and perspectives	87
Materials and Methods	88
I-Zebrafish husbandry and transgenic lines	88
I.1- list of zebrafish lines.....	88
II-Microinjections.....	88
III-DNA extraction and genotyping	88
III.1- <i>mok</i> ^{m632} genotyping	89
III.2- <i>dynactin1b</i> ^{*253} genotyping	89
IV-Molecular cloning.....	89
IV.1-Gateway cloning	90
IV.2-Gibson assembly cloning.....	91
IV.3-List of constructs used	92
V-Touch-evoked escape response assay	93
VI-Microscopy and image analysis.....	93
VI.1-Morphological images	93
VI.2-Spinning disk confocal	93
VII-Whole-mount immunohistochemistry	94
VII.1-List of antibodies	95
VIII-Quantitative RT-PCR.....	95
VIII.1-List of primers.....	96
IX-Calcium imaging of fictive swimming (Kevin Fidelin, Claire Wyart laboratory)	96
X-Electrophysiology (Jeffrey M. Hubbard, Claire Wyart laboratory).....	97
XI-CRISPR/Cas9-mediated knock-in of <i>dynactin1b</i>	98
XII-Graph generation and statistical analysis	99
References	100
Annex	114
Annex 1-Research article: Deletion of a kinesin I motor unmask a mechanism of homeostatic branching control by neurotrophin-3. Auer, Xiao, Bercier et al, eLife, 2015	114
Table of figures	141
List of tables	148

Introduction

I-ALS

Amyotrophic lateral sclerosis (ALS) is a neurodegenerative disease arising in mid-life, which is mainly sporadic in nature (sporadic ALS, sALS, over 90% of patients). World-wide incidence is 1-2 per 100 000, making it the most common adult-onset motor neuron disease, and one of the most common adult-onset neurodegenerative disease. This progressive pathology causes dysfunction leading to cell death of upper and lower motor neurons in a non-cell-autonomous manner, and is characterized by insoluble inclusions of ubiquitinated protein in the cell body, as well as axonal accumulation of neurofilament (Shaw, 2005; Wijesekera & Leigh, 2009).

It generally leads to the demise of patients within 2-5 years of diagnosis owing to respiratory failure caused by muscle wasting and severe motor neuron loss. ALS symptoms vary between patients and is diagnosed based on clinical presentation of typical signs and progression (according to the El Escorial Diagnosis Criteria) as well as on exclusion of other disease with similar symptoms (Wijesekera & Leigh, 2009). Moreover, it is a heterogeneous pathology, where several causative genes and risk factors have been identified in both sALS and familial ALS (fALS) patients. To date, more than 20 different genes have been linked with this disease, leading to ALS subtype classifications, including the well-known *SOD1*, *TARDBP*, *FUS/TLS*, and *C9orf72*, but also more rare occurrences like *UBQLN2* and *DCTN1*, which were identified in very few patients (Moloney, de Winter, & Verhaagen, 2014). Furthermore, many patients often have mutations in more than one gene at once, which could be explained by low penetrance, and supported by the interindividual variability exhibited in clinical presentation within carriers or the same mutation of the same family (Therrien, Dion, & Rouleau, 2016). Accordingly, the pathophysiology of ALS when considering the disease as a whole is complex. While most ALS cases exhibit the same early signs like electrophysiological abnormalities and degeneration of the connection between motor neuron and muscles cells (Sleigh, Burgess, Gillingater, & Cader, 2014), many mechanisms have been proposed to explain the specific degeneration of motor neurons and could possibly be used to strengthen classification and for the elaboration of targeted therapy in personalized medicine.

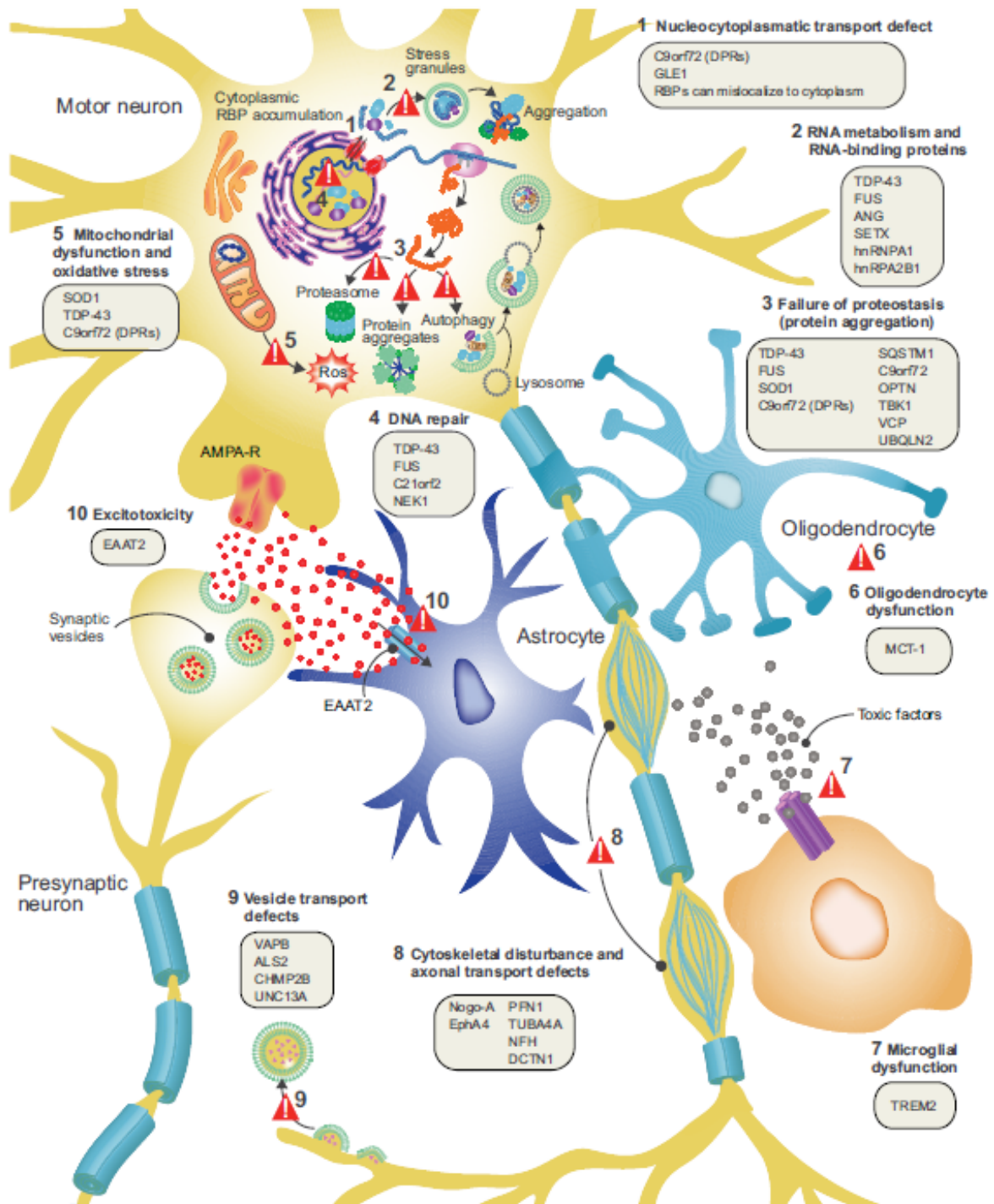


Figure 1: Pathophysiological mechanisms proposed to underlie ALS motor neuron degeneration. The mechanisms shown here include 1- changes in transport of mRNAs and RNA-binding proteins in the cytosol and nucleus, 2-impaired RNA metabolism due to mislocalization of RNA-binding proteins, formation of stress granules, aggregate formation, 3-impaired proteostasis overloading the proteasome with reduced autophagy lead to protein aggregate accumulation, 4-impaired DNA repair, 5-mitochondrial dysfunction and oxidative stress caused by disruption of the organelle's normal function, and the accumulation of ROS, 6-glia implication, degeneration and dysfunction leading to reduced support of neurons, 7-neuroinflammation caused by activated astrocytes and microglia, 8-perturbed axonal transport due to disorganization of the cytoskeleton, 9-impaired vesicular transport, 10-escitotoxicity caused by impaired EAAT2 function. (Adapted from Van Damme, Robberecht, & Van Den Bosch, 2017)

I.1-Pathophysiology

Protein misfolding and aggregation has historically been thought to be a major component of the ALS pathogenic mechanism. This is due to the fact that ubiquitinated protein inclusions are a prominent feature of ALS and other neurodegenerative diseases, but also because the insoluble aggregates found in patients' brain tissue contain misfolded and truncated versions of mutant proteins like TDP-43 (*TARDBP*), FUS and SOD1. However, multiple other mechanisms of action have been proposed to be involved, perhaps even acting synergistically or in succession, in the pathogenesis of ALS. Notable examples include mitochondrial disturbances, endoplasmic reticulum (ER) and oxidative stress, excitotoxicity and axonal transport defects. In addition, the implication of non-neuronal cells, like glia and muscle fibers, has also been demonstrated to have an essential role in disease progression (Ilieva, Polymeridou, & Cleveland, 2009; Shaw, 2005).

I.1.1-Protein aggregates

The presence of protein aggregates present in motor neuron cytosol of ALS patients is a hallmark of this neurodegenerative disease, but their role is debated. It has been hypothesized that these aggregates could interfere with normal cellular function by sequestering essential proteins, by acting as hindrance in the way of axonal transport or by mobilizing the proteasomal degradation pathway (Atkin et al., 2013). However, whether these defects are causative of degeneration or a way for the cell to manage the chaos by clearing away defective proteins is still uncertain (Wijesekera & Leigh, 2009).

As these aggregates often contains proteins encoded from genes mutated in ALS patients (like TDP-43, FUS, OPTN, UBQLN2 and C9ORF72), are found in tissues of fALS and sALS patients alike, as well as in the context of other neurodegenerative disease, this mechanism suggests a convergence to defects in the protein quality control process leading to neurodegeneration (Blokhuis, Groen, Koppers, van den Berg, & Pasterkamp, 2013).

I.1.2-Mitochondrial dysfunction

Mitochondria are essential to proper function of a neuron, as they are the “cell powerhouses”, providing energy by production of ATP, but are also involved in calcium

homeostasis and apoptotic mechanisms. ALS patients often have mitochondrial abnormalities, where energy metabolism is impaired (Wijesekera & Leigh, 2009) and present with misregulated intracellular calcium (Jaiswal, 2013). As calcium is a known secondary messenger, with roles in regulating metabolic pathways, cell development, and growth of synapses, many studies have focused on how this could lead to motor neuron degeneration (Aren et al., 2015).

The first gene identified as causative in ALS was superoxide dismutase 1 (*SOD1*), which encodes a cytoplasmic antioxidant found at the mitochondrial outer membrane. This mutant protein leads to misfolding and ubiquitinated accumulations, but also to mitochondria vacuolation and degeneration (Soo, Farg, & Atkin, 2011). In a mouse model, it was found that misfolded mutant *SOD1* formed aggregates inside mitochondria, leading to fragmentation and depolarization of the membrane potential before the onset of symptoms (Luo et al., 2013). A new mutation has also been identified in ALS patients, disrupting the gene encoding coiled-coil-helix- coiled-coil-helix domain containing protein 10 (*CHCHD10*). The function of this protein is still unknown but it localizes at the mitochondrial inner membrane and is reported to be involved in oxidative phosphorylation (Therrien et al., 2016).

In addition, abnormal mitochondrial dynamics and altered localization were also seen in TDP-43 overexpression and loss-of-function mice models, suggesting that mitochondrial dysfunction could be a common mechanism among multiple disease models and patients alike (Magrané, Cortez, Gan, & Manfredi, 2014; W. Wang et al., 2013).

I.1.3-ER and oxidative stress

Post-mortem studies have revealed evidence for free radical damage in the (cerebrospinal fluid) and CNS tissue of ALS patients. This is not surprising as reactive oxygen species cause stress, which can lead to cell death, especially in post-mitotic cells like neurons, and as these effects can be cumulative it corroborates the link between ALS and aging. Moreover, mutations in *SOD1*, coding for superoxide dismutase, an enzyme involved in the clearance of the superoxide radical O_2^- , supports the involvement of this mechanism in neurodegeneration (Shaw, 2005).

ER stress can be triggered by multiple events in a diseased neuron, like the production of misfolded proteins or defects in trafficking, and can induce a number of pathways of stress

response. In many cases, this leads to the activation of the unfolded protein response (UPR), which acts as a quality control for misfolded proteins and helps restore homeostasis by inducing degradation, and when overactivated, it can lead to apoptosis (Matus, Valenzuela, Medinas, & Hetz, 2013). It was also suggested that different types of motor neurons have a variable degree and threshold for ER stress response, which might explain selective vulnerability of certain types of muscle fibers to denervation and degeneration (Matus et al., 2013; Saxena & Caroni, 2011).

I.1.4-Excitotoxicity

Excitotoxicity is a result of the overstimulation of glutamate receptors resulting from defective intracellular calcium homeostasis or free radical abundance. Glutamate is the preponderant excitatory neurotransmitter in human CNS and its role in fast synaptic transmission relies on the cell-surface expression of AMPA receptors found in neurons, and on reuptake mechanisms via glutamate transporters like *EEAT2*, which are found in neurons and glia. This supports a role for non-cell autonomous mechanisms in ALS pathogenesis (Shaw, 2005). Reduced levels of *EEAT2* mRNA have been found in ALS patient CSF, which is thought to lead to the decreased expression of the transporter. Diminished *EEAT2* function, and thus excess extracellular glutamate, lead to increased stimulation of glutamate receptors and excess calcium influx into the cell, which impairs calcium signaling and could lead to degeneration (Aren et al., 2015).

Interestingly, the only approved treatment for ALS at this time, riluzole, is known to enhance glutamate clearance.

I.1.5-Axonal transport

Motor neurons have a high metabolic rate and need to extend very long axons to form contact with muscles. They also have a high expression of AMPA receptors and glutamate transporters, as well as low expression of calcium-binding proteins, which are necessary for calcium buffering. In addition, they have a high threshold for the initiation of heat shock response, which lowers their ability to cope with stress (Shaw, 2005). All these characteristics could make motor neurons particularly vulnerable to defects arising from the pathogenic mechanisms described above, but most importantly means that they rely heavily on axonal transport to supply mitochondria as well as newly synthesized proteins and mRNAs to

synapses, for the distal clearance of detritus, aging organelles and vesicles, and for relaying back signals from the periphery to the cell body.

It is therefore no surprise that axonal transport defects have been reported in ALS patients and models alike, with hallmark signs like organelle and vesicle accumulation, degradation defects, impaired stress signaling and mitochondria dysfunction (Soo et al., 2011). Some studies investigated transport dynamics in transgenic mice or neuronal cell culture and found a reduction in both slow and fast axonal transport affecting various cargoes such as mitochondria, early and late endosomes, as well as TrkB vesicles (Brady & Morfini, 2017; De Vos & Hafezparast, 2017; Encalada & Goldstein, 2014; Millecamps & Julien, 2013; Eran Perlson, Maday, Fu, Moughamian, & Holzbaur, 2010).

Considering the dynamics of axonal transport, the defects observed in neurodegenerative diseases could have different causes: preferential type of cargo selection for transport, varying load size (possibly due to protein aggregation) or depletion/dilution of the motor protein population, which could affect development, maintenance or survival of the neurons (Mitchell & Lee, 2012). Independently from the motor dynamics defects, there could be other impairments depending on cargo adapter proteins or chemical mediators, like phosphorylation (Blasier et al., 2014; Gibbs, Greensmith, & Schiavo, 2015).

In the context of ALS, whether the observed axonal transport defects are causative of neurodegeneration or consequences of other pathophysiological processes, like mitochondrial disturbances or protein aggregates, is yet to be determined (Millecamps and Julien, 2013). Indeed, impairments at any level of this process could affect cell survival and lead to neurodegeneration, but the identification of particular dysfunction, a disease-specific “pathogenic signature” which might be particular to mutations or pathophysiological mechanism, could open up new therapeutic avenues and warrants investigation.

I.2-The neuromuscular junction (NMJ)

The neuromuscular junction is an early target in ALS, as molecular changes at this level occur before the onset of neurodegeneration (Moloney et al., 2014).

Fast-fatigable, fast-fatigable-resistant, and slow muscle fibers are the three functional types of mammalian muscle units innervated by motor neurons. In ALS mice models, fast-fatigable muscle fibers get denervated first, before onset of clinical symptoms. This is followed

by denervation of fast-fatigable resistant fibers in the late symptomatic phase, and finally the slow muscles lose their connections in the end stage (Saxena & Caroni, 2011).

These three functional muscle subtypes express distinct muscle protein isoforms, and were studied in mice to determine their specific synaptic plasticity. Selective synapses were shown to be weakened in various mice models of motor neuron disease, including the *SOD1* (G93A) mice, leading to denervation before motor neuron death and onset of clinical symptoms. This weakening was attributed to the intrinsic properties of various types of synapses present at the NMJ, with the most vulnerable ones, present on fast-fatigable muscle fibers, as they were shown to have a low competence for terminal sprouting (Frey et al., 2000). Thus, the specific properties of motor neurons, muscles and NMJ synapses, which could be affected by pre- and postsynaptic environment, are thought to be responsible for the selective vulnerability of fast-fatigable neuromuscular synapses to degeneration in motor neuron disease.

II-Dynactin1

Neurons are highly polarized cells, with a network of dynamic microtubules connecting distal synapses with the soma. These tubules, polymers of tubulin, are composed of a fast growing (+) and a slow growing (-) end; in axons, they are organized with the fast growing, unstable end (+) oriented towards the synapse and the more stable (-) end is oriented towards the nucleus at the level of the soma. This component of the cytoskeleton provides the rails on which intracellular transport is carried out. As the synthesis of new proteins takes place in the cell soma, axonal transport is known to be essential for growth and maintenance of synapses.

During this process, ATP-driven molecular motors that move unidirectionally along the axonal microtubule network transport organelles and vesicles. This transport is mediated by two types of molecular motors: the kinesin superfamily, transporting cargoes towards the synapse (anterograde, towards microtubule fast-growing ends) and the dynein motor protein complex, moving from the synapse to the cell body (retrograde). The 45 diverse kinesin members have different roles and are subdivided into 14 families based on the heterogeneous structure of their motor and tail domains, while the dynein motor, which has one major assembly, relies partly on isoform expression and mostly on adaptor polypeptides, like the dynactin complex, for functional versatility. Many motor proteins are present on cargoes

simultaneously, and most cargoes alternate between them by coordinated regulation, allowing for bidirectional transport along microtubule tracks (Akhmanova & Hammer III, 2012).

The dynein macromolecular complex has been proposed to regulate dynein activity, and to be essential for the motor complex recruitment to microtubules distal ends, which serve as a loading point for the dynein motor and the recruitment of cargo, while providing a supposed “crutch” of extra support for attachment (Chowdhury, Ketcham, Schroer, & Lander, 2015; Waterman-Storer, Karki, & Holzbaaur, 1995).

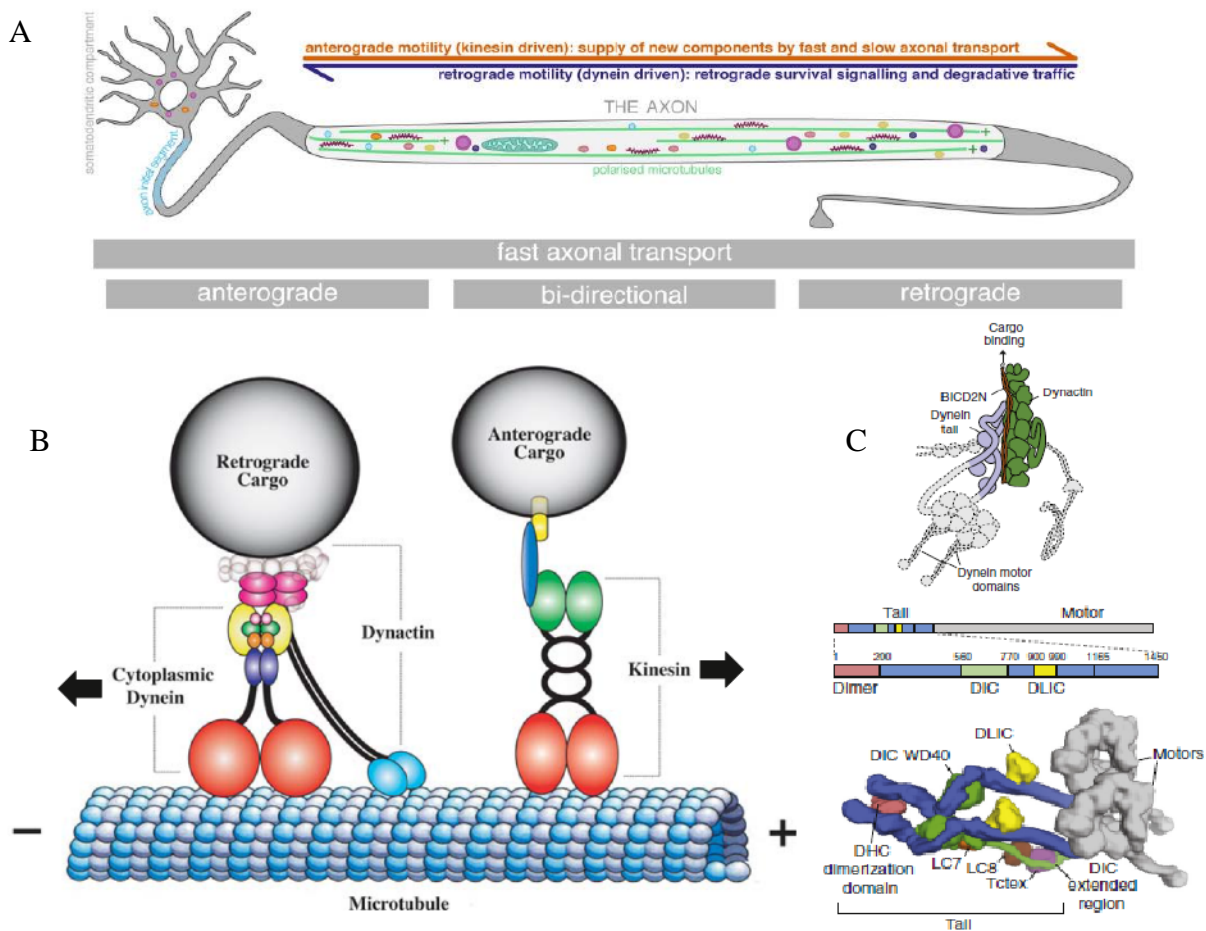


Figure 2: Axonal transport and its molecular motors. A) Representation of axonal transport in a motor neuron, where a very long axon separates the site of protein synthesis, the soma, from the synapse. This highlights the dependence of those neurons on a functional process, both for signaling between the growing synapse and the cell body, the supply of proteins and organelle for growth, but also for the removal of detritus for degradation. B) Schematic illustration of the anterograde dynein-dynactin motor complex and the retrograde kinesin complex on a microtubule track. The dynactin complex is an adaptor complex that binds the motor complex of dynein to regulate its activity. The dynactin1 subunit is represented here as a dimer, demonstrating its binding capacity for dynein and the dynactin complex-black stripes, and with microtubules-blue circles. C) Protein structure with identified structural domains of the dynein motor complex. A reconstruction of the complex shows how the heavy motor chains are assembled with the intermediate and light chains, forming the tail that binds the motor complex to the dynactin complex. (Adapted from Carter, Diamant, & Urnavicius, 2016; Duncan & Goldstein, 2006; Maday, Twelvetrees, Moughamian, & Holzbaaur, 2014)

It is composed of 11 subunits organized into structural domains: dynactin1 (*DCTN1*, also called p150), dynamitin (*DCTN2*, also called p50), and p22/p24 (*DCTN3*), forming the “projecting arm”, and Arp1 (*ACTRIA*), CapZ and β -actin, forming the “Arp1 rod”, and Arp11 (*ACTR10*), p62 (*DCTN4*), p25 (*DCTN5*), and p27 (*DCTN6*) forming the “pointed end complex”. In the projecting arm, subunits are present as self-associated polymers, where four copies of dynamitin, two copies of both dynactin1 and p22/24 are present (Schroer, 2004).

Dynactin1 is the largest subunit of the dynactin adaptor complex (Schnapp & Reese, 1989) and serves as the link between the two heavy chains of the dynein motor and their cargo, where the interaction occurs at the level of the intermediate chains (K. T. Vaughan & Vauee, 1995). In addition to dynein intermediate chains, dynactin1 has been found to bind directly to microtubules and to another subunit of the dynactin complex, namely actin-related protein contractin 1 (Arp-1) (Waterman-Storer et al., 1995).

The dynactin1 subunit is encoded by the *DCTN1* gene in humans (ENSG00000204843; OMIM 601143) and is composed of 32 exons, forming a full-sized protein of 150kDa harboring multiple functional domains.

II.1-The different domains of dynactin1

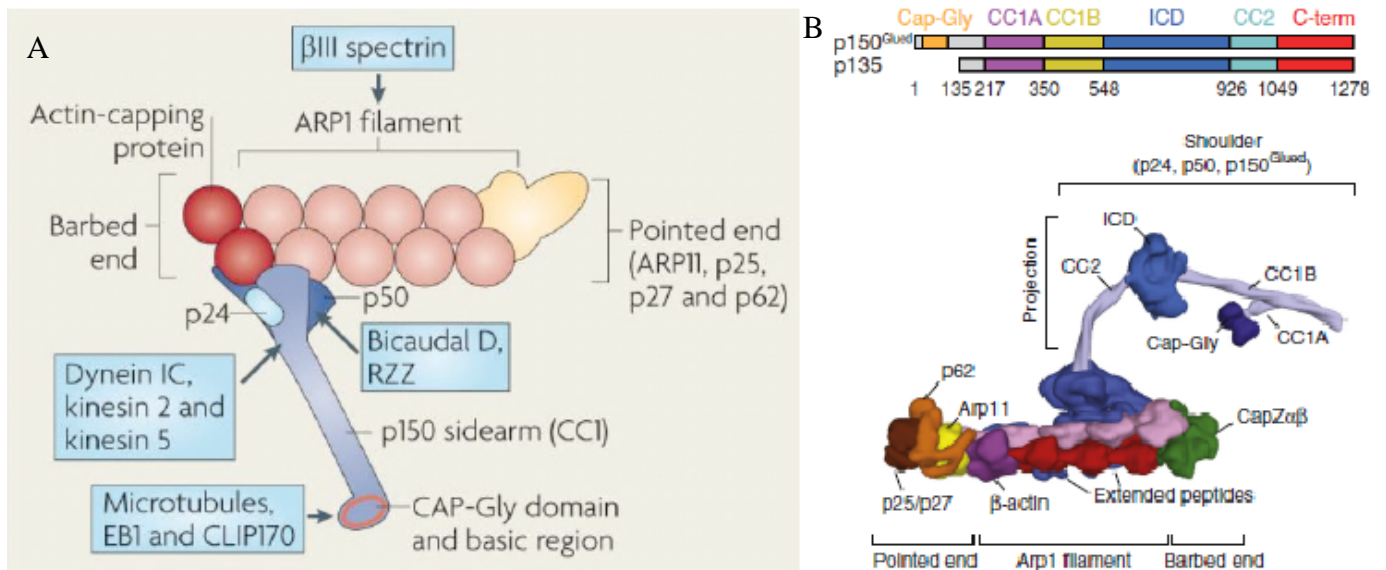


Figure 3: Schematic representation of the dynactin complex. A) The dynactin complex is composed of 11 subunits that are assembled into three structural domains: the projecting arm domain (dynamitin/p50, dynactin1, and p22/24), the arp rod domain (Arp1, CapZ and β -actin), and the pointed end domain (Arp11, p62, p25 and p27). Many of the subunits in this complex are known to interfere with other proteins (identified in blue boxes), which could regulate the assembly or function of the complex. B) Protein domains of the dynactin1 subunit with identified functional domains. This gene produces two isoforms, including a shorter 135kDa isoform lacking the microtubule-binding CAP-Gly domain. The functional domains of dynactin1 gives the subunit an arm-like shape, which allows interaction with other subunits of the complex, as well as the dynein motor and microtubules. (Adapted from Kardon & Vale, 2009; Sorbara et al., 2014; Urnavicius et al., 2015)

The N-terminal cytoskeletal-associated protein glycine-rich domain (CAP-Gly) is responsible for this subunit's interaction with microtubules, a process which is concentration dependent (Ayloo et al., 2014), and regulated by phosphorylation (Vaughan, Miura, Henderson, Byrne, & Vaughan, 2002). This domain is however not necessary for processivity of dynein, once it is loaded onto microtubule, as a truncated dynactin1 lacking the N-terminus, does not interfere with retrograde transport (Kim et al., 2007; Tripathy et al., 2014). The CAP-Gly domain has however been shown to confer dynactin1 with a “skating” function along microtubules which allows for greater stability in dynein's binding to microtubules, thus preventing the detachment of the dynein-dynactin-cargo complex during active transport (Culver–Hanlon, Lex, Stephens, Quintyne, & King, 2006). Furthermore, it has been proposed that the CAP-Gly domain's interaction with microtubule during axonal transport enhances the processivity of dynein under heavy load, also by preventing detachment, meaning it could act as a module necessary for greater force generation by the retrograde motor (Moore, Sept, & Cooper, 2009). This domain has been reported to bind to other +tip microtubule-binding proteins like CLIP-70 and end-binding protein 1 (EB1) (Schroer, 2004), where these interactions have been respectively involved in loading of dynein at microtubule + end and modulation of microtubule anchoring at the centrosome (Askham, Vaughan, Goodson, & Morrison, 2002; Vaughan, Tynan, Faulkner, Echeverri, & Vallee, 1999). Importantly, the interaction of dynactin1 with microtubules is known to be independent of its interaction with dynein.

The basic domain, rich in basic amino acids, immediately follows the CAP-Gly domain, and is also within the microtubule-binding region of dynactin1. It was shown to be present only in neuron-specific splice forms of the protein and could be sufficient for microtubule-binding, but both this domain and the CAP-Gly domain are necessary for microtubule polymerization, and the reduction of microtubule catastrophe (Lazarus, Moughamian, Tokito, & Holzbaur, 2013).

The first coiled-coil domain (CC1) is responsible for binding to dynein, and is split into two separate domains with different functions: CC1A and CC1B. Both of these subdomains were found to bind dynein directly. It was also reported that they both have an effect on dynein processivity, CC1B by promoting it and CC1A by favoring a diffusive state, and that they interact with each other and with the N-terminal portion of dynactin1 to coordinate the different states of dynein motility (Tripathy et al., 2014). Additionally, when expressed by itself, the CC1

fragment has been shown to inhibit dynein motility due to its ability to compete with the binding of both a fully assembled dynactin complex and NudE-Lis1, another regulatory complex, to dynein.

The second coiled-coil domain (CC2) is responsible for many protein-protein interactions and contains an actin-binding motif that acts as a link with the Arp-1 subunits, which forms the base of the dynactin complex (Schroer, 2004; Waterman-Storer et al., 1995).

The C-terminus of dynactin1 also has a “cargo-binding” domain known to bind to vesicular adaptors like rab7-interacting lysosomal protein (RIPL) (Johansson et al., 2007), huntingtin-associated protein1 (HAP1), retromer protein sortin nexin 6 (SNX6) and c-Jun regulator JIP1 (MAPK8IP1) (Fu & Holzbaur, 2014).

The existence of an additional dynein-interacting domain of dynactin, located between the CC1 and the CC2 is debated, but known to be involved in the unloading of cargo by interaction with ADP-ribosylation factor-like 3 (Arl3). This function is carried out by dissociation of dynactin from dynein, with the help of LC8 (dynein light chain 8, smallest subunit of the dynein motor) which interacts with DIC (dynein intermediate chain) (Jin, Yamada, Arai, Nagai, & Hirotsune, 2014).

II.2-Disassembly of the dynactin complex from dynein

The disassembly of dynactin from dynein is thought to be part of the mechanism of cargo unloading and relies on the interaction between AnkyrinB (AnkB), which is bound to membrane cargoes, and dynactin1, which is bound to the rest of the dynactin complex as well as dynein (Lorenzo et al., 2014). However, many ways to disrupt the dynein-dynactin interaction have shown to affect the function of this complex.

Dynamitin (*DCTN2*) is known to be the link between the projecting arm structure and the rest of the dynactin complex via interactions with Arp-1 (Cheong, Feng, Sarkeshik, Yates, & Schroer, 2014) and dynactin1 (Carter et al., 2016) and its overexpression has been found to lead to disassembly of the dynein-dynactin complex, inhibiting minus-end directed movement (Burkhardt, Echeverri, Nilsson, & Vallee, 1997; Echeverri, Paschal, Vaughan, & Vallee, 1996). Interestingly, it was reported that this overexpression led to the loss of the ARP1 portion of the complex from microtubules without affecting microtubule-associated dynactin1 or CLIP-70 (Vaughan et al., 1999).

Furthermore, the overexpression of the CC1 domain of dynactin1 has also been shown to interfere with the dynein-dynactin complex assembly, as well as affecting microtubule organization. In this case, the overexpressed fragment is acting in a competitive manner where free CC1 binds to dynein and leaves the rest of dynactin assembled independently of dynein (Quintyne et al., 1999). Many of these methods have been used to probe the function of the dynactin complex and dynactin1 specifically, but the disassembly might also affect regulation or the assembly of different regulatory complexes or disrupt normal interactions.

II.3-Axonal transport

The dynactin complex is thought to be essential for axonal transport via the dynein motor complex and the dynactin1 subunit has a very important role to play in many aspects of this crucial function.

For instance, dynactin1 is known to interact with kinesin motors and has been suggested to be involved in the control of bidirectional transport. As kinesins and dyneins are found bound to the same cargoes, a tug-of-war mechanism was proposed to direct the switching between retrograde and anterograde movement, but it was noted that enhanced recruitment or inhibition of motors could produce a directional bias in the movement of vesicles and organelles (Hendricks et al., 2010).

Dynactin was also reported to interact with kinesin-2 via the dynactin1 subunit, which enhances its processivity by increasing run lengths. This interaction was shown to depend on dynactin1's binding to microtubules (Berezuk & Schroer, 2007). Another study reported that dynactin1 bound kinesin-2 and dynein's intermediate chain via the same domain, but not simultaneously (Deacon et al., 2003). This subunit is thus believed to be involved in the regulation of bidirectional transport, and that the inhibition of a motor in one direction can affect a motor in the opposite direction.

Axonal transport-regulating scaffolding proteins also have an important role to play, like C-jun-amino-terminal kinase-interacting protein 1 (JIP1), which also requires binding to dynactin1 to interact with kinesin heavy chain in order to regulate bidirectional transport of APP in neurons. It was reported that the interaction of JIP1 with dynactin1 and kinesin was mutually exclusive, competitive when bound to dynactin1, and regulated by phosphorylation (Fu & Holzbaur, 2014).

Furthermore, interaction of dynactin1's CAP-Gly domain with EBs has also been shown to be necessary for the retention of this subunit at microtubule distal ends, a necessary process to initiate axonal transport (Moughamian & Holzbaaur, 2012). As dynactin1 was first identified as part of the dynactin complex regulating dynein activity, and its most studied domain is the CAP-Gly domain, a major part of this subunit's function will involve interactions with the neuronal cytoskeleton, an important player in axonal transport.

II.4-The neuronal cytoskeleton

The cytoskeleton is composed of three components: microtubules, actin, and neurofilaments. Microtubules are essential to neuronal polarity, and the polymerization of their tubulin subunits into protofilaments results in the assembly of dynamic fast-growing +ends oriented towards the synapse in axons. Neurofilaments are also part of the axonal architecture, where they provide structure and regulate axonal caliber. Actin filaments constitute the network supporting the growth cone and pre-, as well as postsynaptic region, essential for plasticity, and play an important role in dendrites where they form the spines. Transport on actin is mediated by myosins is essential at the synapse for the recycling of receptors or vesicles, and tethering of synaptic components. The actin and microtubule components of the cytoskeleton can influence each other's polymerization, and interact with each other for proper guidance during growth cone migration, and for establishment of arborisation, a process which requires reorganization of existing cytoskeletal structures (Dent & Kalil, 2001).

The microtubule network, providing the rails for active axonal transport, is regulated by motor proteins and microtubule-associated proteins (MAPs), which influence both its dynamics and function. End-binding proteins belong to the latter category, and bind to the + ends of microtubules (+ tip proteins) to play a role in stability, but also to regulate interactions with organelles, coordinate the actin cross-talk between axonal microtubule and growth cone actin, as well as mediate downstream signaling events via guidance receptors during migration (Bearce, Erdogan, & Lowery, 2015).

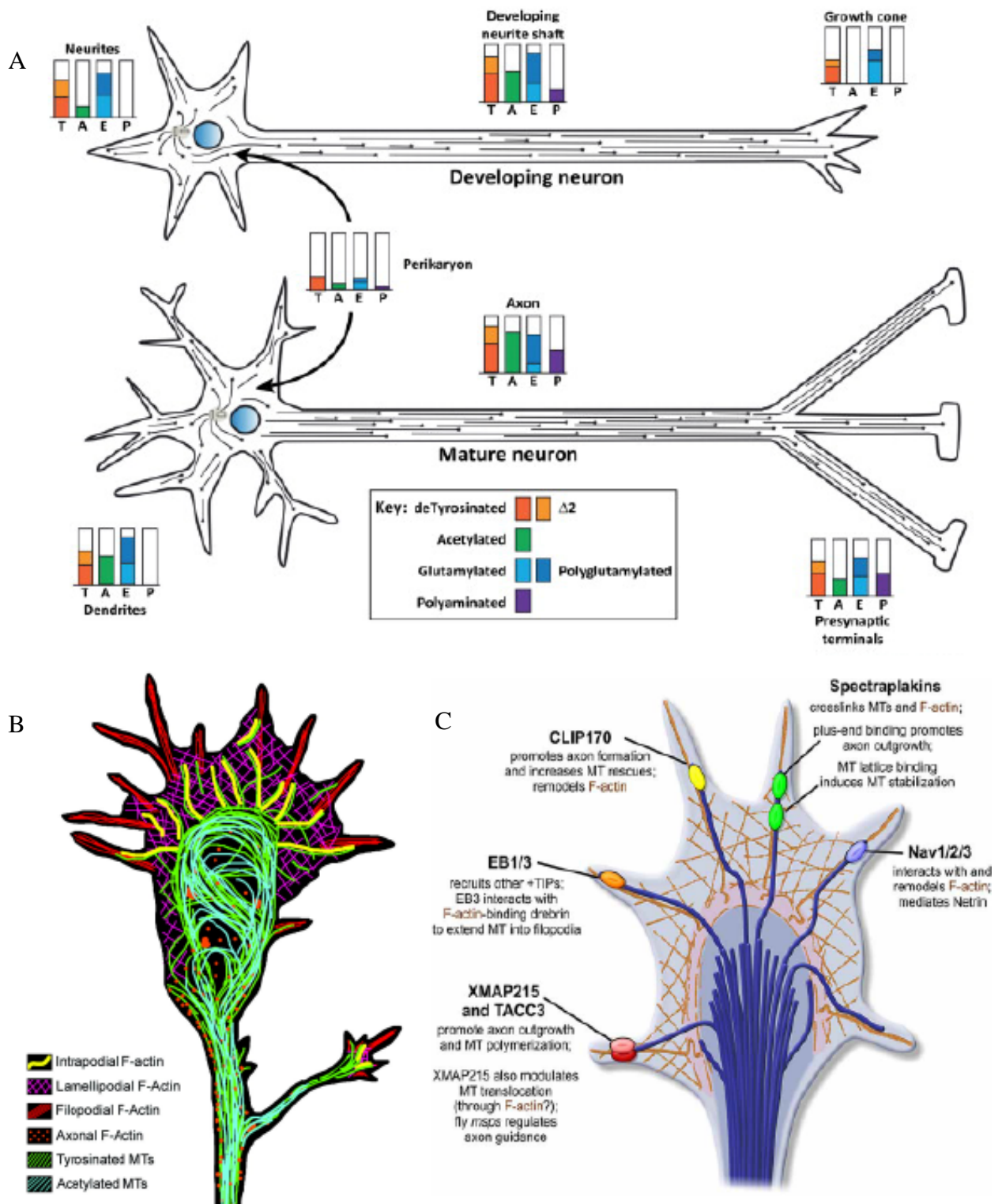


Figure 4: The neuronal cytoskeleton during development. A) Neurons have a very complex and dynamic microtubule cytoskeleton that is subject to many types of post-translational modifications regulating its dynamics and interactions. These modifications vary according to location in the cell, as well as throughout the life of the neuron. B) The growth cone is an interface between microtubules and actin, where different types of cytoskeletal structures participate in forming the dynamic growth cone. Stable acetylated microtubules form the axon, whereas unstable tyrosinated microtubules are present in the growth cone. At the growth cone, filopodial actin is necessary for sensing of environmental factors that will guide the axon during migration. Interaction between the two cytoskeletons is essential for axon branching. C) +tip proteins are located at the fast-growing end of microtubules, at the level of the growth cone where they play a role in coupling between the microtubules and the actin cytoskeleton for outgrowth and guidance. (Adapted from Bearce et al., 2015; Dent & Kalil, 2001; Song & Brady, 2015)

Dynein, dynactin and CLIP-170 have been found to accumulate at microtubule +ends, where the dynactin complex is necessary for dynein to be present (Vaughan et al., 1999), where CLIP-170's cargo-binding domain is necessary for dynactin's recruitment (Valetti et al., 1999), and where EB1 is necessary for the recruitment of CLIP-170 (Moughamian, Osborn, Lazarus, Maday, & Holzbaur, 2013). However, in the absence of dynein, dynactin and CLIP-170 can each be found independently bound to microtubules (Vaughan et al., 1999). It has been demonstrated that the binding of these +tip-associated proteins depends on microtubule tyrosination, where the absence of tubulin-tyrosine ligase in fibroblasts leads to protein mislocalization and cytoskeletal defects (Peris et al., 2006).

The p62 subunit of dynactin is located at the pointed end of the complex and found to interact with the actin cytoskeleton (Garces, Clark, Meyer, & Vallee, 1999). This interaction of this subunit with the membrane could also be the anchor necessary for dynein-dynactin's role in microtubule sliding involved in cytoskeleton remodeling during growth. This process relies on the action of severing enzymes like spastin and katanin and motor proteins like dynein to reorient small microtubule fragments in a growing cell by interaction with filamentous actin (Baas, Karabay, & Qiang, 2005; Baas, Nadar, & Myers, 2006).

Another role at the level of the actin cytoskeleton is dynactin1's interaction with MISP (*CI9ORF21*), thought to contribute to the formation of focal adhesion sites by serving as a link between actin and microtubules, although this has not been confirmed in neurons (Maier, Kirsch, Anderhub, Zentgraf, & Krämer, 2013). On another note, it was found in flies expressing *glued*, a dominant-negative mutant of dynactin1, that a gap was present between the pre- and post-synaptic sites of the neuromuscular junction (NMJ). This detachment was not known to be causative, or a consequence of the synapse disassembly also observed in this model, but supports a role for dynactin at the level of adherens junctions (Eaton, Fetter, & Davis, 2002).

In addition, it has been reported that dynactin1 interacts with tubulin-binding cofactor B (TBCB), a protein involved in microtubule assembly and polymerization. Recruitment of dynactin1 by TBCB was shown and overexpression of TBCB leads to dynactin1 dissociation from the microtubules. However, disruption of this interaction had no apparent effect on the cytoskeleton, synaptogenesis or neuronal maturation (Kuh et al., 2012).

As previously mentioned, dynactin1 was also reported as binding to both microtubules and free, soluble tubulin, to promote polymerization. Both the CAP-Gly domain and the basic

domain are required for this anti-catastrophe activity at microtubule +ends (Lazarus et al., 2013).

Dynactin and dynein are also known to have a role in chromosome alignment and spindle organization during mitosis (Crowder et al., 2015; Echeverri et al., 1996) and the CAP-Gly domain of dynactin1 appears to be essential for the organization of spindle microtubule arrays, suggesting that this particular subunit is necessary for cell division (Kim et al., 2007). New evidence however suggests that the dynactin complex might be dispensable for some mitotic functions of dynein, as it was shown that another dynein regulator, the Lis1/NudE complex, prevented dynein detachment from microtubules and is now thought to regulate spindle dynein. As this complex and dynactin bind competitively to dynein, and as depletion of only components of Lis1/NudE cause severe chromosome alignment defects, it is possible different aspects of dynein function are regulated by different regulating complexes (Wadsworth & Lee, 2013).

II.5-Synapse stability

Synapses are complex structures composed of a pre- and post-synaptic component. The presynaptic side is formed by assembly of necessary components at specialized sites called active zones, which include among others, calcium channels, synaptic vesicles and scaffolding proteins (Petzoldt, Lu, & Sigrist, 2016). Presynaptic vesicles are filled with neurotransmitters that are released into the extracellular space by fusion with the membrane. In order to maintain a ready-pool of vesicle close to the active zones where the capture and release machinery is located, synapses rely on the endosomal system to provide recycling of synaptic vesicles and receptors as well as means for degradation of damaged proteins. As dynactin1 is found accumulating at presynaptic sites, interacting with microtubules and with the actin cytoskeleton via other dynactin subunits, a role at the level of the synapse could be considered.

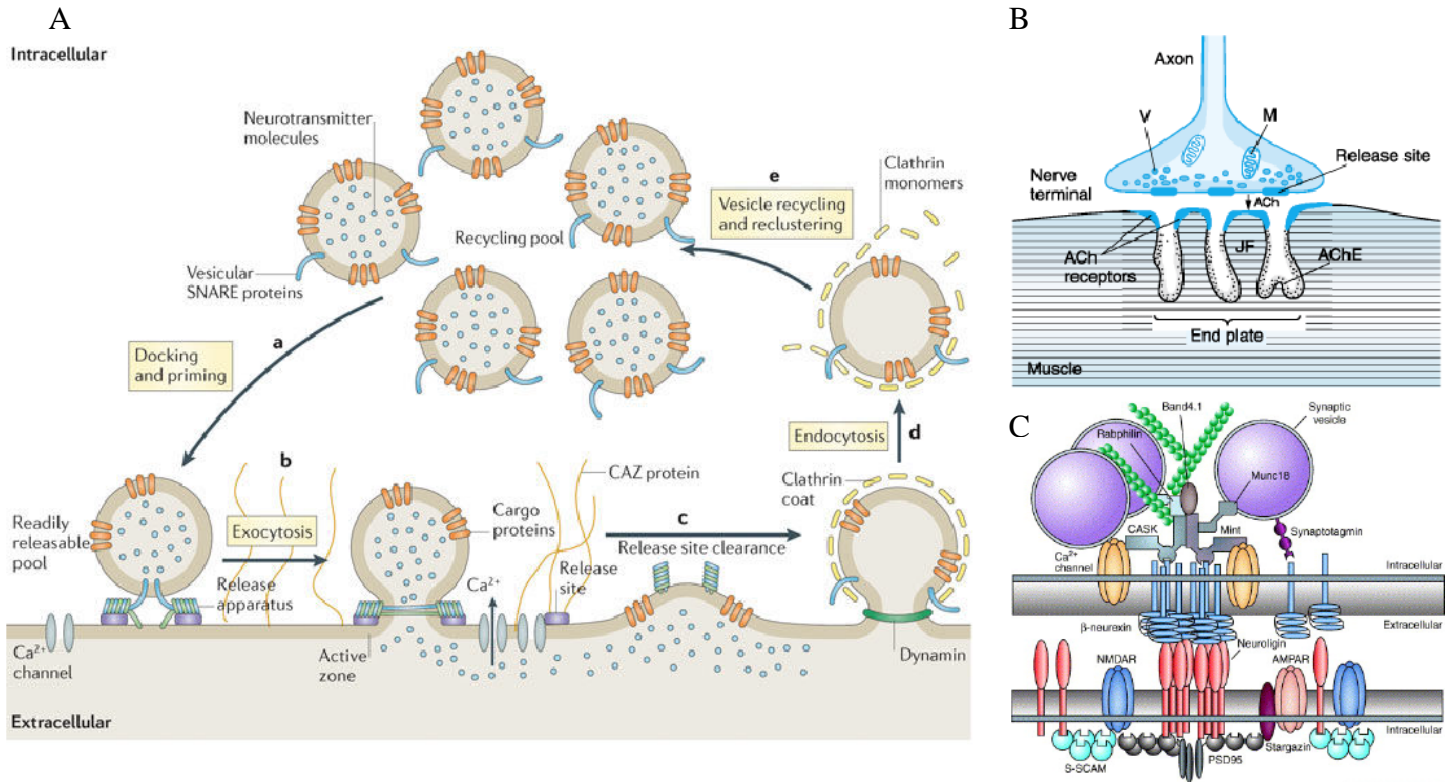


Figure 5: The synapse organization and function. A) The synapse is site dense with protein, organized in specialized domains called active zones, where the synaptic release machinery is localized adjacent to calcium channels. At these sites, synaptic vesicles fuse with the membrane to release neurotransmitters into the synaptic cleft and need to cycle back to the ready, releasable pool. They do so via the clathrin-dependent endocytosis, which then takes them to be refilled in the recycling pool before moving back to the ready pool. B) The neuromuscular junction is a special synaptic connection, where a motor neuron is innervating a muscle fiber. The presynaptic site is apposed to acetylcholine receptors organized in end plates, which are located a short distance away from the active zones, across the synaptic cleft. C) Adhesion molecules have a very important role at the synapse, as they organize the active zone proteins and fusion machinery to efficiently recruit the synaptic vesicle and produce a flow of neurotransmitters. They are also involved in trans-synaptic connectivity, which allows proper alignment of pre- and postsynaptic sites. (Adapted from Dean & Dresbach, 2006; Haucke, Neher, & Sigrist, 2011; Drachman, 1978)

In support of this, dynactin was found to promote synapse stability at the fly neuromuscular junction, where disruption of dynein-dynactin by either expression of the *glued* dominant-negative dynactin1 subunit, or the inhibition of Arp-1 expression by RNAi caused disruption of the microtubule cytoskeleton, electrophysiological deficits, and synaptic retraction in a cell-autonomous manner (Eaton et al., 2002).

At the level of the NMJ, a role for dynactin1 in synapse growth appears to be mediated via interaction with arfaptin2, a membrane-binding protein localized at the golgi, essential for the dynactin complex binding to membranes in neurons. This interaction was reported to be dispensable for axonal transport and synapse stability, as assayed by the presence of synaptic footprints, a sign of degeneration where post-synaptic sites are left behind without a presynaptic site. It was suggested that this interaction could regulate the sorting and delivery of particular

proteins involved in synapse growth, or that it could affect ion channel expression at the membrane (Chang et al., 2013).

Overall, both of these studies suggest a role for dynactin1-mediated axonal transport in synapse growth and stability, but could be due to long-range effects (like improper signaling or delivery of synaptic components) or short-range effects (like cytoskeleton anchoring and synaptic vesicle dynamics).

II.6-Alternative splicing: p135 versus p150

Interestingly, as a result of alternative splicing, the *DCTN1* gene produces two major isoforms: a full-size 150kDa protein, and a shorter 135kDa protein lacking the N-terminus region where the microtubule-binding domain is located. Both of these isoforms bind dynein in independent complexes, which indicates a role for dynactin1 independent of microtubule binding (Tokito, Howland, Lee, & Holzbaur, 1996). In addition, both of these isoforms are found in neuronal populations (Carter et al., 2016) and it was suggested that because it can still recruit dynein, the 135kDa isoform dynein-dynactin complex would have a reduced initiation rate and lower affinity for tyrosinated microtubules, due to its lack of CAP-Gly domain (McKenney, Huynh, Vale, & Sirajuddin, 2016).

As the CAP-Gly domain was reported to have a role in regulating the cytoskeleton and be essential for initiation but dispensable to the processivity of axonal transport, the shorter 135kDa isoform could still support active transport, as was observed in drosophila S2 cells (Kim et al., 2007) and in human retinal pigmented epithelial cells (RPE-1) (McKenney, Huynh, Tanenbaum, Bhabha, & Vale, 2014).

II.7-Mutations and associations with human disease

Defects in both transport of material for development or clearance of detritus in the axon can lead to neuronal stress and culminate in cell death. Predictably, axonal transport deficits have been reported in various neurodegenerative diseases like Huntington's disease, Alzheimer's disease, spinal bulbar muscular atrophy (SBMA), Charcot-Marie-Tooth type 2F (CMT2F) and amyotrophic lateral sclerosis (ALS) (Chevalier-Larsen & Holzbaur, 2006; Duncan & Goldstein, 2006; Soo et al., 2011).

Additionally, mutations in many components of the axonal transport machinery have been associated with human pathology, for instance *KIF5a* in Hereditary Spastic Paraplegia (James & Talbot, 2006), *DYNC1H1* in CMT2F (Lipka, Kuijpers, Jaworski, & Hoogenraad, 2013) and MND (Hafezparast et al., 2003), and *DCTN1* with SBMA and Perry syndrome. Mutations in the gene coding for dynactin1 (DYNACTIN1; DCTN1), have also been reported in motor neuron disease and ALS patients (Table1).

Protein domain	Mutation	Associated disease	Phenotype description	Inheritance	Reference
Dynactin1 CAP-Gly	G59S	Motor neuron disease	Lower motor neuron disease, no sensory symptoms, slow progression	Autosomal dominant	(Puls et al., 2003)
Dynactin1	T1249I	sALS	Middle-age onset; gait disturbance, distal limbs weakness and muscle atrophy, slow progression	Autosomal dominant	(Münch et al., 2004)
Dynactin1 Dynein-binding domain	M571T	fALS	Middle-age onset; upper limb onset with bulbar symptoms	Autosomal dominant	(Münch et al., 2004)
Dynactin1 Dynein-binding domain	R785W	fALS incomplete penetrance	Middle-age onset; upper limb onset or bulbar onset	Uncertain	(Münch et al., 2004)
Dynactin1	R1101K	ALS/FTD	Middle-age onset; speech impairment, upper limb weakening, lower muscle atrophy	Autosomal dominant	(Münch et al., 2005)
Dynactin1	E34Q, D63Y, I196V and R1049Q	ALS	Not reported	Not reported; likely autosomal dominant	(Stockmann et al., 2013)

Table 1: Mutations identified in *DCTN1* in the context of ALS or MND. Many pathogenic mutations have been reported within *DCTN1*, this table displays the reports of cases where patients were diagnosed as having either ALS or MND. The clinical presentation is included, as is the inheritance, when the data was available.

The G59S point mutation is perhaps the most studied and in patients has been linked with an early adulthood onset motor neuron disease (MND), presenting with breathing difficulties, and progressive facial muscle and hands weakening, followed by lower extremities impairment (Puls et al., 2003). In mice, a homozygous knock-in of this mutation leads to embryonic lethality, as does a homozygous deletion of the whole gene, similarly to the loss of dynein heavy chain. Heterozygous carriers however develop progressive motor neuron impairments. This suggests that the dynein-dynactin complex and dynactin1 have an essential

function in cell division which is not affected by a possible haploinsufficiency or toxic gain of function (Lai et al., 2007). Mice overexpressing the mutant peptide, which is found to form aggregates, exhibit defects in vesicular transport, autophagic cell death, as well as NMJ degeneration and muscle atrophy (Laird et al., 2008).

This mutation has also been linked with SBMA. In a mouse model, a proliferation of lysosomes was seen, as well as a reduction in motor neuron axonal caliber and NMJ disturbances, without any reported effect on retrograde axonal transport (Chevalier-Larsen, Wallace, Pennise, & Holzbaur, 2008). Another disease linked to this mutation is distal hereditary motor neuropathy type VIIIB (HMN7B), where G59S appears to have a dominant-negative effect: the produced peptide is not incorporated correctly in the dynactin complex, forms aggregates and was found to disrupt axonal transport of lysosomes in the axon of primary dorsal root ganglion neurons (Moughamian & Holzbaur, 2012).

Other mutations in the CAP-Gly domain of dynactin1 (G71R, Q74P), associated with Perry syndrome (Vilariño-Güell et al., 2009), a disease characterized by parkinsonism and TDP-43 inclusions, cause a phenotype similar to a loss of the whole domain (Moughamian & Holzbaur, 2012). In the fly, a different mutation (G38S) has been linked with Perry syndrome was shown to lead to adult-onset behavioral deficits, disrupted vesicular transport, and impaired neurotransmitter release (Lloyd et al., 2012).

However, many studies have looked at these ALS and MND- linked mutations and aside from the G59S, their role in motor neuron degeneration is not clear. It has been suggested that rather than be causative, that they could act as a risk factor (Vilariño-Güell et al., 2009). In support of this hypothesis, a study has looked at expression of four ALS-associated mutations in dynactin1 (M571T, R785W, R1101K, and T1249I (Levy et al., 2006)) and found that the incorporation of the mutant subunit into the dynactin complex was normal, and that their expression did not lead to aggregate formation or golgi disruption, unlike what is seen for G59S. It was however noted that the regulation of dynactin1 expression is tightly controlled in cells and that mutations altering protein expression or stability might be considered a risk factor in itself (Dixit, Levy, Tokito, Ligon, & Holzbaur, 2008). Another study looked at variants found in ALS patients (particularly E34Q, D63Y, I196V and R1049Q out of 24 identified targets) and characterized their effect on the cell biology of cultured motor neurons. While they report changes like aggregate formation, effect on microtubule network and ubiquitination, most of the variants studied were of too low occurrence to determine if they are rare causes and

pathogenic, perhaps with incomplete penetrance, or simply risk factors of ALS (Stockmann et al., 2013).

To support a role for dynactin in ALS, *DCTN1* was found to be downregulated in the spinal motor neurons of sALS patients, even in well-preserved populations of neurons. Furthermore, this downregulation was shown to be pre-symptomatic (Tanaka, Ikenaka, Yamamoto, & Sobue, 2012). Another study reported lower levels of *DCTN1* mRNA and protein in sALS patient cortex and spinal cords (Kuźma-Kozakiewicz et al., 2013).

Moreover, it was found in mice models with fALS *SOD1* mutations (A4V, G85R, and G93A) that the mutant proteins co-localize and interact with the dynein-dynactin complex. This interaction has been shown to be essential for aggregate formation, where disruption of the dynactin complex by overexpression of dynamitin prevented the formation of inclusions and improved cell survival (Ström et al., 2008).

In addition, mice overexpressing dynamitin have been found to exhibit a degenerative phenotype at the level of spinal motor neurons, leading to skeletal muscle atrophy, which was attributed to the loss of retrograde axonal transport (LaMonte et al., 2002). Similarly, SBMA mice with trinucleotide expansions in the androgen receptors (AR) have significantly reduced levels of dynactin1 mRNA as a result of AR-related transcriptional dysregulation, which leads to impaired retrograde transport. The subsequent neuronal dysfunction is however rescued by overexpression of dynactin1 (Katsuno et al., 2006). Mice mutant for another interactor of the dynein-dynactin complex, Bicaudal D2 (BICD2) also show impaired axonal transport and develop motor abnormalities and motor neuron degeneration (Teuling et al., 2008). Hence these studies support a role for dynactin1 and axonal transport in MND pathogenesis.

While it is not clear if dynactin1 is causative of ALS or MND, a role for axonal transport in these diseases is clear, and a role for dynactin1 and the dynactin complex in this process is known to be essential. We have chosen to investigate the loss of dynactin1 function in motor neuron-specific neurodegeneration in order to determine if *in vivo* compensation mechanisms could underlie defects resulting in pathogenicity.

III-The zebrafish animal model

III.1-The zebrafish spinal cord and NMJ

The zebrafish embryo develops quickly, leading to simple stereotyped behavior as early as 17-19 hours post-fertilization (hpf). By 48hpf, the embryos have hatched from their chorion and can swim in reproducible escape bouts. These behaviors rely on the innervation of axial muscle fibers by motor neurons sprouting from the embryonic spinal cord, easily identifiable due to their simple organization and morphological characteristics. The motor neurons are organized in tight bundles of axons called ventral roots, grouping the axons of neurons whose soma is located within one spinal segment, innervating a single muscle segment (Myers, 1985).

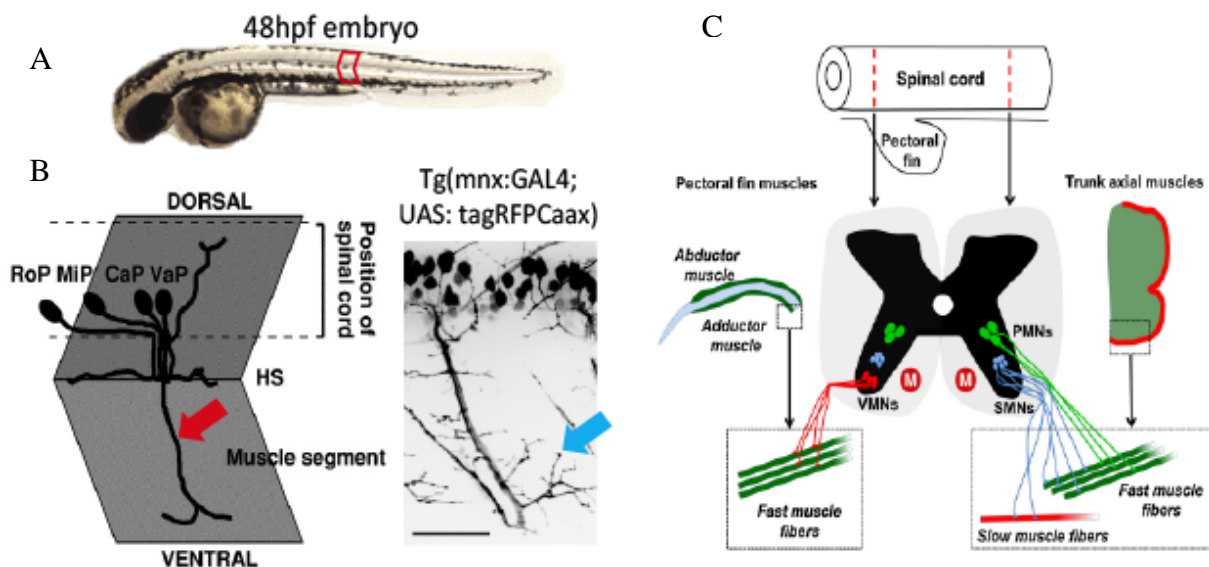


Figure 6: The embryonic zebrafish spinal cord, its primary motor neurons, and their innervation pattern on the ventral musculature. A) 48hpf embryonic zebrafish are already able to produce complex swimming behavior and rely on their spinal cord motor neurons to do so. B) One somatic segment (delineated in red in A) contains various types of primary motor neurons, with different morphologies, cell body position and innervation patterns, which are repeated on each side of the embryo, and at each somite along the trunk and tail. The primary motor neurons can be visualized and studied by using a transgenic line where GAL4 is placed under the expression of a specific enhancer called *mnx1* (shown here in combination with a UAS-driven membrane-bound fluorophore). The caudal primary-CaP- motor neuron we use in this study (at 24hpf, red arrow, at 48hpf, blue arrow). C) The CaPs innervate ventral fast-twitch muscle fibers, located in deeper levels below the slow-twitch muscle layer. (Adapted from Ashworth, Zimprich, & Bolsover, 2001; Babin, Goizet, & Raldúa, 2014)

Primary motor neurons are the first ones to appear and extend axons out of the spinal cord and are classified in three types (CaP, RoP and MiP, for caudal, rostral and middle primary) depending on the section of muscle where it extends its peripheral arbor. They also exhibit particular morphological features including the size and shape of their soma, and the caliber of their axon, as well as subtype-specific electrical excitability signatures (Moreno &

Ribera, 2009). The caudal primary motor neurons (CaP) starts migrating ventrally as early as 18hpf to innervate the ventral muscle fibers at the horizontal myoseptum, and are soon joined by many secondary motor neurons that grow alongside the CaP axon to form the ventral root (Myers, Eisen, & Westerfield, 1986). These motor neurons reach their target by 22-24hpf, innervating only fatigable type II (fast-twitch) muscle fibers, which are responsible for burst swimming (Jackson & Ingham, 2013). They are the zebrafish equivalent of the alpha motor neuron-innervated lower fast-twitch fatigable (FF-subtype) fibers affected in many neurodegenerative disorders including ALS, which make CaPs an excellent target in the present study (Babin et al., 2014).

III.2-Mutant zebrafish line for *dynactin1a*

We have obtained a mutant zebrafish line for *dynactin1a* (*mikre oko*; hereafter referred to as *mok^{m632}*), which was generated in a large screen to identify developmental defects of the retina, a product of random mutagenesis induced by N-ethyl-N-nitrosourea (ENU) (Malicki et al., 1996). The *mok^{m632}* line features a point mutation in the *dynactin1a* gene, the zebrafish ortholog for DCTN1, corresponding to a nucleotide 2395C to T transition. This mutation results in the appearance of a premature stop codon at position 799 of the polypeptide (Tsujikawa, Omori, Biyanwila, & Malicki, 2007). The homozygous mutant larvae (*mok^{m632/-}*) exhibit smaller eyes and protruding lenses detectable by 4dpf, a morphological phenotype resulting from defects in the photoreceptor cell layer, where improper differentiation of photoreceptors and synaptic termini in the outer segment leads to progressive cell death from 3dpf. No other morphological phenotype was reported for homozygous mutants, and none for heterozygous siblings, but the larvae do not survive past the second week of development (Doerre & Malicki, 2001).

Tsujikawa and colleagues have reported RT-PCR evidence showing that the level of *dynactin1a* mRNA is severely reduced in *mok^{m632}* homozygous mutants, probably owing to nonsense-mediated decay (Mühlemann, Eberle, Stalder, & Zamudio Orozco, 2008). They have also found that no truncated protein product was detectable on Western blot from extracts of embryos and heterozygous adult carriers and observed no detectable maternal protein contribution (at 2 hpf) (Tsujikawa et al., 2007). However, a study using another allele of the *mok* mutant (*mok^{s309}*) reported low full-size protein expression in both homozygous mutants and wild-types for the first three days of development, but not afterwards in mutants (Del Bene et al., 2007). The presence of maternally-provided *dynactin1* is thought to be essential to

survival during the larval stages, most likely via its role in cell division, as it has proven embryonic lethal in other models (Lai et al., 2007; Lloyd et al., 2012).

We therefore consider this mutation to be either amorphic or strongly hypomorphic, leading us to treat *mok*^{m632/-} as a loss-of-function model.

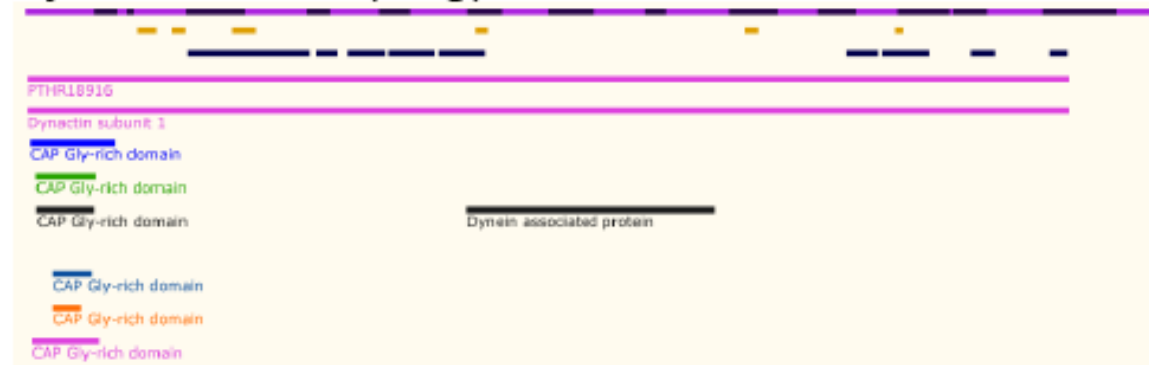
III.3-Role of *dynactin1b*

The zebrafish has two paralogs for *dynactin1*: *dynactin1a* and *dynactin1b*, the latter being unique to teleost fish (Tsujikawa et al., 2007). Previous alignments of the zebrafish genome predicted *dynactin1b* to be less conserved, lacking a part of the N-terminus where the CAP-Gly domain is located. With the most recent alignment (GRCz10:CM002897.1), two transcripts are predicted: one full-size (*dctn1b-201*, ENSDART00000102411.4) and a shorter one lacking the CAP-Gly domain (*dctn1b-202*, ENSDART00000169953.1). Interestingly, the process to maintain functional protein diversity following genome duplication in the zebrafish model has been shown to operate via constitutively spliced exons in separate genes (Abascal, Tress, & Valencia, 2015). As supporting evidence is only available for the second transcript in the latest alignment of the zebrafish genome, this lends credence to the hypothesis that the *dynactin1b* paralog could in reality lead to a short transcript lacking the CAP-Gly domain, fulfilling the function of the p135 isoform found in mouse and human. However, due to the lack of available antibodies, the shorter isoform was not detectable in our study or others (Del Bene et al., 2007; Drerup, Herbert, Monk, & Nechiporuk, 2017).

dynactin1a



dynactin1b-201 (long)



dynactin1b-202 (short)

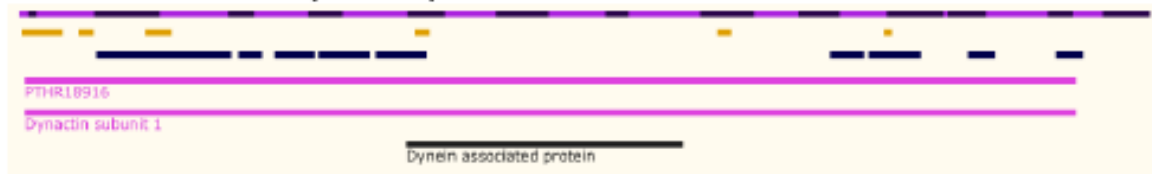


Figure 7: Zebrafish paralogs for *dynactin1*. The zebrafish genome has been duplicated along evolution and now contains two copies of the *dynactin1* gene. These paralogs, *dynactin1a* and *dynactin1b*, are both predicted to produce full-sized protein transcripts, while *dynactin1b* could also lead to a shorter transcript lacking the CAP-Gly domain in N-terminus. These two transcripts are depicted here, along with the full-sized transcript produced from *dynactin1a*, with their identified functional domains (graphics from ENSEMBL, ZV10 assembly of the zebrafish genome).

A morpholino-based study has previously reported a more severe phenotype in photoreceptors of the zebrafish retina when knocking down both paralogs of *dynactin1* (Insinna, Baye, Amsterdam, Besharse, & Link, 2010). However, they also noted the phenotype at this level was weaker than a full loss of dynein function (via the use of the *cannonball* and *dync1h1* mutant embryos), suggesting dynein might have an additional dynactin-independent role in this biological context.

Recently, a paper reported the creation of a CRISPR-Cas9 mutant for *dynactin1b* (*p150b^{nl16}*). The CRISPR target used is located in exon3 of the short transcript (exon 5 of the full-size transcript) and leads to homozygous mutants, which are indistinguishable from wild-

type embryos. However, in double *dynactin1* mutants ($\text{mok}^{\text{m632-/-}}$; $\text{p150b}^{\text{nl16}}$) the phenotype observed at the level of mitochondria in the peripheral lateral line nerve was reported to be similar to a full loss-of-function of the dynein motor (Drerup et al., 2017). It is therefore possible that the two paralogs share duties based on the presence or absence of a microtubule-interacting CAP-Gly domain.

In this study, we have generated a CRISPR-Cas9-mediated genome editing mutant for *dynactin1b*, which is homozygous viable and did not show any morphological phenotype. Full *dynactin1* mutants, also homozygous for mok^{m632} , did not yield a more severe phenotype and for this reason, we chose to continue the characterization of the single mutant $\text{mok}^{\text{m632-/-}}$.

IV-Aim of the thesis

Axonal transport defects have been reported in patients and animal models of ALS, even before the onset of neurodegeneration. As mutations in the gene coding for *dynactin1*, a subunit of axonal transport regulatory complex dynactin, have been found in patients afflicted with ALS and other forms of motor neuron disease, we hypothesized that a loss of function of this gene could lead to neurodegeneration of motor neurons. Our aim was to understand the role this protein plays in motor neuron development and degeneration, as well as in neuromuscular junction structure and function by looking at defects that arise *in vivo* when it has been lost.

As ALS is a neurodegenerative disease affecting motor neurons, we focused on characterizing defects in a single cell type in order to reduce variability, and selected the CaP primary motor neuron of the zebrafish spinal cord. This cell type is easily identifiable and is similar to the type of motor neurons affected in ALS patients, as it innervates fast-twitch muscle fibers, similar to fast-fatigable muscles, which are the target of degeneration. The zebrafish model is ideal for our study as it develops externally, circumventing a possible embryonic lethality, is virtually transparent, allowing us to probe processes like live axonal transport in an intact animal, and is amenable to a variety of genetic manipulation. It can also be used to probe behavioral modifications as well as changes in electrophysiological properties stemming from the dysfunction of motor neurons. Furthermore, other models of ALS have been established in this system and can serve as a reference for phenotypic assessment.

We first characterized the behavioral deficits present in this mutant to validate its use as an ALS model. Because *dynactin1* has been discovered and studied in the context of axonal

transport, we then analyzed the movement of several types of cargoes, and have also investigated its role in NMJ function, synapse formation and stability as well as possible interactions it might have with the cytoskeleton.

Since much of what is known about dynactin1 has been reported from *in silico* or from *in vitro* approaches, our goal was to understand how neurons within a living organism compensate for a lack of dynactin1 and how these measures could lead to degeneration of motor neurons in the hope of elucidating key molecular mechanisms in in NMJ maintenance and possibly in ALS etiology.

Results

In order to study the function of dynactin1 in the context of ALS, we made use of a loss-of-function mutant line for *dynactin1a* (*mok*^{m632}), which had been generated in an ENU-based mutagenesis screen aimed at identifying defects in eye development (Del Bene et al., 2007; Doerre & Malicki, 2001; Malicki et al., 1996; Tsujikawa et al., 2007). No phenotypic assessment was reported at the level of the spinal cord, and in particular, with regard to the motor neurons and their connections to the muscle.

I-Morphological phenotype of the *mikre oko* (*mok*)^{m632/-} embryos

As we aimed to investigate ALS-related motor neuron deficits that arise when dynactin1 is lost, we first wanted to determine if our model had any phenotype that could be consistent with an ALS zebrafish model. Most studies focus on a developmental stage of 48hp (Ciura et al., 2013; Kabashi et al., 2009, 2011; Lattante et al., 2015; Ohki et al., 2017; Schmid et al., 2013), as it confers many advantages like a newly developed but mature NMJ, optical transparency (due to low pigmentation), and stereotyped behavioral assay. We therefore used this timepoint as a first look at the development of the CaP motor neurons and their NMJ but also performed most experiments on 6dpf larvae in order to assess if processes akin to degeneration took place later on.

The *mok*^{m632/-} embryos are indistinguishable from their wild-type siblings at 48hpf, as was previously reported (Doerre & Malicki, 2001; Malicki et al., 1996) and while heterozygous siblings do not display an altered morphology, homozygous mutants can be identified as early as 4dpf due to their “bug-eye” phenotype caused by the loss of their retinal photoreceptor layer, also rendering them blind (Del Bene et al., 2007; Doerre & Malicki, 2001; Tsujikawa et al., 2007). Based on this particular trait, we selected *mok*^{m632/-} and examined the gross morphology of the homozygous *mok*^{m632} embryos at 6dpf (Figure 8B). We found no obvious defects at the level of the trunk or tail section, where somites were properly formed and spaced, but confirm the heightened pigmentation (caused by background adaptation, as seen in another blind mutant (Auer et al., 2015)), as well as smaller head and eye diameter previously reported (Doerre & Malicki, 2001; Malicki et al., 1996).

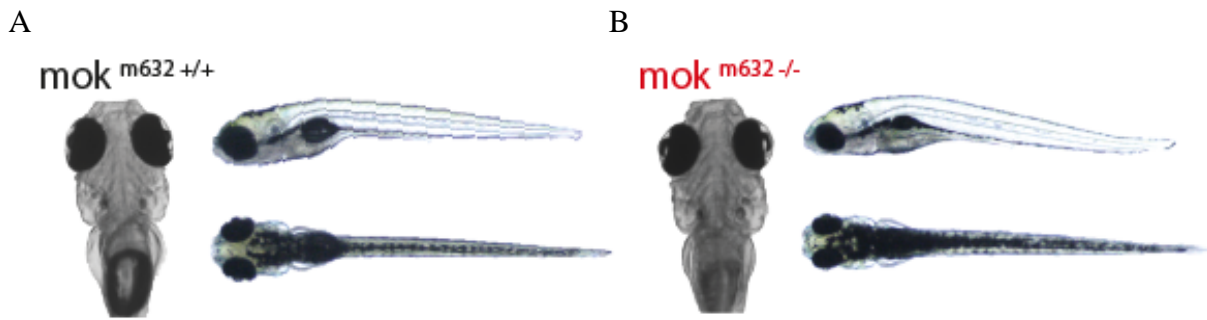


Figure 8: General morphology of the mok^{m632} embryos at 6dpf. A) Wild-type sibling and B) $mok^{m632/-}$ embryo at 6dpf, side view and dorsal view, close-up showing a dorsal view of the head, with visible “bug eye” phenotype due to the loss of the photoreceptor layer in the $mok^{m632/-}$ embryo. Pigmentation is more visible in $mok^{m632/-}$ embryos (B), as a result of background adaptation in these blind fish.

II-Motor behavior at 48hpf

ALS leads to progressive paralysis owing to muscle denervation. Thus, we investigated locomotion defects in 48hpf $mok^{m632/-}$ embryos, by performing a touch-evoked escape response assay (TEER), as has been done previously for other ALS zebrafish models (Armstrong & Drapeau, 2013, 2013; Ciura et al., 2013; Kabashi et al., 2009, 2011; Lattante et al., 2015; Vaccaro et al., 2013). In this assay, the embryos are placed in a large petri dish covered with embryo medium. As they do not swim spontaneously at this developmental stage (Saint-Amant & Drapeau, 1998), they perform an escape-response swimming episode upon presentation of a stimulus, in this case, a brush on the tail with blunt forceps. This type of locomotion relies on fast-twitch muscle fibers, innervated by CaPs motor neurons, and metrics such as swimming distances, swimming duration and instantaneous maximum speed allow the quantification of this escape response.

While the behavior we observed for wild-type embryos was similar to what is described in the literature (Armstrong & Drapeau, 2013; Kabashi et al., 2009, 2011), our $mok^{m632/-}$ embryos exhibit significantly shorter swim durations (Figure 9 C), as well as a reduced swim distance per episode (Figure 9 D). In this context, maximum instant speed (Figure 9 E) serves as readout of muscle function (Sztal, Ruparelia, Williams, & Bryson-Richardson, 2016), which appears to be unaffected. Overall, the behavior of our $mok^{m632/-}$ embryos is indicative of fatiguing at the level of the NMJ, and consistent with animal models of ALS.

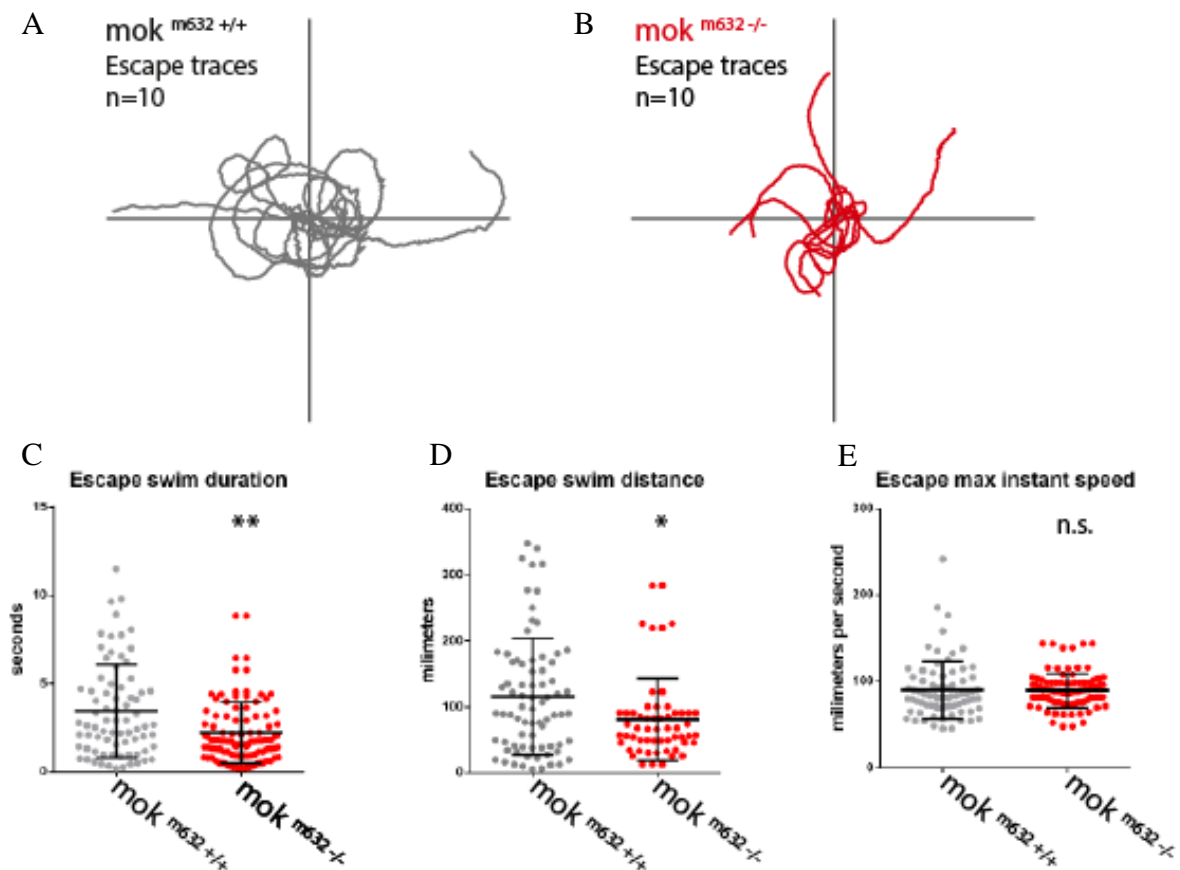


Figure 9: Behavioral analysis at 48hpf by touch-evoked escape response assay. A) Superimposed traces of escape episodes for ten wild-type sibling embryos and for B) ten *mok*^{m632-/-} embryos. C) Average swim duration ($p \leq 0,01$), D) average swim distance ($p \leq 0,05$), and E) maximum instant speed of evoked escape responses. All data shown as average \pm SD, where one symbol represents one escape done by one embryo ($n \geq 30$)

III-Axonal morphology and neuromuscular junction structure

Many of the previously described ALS zebrafish models exhibit abnormal CaP morphology, with a combination of axon growth or overbranching defects (Armstrong & Drapeau, 2013; Ciura et al., 2013; Kabashi et al., 2009, 2011; Schmid et al., 2013). As integrity of the cell and its connection to muscle is paramount to its function, it is not surprising that behavioral defects were reported in these models.

To determine if the behavioral defect observed in our mutants were due to improper development of the CaPs or to functional deficits, we next investigated defects at the axonal morphology level using single-cell labeling, which we visualized in live embryos. To achieve this, we injected a genetic construct in zygotes to drive the expression of a membrane protein-bound fluorophore under the control of the *mnx1* transcription factor (formerly called *hb9*)

(Flanagan-Steet, Fox, Meyer, & Sanes, 2005), which is a selectively expressed in postmitotic motor neurons of the spinal cord.

IV-Axonal morphology at 48hpf and 6dpf

To reduce variability in cell size, which can fluctuate due to the rostro-caudal developmental wave in the spinal cord, as well as between individuals, the embryos were staged at 48hpf by counting somites and single-labeled cells located between somite 10 and 14 were selected for analysis. At 6dpf, embryo staging can no longer be done by counting somites, therefore cells within a 4-somite area situated around the cloaca were selected.

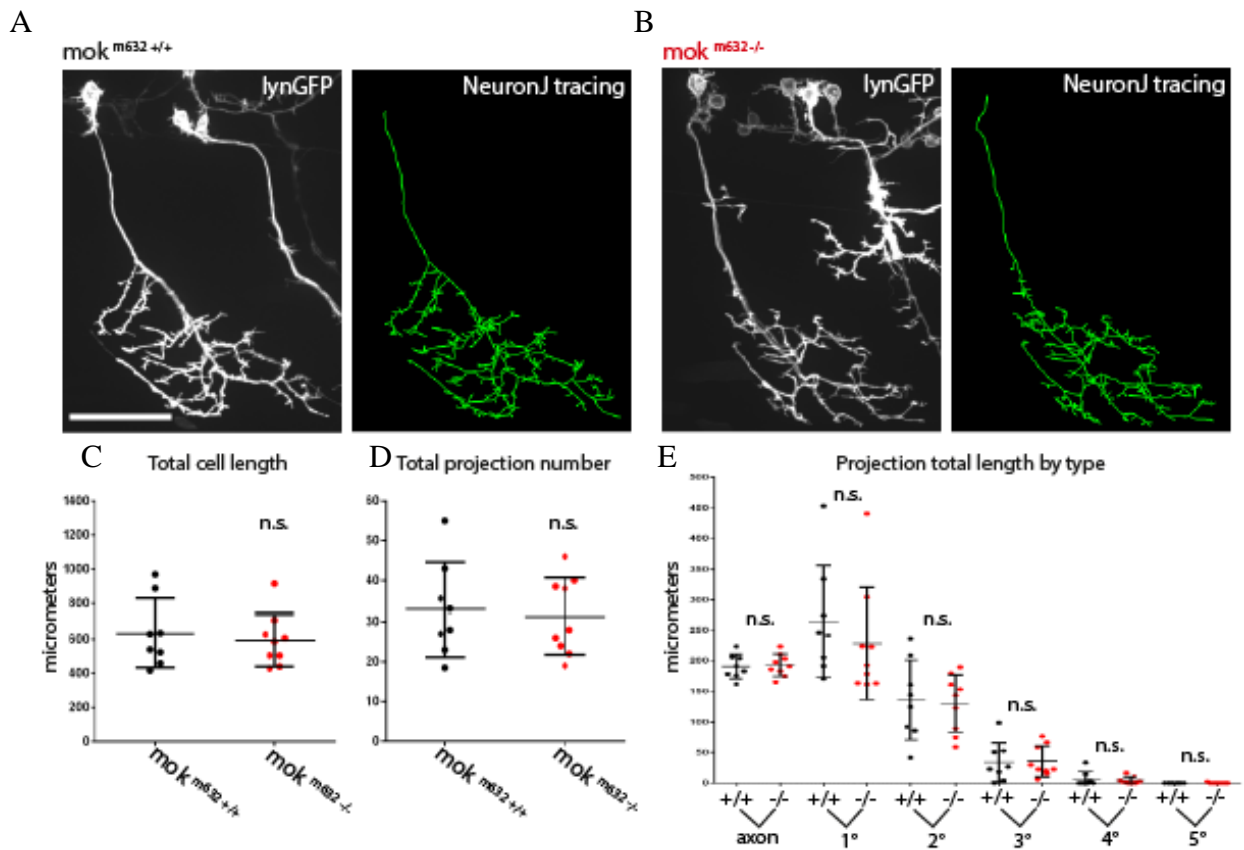


Figure 10: Axonal morphology of CaPs at 48hpf. A) Confocal z-stack projection of a single CaP cell, visualized by expression of *mxn1:lynGFP*, with tracing of the axonal arbor done with NeuronJ (ImageJ) for a wild-type sibling embryo at 48hpf and for a B) *mok*^{m632-/-} embryo. C) Quantification of the axonal arbor size, by total cell length, D) total number of projection, and E) analysis of complexity by comparing the total length of projection grouped by type (branch order). All data presented as average +/- SD; (n=9, 9)

We did not observe overbranching (production of aberrant, supernumerary branches) or changes in either the total size (Figure 10 C), or complexity, of CaP motor neurons in *mok*^{m632-/-} embryos at 48hpf, as revealed by the total number of projection (Figure 10 D) or their branch order (Figure 10 E). This suggests that initial development and migration of the cells is normal and that the behavioral defects presented in the previous section is not due to morphological deficits.

When we looked at the later timepoint of 6dpf however, *mok*^{m632-/-} embryos did exhibit CaPs with a significantly reduced arbor size (Figure 11 C) and complexity, as revealed by a reduced number of projections (Figure 11 D) which maintained their average size (Figure 11 E). Since no difference was seen in cell morphology at 48hpf, this result could either suggest that these motor neurons undergo degeneration or that improper development mechanisms occur between 48hpf and 6dpf, perhaps due to functional defects.

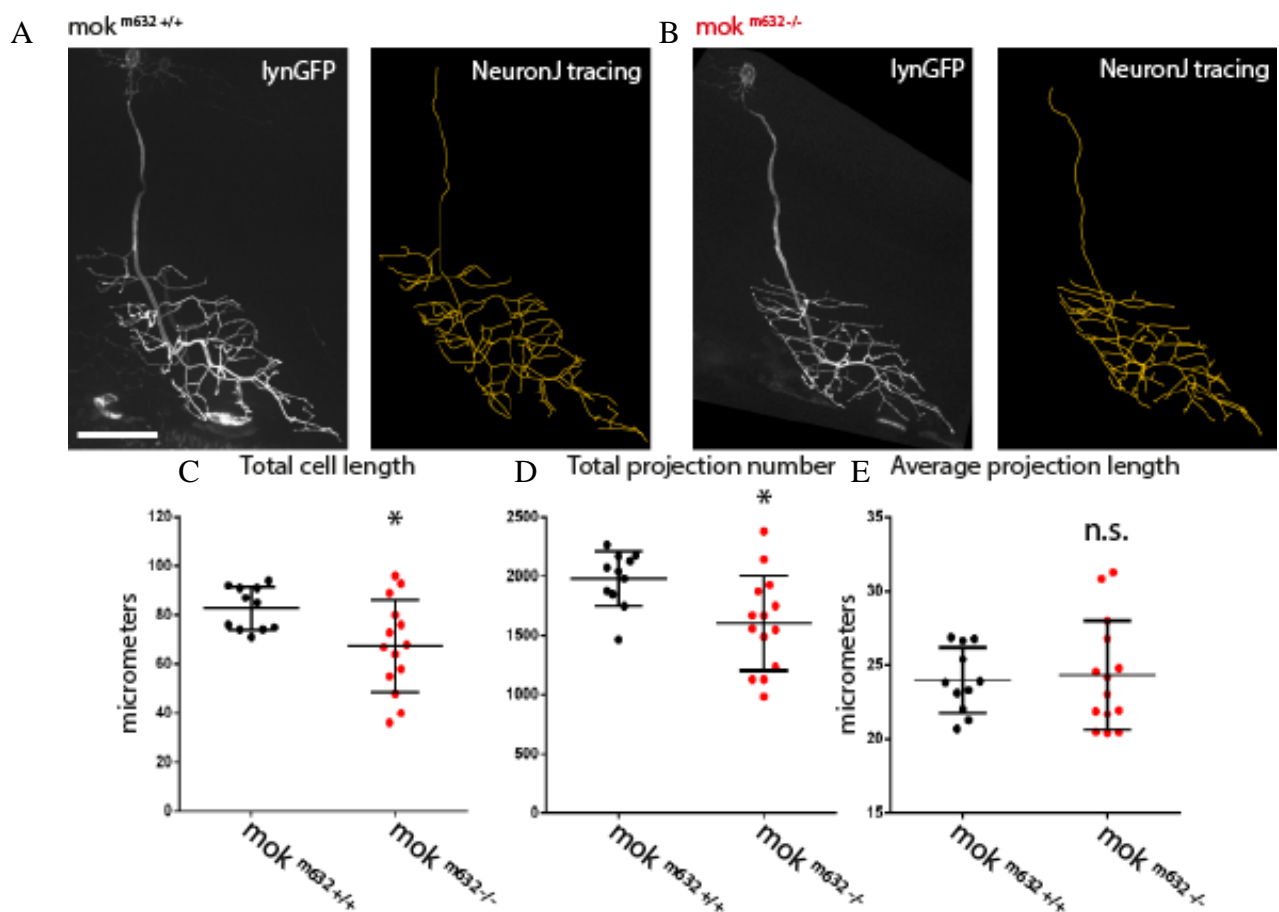


Figure 11: Axonal morphology of CaPs at 6dpf. A) Confocal z-stack projection of a single CaP cell, visualized by expression of *mx1:lynGFP*, with tracing of the axonal arbor done with NeuronJ (ImageJ) for a wild-type sibling embryo at 48hpf and for a B) *mok*^{m632-/-} embryo. C) Quantification of the axonal arbor size, by total cell length ($p \leq 0,05$), D) total number of projection ($p \leq 0,05$), and E) analysis of complexity by comparing the total length of projection grouped by type (branch order). All data presented as average \pm SD; (n=11, 14)

V-Neuromuscular junction structure at 48hpf and 6dpf

Since cell morphology only reveals the presynaptic side of the NMJ, we then performed immunohistochemistry on fixed embryos to determine if structural integrity was conserved (Armstrong & Drapeau, 2013), as defects at this level could explain the behavioral abnormalities found in our mutant embryos. The presynaptic side was visualized via labeling of synaptotagmin2 (znp1 antibody), while the postsynaptic side was bound by a fluorophore-conjugated α -bungarotoxin, which binds irreversibly to AChR on the muscle. Synaptotagmin2 is a synaptic vesicle protein located at the membrane of the active zone. It acts as a calcium sensor, and is involved in vesicle docking and fusion in calcium-evoked synaptic release (Pang et al., 2006; Rizo & Xu, 2015). This presynaptic synaptotagmin2 is therefore essential to neurotransmission (Pang et al., 2006) and its location at the membrane provides more information than the labeling of synaptic vesicle proteins, like SV2, which is more broadly distributed in the neuron. As we are visualizing the NMJ in whole embryos, we only have the resolution to determine the presence or absence of the presynaptic marker at the synapse, and not particularly at the active zone.

We performed the analysis of colocalization on confocal z-stack projections by using both the Pearson's coefficient, which measures correlation, combined with the overlap coefficient, which measures the intersection of both fluorescent fields. We also used the Mander's coefficients, which measures co-occurrence based on area, which can indicate if the defects in co-occurrence arise from the misalignment of the pre- or postsynaptic side (M1 vs M2). We are however aware that this method of measurement has been debated (Adler & Parmryd, 2010, 2013) and so we will report all the measurements and comment on the Pearson's coefficient.

Double-labeling of whole mount immunohistochemistry of pre- and postsynaptic structures at 48hpf revealed no significant changes between the *mok*^{m632/-} embryos and their wild-type siblings (Figure 12 A, C), indicating that the coverage of pre- and postsynaptic markers for the entire ventral root of the spinal cord are conserved and that the alignment of both structures are sound at this timepoint in *dynactin1a* mutants. On the contrary, 6dpf *mok*^{m632/-} embryos had a significantly reduced area of both markers, as well as a reduced alignment of pre- and postsynaptic structures (Figure 12 D, F). As we have previously shown 6dpf *mok*^{m632/-} CaP arbors to have a reduced size (Figure 11), the reduced area of presynaptic

marker is consistent with the reduced size of the presynaptic cell. In addition, we did not observe a higher frequency or orphan vesicle or receptors as reported in other ALS models (Armstrong & Drapeau, 2013), indicating that the reduced arbor size at 6dpf might be due to improper development and not degeneration.

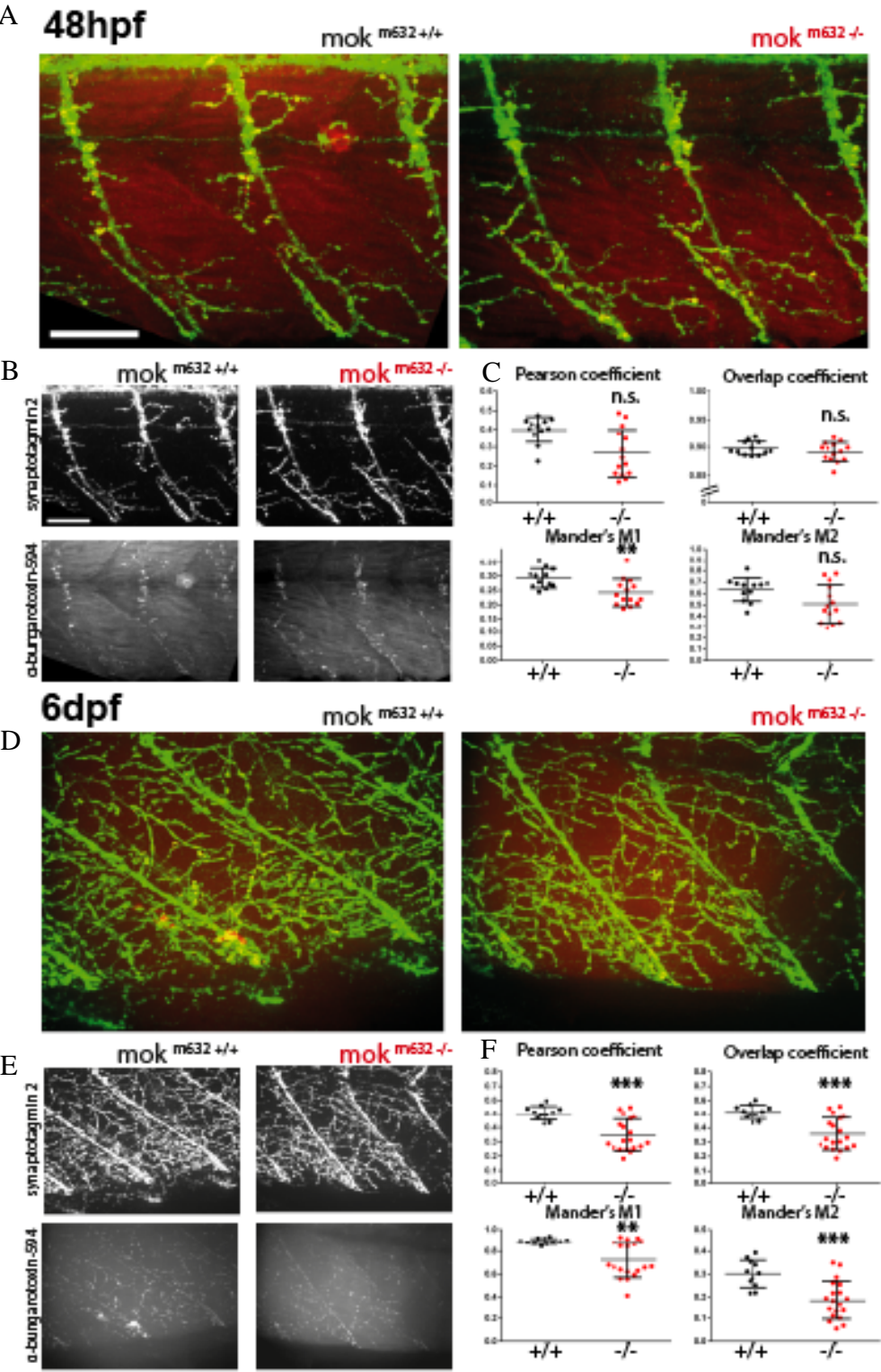


Figure 12: Integrity of the NMJ structure by double immunohistochemistry at 48hpf and 6dpf. Integrity of the NMJ is determined by the coverage and colocalization of the pre- and postsynaptic components of the synapse, which are respectively labeled by anti-synaptotagmin2 (Alexa488; in green) and Alexa594 conjugated α -bungarotoxin (in red). The colocalization is visualized in yellow in merged images of the two channels. Representative z-stack projection of a double labeled NMJ for wild-type and *mok*^{m632/-} embryo A) 48hpf and D) 6dpf. Each channel shown separately in B) for 48hpf and E) for 6dpf. The colocalization was quantified in C) and F) using Pearson's coefficient in combination with the overlap coefficient, and Mander's coefficients are also presented. All data shown as average \pm SD, ($p \leq 0,01$, $p \leq 0,001$) (48hpf n=12, 14; 6dpf n=11,19)

VI-Quantitative RT-PCR profile of 6dpf *mok*^{m632/-} embryos

We know from previous studies that *dynactin1a* is expressed throughout development and that the *mok*^{m632} mutation leads to a loss of function as no protein product is detected in mutant embryos after 3dpf (Del Bene et al., 2007; Tsujikawa et al., 2007). If dynactin1 is essential to the formation of the dynactin complex, it is possible that a reduction in the production of this subunit would reduce the formation of full dynactin-dynein complexes and lead to a downregulation of other genes coding for dynactin or dynein subunits. Indeed, we know that transcription of these axonal transport components is dynamic as it was reported that the local synthesis of dynein cofactors Lis1 and dynactin1 is adjusted according to the varying demand of axonal transport (Villarin, McCurdy, Martínez, & Hengst, 2016). In order to determine how loss of *dynactin1a* function led to the reduced axonal arbor and behavioral phenotype, we needed to assess whether it affected the expression of other subunits of dynactin, dynein, or other known interactors, which could help define an impaired function in our mutants.

We performed quantitative RT-PCR on 6dpf *mok*^{m632/-} embryos to first validate the loss of mRNA in our mutant, and to determine if loss of *dynactin1a* leads to altered expression of genes coding for other components of the complex (p22/24, p25, dynamitin/p50, actr1/ARP1), other regulators of dynein (*ndle1b*, *pafah1b1a* and *b/LIS1*) or if there was trophic compensation from the muscle in response to the reduced arbor size observed in the *mok*^{m632/-} embryos at this timepoint (*bdnf*) (Matthews et al., 2009) (Figure13). In addition, we also looked at the expression of kinesin-14, as it is an atypical family member of the kinesins that has been shown to move in the retrograde direction (Heuston, Bronner, Kull, & Endow, 2010).

Other than the expected reduction of *dynactin1a* due to nonsense-mediated decay, we found no significant changes in the expression levels of these genes.

In addition, as it has been reported that mutant zebrafish embryos can alter the expression and splicing of their paralogs in order to compensate for loss-of-function, as was the

case for *tardbp* and its paralog *tardbp-like*, which usually lacks the C-terminal domain (Schmid et al., 2013). We observed that the expression of *dynactin1b* was not altered by the loss of *dynactin1a* (Figure 13), indicating that this paralog does not get overexpressed in compensation. Furthermore, we also selected primer pairs that lay in the predicted CAP-Gly domain of *dynactin1b* but were unable to amplify a product by RT-PCR in either mutants or wild-type embryos (data not shown), further supporting the hypothesis that the domain is not included in the produced mRNA and probably leads to a protein similar to the 135kDa short isoform encoded by *DCTN1* (Tokito et al., 1996).

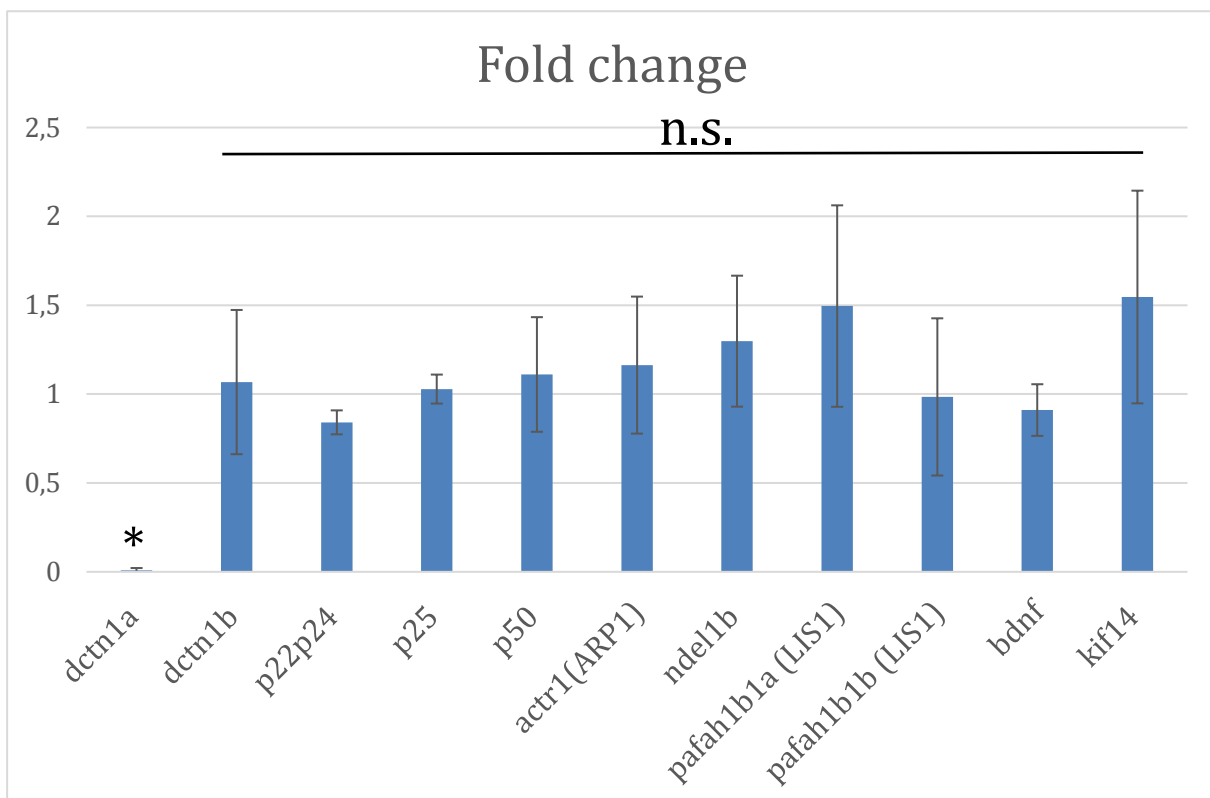


Figure 13: Quantitative RT-PCR of dynein and dynactin components and interactors for 6dpf *mok^{m632/-}* embryos. Ratio is expressed in fold change over wild-type siblings expression. ($p \leq 0,05$) (N=3, n=50 embryos)

VII-Rescue of the axonal morphology phenotype with human DCTN1

We next used an overexpression of the human wild-type gene to rescue the morphological phenotype observed in single *mok^{m632/-}* CaPs at 6dpf in order to provide a link between the model and the human pathology (Babin et al., 2014). We performed a Gibson cloning reaction to obtain a 14xUAS:ubc-hDCTN1-eGFP-E2A-tagRFPCaax-pA construct,

which would allow us to express simultaneously and under the expression of the same 14xUAS element an eGFP-tagged version of the human wild-type *DCTN1* (Stockmann et al., 2013) and an E2A-linked (Weber & Köster, 2013) reporter in the form of a membrane-bound fluorophore. The *ubc* intron was added to the sequence as it was shown to provide stability to the mRNA transcripts (Horstick et al., 2015).

We used the *mnx1* enhancer sequence described previously, which can be used in combination with the GAL4/UAS bipartite system, or directly combined with a minimal promoter, to allow for labeling of primary motor neurons in the zebrafish embryo (Zelenchuk & Brusés, 2011). In this case, we crossed our *mok*^{m632} line into the *mnx1*:GAL4 background (Tg (*mok*^{m632/-}; *mnx1*:GAL4)) to allow the injection of our rescue construct and thus the labeling of single rescued cells in an otherwise mutant background.

VII.1- Axonal morphology at 6dpf

With the expression of our construct, it was possible to see the accumulation of human Dynactin1-eGFP at synapses (Figure 14 A, B), which was confirmed by immunohistochemistry visualization of postsynaptic AChR by conjugated α -bungarotoxin (Figure 14 F). This is consistent with what has been reported about the localization of dynactin1, found enriched at the presynaptic terminal in drosophila (Eaton et al., 2002), a localization which is thought to be dependent on the function of the CAP-Gly domain and EB proteins (Moughamian & Holzbaur, 2012).

Overexpression of the human wild-type Dynactin1-eGFP did not affect the morphology or size of CaP arbors in wild-type embryos at 6dpf (Figure 14 D), which were not significantly different than what we observed upon expression of membrane-bound fluorophore (Figure 11). However, the overexpression successfully rescued the previously described reduced arbor size and complexity in our *mok*^{m632/-} embryos (Figure 14 D, C). We also noted that the rescued arbors were significantly larger and more complex than their wild-type counterparts, while still maintaining a normal average projection length (Figure 14 E), which could indicate a lack of competition for NMJ connections by surrounding cells, which do not overexpress Dynactin1-eGFP, and thus extended smaller arbors around the rescued CaPs.

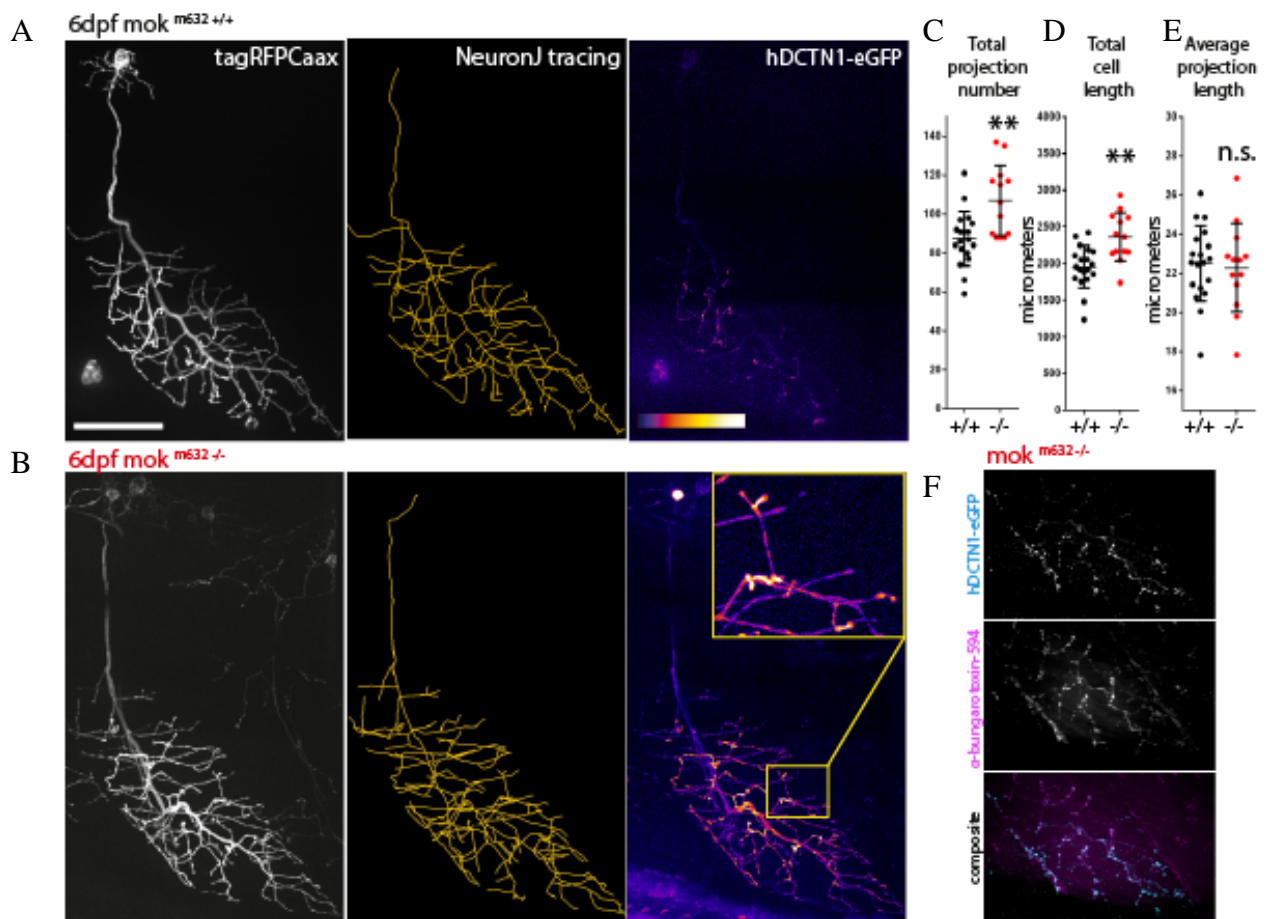


Figure 14: Axonal morphology of 6dpf cells overexpressing the human wild-type Dynactin1-eGFP. Confocal z-stack projection showing the membrane reporter, the tracing of the arbor and the signal from hDCTN1-eGFP in heatmap. Close-up showing synapse accumulation for A) a wild-type embryo and B) a *mok*^{m632-/-} embryo. Quantification of the tracings for C) total number of projection ($p \leq 0.01$), D) total cell length ($p \leq 0.01$), and E) average projection length. F) Double immunohistochemistry was done to confirm accumulation of hDCTN1-eGFP (in cyan) at synaptic sites by labeling of post-synaptic receptors with Alexa594 conjugated α -bungarotoxin (in magenta; colocalization is white). All data shown as average \pm SD (n=19,13)

As the rescue led to an overgrowth of the *mok*^{m632-/-} embryo arbors, we next wanted to determine if the overexpression of human wild-type *DCTN1* affected the development of CaP at 48hpf, where we did not observe an altered morphology in *mok*^{m632-/-} embryos.

VII.2-Axonal morphology at 48hpf

To confirm that the overexpression of the rescue construct did not in itself cause overgrowth, we also assessed the axonal morphology at 48hpf, when our mutants CaP are of normal size. At this timepoint, we did not observe an arbor overgrowth in either wild-type or mutant *mok*^{m632-/-} embryos (Figure15 C, D, E, F). In addition, the human Dynactin1-eGFP was found to be highly expressed and localized throughout the neuron, as opposed to the synaptic

accumulation seen at 6dpf (Figure 15 A, B). Together, these results suggest that the overexpression of human wild-type *DCTN1* is sufficient to rescue the axonal morphology defects in *mok*^{m632/-} embryos in a cell-autonomous manner.

VIII-Putative synapse number at 48hpf and 6dpf

Improper formation of synapses could explain both the behavioral phenotype observed at 48hpf and the growth defects seen at 6dpf in our *mok*^{m632/-} embryos. We therefore used *rab3* as a marker for putative synapses (Campbell et al., 2007). As opposed to synaptophysin, a synaptic vesicle-associated protein, which has been used in the past (Auer et al., 2015; Meyer & Smith, 2006), *rab3* has a docking role at active zone membranes and is known to interact with the SNARE complex (Rizo & Xu, 2015), making it a better readout for synapse structure than synaptophysin clusters which are very dynamic and require a size discrimination in order to sort putative synapses from large mobile clusters.

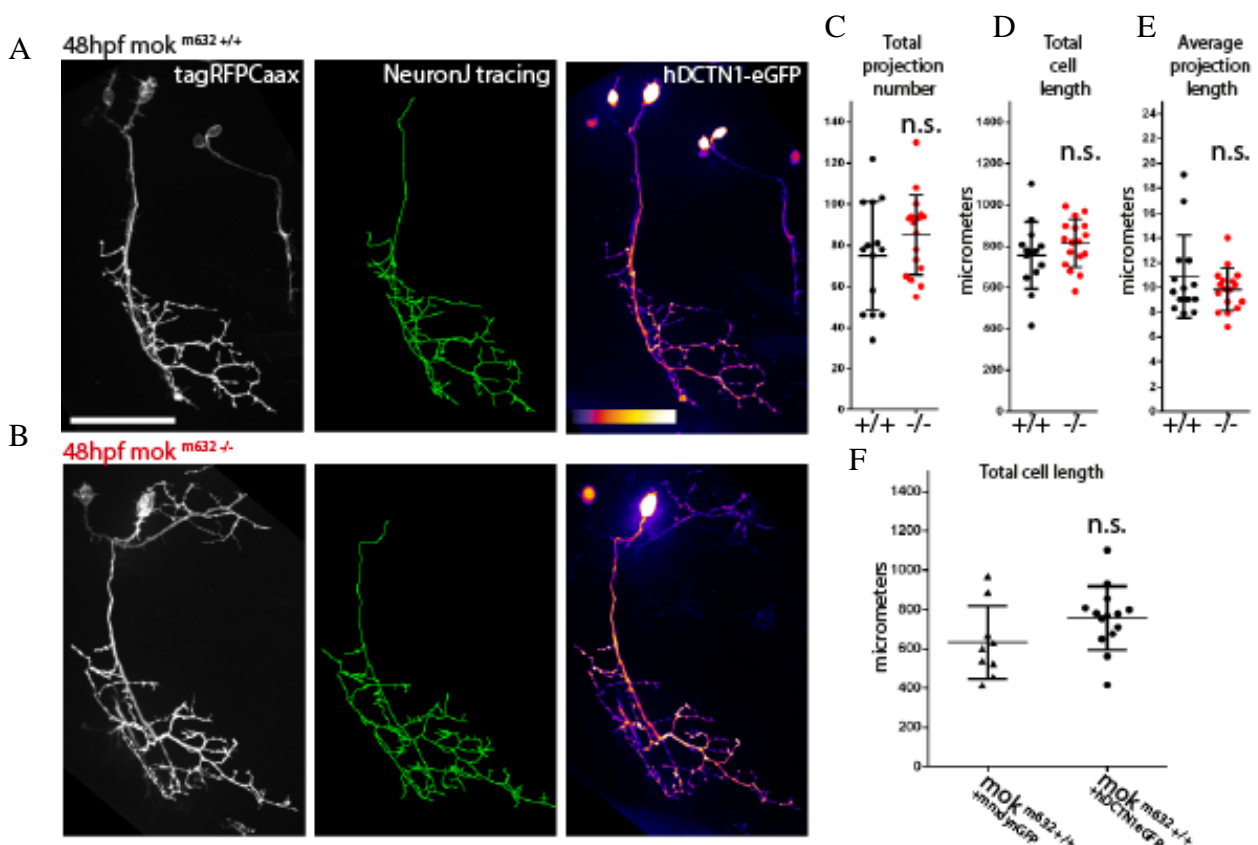


Figure 15: Axonal morphology of 48hpf cells overexpressing the human wild-type Dynactin1-eGFP. Confocal z-stack projection showing the membrane reporter, the tracing of the arbor and the signal from hDCTN1-eGFP in heatmap. Close-up showing synapse accumulation for A) a wild-type embryo and B) a *mok*^{m632/-} embryo. Quantification of the tracings for C) total number of projection, D) total cell length, and E) average projection. F) Comparison of total cell length with wild-type cells labeled with *mx1:lynGFP* from Figure 10 to show no effect on growth. All data shown as average \pm SD (n=8,14)

Furthermore, *rab3* has been reported to be essential for synaptic vesicle formation and trafficking (Tanaka et al., 2001), for the localization of presynaptic proteins at the active zone (Graf, Daniels, Burgess, Schwarz, & DiAntonio, 2009) and is known to be required for synaptic vesicle exocytosis in response to calcium (Schluter, Schmitz, Jahn, Rosenmund, & Südhof, 2004).

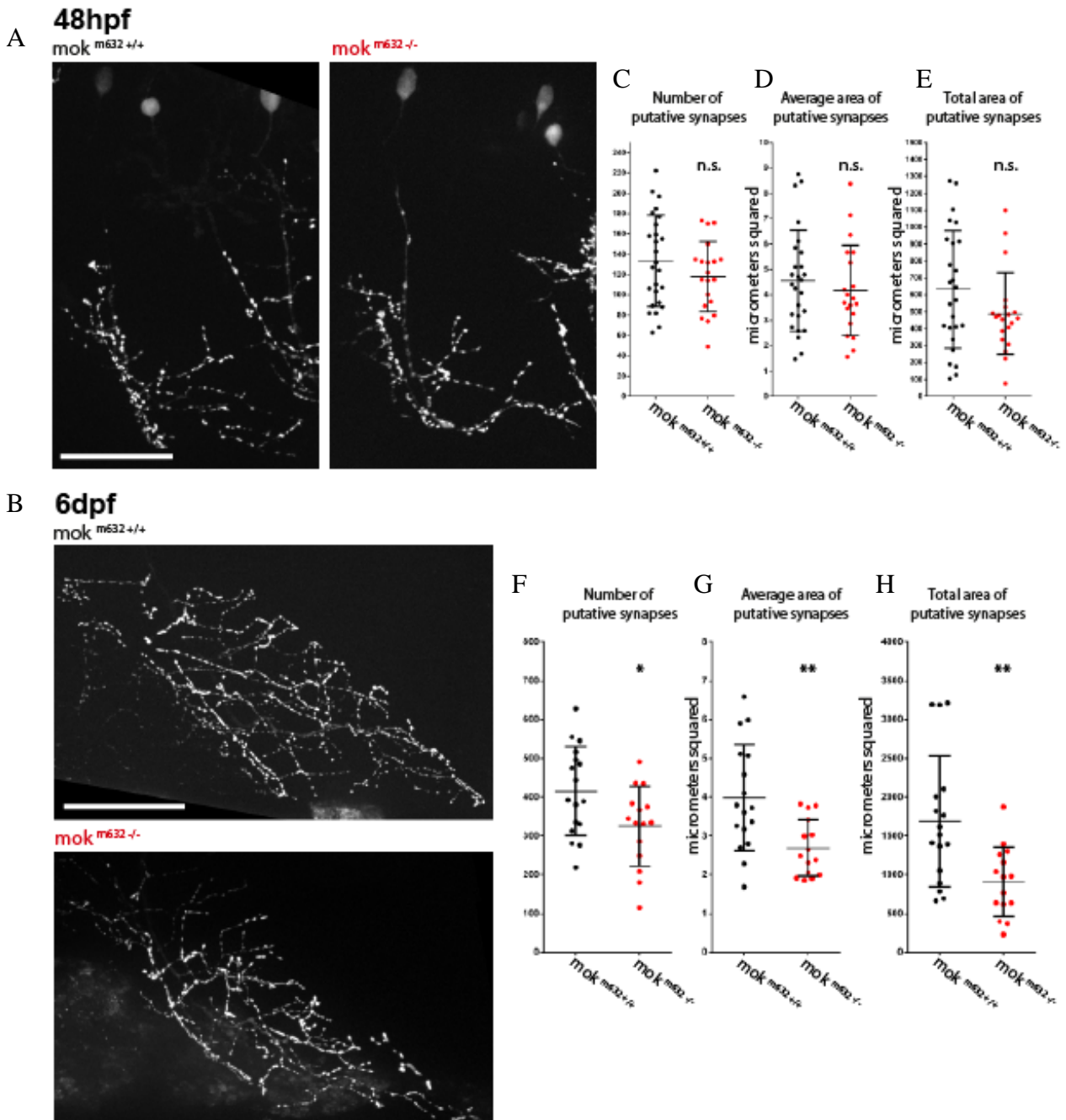


Figure 16: Quantification of putative synapse of CaP arbors at 48hpf and at 6dpf. Putative synapses were visualized by single-cell expression of UAS:*rab3-dendra2* in A) 48hpf embryos and B) 6dpf embryos. Quantification of the puncta observed for C/F) number (n.s./ $p \leq 0,05$), D/G) average area (n.s./ $p \leq 0,01$), and E/H) total area covered by of putative synapses (n.s./ $p \leq 0,01$) in arbors of 48hpf/6dpf embryos. All data shown as average \pm SD (n=26,20/n=17,15)

As our previous look at the NMJ was done on whole-mount preparations, it included all motor neurons in the ventral root and did not allow for determination of a specific effect on CaPs. We therefore cloned a pUAS-dendra2-rab3-pA construct and injected it in our Tg(*mok*^{m632/-}; *mnx1*:GAL4) background to observe the size and coverage of putative synapses in single cells of live *mok*^{m632/-} embryos.

At 48hpf, *mok*^{m632/-} embryo CaPs did not exhibit any difference from their wild-type siblings, as their arbors contained the same number of putative synapses (Figure 16 C), which were the same average area (Figure 16 D) and covered the same total area of the cell (Figure 16 E). At 6dpf however, the CaP arbors of *mok*^{m632/-} embryos contained less putative synapses (Figure 16 F), which were also of smaller size on average (Figure 16 G) and consequently covered less total area (Figure 16 H).

These results suggest that the smaller arbors observed in 6dpf *mok*^{m632/-} embryos do not compensate for their morphological defect by increasing the density of their synapses, which could ensure proper NMJ connection. This is in line with the structural NMJ defects revealed by the co-immunohistochemistry, where coverage is diminished in pre- and postsynaptic. In fact, the lack of putative synapses could possibly explain the growth defect, as synapses are known to be necessary for the stabilization of new branches in arbor development (Meyer & Smith, 2006).

IX- Putative synapse stability at 48hpf

We next hypothesized that synapse instability could lead to the behavioral growth defects described previously. Indeed, a role for dynactin1 in synapse growth and stability has been reported in drosophila studies (Chang et al., 2013; Eaton et al., 2002), so we used the same pUAS-dendra2-rab3-pA construct described previously to perform timelapse imaging of putative synapses at 48hpf. As we already observe a behavioral phenotype at this timepoint without morphological defects, the synapse stability would not be affected by possible compensatory mechanisms set forth by a cell in distress, as could be the case at 6dpf.

Confocal z-stacks were acquired initially (t=0) then 3h later in the same cell. This particular interval was reported to be a benchmark lifetime for putative synapse stabilization (Meyer & Smith, 2006). While there was no significant difference between *mok*^{m632/-} embryos and their wild type siblings at t=0 or at t=3h in the metrics presented in the previous section

(data not shown), we found that the fold change of synapse number (Figure 17 C) and synapse total area (Figure 17 E) between the two acquisitions was significantly lower in *mok*^{m632-/-} embryos than their wild-type siblings, while the fold average area of putative synapses did not change (Figure 17 D). These results suggest that dynactin1 has a role in synapse stabilization, as putative synapses are unstable in our loss-of-function model.

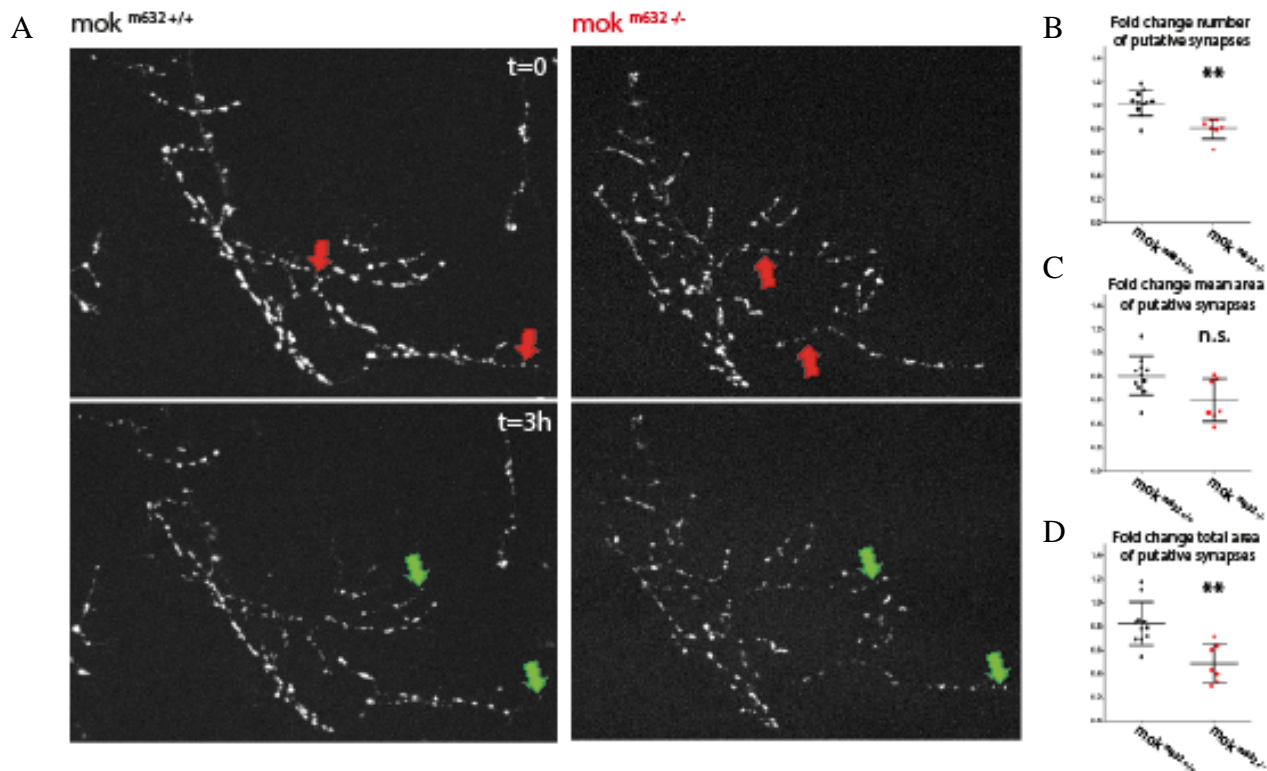


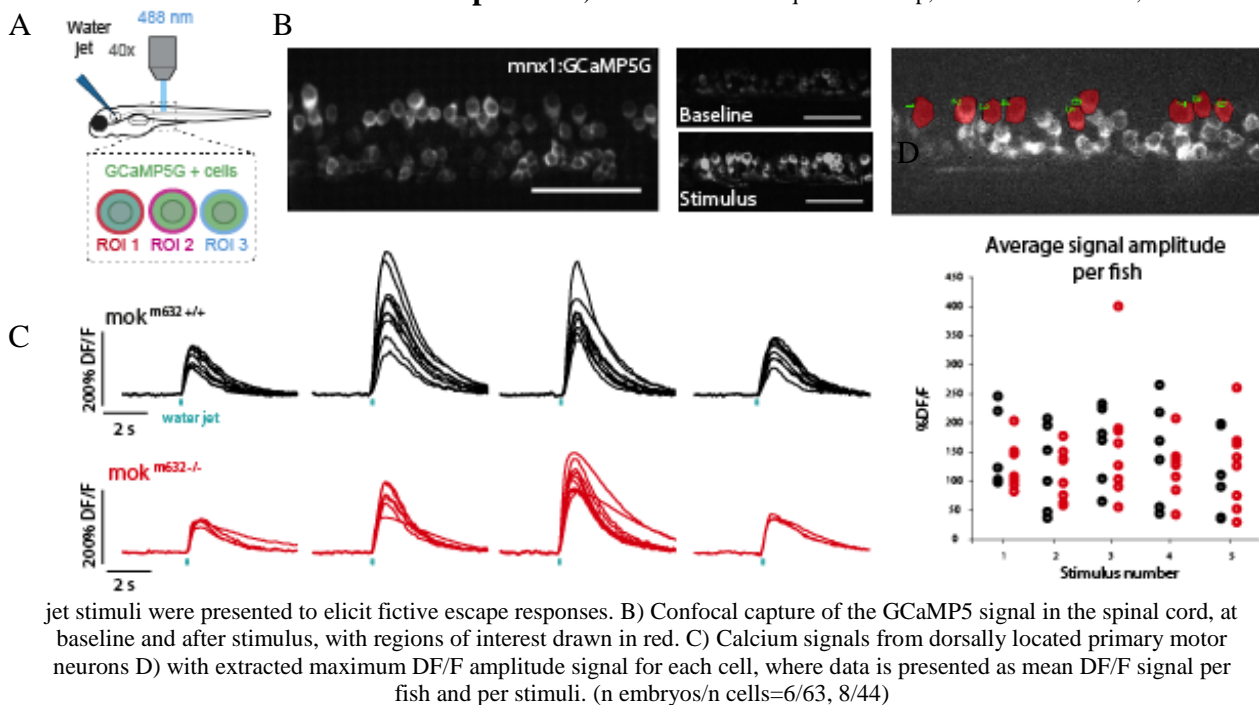
Figure 17: Putative synapse stability assay in 48hpf CaP arbors. Putative synapses were visualized as previously by single-cell expression of UAS:rab3-dendra2 in 48hpf embryos. A) Z-stacks of cell arbors were acquired initially and B) 3h later to compare numbers of synapses lost and added during this time. Quantification was done by particle analysis, and presented as fold-change for each cell with regard to B) number ($p \leq 0,01$), C) mean area, and D) total area of putative synapses ($p \leq 0,01$). All data shown as average \pm SD (n=11,7)

X-Spontaneous activity of the CaPs in the spinal cord at 4dpf

Unstable synapses likely cause electrophysiological abnormalities at the NMJ, which could explain the behavioral phenotype we observed at 48hpf. However, as swimming is a complex behavior requiring the activity of many different types of neurons in the spinal cord, we first needed to demonstrate that the defects were not coming from upstream of the CaPs. We therefore used optogenetics to determine if the motor neurons were recruited in an orderly fashion during fictive swimming (when the muscle is paralyzed to allow imaging). In this experiment, a genetically-encoded calcium indicator (Akerboom et al., 2012) is under

expression of our *mnx1*:GAL4 driver in $Tg(mok^{m632}; mnx1:Gal4; UAS:GCaMP5G)$ (Figure 18 B) and reveals the firing pattern as imaged by calcium transients in the cell bodies of primary motor neurons upon presentation of a stimulus (Figure 18 A) (Knafo et al., 2017). No difference in response to stimulus was observed in the *mok*^{m632/-} embryos, and no change was found in maximum DF/F amplitude signal for each cell (Figure 18 D), suggesting no defects upstream of CaPs, as the primary motor neurons are recruited normally in a fictive escape behavior.

Figure 18: GCaMP analysis of spinal cord primary motor neuron recruitment during a fictive evoked response. A) Schematic of the acquisition setup, where for each larva, five water



XI-Neuromuscular junction mEPC at 6dpf

As determined by the previous experiment, the behavioral defects observed at 48hpf, suggesting a fatiguing of the NMJ, did not arise from alterations in the spinal cord signaling upstream of the CaPs. We then set out to characterize the electrophysiological properties of *mok*^{m632/-} NMJs by looking at spontaneous properties of single vesicle release (quantal events) by monitoring the miniature end-plate currents (mEPC), as was done previously for other ALS models (Armstrong & Drapeau, 2013, 2013).

We did not observe any differences in the metrics analyzed, as mEPCs in *mok*^{m632/-} embryos exhibit the same kinetics as in their wild type siblings, with no significant difference found in average amplitude or frequency of events (Figure 19 B). In addition, quantal content was also unaffected, and parameters like rise and decay time (Figure 19 C,D) did not change,

indicating that in *mok*^{m632-/-} embryos, synaptic vesicles are able to fuse efficiently with the membrane, at the same frequency as in wild-type siblings, that they contain a similar quantity of neurotransmitters, and that the properties of the AChR in both conditions are similar. The data shown here is for larvae at 6dpf, but we also performed this assay at 48hpf, also with no significant difference observed (not shown).

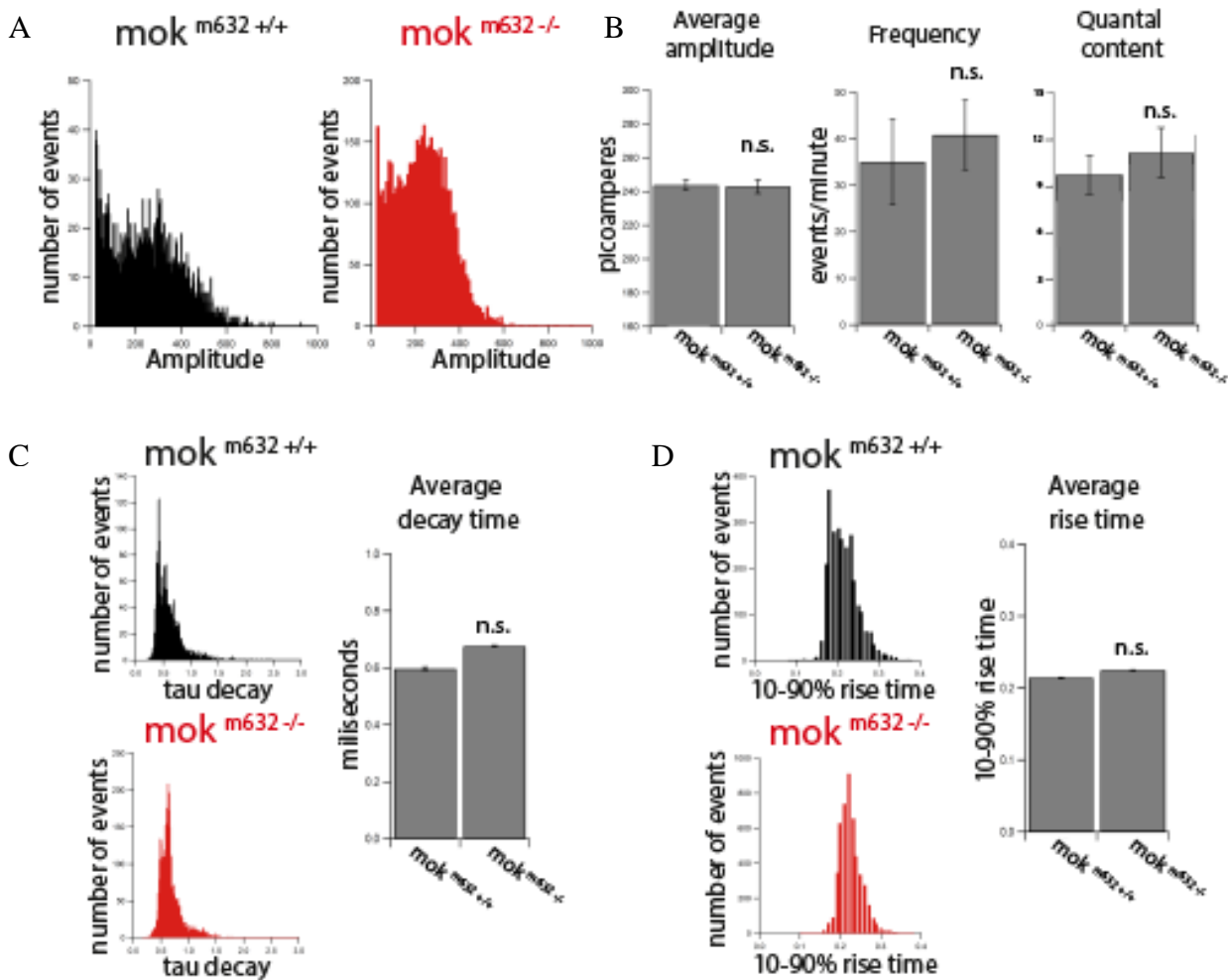


Figure 19: Quantification of spontaneous synaptic release by mEPC measurement at 6dpf. A) Number of spontaneous releases of quanta, where the kinetics were quantified in terms of a B) average amplitude, frequency and quantal content, and in terms of the C) decay constant, and D) rise time. (n=17, 6)

It was previously reported in drosophila that loss of dynactin function via disruption of the dynein-dynactin complex by expression of the dominant-negative *glued* protein led to a reduction in quantal content in spontaneous release, but no change in frequency or amplitude of these events (Eaton et al., 2002). Another fly model with a Perry syndrome-associated mutation (G38S) also revealed no change in the amplitude or frequency of spontaneous synaptic release (Lloyd et al., 2012), suggesting that dynactin does not play a role in spontaneous release

of neurotransmitter. It is to be noted that both of these reports used models that could lead to stronger phenotypes than the present study, as in the first instance, they disassembled the entire dynactin complex, and in the second, they expressed a mutant protein with dominant-negative potential. Nevertheless, although we did not observe changes in quantal content, our result corroborate the hypothesis that dynactin1 does not play a role in spontaneous release.

XII- Neuromuscular junction paired-recordings at 6dpf

While we know that CaPs are recruited normally, as they have normal calcium transients at the level of the cell body, during escape response, and that their capacity for vesicle fusion is maintained at the synapse, we wanted to determine if CaP NMJ performed normal synaptic transmission when reached by an action potential. We therefore performed paired-recordings at 6dpf, where current is injected in the CaP cell body and the response (end-plate current-EPC) is recorded at the fast-twitch muscle fiber it innervates (Armstrong & Drapeau, 2013a, 2013b; Wang, Wen, & Brehm, 2008).

We observed defects in response, where the muscle fiber in *mok*^{m632/-} embryos failed to produce a spike when the CaP was injected with current (Figure 20 C, asterisks). Stimulation frequencies of 1Hz to 100Hz were used (Figure 20 B) and *mok*^{m632/-} embryos produced significantly more EPC failures in response to stimulation than their wild-type counterparts. In addition, mutant embryos also displayed asynchronous release (Figure 20 C).

The previously mentioned Perry syndrome fly model exhibited a reduced amplitude of evoked junction potential at the NMJ, and while it presented a normal number of synapses at terminal boutons, a reduction in quantal content was also reported (Lloyd et al., 2012). We did not observe these defects in our model. However, when compared with zebrafish ALS models, which also had a higher EPC failure frequency for *TARDBP* (Armstrong & Drapeau, 2013), and for *FUS* (Armstrong & Drapeau, 2013), we do find that overall, the NMJ in ALS fail to responds efficiently to stimulation. In both these models, spontaneous release defects could explain the higher failure rate, which was not the case for dynactin1.

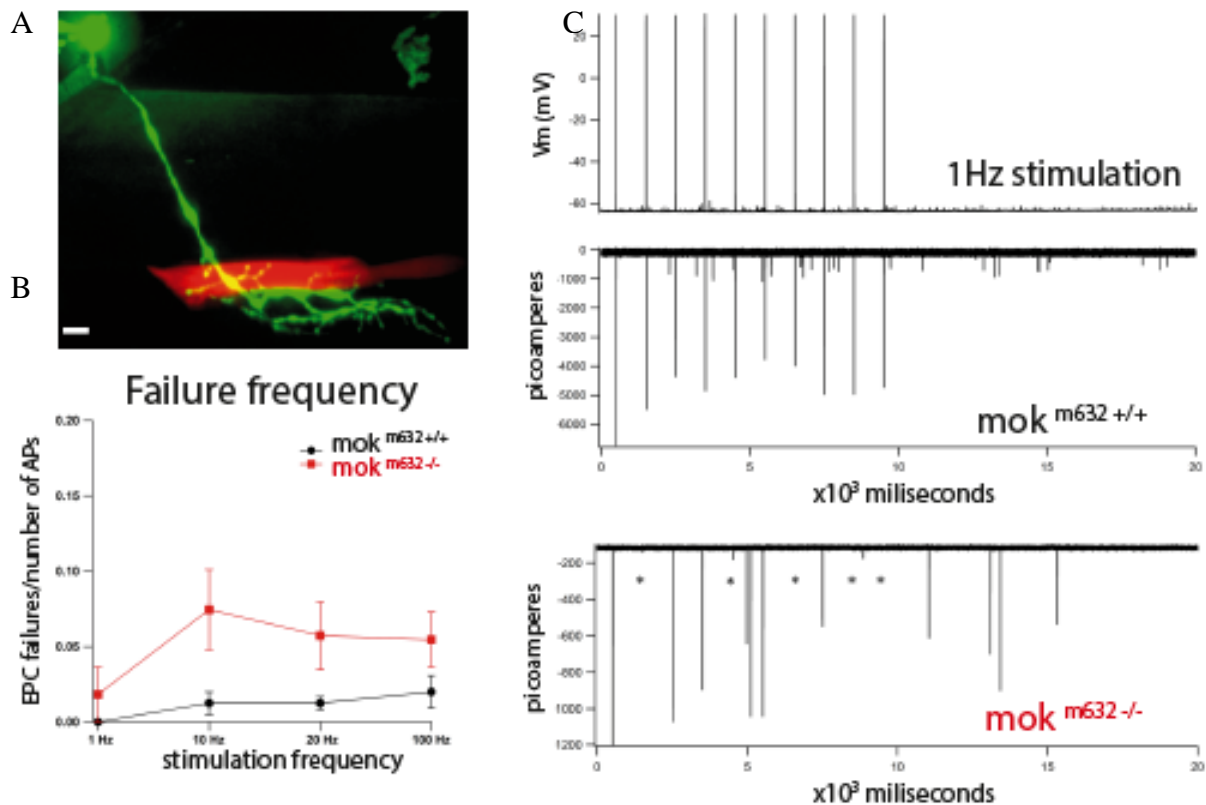


Figure 20: Paired-recordings of CaP motor neurons and fast-twitch muscle fiber. Paired recordings were obtained by injecting current into the cell body of CaPs and recording the response at the level of the muscle fiber it innervates. A) Dye-filled CaP (green) and its paired dye-filled muscle fiber (red). Mutant embryos display higher rates of failures in response to stimulation, B) example trace shown here for a frequency of 1Hz, failures labeled with asterisks. Mutants also display higher frequency of asynchronous release (out-of-synch peaks). C) The failure frequency is plotted here as a relation of stimulation frequency, data presented as mean with confidence interval, showing significance ($p \leq 0,05$).

XIII- Axonal transport

Dynactin1 has been reported to have an essential role in axonal transport, whether by regulating the microtubule cytoskeleton assembly (Lazarus et al., 2013), by directing dynein processivity (Moughamian & Holzbaur, 2012) or by coordinating bidirectional movement (Marjan et al., 2007). We made use of the $mok^{m632-/-}$ model to investigate defects *in vivo* at the level of axonal transport by live, *in vivo* timelapse imaging of fluorophore-labeled cargo, in order to determine if they could underlie synapse instability and impaired growth. The loss of function of dynactin1 could lead to various types of defects: reduction of functional dynactin-dynein complexes available for transport (motor depletion or dilution), preferential selection of cargo (mediated by protein-protein interaction), and reduced processivity of retrograde movement (impaired stability), which could lead to the formation of aggregates or accumulation of cargo at distal ends. Also, due to the nature and the regulation of bidirectional transport, it is possible that the loss of dynactin1 function, and possibly of dynactin and dynein activity, would

lead to defects in anterograde-directed axonal transport. We have thus investigated axonal transport along the mid-axon of CaP motor neurons

XIII.1-Choice of cargo and method of expression

We developed an assay to follow axonal transport in live zebrafish neurons by the use of constructs expressing fusion proteins of known vesicle markers and organelle proteins. Our method is based on previous work by the Link lab (Clark, Winter, Cohen, & Link, 2011) for the labeling of endosomes, and work by the Misgeld lab (Paquet, Plucińska, & Misgeld, 2014; Plucińska et al., 2012) for mitochondria. Our constructs and method were validated in previous work focused on the role of another motor protein, Kif5A, in the development of retinal ganglion cells of the zebrafish optic tectum (article in Annex (Auer et al., 2015)).

The constructs were generated via Gateway cloning, which allowed us to easily recombine various fragments to obtain different proteins, tagged with fluorophores and co-expressing a membrane-bound reporter. We thus generated the following constructs in parallel, to respectively label mitochondria (with prohibitin, phb, an inner membrane protein), early endosomes (rab5c), late endosomes/multivesicular bodies (MVB; rab7), and recycling endosomes (rab11a), where the fusion protein and the membrane reporter are under the expression of a sequence of four non-repeated UAS: p4nrUAS:tagRFPCaax-pA-4nrUAS:PhbGFP-pA-Tol2;cmcl2:eGFP, 4nrUAS-tagRFPCaax-pA-4nrUAS-eGFP-Rab5c-pA;cmcl2:eGFP, 4nrUAS-tagRFPCaax-pA-4nrUAS-eGFP-Rab7-pA;cmcl2:eGFP, 4nrUAS-tagRFPCaax-pA-4nrUAS-eGFP-Rab11a-pA;cmcl2:eGFP. To get a broad view of axonal transport in the cell, we selected general markers for endosomal vesicles (early, late and recycling), which are known to be reliant on transport, as well as mitochondria, which is an essential organelle for energy production and calcium buffering.

The membrane reporter co-expressed with the cargo of interest was used to confirm the targeted expression in CaPs and the use of the bipartite UAS/GAL4 system allow for these constructs to be used in various backgrounds (article in Annex (Auer et al., 2015)). In this case, the constructs were injected, along with transposase mRNA into Tg(*mok*^{m632}; *mnx1*:GAL4) to allow for single-cell labeling and tracking of axonal transport *in vivo*.

To support our choice of cargo, numerous studies have reported a role for dynactin1 in specific processes or particular interactions. For instance, it was previously shown that the

dynactin complex was necessary for the retrograde transport of endosomes, but not for endocytosis, endosome maturation or local recycling, although independently of recycling endosomes (Valetti et al., 1999).

In addition, a fly model of Perry syndrome, harboring a mutation in the CAP-Gly domain of dynactin1, exhibited accumulations of endosomes at the NMJ terminal boutons (Lloyd et al., 2012). This subunit has also been shown to be required for the recruitment of the Rab7 to dynein, via interaction with a complex formed of Rab7-interacting lysosomal protein (RILP) and oxysterol-binding protein-related protein 1 (ORPL1). The binding of this complex to dynein is however not sufficient to induce processivity of the motor, which relies on binding to β III spectrin dependent on RIPL and ORPLI1 (Johansson et al., 2007).

Dynactin1 was also reported to be necessary for axonal transport of mitochondria, early and late endosomes, as well as TrkA, TrkB and APP-containing vesicles. In this model, they had achieved an 80% reduction in protein expression by siRNA (Moughamian et al., 2013). Furthermore, mitochondria are known to be transport to areas of high energy demands like synapses and nodes of Ranvier. Improper localization was shown to lead to energy deficits and impaired calcium buffering, which affects growth and synapse development (Aren et al., 2015). Defects in axonal transport of this organelle will undoubtedly impair the recycling and degradation processes.

Overall, this assay casts a wide net to try to identify axonal transport defects that could arise when the function of *dynactin1* is lost. Particular dysfunctions affecting specific cargoes could be then characterized further to suggest a mechanism of action leading to growth defects and synapse instability.

XIII.2-Cargo distribution at 48hpf

In order to first assess if cargo was indeed being properly distributed, we used the construct described above and acquired z-stacks of single CaPs in our *mok*^{m632/-} embryos. If dynein function was abolished by lack of dynactin1, we would expect to see accumulation of cargo at the distal end of the arbor, as they could not be transported in the retrograde back to the cell body. If lack of dynactin1 caused a total loss of bidirectional transport, we would expect to see no cargo in the axon or arbor, as it would not be transported at all from the site of synthesis at the soma. If dynactin1 is however involved in cargo selection or stability, we could expect

defects for only some cargos and not others, or to observe the formation of aggregates. Additionally, impaired transport could lead to improper fusion and fission of endosomal vesicles and mitochondria, a process essential to their function, which would alter their size and possibly, their number.

Another hypothesis that can be tested with this assay is whether dynactin1 is essential to the unloading of cargo as was previously reported. Indeed it was shown that impairment of this function led to perinuclear accumulation of cargo like mitochondria and early endosomes, as a result of inhibition of normal recycling of dynein and dynactin (Jin et al., 2014).

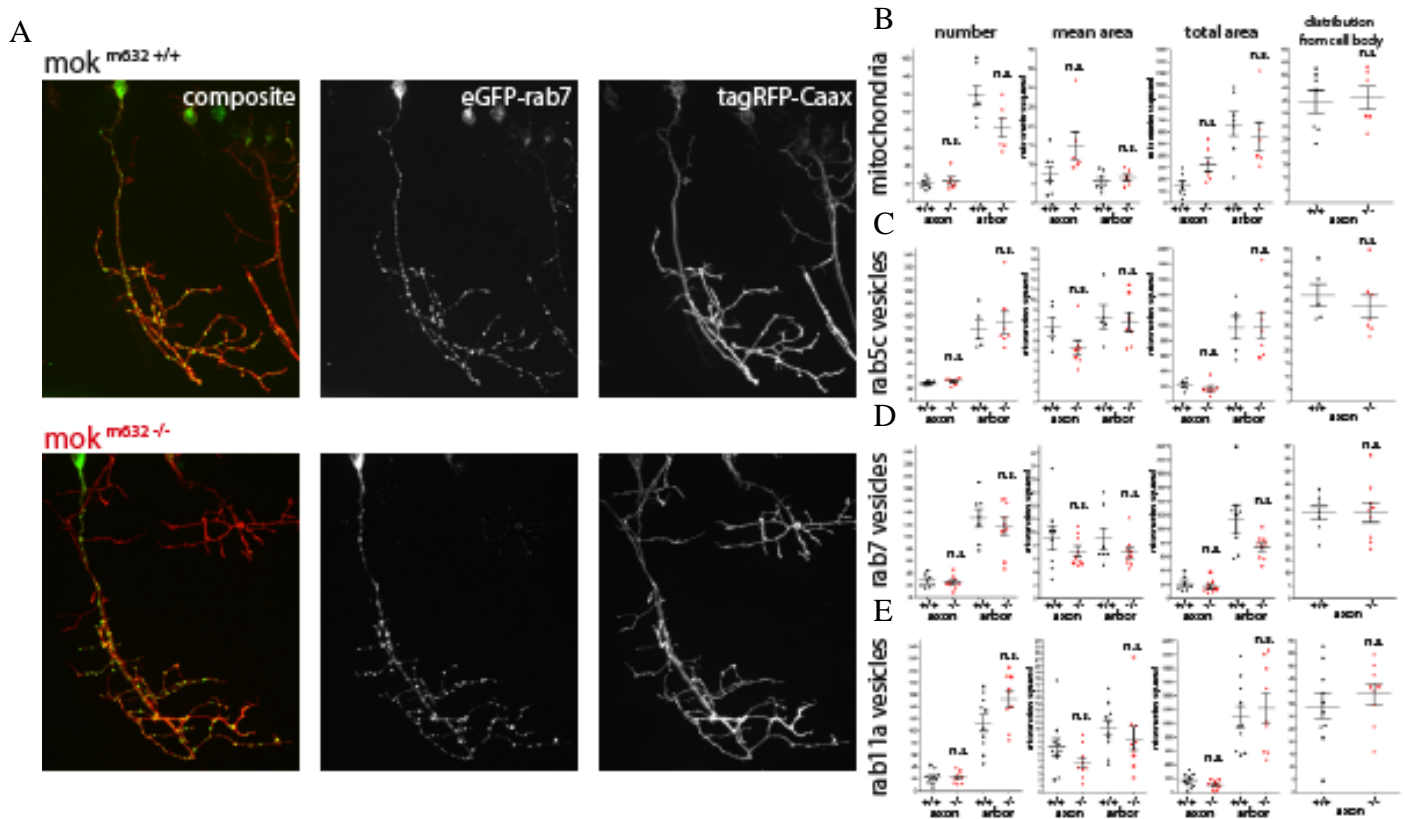


Figure 21: Cargo distribution in live CaP cells at 48hpf. Cargo was visualized *in vivo* by co-expression of a membrane reporter (tagRFP-Caax, in red) and a cargo-specific tagged protein (in this case, eGFP-rab7, green). A) Examples of z-stack projections for late endosomes/MVB for 48hpf wild-type and *mok*^{m632/-} embryos. The quantification for cargo distribution was done by separating the axonal compartment from the arbor (determined by first branching point). The distribution from cell body metric is done in the axon and represents the average distance, based on the center of mass of each cargo, in order to determine if there is distal accumulation. B) Quantification for mitochondria, C) early endosomes (rab5c), D) late endosomes/MVB (rab7) and E) recycling endosomes (rab1a). All data shown as average +/- SD. (B n=7,6; C n=5,7; D n=7,9; E n=10,9)

We did not observe any changes in size, number, total coverage or distribution of early (rab5c), late/multivesicular bodies (rab7), or recycling endosomes (rab11a), or for mitochondria (Figure 21). Furthermore, no accumulation or aggregates of these cargos were visible in either wild-type or *mok*^{m632/-} embryos at 48hpf. As all our assayed cargo is normally distributed, our results at this point suggest that dynactin1 does not lead to the preferential selection of cargo and is not essential to axonal transport.

XIII.3-Cargo behavior and run metrics at 48hpf

While the loss of dynactin1 could have no effect on general distribution of cargo, it could alter the dynamics of movement in either direction, for example by reducing processivity or by interfering with the mechanisms regulating bidirectionality. Live timelapse imaging of cargo dynamics allowed us to observe the movement of cargo along a single-plane, linear segment at the level of the mid-axon of CaPs. The acquisition frequency was adjusted to the speed of movement (one image acquired every second for 10 minutes or 1s/10min, for mitochondria, 500ms/5min for endosomes), and the resulting timelapse image sequence was used to generate kymograms. These two dimensional representation of movement follow Cartesian rules and plot the axonal length (on the x axis, in μm) against time (one pixel for each timepoint, on the y axis) to allow the visualization of stable cargo, which form columns as they do not move in the x axis from timepoint to timepoint, or mobile cargo, by the formation of diagonal lines, where each unbroken segment represents individual “runs” of a mobile cargo. The speed of individual runs can then be calculated based on the slope of these runs, and ratios of movement directionality, plus mobile versus non-mobile cargo can be determined.

Below we included examples of kymograms with labeled runs in the anterograde (cyan) and retrograde (magenta) direction for mitochondria and early endosomes (Figure 22 A) and the following sections will present the results of analysis based on those tracings for each tracked cargo (Figure 23, 24, 25, and 26). We first determined the density of cargo on the axonal segment, then analyzed the dynamics by dividing movement into a retrograde (towards the cell body, dynein-mediated) and anterograde (towards the synapse, mediated by kinesins) component. We extracted metrics such as area flux (number of cargo moving within the acquisition frame during a set time for a normalized axonal segment length), average run duration (in seconds), average run length (in μm) and average speed of runs (in $\mu\text{m/s}$), where all data is averaged per kymogram to reduce variability. We also determined the directionality ratio by reporting the percentage of cargo classified as stable (no movement; column),

oscillating (unstable non-mobile; zig-zag column), net anterograde-directed (slope to the right) or net retrograde-directed (slope to the left) cargo. Bidirectional cargo, where no net direction over the timelapse sequence can be determined, was counted as a half point in each direction. While oscillating cargo is considered non-mobile, we classified it apart from the stable cargo as it could indicate defects in bidirectional regulation of movement. Indeed, the zig-zag movement of these cargoes could represent motors of opposite directions engaged in a tug-of-war, as they are both bound to the microtubule tracks.

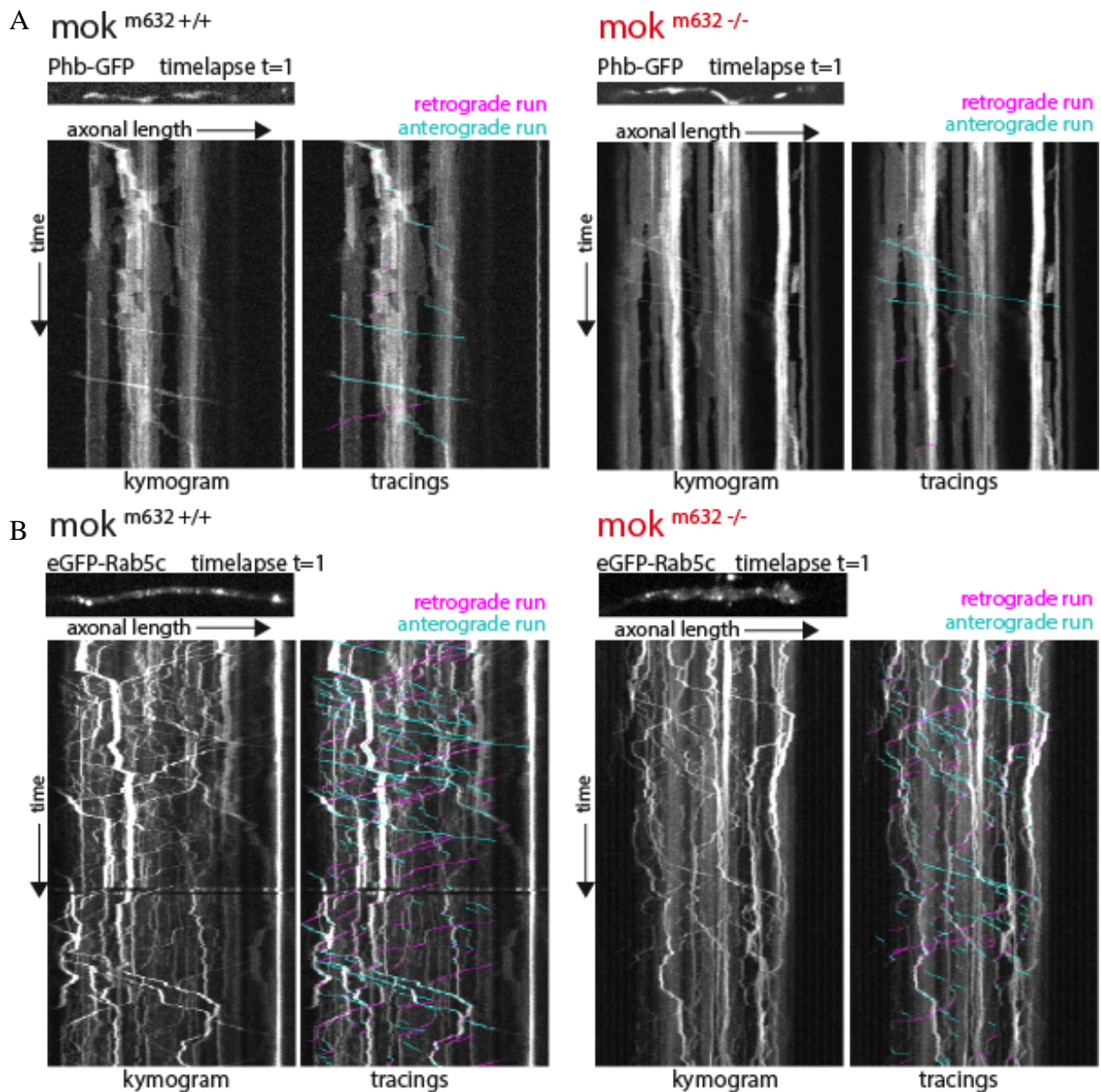


Figure 22: Live *in vivo* axonal transport of cargo in 48hpf CaPs. Timelapse imaging was performed by spinning disk confocal microscopy on single-plane linear segments of the mid-axon in CaP cells. By convention, the axonal segment is presented with the cell body oriented to the left, and the arbor to the right, where cargo moving to the right would be going in the anterograde direction. The timelapse image sequence (first timepoint shown here) is used to generate a kymogram, which is a 2D representation of movement, where the axonal segment length in μm is in the X axis, and time is in the Y axis, where each pixel represents one timepoint of the timelapse sequence. Kymograms are shown here with labeled traces for retrograde (magenta) and anterograde runs (cyan), which were used for quantification of transport metrics. A) Example for analysis of mitochondria, imaged every 1s for 10 minutes (1s/10min) B) Example analysis for early endosomes, imaged every 500ms for 5 minutes (500ms/5min).

XIII.3.1-Mitochondria run metrics at 48hpf

We did not observe significant changes for most of the metrics measured for the axonal transport of this organelle in our *mok*^{m632-/-} embryos (Figure 23). Directionality ratio was maintained for the axonal mitochondrial population, and flux was unchanged in either direction. We did however find a higher density of mitochondria in *mok*^{m632-/-} embryos, when compared to their wild-type siblings, and as the axonal coverage by this organelle was not affected this might suggest axonal mitochondria to be slightly smaller in size in our mutants. Average run length in the anterograde direction was also significantly shorter in *mok*^{m632-/-} but no effect was found on average run speed or duration in this direction.

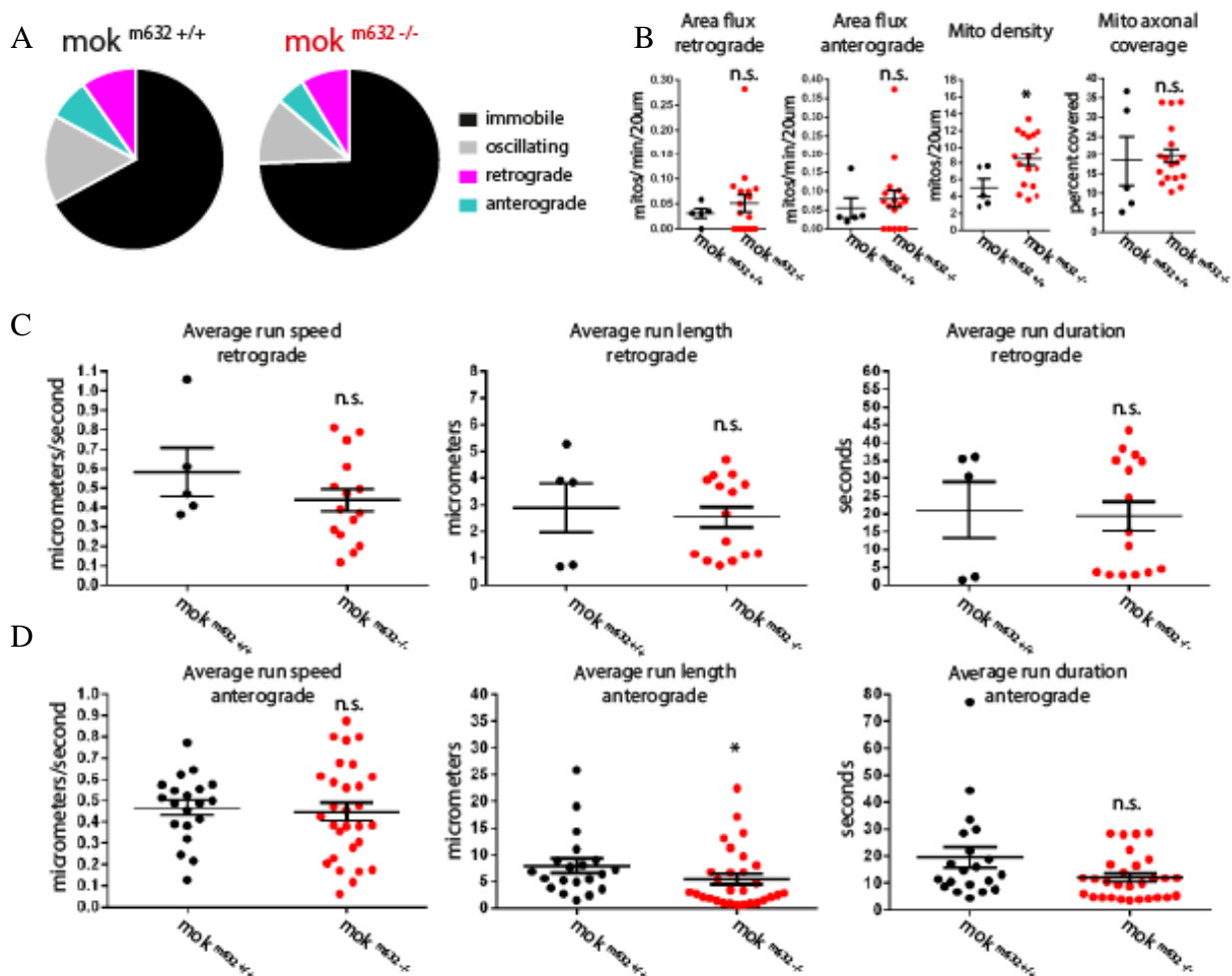


Figure 23: Axonal transport metrics for mitochondria at 48hpf. A) Directionality ratio chart for mitochondrial movement, where stable mitochondria were labeled as “immobile” (black), non-mobile but unstable mitochondria were labeled as “oscillating” (grey), retrograde-directed mobile mitochondria as “retrograde” (magenta) and anterograde-directed mobile mitochondria as “anterograde” (cyan). B) Area flux was determined for both direction (number of moving mitochondria per minute, per 20 μm) and density (number of mitochondria per 20 μm) as well as coverage (ratio of area) was measured. Individual runs are defined as unbroken linear segments of movement, and were used to extract metrics for the C) retrograde direction and the D) anterograde direction for average run speed ($\mu\text{m/s}$), average run length (μm) and average run duration (s). All data averaged by kymogram and presented as average +/-SEM. ($p \leq 0,05$) (n retro/ antero =5/20, 8/19)

XIII.3.2-Early endosomes run metrics at 48hpf

Rab5 is involved in vesicle transport and mediates fusion of membranes from the plasma membrane via clathrin coated vesicles. The early endosomes then formed are responsible for receptor-mediated signaling which depends on retrograde transport to the cell body (Clark et al., 2011).

We did not observe any significant changes in any of the metrics analyzed for this cargo in our *mok*^{m632-/-} embryos (Figure 24) suggesting loss of dynactin1 does not interfere with the axonal transport of early endosomes.

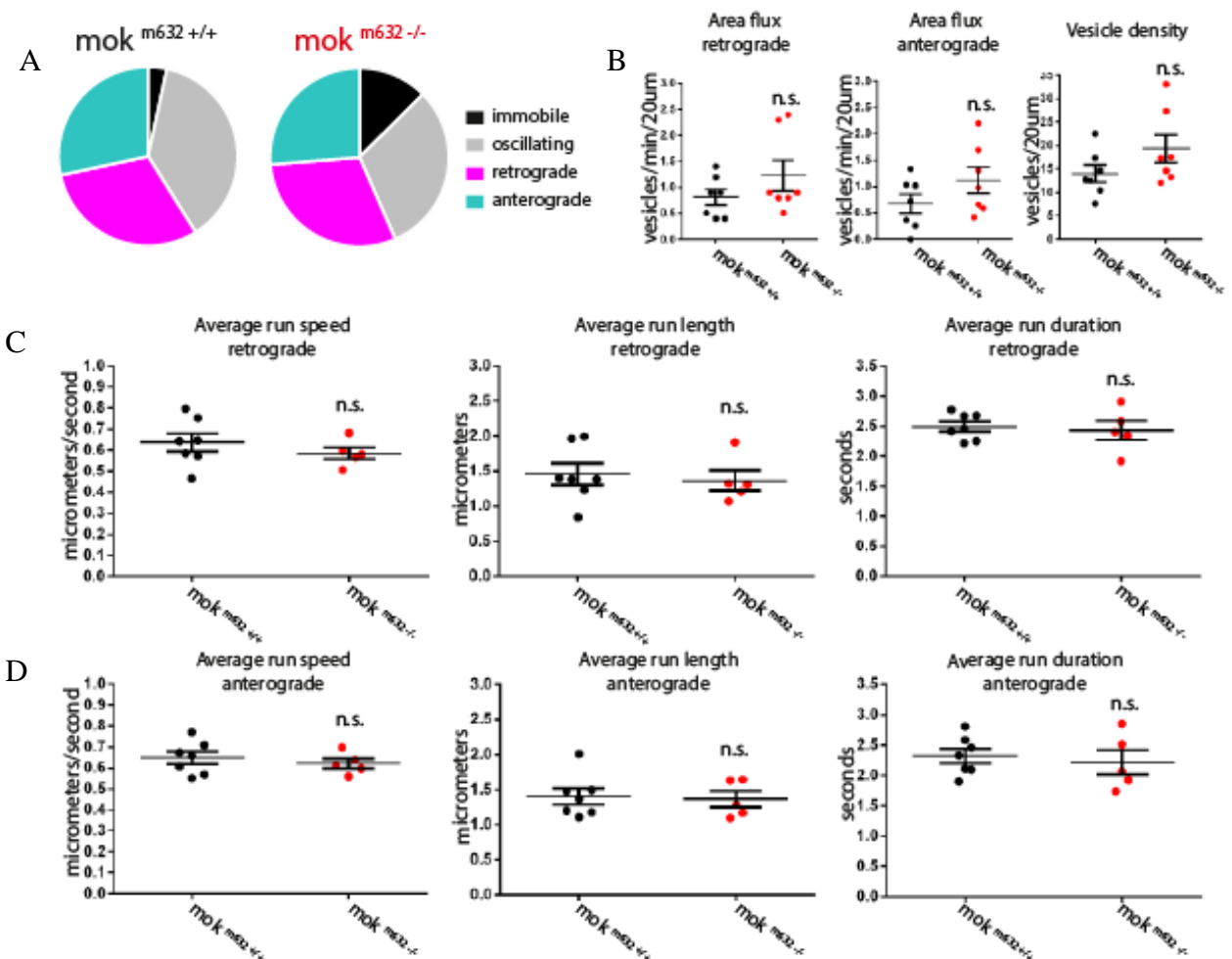


Figure 24: Axonal transport metrics for early endosomes at 48hpf. A) Directionality ratio chart for endosome movement, where stable vesicles were labeled as “immobile” (black), non-mobile but unstable vesicles were labeled as “oscillating” (grey), retrograde-directed mobile vesicles as “retrograde” (magenta) and anterograde-directed mobile vesicles as “anterograde” (cyan). B) Area flux was determined for both direction (number of moving vesicles per minute, per 20 µm) and density (number of vesicles per 20 µm) was measured. Individual runs are defined as unbroken linear segments of movement, and were used to extract metrics for the C) retrograde direction and the D) anterograde direction for average run speed (µm/s), average run length (µm) and average run duration (s). All data averaged by kymogram and presented as average +/-SEM. (n=18,17)

XIII.3.3-Late endosomes run metrics at 48hpf

Rab7 is involved in the maturation of late endosomes from early endosomes. These vesicles regulate the trafficking of cargo destined for degradation, and for this function rely on fusion with lysosome. Late endosomes are often quite large as they result from the fusion of multiple early endosomes. This process also leads to the formation of a large endosome containing tightly-packed smaller vesicles, which is why rab7 labeled endosomes are also called multivesicular bodies (Clark et al., 2011). This compartment is also involved in signaling and autophagy (Wandinger-Ness & Zerial, 2014).

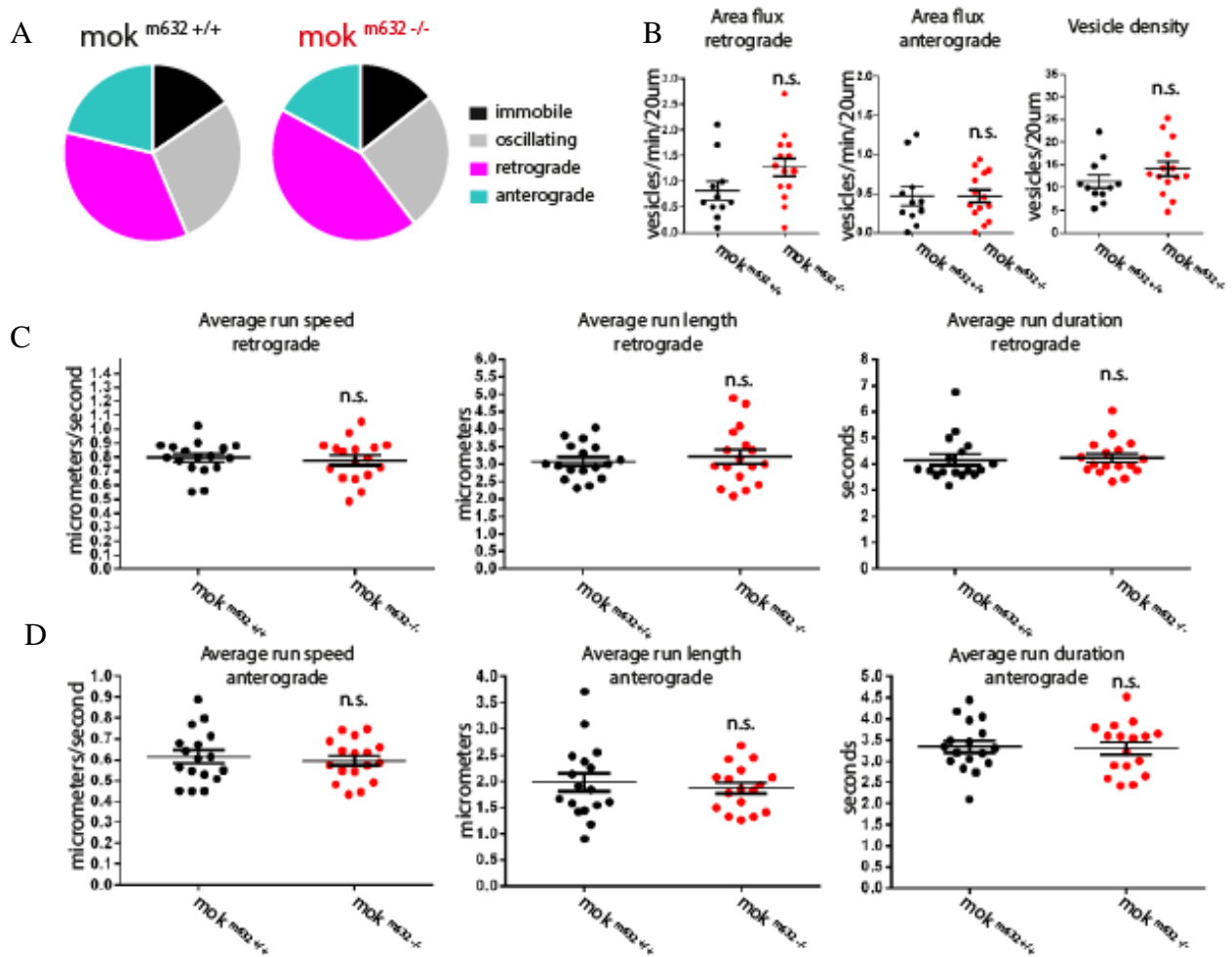


Figure 25: Axonal transport metrics for late endosomes/MVB at 48hpf. A) Directionality ratio chart for late endosome/MVB movement, where stable vesicles were labeled as “immobile” (black), non-mobile but unstable vesicles were labeled as “oscillating” (grey), retrograde-directed mobile vesicles as “retrograde” (magenta) and anterograde-directed mobile vesicles as “anterograde” (cyan). B) Area flux was determined for both direction (number of moving vesicles per minute, per 20 μm) and density (number of vesicles per 20 μm) was measured. Individual runs are defined as unbroken linear segments of movement, and were used to extract metrics for the C) retrograde direction and the D) anterograde direction for average run speed ($\mu\text{m}/\text{s}$), average run length (μm) and average run duration (s). All data averaged by kymogram and presented as average \pm SEM. (n=27,30)

As observed for early endosomes, we did not find any significant changes in any of the metrics analyzed for this cargo in our *mok*^{m632-/-} embryos (Figure 25) suggesting loss of dynactin1 does not interfere with the axonal transport of late endosomes.

XIII.3.4-Recycling endosomes run metrics at 48hpf

Rab11 labels recycling endosomes, which traffic from the plasma membrane to the ER via early endosomes (also called sorting endosomes). One of the functions of this compartment is to package receptors for degradation and to recycle them back to the cell surface (Clark et al., 2011), and like the late endosomes, it is also involved in autophagy (Wandinger-Ness & Zerial, 2014).

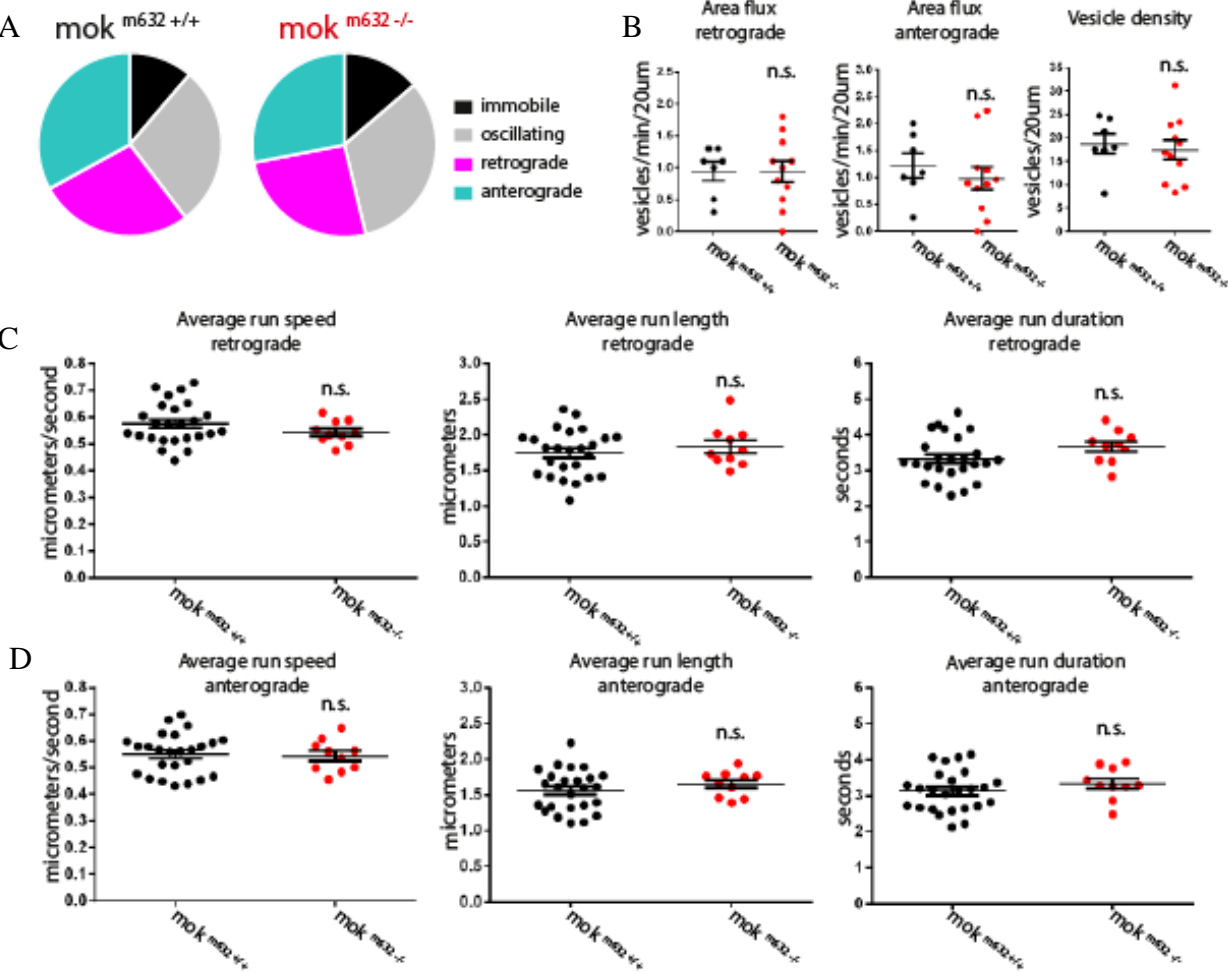


Figure 26: Axonal transport metrics for recycling endosomes at 48hpf. A) Directionality ratio chart for late recycling movement, where stable vesicles were labeled as “immobile” (black), non-mobile but unstable vesicles were labeled as “oscillating” (grey), retrograde-directed mobile vesicles as “retrograde” (magenta) and anterograde-directed mobile vesicles as “anterograde” (cyan). B) Area flux was determined for both direction (number of moving vesicles per minute, per 20 μm) and density (number of vesicles per 20 μm) was measured. Individual runs are defined as unbroken linear segments of movement, and were used to extract metrics for the C) retrograde direction and the D) anterograde direction for average run speed (μm/s), average run length (μm) and average run duration (s). All data averaged by kymogram and presented as average +/-SEM. (n=18,19)

As observed for both early and late endosomes, we did not find any significant changes in any of the metrics analyzed for this cargo in our *mok*^{m632/-} embryos (Figure 26) suggesting loss of dynactin1 does not interfere with the axonal transport of recycling endosomes.

XIII.4-Caveats of the expression method

Surprisingly, we did not observe much effect on axonal transport for many of the cargoes observed in our assay. This suggests that dynactin1 is not essential for axonal transport in our model. It is however important to consider that while the *mok*^{m632} mutation leads to a full loss-of-function of *dynactin1a*, as demonstrated by quantitative RT-PCR at 6dpf (Figure 13), homozygous embryos are not adult viable, and thus *mok*^{m632/-} embryos must be obtained via incrosses of heterozygous carriers. It is therefore possible that some dynactin1 might still be functional in our assay, as provided by maternal contribution to the *mok*^{m632/-} embryos, although the quantity of functional protein present at 48hpf would likely be very limited. Furthermore, other studies of *dynactin1* loss-of-function revealed drastic impairments due to protein reduction, for example, an 80% siRNA-mediated reduction in dynactin1 protein expression impaired bidirectional transport of mitochondria (Moughamian et al., 2013).

Unfortunately, the *mx1* enhancer is not efficient at inducing protein expression at later developmental stages, where its activity is steadily declining from 4dpf onwards (Zelenchuk & Brusés, 2011). It has accordingly proven difficult to obtain expression of our constructs in single CaPs within our limited 4-somite window at later timepoints. Nevertheless, we obtained one complete dataset for live axonal transport analysis at 6dpf, where no protein is detected in the mutants (data not shown), which we use as a proof of principle that no drastic changes occur in this process upon loss of *dynactin1a* function.

XIII.4.1-Proof of principle, recycling endosomes run metrics at 6dpf

To confirm the conclusion drawn from the live axonal transport assay, we performed the assay at 6dpf for rab11. This construct was used because it proved to be the most efficient at labeling appropriate cells at this late timepoint. As the kymograms produced here are much more dynamic than at 48hpf, with vesicles often going bidirectionally, we could not determine the directionality ratio or the area flux, but focused on run metrics. We have observed that at 6dpf, *mok*^{m632/-} embryos do not show significant changes in the retrograde direction, with run length, distance and average speed of similar values as their wild-type siblings. However,

movement in the anterograde direction revealed significantly higher run length and average run speeds (Figure 27). This change could be a result of lack of dynactin1's role on regulation of bidirectionality, or could be due to compensation by the 'cells, which at this timepoint, have a reduced axonal arbor with a lower number of synapses.

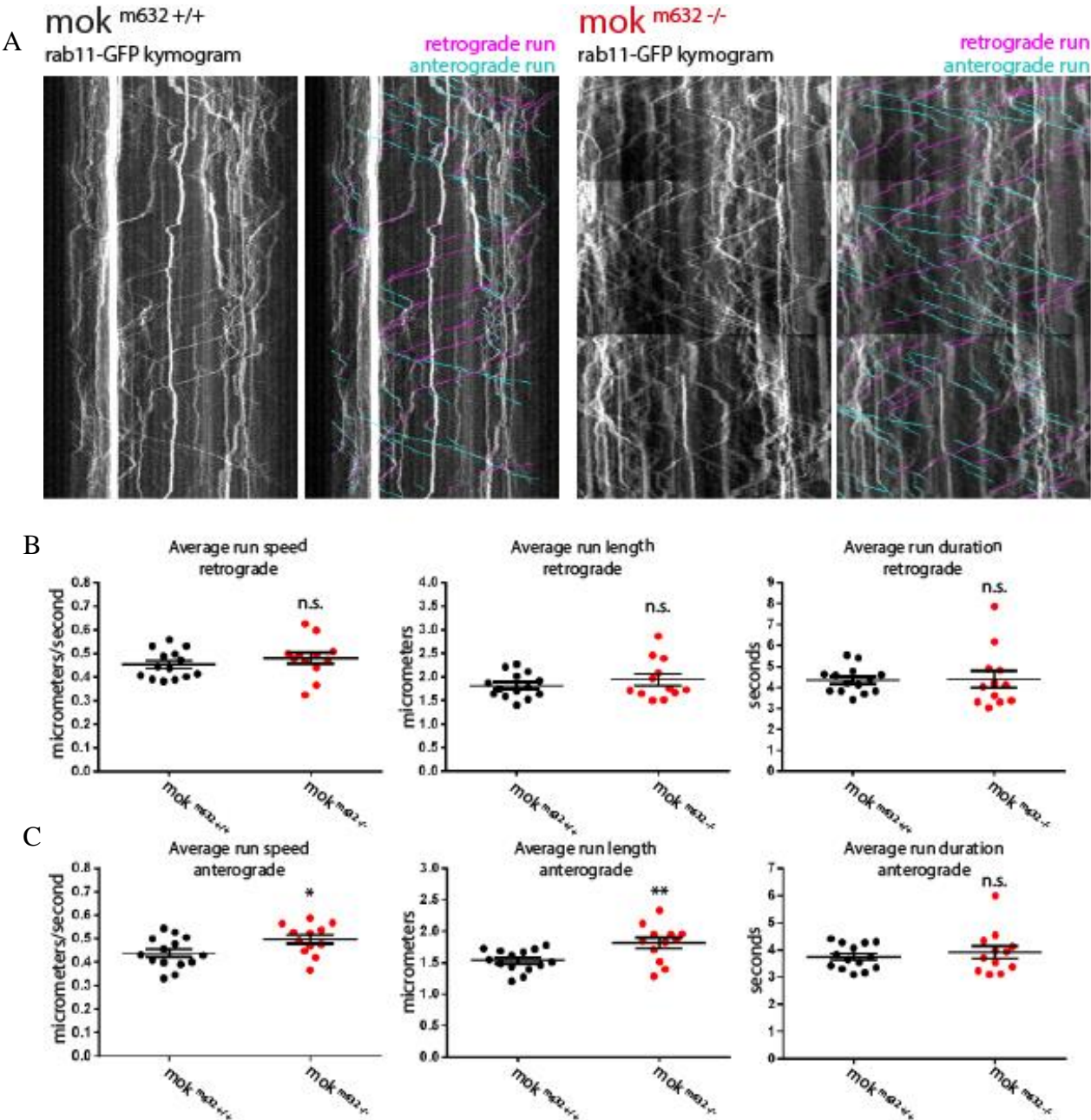


Figure 27: Proof of principle, axonal transport metrics for recycling endosomes at 6dpf.

A) Representative kymograms used for analysis, where retrograde-directed mobile vesicle runs (magenta) and anterograde-directed mobile vesicles runs (cyan) are labeled. Individual runs are defined as unbroken linear segments of movement, and were used to extract metrics for the B) retrograde direction and the C) anterograde direction for average run speed ($\mu\text{m/s}$) (n.s., $p \leq 0,05$), average run length (μm) (n.s., $p \leq 0,01$) and average run duration (s). All data averaged by kymogram and presented as average \pm SEM. (n=14, 12)

XIV-Trophic signaling involvement

CaPs rely on trophic signaling from the muscle, which acts in a feedback loop with NMJ activity, for growth after the initial contact with fast-twitch muscle fibers. As we did not observe changes in BDNF transcription in our mutants at 6dpf, as revealed by quantitative RT-PCR (Figure 13), we are considering that no trophic compensation takes place, however defects in the processing of these signals could explain the smaller arbor size observed in *mok*^{m632/-} embryos at 6dpf.

Trophic factors are indispensable for the growth and plasticity of synapses and induce two types of changes within the NMJ: acute effects which take place very rapidly and are involved in synaptic plasticity, and long-term effects, which affect synaptic structure. As effect on structure requires the synthesis of new proteins, these signals must be transported back to the cell body via axonal transport. Accordingly, neurotrophins like BDNF and NT3 act as retrograde signals to promote the maturation of the NMJ synapses by regulating the excitability of calcium channels, as well as promoting arbor outgrowth and branching, and increasing the production of synaptic vesicle proteins (Lu & Je, 2003).

XIV.1- Actin filopodia dynamics from 48hpf

Filopodia are part of the actin cytoskeleton network and act as a means for growing neuron growth cones to search the environment for guidance cues, trophic signaling, and adhesion molecules provided by muscle fibers (Sanes & Lichtman, 1999). They are quickly extended and once stabilized by a post-synaptic partner get infiltrated by microtubules to form nascent branches of a developing axonal arbor (Baas et al., 2006). When proper signals are absent, the filopodia are retracted (Kishore & Fetcho, 2015; Panzer, Song, & Balice-Gordon, 2006).

Proteins localizing at microtubule + ends (+ tip proteins) are known to be involved in regulation of the actin cytoskeleton and signaling of guidance cues during neuronal development (Bearce et al., 2015). The dynactin1 subunit could therefore play a role at this level in directing filopodial dynamics, either by interacting with the cytoskeleton, or as a consequence of trophic signaling relying on axonal transport.

We therefore set out to characterize filopodial dynamics by an assay we have previously developed, where unstable filopodia dynamics, defined by extensions which were not stabilized, is imaged between intervals of 2 minutes for a total acquisition time of 10 minutes (Auer et al., 2015) (article in Annex). We performed this assay on embryos of 24hpf (Figure 28 B), 48hpf (Figure 28 C), 72hpf (Figure 28 D) and 4dpf (Figure 28 E) to determine if an effect could be seen along development. However, no changes were found in total number, total length or average length of unstable filopodia in our *mok*^{m632/-} embryos in any of the timepoints analyzed, except for total unstable length at 48hpf (Figure 28 C).

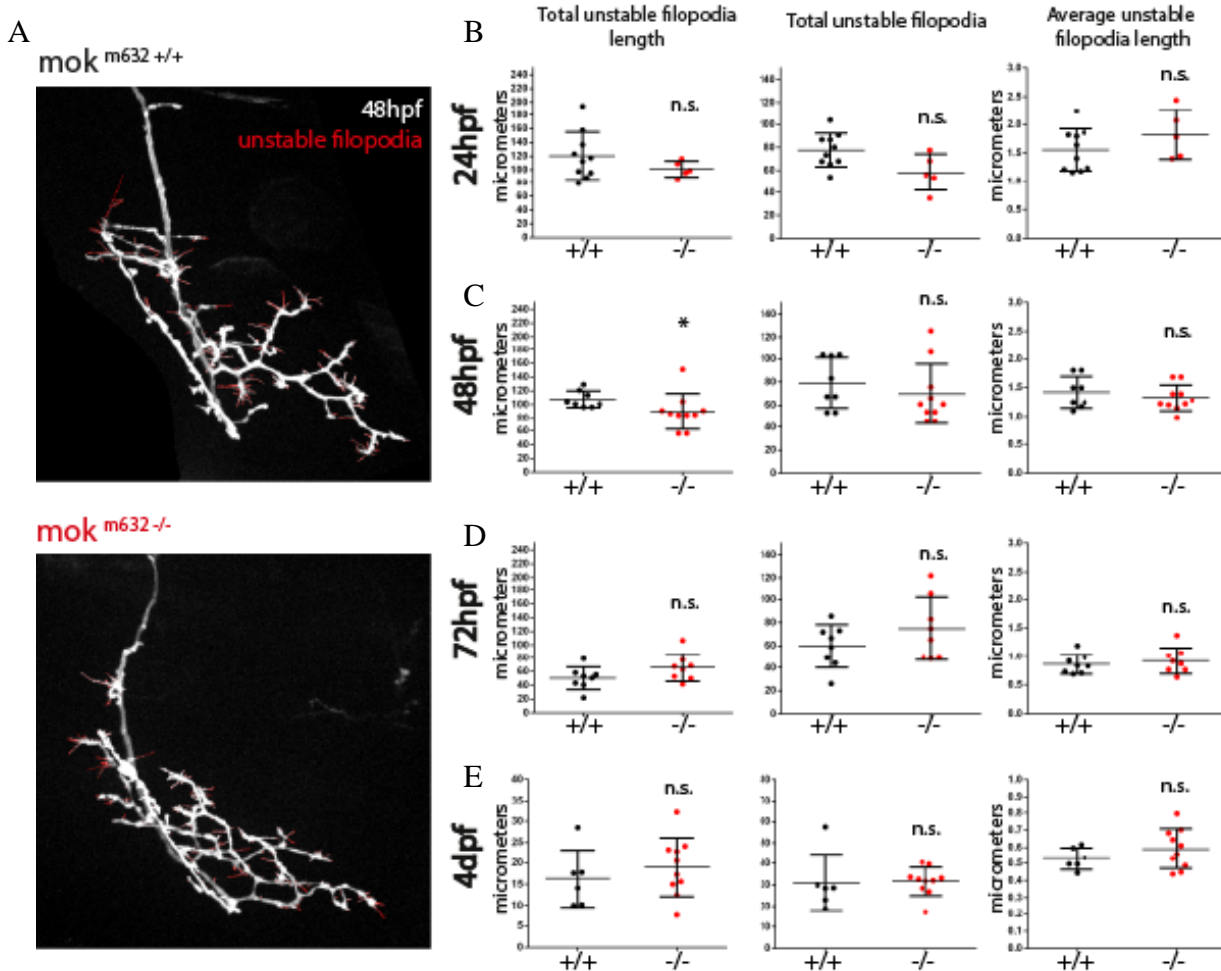


Figure 28: Filopodia dynamics at 24hpf, 48hpf, 72hpf and 4dpf. Filopodial dynamics were acquired by timelapse imaging, where a confocal z-stack of the axonal arbor was acquired every two minutes for a total of ten minutes (2/10minutes). A)The z-stack projections were then used to compare the growth and retraction of filopodia between the 6 timepoints, the sum of which is reported here as total unstable filopodia, with regard to total length, number and average length of unstable filopodia per cell arbor, at B) 24hpf, C) 48hpf, C) 72hpf and D) 4dpf. Data presented as average +/- SEM. ($p \leq 0,05$) (B n=10,5; C n=8,10, D n=8,8, E n=6,10)

The total number and average length is maintained, indicating that while the actin behavior is normal, that perhaps the arbor is going through a transition in trophic signaling at this timepoint, where guidance of the axon and initial growth is finished, and the cell now needs to adapt its connections in a long-term manner, which requires retrograde signaling. This effect is however not observed at later timepoints, indicating that this is a temporary effect or that compensation occurs after 48hpf.

Overall, these results suggest that actin behavior guiding filopodial dynamics is not affected by loss of *dynactin1a* function and that the cell has both the potential for sensing and the support of trophic signaling from the muscle.

XIV.2-p75 receptor axonal transport

Trophic signaling is mediated by two types of receptors present at the presynaptic side of the NMJ: the high-affinity Trk receptors, who bind specific ligands, and the low-affinity p75 receptor, which binds all neurotrophins. These receptors are packaged in late endosomes/multivesicular bodies destined for retrograde transport (Sandow et al., 2000).

It was reported that a switch in retrograde signaling could cause rapid-onset degeneration by increasing the shuttling of stress factors and reducing survival-promoting factors (Perlson et al., 2009). The p75 neurotrophin receptor is a suicide-survival receptor and will lead to different signaling depending on the ligand and cofactors it binds. As p75 is transported in endosomes, which showed no defects in population dynamics in our mutant embryos, we wanted to see if transport of specific p75-containing endosomes in response to trophic signaling could be impaired.

We therefore used Gibson cloning to elaborate a construct, which allowed us to visualize p75 (*ngfra* in zebrafish) in a similar way as what we have done for endosomes and mitochondria, by using similar tools as the ones which produced the 14xUAS construct for the rescue of the morphological phenotype. By injection of our 14xUAS:ubc-ngfra-eGFP-E2A-tagRFPCaax-pA construct, it was possible to perform an axonal transport assay on *mok*^{m632/-} embryos at 48hpf, as done previously.

This assay did not reveal any difference in the axonal transport of vesicles containing p75 for our *mok*^{m632/-} embryos as compared with their wild-type siblings, as we did not observe changes in vesicle density, flux, ratio of directionality (Figure 29 B), or average run length,

distance or speed in either retrograde (Figure 29 C) or anterograde (Figure 29 D). This suggests that long-distance neurotrophic signaling is unlikely to be impaired in our *mok^{m632-/-}* embryos, since both the endosomes responsible for transport to the cell body, and the receptors themselves, do not show any defects in axonal transport dynamics.

Defects in trophic signaling via transport of the p75 receptor can therefore not explain the reduced CaP arbor size seen in *mok^{m632-/-}* embryos at 6dpf.

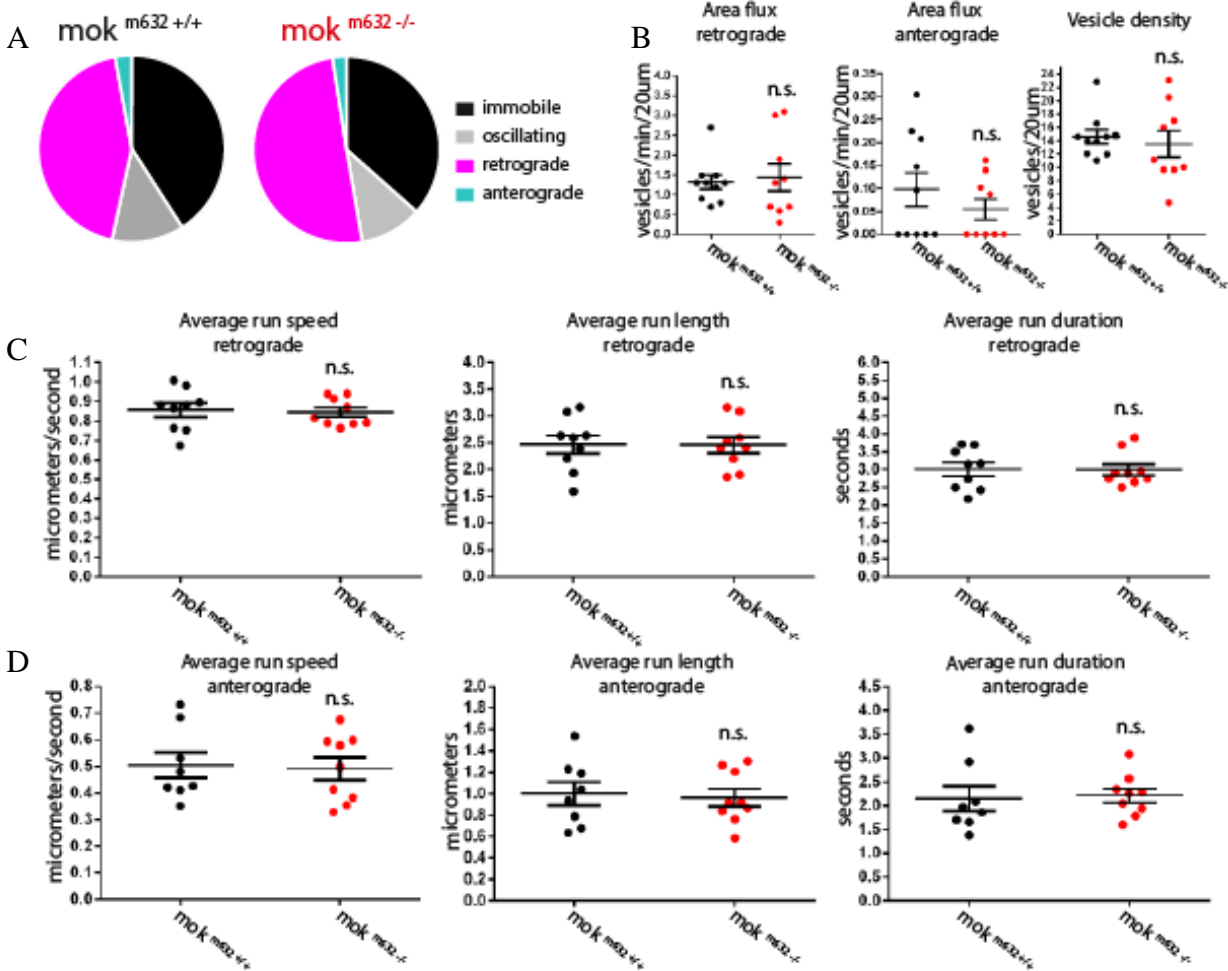


Figure 29: Axonal transport metrics for p75 receptor-containing vesicles. Directionality ratio chart for p75-containing vesicle movement, where stable vesicles were labeled as “immobile” (black), non-mobile but unstable vesicles were labeled as “oscillating” (grey), retrograde-directed mobile vesicles as “retrograde” (magenta) and anterograde-directed mobile vesicles as “anterograde” (cyan). B) Area flux was determined for both direction (number of moving vesicles per minute, per 20 μm) and density (number of vesicles per 20 μm) was measured. Individual runs are defined as unbroken linear segments of movement, and were used to extract metrics for the C) retrograde direction and the D) anterograde direction for average run speed (μm/s), average run length (μm) and average run duration (s). All data averaged by kymogram and presented as average +/-SEM. (n=10,9)

XV- Microtubule stability at 48hpf and 6dpf

Microtubules are composed of stable and dynamic sections, which are essential to their function in neurons (Baas, Rao, Matamoros, & Leo, 2016). In addition, they undergo a series of post-translational modifications regulating their dynamics and binding capacity, which contribute to the modulation of motor protein binding and movement along microtubule tracks (Janke & Bulinski, 2011). We therefore visualized microtubule acetylation, a marker for stable microtubules, by whole-mount immunohistochemistry, to determine if loss of *dynactin1a* led to impaired stability of the ventral root motor neurons, which could possibly explain improper growth or synapse instability.

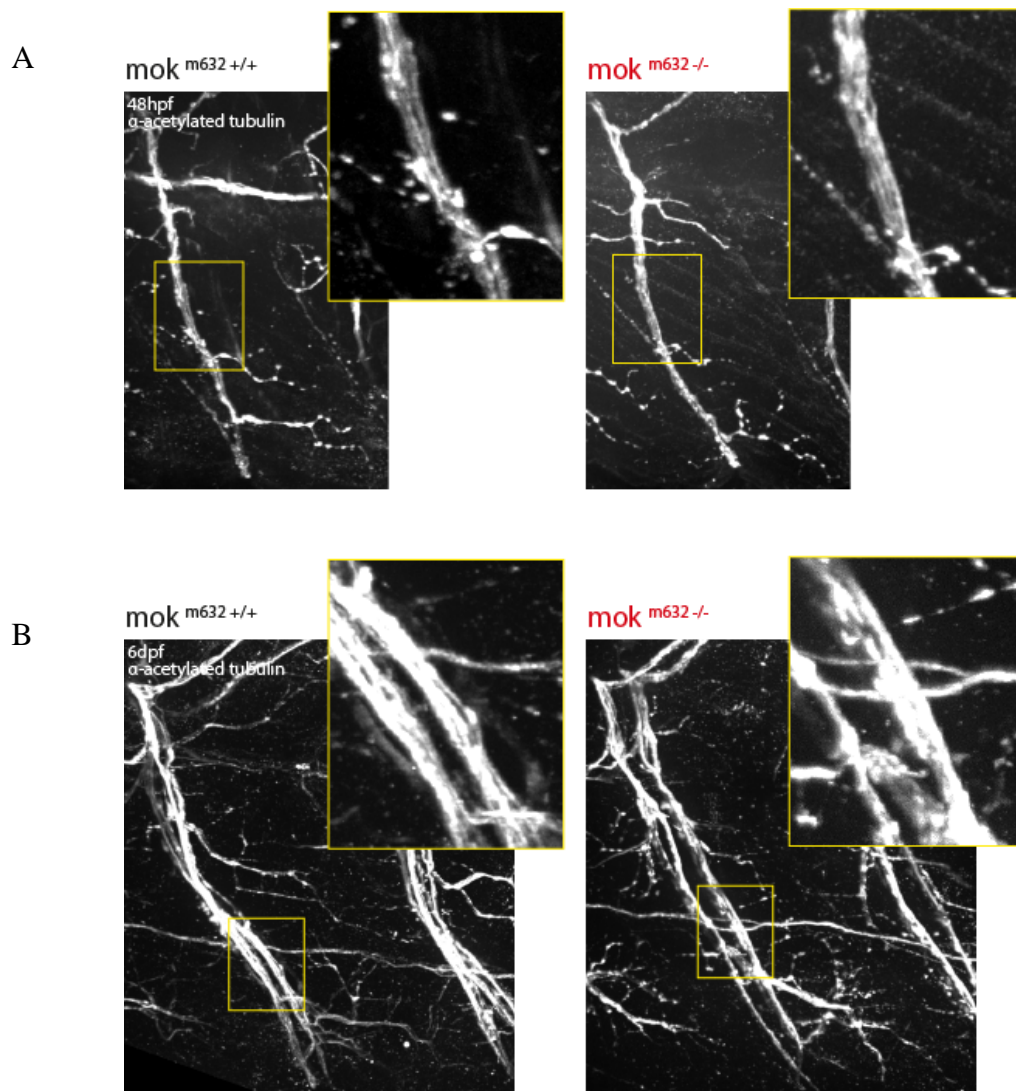


Figure 30: Immunohistochemistry against acetylated tubulin in 48hpf and 6dpf embryos. Acetylated tubulin is a marker for stable microtubule, a modification that is site and developmental stage specific. We performed whole-mount immunohistochemistry to visualize microtubule acetylation in A) 48hpf CaPs and in B) 6dpf ventral roots. Close-up boxes show axonal caliber and distribution of microtubule acetylation.

We did not observe any obvious changes in the acetylation state of the axonal microtubules of *mok^{m632/-}* embryos when compared with wild-type siblings, at either 48hpf (Figure 30 A) or 6dpf (Figure 30 B), which was confirmed by western blot analysis (not shown). This suggests that ventral root microtubules stability is not affected by loss of *dynactin1a*.

XVI- Microtubule growth at 48hpf and 6dpf

Microtubule dynamics are also known to be modulated by +tip-binding proteins like dynactin1, as well as by molecular motors like dynein. Reciprocally, microtubule stability affects motor protein behavior (Yogev, Cooper, Fetter, Horowitz, & Shen, 2016) as axonal transport necessitates stable microtubule tracks and dynein was reported to be more processive on tyrosinated microtubules (Peris et al., 2006). Growth of microtubules can be assayed via visualization of EB3 comets. This +tip protein binds the labile end tip of the tubules during bouts of assembly (Baas et al., 2016), and by driving the expression of a fusion proteins in cells, these bouts can be analyzed in timelapse imaging, as has previously been done in the zebrafish model (Revenu et al., 2014). We used the previously described construct 10xUAS:eb3-GFP-pA (Revenu et al., 2014) to obtain single-cell labeling of CaPs in our *mok^{m632/-}* embryos at 48hpf. We did not investigate the effect of this construct on cell morphology as overexpression of EB3 has previously been shown not to alter neuronal morphology (Moughamian & Holzbaur, 2012).

Our results show that there is a significant increase in number of EB3 comets (comet area flux) at 48hpf in the terminal branches of *mok^{m632/-}* embryos CaP arbors, when compared with their wild-type siblings (Figure 31 C). However, the distance, duration and average speed of the comets were maintained. This result could also indicative of a compensation in trophic signaling at this timepoint, as was suggested for actin filopodia dynamics analysis (Figure 28). At 6dpf, we did not observe any significant difference in any of the metrics analyzed, including the comet area flux (Figure 31 D). Overall, microtubules in *mok^{m632/-}* embryos exhibit normal growth dynamics, even at 6dpf when the CaP arbors have a reduced size.

It was previously reported that a reduction of *dynactin1* levels by 80% via siRNA did not affect microtubule polymerization rates or number of EB3 comets, but did increase the frequency of microtubule catastrophe, or rather diminished the distance the comets travelled.

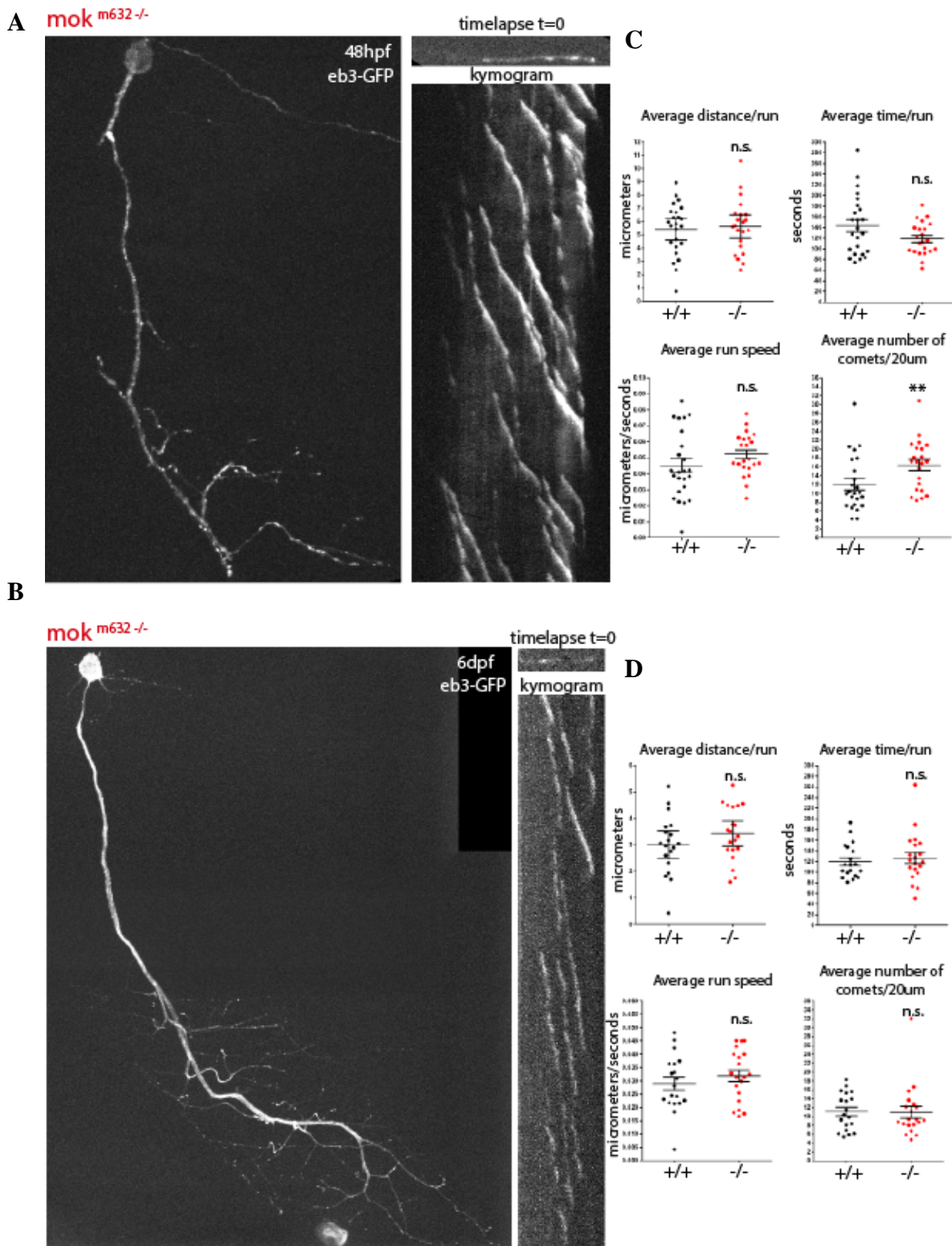


Figure 31: Microtubule growth dynamics by EB3-GFP comet assay. Microtubules are dynamic structures that constantly undergo growth and retraction of their protofilaments by tubulin subunit polymerization. In the arbor, the fast-growing +ends are located at the synapse, where end-binding proteins like EB3 associate with the microtubule during growth episodes, where they form runs called “comets”. We visualized and quantified these comets by timelapse confocal imaging and quantified the metrics of their runs. Representative z-stack projections and timelapse stills with kymograms at A) 48hpf and B) 6dpf, shown here for mutant embryos. Quantification of comet distance, time and speed of runs, as well as comet area flux at C) 48hpf and D) 6dpf. Data presented as average +/- SEM. ($p \leq 0,01$) (A/C n=24, 22; B/D n=22,20)

This defect could be rescued upon expression of full-length dynactin1, but not the shorter 135kDa isoform (Lazarus et al., 2013).

We did not observe an increased rate of catastrophe in *mok*^{m632/-} embryos, which is measured by comet distance in our assay. It is possible this difference is due to the use of different cell types (primary dorsal root ganglion cells in the study versus motor neurons *in vivo*, in ours), which could have different microtubule properties, molecular composition, or specific +tip protein interactions.

XVII- Synaptic microtubule capture at 48hpf and 6dpf

Dynein has been shown to interact with adhesion molecules, which binds to the cell membrane where they capture microtubules to anchor them at synapses. It has been reported that NCAM180 recruits dynein at this level, leading to the tethering of microtubules, and that this process requires the presence of the dynactin complex, although a role for of the dynactin1 subunit was not investigated. Microtubule dynamics were assayed with EB3-comets and were shown to preferentially terminate at synaptic sites, as visualized by GFP-synaptophysin, and this particularity was lost upon loss of NCAM180 (Perlson et al., 2013).

The interaction of dynein with NCAM180 in microtubule capture was not shown to affect microtubule dynamics, as revealed by maintained duration and speed of EB3 comets (Eran Perlson et al., 2013). To determine if loss of dynactin1 led to loss of microtubule capture at synapses, which could explain their instability, we generated a construct to express eb3-eGFP simultaneously with tagRFP-rab3 (10xUAS:eb3-GFP-E2A-tagRFP-rab3-pA) and assayed microtubule capture at synapses in our *mok*^{m632/-} embryos by analyzing the ratio of comets terminating at putative synapses. We did not observe any change in synapse and terminating comet density, and in proportion of comets terminating at synapses at the level of arbor synapses either at 48hpf (Figure 32 B) or at 6dpf (Figure 32 C).

As we also did not observe any effect on comet speed or duration, as presented in the last section (Figure 31 C, D), these results suggest that the microtubule capture function of dynein is independent of dynactin1.

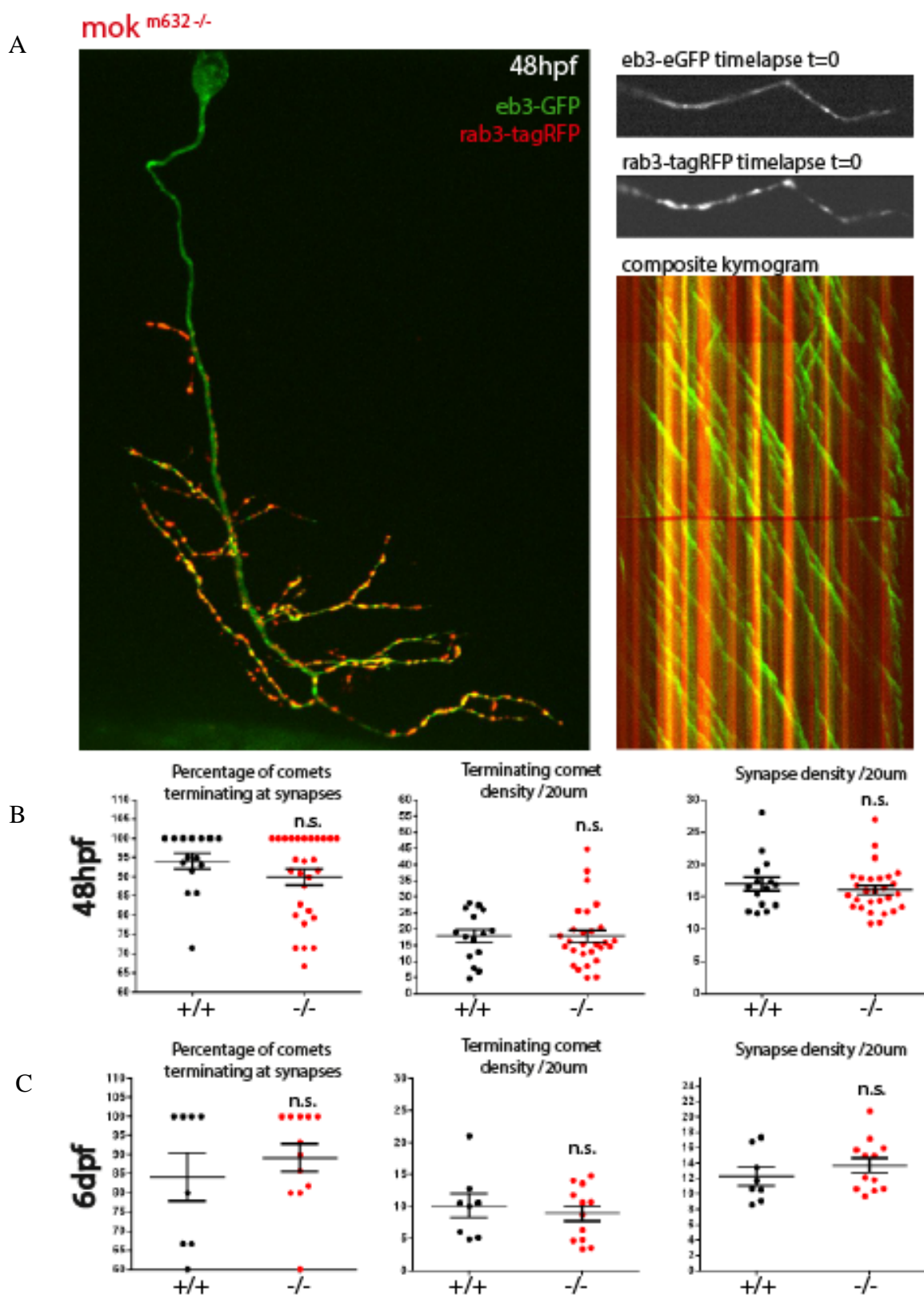


Figure 32: Dynein-mediated EB3-GFP comet capture at synapses. We visualized and quantified the microtubule growth comets (eb3-GFP in green) simultaneously with putative synapses labeled by rab3-tagRFP (red) by timelapse confocal imaging and quantified the metrics of their runs. A) Representative z-stack projections and timelapse stills with kymograms at 48hpf shown here for a mutant embryo. Quantification of ratio of comets terminating at synapses, with control for comet density, and synapse density at B) 48hpf and C) 6dpf. Data presented as average +/- SEM. (B n=15, 28; C n=8,12)

We therefore propose that the synapse instability observed in our model is not due to a loss of *dynactin1a* function involving microtubule capture or tethering at synapses via interaction with dynein and NCAM180.

XVIII- Adhesion molecules at the NMJ (N-Cadherin)

In addition to the microtubule cytoskeleton, dynactin is known to interact with the actin cytoskeleton at adherens junctions. To investigate whether dynactin1 is involved in localizing adhesion molecules to the synapses, we used a previously described zebrafish Bac line where N-cadherin is tagged with GFP, namely Tg(cdh2:Cdh2-GFP) (Revenu et al., 2014) and crossed it into our mutant background, to obtain Tg(cdh2:Cdh2-GFP; *mokm632*; *mnx1:Gal4*). In this zebrafish line, the N-Cad-GFP forms puncta at the center of the presynaptic sites of the NMJ and we wanted to know if loss of *dynactin1a* led to the disruption of this particular organization. Indeed, a disorderly active zone assembly could lead to unstable synapses, which were previously observed in *mok^{m632/-}* embryos.

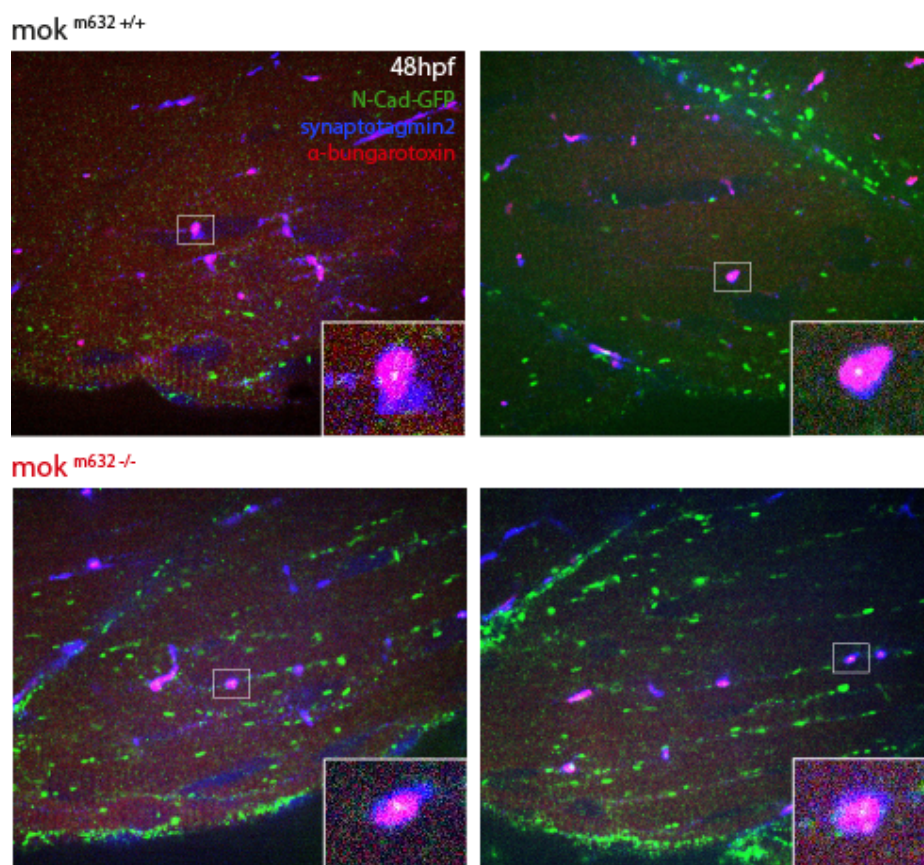


Figure 33: N-Cadherin-GFP at the synapse. Whole-mount immunohistochemistry was performed in 48hpf Tg(cdh2:Cdh2-GFP; *mokm632*; *mnx1:Gal4*) embryos showing N-Cadherin-GFP (antiGFP, 488 in green) located at the center of a NMJ synapse, which was co-labeled by synaptotagmin2 (red) showing the presynaptic site and conjugated α -bungarotoxin showing the postsynaptic site (blue). Z-stacks of ventral somatic segment for wild-type and mutant embryos, with boxes showing close-up of the synaptic structure.

We performed immunohistochemistry on fixed 48hpf (Figure 33) and 6dpf (not shown) embryos in order to label the pre- and postsynaptic sites as previously described but did not observe any change in the localization of N-Cad-GFP in *mok*^{m632/-} embryos when compared with wild-type siblings (Figure 33).

XIX- Controls and validation

In this study we came upon unexpected results, where loss of dynactin1, a subunit thought to be essential for functions from microtubule stabilization to dynein processivity, did not drastically affect motor neurons development and function *in vivo*. Undeniably, difference should be expected from the use of different systems, cell types, or even developmental stages, but according to our experiments, many of the essential roles of dynactin1 appear to be fulfilled by other means in *mok*^{m632/-} embryos, perhaps by compensatory mechanisms which we were unable to identify.

In this section, we present a few measures of validation and controls performed in order to ensure the reliability of our methods and conclusions.

XIX.1-dynactin1b CRISPR/Cas9 mutant generation

Zebrafish has two paralogs for *DCTN1*: *dynactin1a* and *dynactin1b*. In order to determine if the second paralog could compensate for the loss of *dynactin1a* in *mok*^{m632/-} embryos, we generated a CRISPR/Cas9 mutant.

This paralog has two predicted transcripts, a full-sized transcript and a shorter one which could lead to a shorter transcript of the dynactin1 protein lacking the CAP-Gly domain, similar to the 135kDa isoform found in human and mice (Tokito et al., 1996). The target site for guide RNA sequences (CCATGTAACGCTCTTTAGCT) was exon 5 of the sequence found for transcript *dctn1b-202* of the gene *dynactin1b* (ENSDART 00000169953.1) and exon 8 of transcript *dctn1b-201* (ENSDART00000102411.4).

The successful founder we used exhibited an insertion of 180bp at the target site, causing a frameshift in the ORF from amino acid (a.a.) 746 onward and leading to a premature stop codon at position 253 of 1258 a.a.(hereafter, the mutant is referred to as *dynactin1b*^{*253}). This mutant was outcrossed into our *mok*^{m632} transgenic line to raise a new generation of double carriers which were then incrossed to generate adults homozygous for *dynactin1b*^{*253}, and

heterozygous for *mok*^{m632}. These adults were incrossed to produce double homozygous embryos for analysis but, like *mok*^{m632/-} embryos, are not viable.

XIX.1.1-Axonal morphology at 6dpf of *dynactin1b*^{*253/*253} and *dynactin1b*^{*253/*253}; *mok*^{m632/-} double homozygous mutant embryos

To determine if double mutants of *dynactin1b* would lead to a more severe phenotype, we visualized the CaP morphology at 6dpf as was done previously for *mok*^{m632/-} embryos. We found that loss of *dynactin1b* did not affect cell morphology, as *dynactin1b*^{*253/*253} CaPs (Figure 34 B) were indistinguishable from wild-type cells from Figure 11, and had a normal total cell length (Figure 34 E), total number of projection (Figure 34 D) and average length of projection (Figure 34 F).

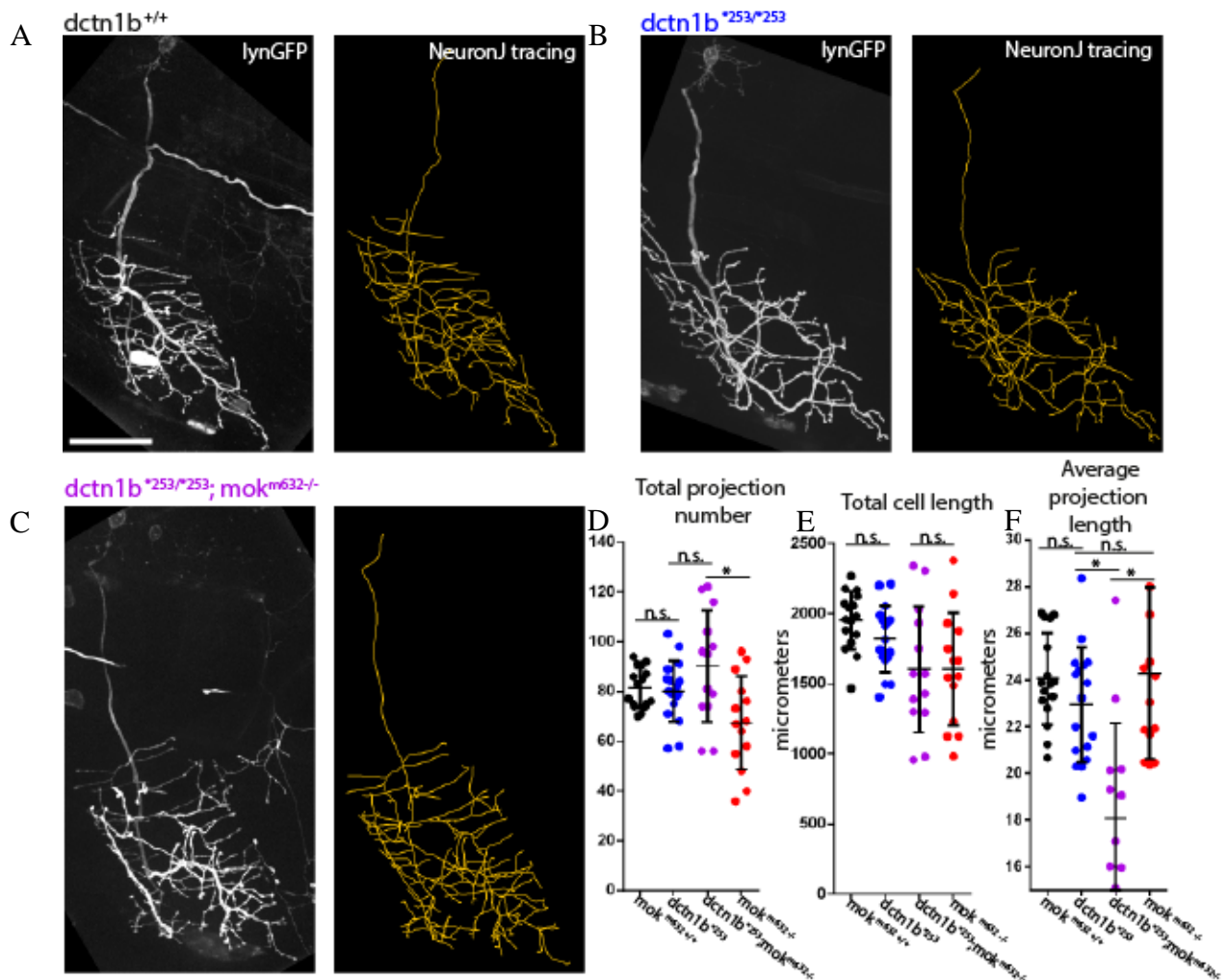


Figure 34: Axonal morphology at 6dpf for homozygous *dynactin1b*^{*235}, and double homozygous *dynactin1b*^{*235}; *mok*^{m632/-}, compared with *mok*^{m632/-} embryos. Confocal z-stack projection of a single CaP cell, visualized by expression of *mxn1:lynGFP*, with tracing of the axonal arbor done with NeuronJ (ImageJ) for A) wild-type sibling embryo (black) at 48hpf, for B) homozygous *dynactin1b*^{*235} (blue) and for C) double homozygous *dynactin1b*^{*235}; *mok*^{m632/-} embryo (violet). Quantification of the axonal arbor size, by D) total projection number, E) total cell length, and F) average length of projection, compared with *mok*^{m632/-} embryo data (red) compiled in Figure 11. All data presented as average +/- SD. (p < 0.05) (A n=16, B n=14, C n=13)

Double mutant embryos also had a normal total cell length, but had a shorter average projection length, when compared with *mok*^{m632-/-} embryos. As the cell morphology defect observed in double mutants (Figure 34 C) did not appear to be more severe than in single *mok*^{m632-/-} embryos, it is unlikely the second paralog compensates for the loss of the first, as suggested by the quantitative RT-PCR results (Figure13).

XIX.1.2-Proof of principle: axonal transport at 48hpf in *dynactin1b*^{*253/*253}; *mok*^{m632-/-} double homozygous mutant embryos

To further confirm that *dynactin1b* did not compensate for the lack of *dynactin1a* in our *mok*^{m632-/-} embryos, we performed a test for live axonal transport of rab11 recycling endosomes at 48hpf. As this was a proof of principle control, we did not obtain a full dataset and only show one kymogram here. We did not see further impairment in axonal transport in double mutant embryos, and the metrics extracted for run measurements are similar to what was obtained for *mok*^{m632-/-} embryos (Figure 35), here compared with the results presented previously in Figure 26.

The effect we see here differs from what has previously been reported in a similar experiment, where a double mutant embryos, the combination of a new CRISPR/Cas9 mutant for *dynactin1b* and the *mok*^{m632} line, produced a full *dynactin1* mutant with a stronger phenotype (Drerup et al., 2017). However this difference could be due to cell-type specific axonal transport (Bisby, 1977), or to a different isoform expression of dynein motor components, like intermediate and light chains, which are known to have acquired specific association with cargo, independent of the dynactin complex (Fejtova et al., 2009; Hirokawa, Niwa, & Tanaka, 2010).

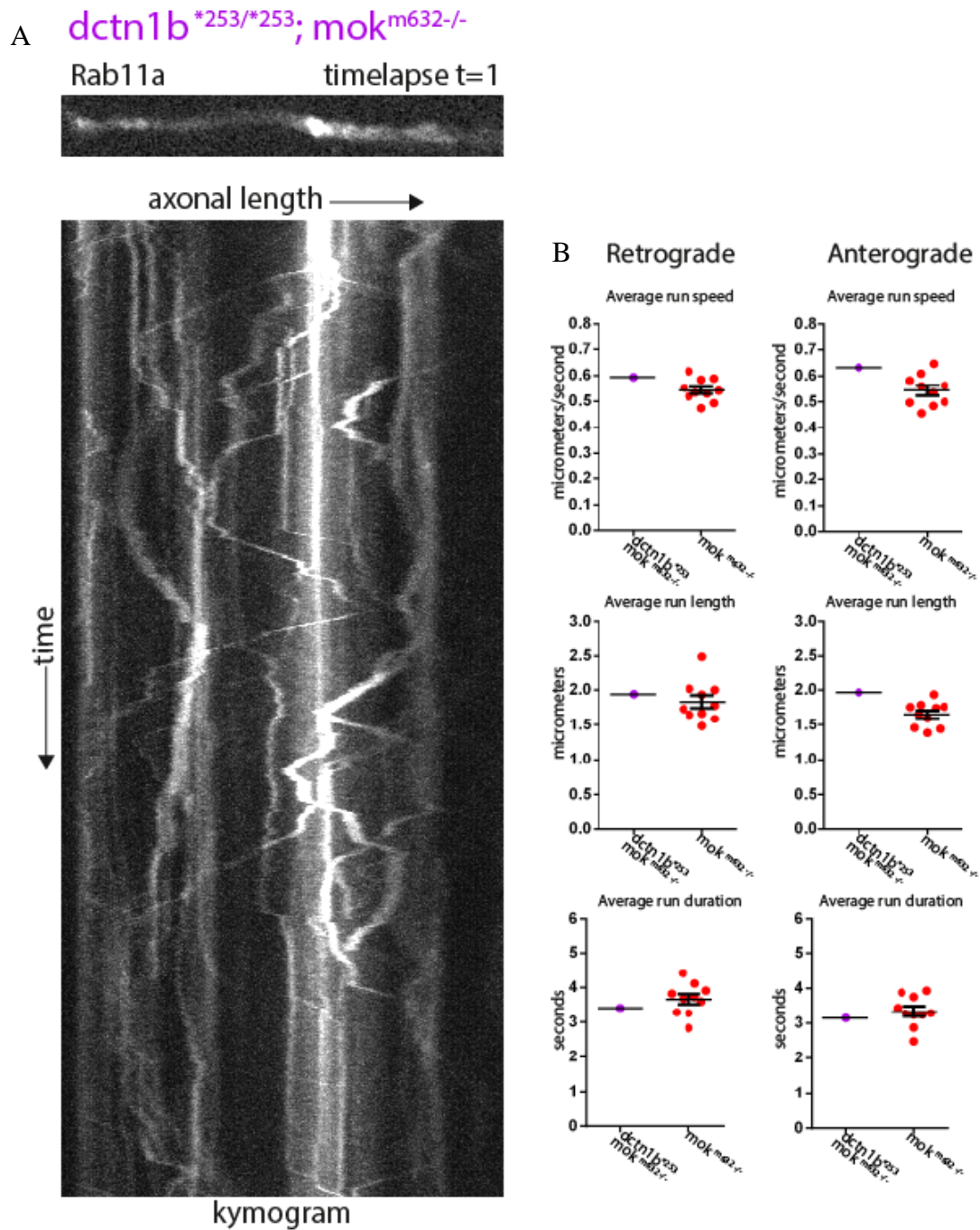


Figure 35: Proof of principle for maintained axonal transport in full *dynactin1* mutant embryos at 48hpf. A) Timelapse still and kymogram for recycling endosome axonal transport in double homozygous *dynactin1b*^{*253/*253}; *mok*^{m632-/-} embryos. B) Quantification of retrograde and anterograde runs compared with *mok*^{m632-/-} embryos metrics presented in Figure 26. Double homozygous mutant data presented as average of runs from one kymogram compared with average +/-SEM for *mok*^{m632-/-} data.

XIX.2-Other dynein/dynactin mutant and DN-dynactin1 axonal morphology

We also looked at the CaP morphology in 6dpf homozygous mutant embryos of other mutant lines, where components of the dynactin, or dynactin complex were altered (respectively *dctn2^{ij50}* and *dync1h1^{mw20}*, Figure 36 B, C). These embryos are also not adult viable and display a more severe phenotype, when compared with CaP morphology in *mok^{m632/-}* embryos (Figure 36 A). As an added control, we overexpressed the dominant-negative CC1 fragment of dynactin1 in a wild-type embryo, which is known to cause disassembly of the dynactin complex, and the loss of dynein function (construct 4nrUAS:zfCC1-E2A-tagRFPCaax-pA) (Figure 36 D). The morphological phenotype observed in these embryos was also more severe than in *mok^{m632/-}* embryos.

These results suggest that loss of function of *dynactin1* most likely does not cause the loss of function of the dynein motor, or even of the dynactin complex, as a more severe phenotype is seen in embryos lacking the dynamitin/p50 subunit (*dctn2^{ij50}*), the dynein heavy chain essential for transport (*dync1h1^{mw20}*) or in embryos where the functional dynein-dynactin complex is disassembled by overexpression of the dynactin1 CC1 fragment (4nrUAS:zfCC1-E2A-tagRFPCaax-pA).

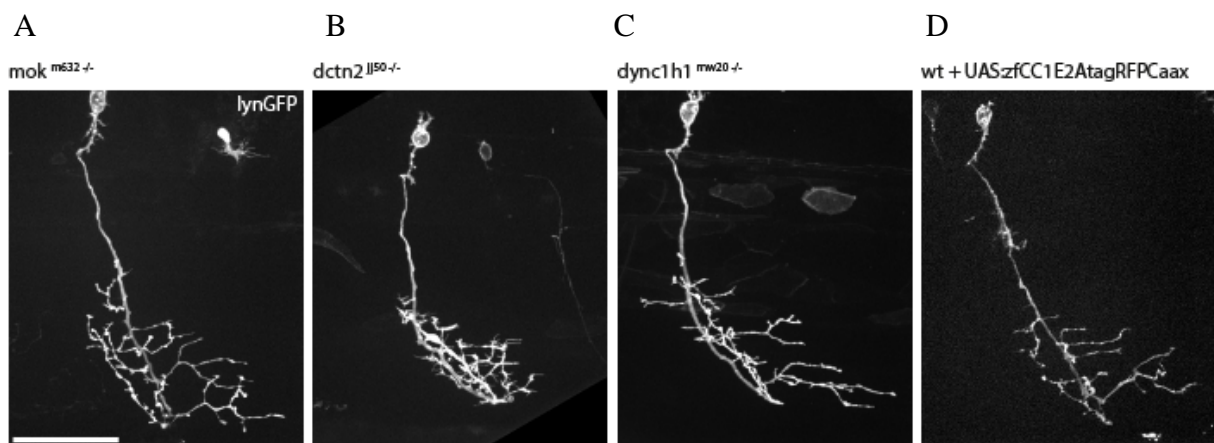


Figure 36: Axonal morphology of 6dpf CaPs in homozygous *dctn2^{ij50}*, *dync1h1^{mw20}* mutant embryos, as well as in CaPs expressing the dominant-negative CC1 fragment (4nrUAS:zfCC1-E2A-tagRFPCaax-pA) compared to *mok^{m632/-}* embryos. Confocal z-stack projections of single CaP cells, visualized by expression of *mnx1:lynGFP*, for A) *mok^{m632/-}* embryo, B) *dctn2^{ij50/-}* embryo, C) *dync1h1^{mw20/-}* embryo, and D) a wild-type embryo overexpressing the CC1 fragment of dynactin1, resulting in disassembly of the dynactin complex.

Discussion

In this study, we investigated the consequences of loss of *dynactin1* function in the development of CaP motor neurons and the NMJ they establish with fast-twitch muscle fibers. *DCTN1* was found to be mutated in ALS patients and hypothesized as being either causative or a risk factor in the progressive motor neuron degeneration involved in this disease, which also counted axonal transport defects as a potential pathogenic mechanism. Our aim was to determine if loss of *dynactin1* function could lead to defects in motor neurons that could be related to ALS, and to investigate possible explanations based on the known roles and interactions of dynactin1. Throughout our experiments, we used an established zebrafish transgenic line (*mok*^{m632}) where a point mutation disrupts the gene coding for dynactin1, leading to a loss-of-function. We also focused our analysis on a single cell-type, the primary CaP motor neuron, which innervates fast-twitch muscle fibers located on the ventral side of the zebrafish trunk and tail, in order to reduce the variability that can arise from different molecular backgrounds or physiological properties.

***Dynactin1a* loss-of-function leads to behavioral defects in the zebrafish embryo**

Initially, we tested the behavior of our mutant embryos to determine if they had ALS-relevant locomotion defects similar to what has been described for previous models of the disease. We report here that *mok*^{m632/-} embryos exhibit a behavioral phenotype suggesting underlying NMJ function defects, as the escape responses they produced upon presentation with a touch stimulus at 48hpf were not as extensive as wild-type embryos. These defects are similar, although certainly not as severe, as what has been reported in other ALS models, possibly due to the developmental defects they see at 48hpf which are absent in our mutant, and support the use of our mutant in the study of an ALS phenotype (Armstrong & Drapeau, 2013; Kabashi et al., 2009, 2011).

***Dynactin1a* loss-of-function causes growth defects in CaP motor neurons**

In our model, the loss of dynactin1 led to morphological differences in CaP motor neurons morphology at 6dpf but not at 48hpf. Whole-mount immunohistochemistry to probe NMJ integrity, as determined by colocalization of pre- and post-synaptic structures, revealed impairments at this level for the 6dpf embryos only. This indicates that initial development and migration of the motor neuron is unaffected, and that a proper NMJ has been established at this

early timepoint. Indeed, the growing motor neuron is directed by guidance cues during migration from the spinal cord to the muscle fiber (Bonanomi & Pfaff, 2010; L. Jing, Lefebvre, Gordon, & Granato, 2009), but needs to respond to local trophic factors after initial innervation to properly innervate its target over the lifetime of the fish (Cosker, Pazyra-Murphy, Fenstermacher, & Segal, 2013; Smith, Machamer, Kim, Hays, & Marques, 2012). Hence, we hypothesized that the defects observed at 6dpf could either be due to improper growth after 48hpf or to degeneration, but lack of orphan receptors in NMJ structural immunohistochemistry suggest the former hypothesis to be accurate.

***Dynactin1a* growth defects in CaP motor neurons are rescued with human DCTN1**

Overexpression of the human Dynactin1-GFP fusion protein (Stockmann et al., 2013) in a cell-specific manner was sufficient to rescue the *mok^{m632}* axonal morphology phenotype observed at 6dpf, while a similar level of expression in wild-type embryos led to normal arborisation and size of CaPs. This confirms that the defect observed was due to the loss of *dynactin1a* function and that contribution of non-cell autonomous mechanisms was negligible. We however observed that the mutant rescued cells had a significantly larger arbor size when compared with wild-type cells expressing a membrane-bound reporter, or when compared with wild-type cells overexpressing human Dynactin1-GFP. This is likely due to the lack of competition for innervation at the level of the muscle, as surrounding motor neurons are still devoid of dynactin1 and therefore have smaller arbors with fewer synapses.

In the *Drosophila* model, overexpression of wild-type human or fly Dynactin1 (p150) was found to be toxic: leading to lethality or when confined to neurons, to a severe phenotype. However, overexpression of mutated forms, either from fly or human, lead to a mild phenotype (Lloyd et al., 2012). In the same study, rescue of the mutant phenotype was nonetheless achieved by low expression of the wild-type protein. An explanation that could reconcile these reports with our results is that other regulation mechanisms could be present in zebrafish to regulate protein expression (leading only to a slight overexpression). In support of this hypothesis, we observed that the overexpression of ALS mutant forms of human Dynactin1 (Stockmann et al., 2013) in our model did not yield conclusive results, as the expression of the fusion proteins was greatly reduced when compared with the overexpression of the wild-type version (data not shown). In these embryos, we could however observe that the E2A-linked membrane reporter found in the same construct, and under the expression of the same 14xUAS element, had similar levels as when expressed with the wild-type Dynactin1-GFP construct.

This leads us to speculate that either the transcription of these mutant genes is regulated or that the mutant proteins are unstable, leading to low expression level that might not be enough to yield a dominant-negative effect in our model.

***Dynactin1a* loss-of-function causes putative synapse instability**

Our mutant embryos displayed a behavioral phenotype at 48hpf, without showing morphological or structural NMJ defects at this early timepoint, and as the reduced arbor size at 6dpf was deemed to be due to impaired growth, we investigated synapse stability in our mutant. Indeed, impaired synapse function would explain the behavioral phenotype at 48hpf, and could also be implicated in the growth defect as it has been shown that synapses are necessary to stabilize nascent branches and restrict retraction (Meyer & Smith, 2006). We therefore used a rab3 fusion protein to observe synapse distribution and dynamics in our *mok^{m632/-}* embryos. We selected this protein as a marker, as it is involved in regulating local dynamics and scaffolding at active zones (Petzoldt et al., 2016), and forms stable, localized puncta as opposed to synaptophysin-containing vesicle, which are highly dynamic and must go through a size discrimination to determine which correspond to putative synapses (Auer et al., 2015; Meyer & Smith, 2006).

We observed that while CaP putative synapses were present in the same number and of similar size in mutant as in wild-type siblings at 48hpf, they were smaller and less numerous in the smaller arbors of 6dpf *mok^{m632/-}* embryos. In addition, we also determined that the synaptic sites were significantly more unstable in mutants, an assay which was performed at 48hpf, where the number and size of rab3-labeled vesicles is normal. This synapse instability could therefore explain the growth defects observed at 6dpf, as the unstable synapses are unable to properly stabilize the developing arbor.

***Dynactin1a* loss-of-function alters electrophysiological properties of CaPs**

We hypothesized that the observed synapse instability could lead to functional abnormalities at the NMJ, which, as suggested, could explain the behavioral defects. We first investigated the electrophysiological properties of the CAPs in *mok^{m632/-}* embryos by looking at spontaneous release of quanta (mEPC) and at NMJ connectivity by paired recordings, where CaPs were stimulated and the response was recorded in the fast-twitch muscle fibers they innervate.

No change was found in the spontaneous release properties of single synaptic vesicles at the NMJ of *mok^{m632/-}* embryos either at 48hpf or at 6dpf. In comparison, other zebrafish ALS models do exhibit defects at the level of the NMJ, either at the presynaptic level, which is the case for models of *FUS* (Armstrong & Drapeau, 2013), or both at the pre- and postsynaptic side, in models of *TARDBP* (Armstrong & Drapeau, 2013). We did however observe a significantly higher failure rate of response during paired recordings, as well as asynchronous release in the mutant embryos at 6dpf. Failures in response indicate defects in synaptic transmission and could be due to local defects at the active zone organization. For instance, poor recruitment or recycling of synaptic vesicles could lead to a faster depletion of the ready-pool during high-frequency stimulation.

Asynchronous release has been reported to be due to changes in calcium buffering (Kaesler & Rgehr, 2014). Interestingly, motor neurons of ALS patients often have an impaired intracellular calcium regulation and a reduced expression of calcium-binding proteins (Aren et al., 2015; Jaiswal, 2013; Leal & Gomes, 2015). Cytosolic calcium concentration is known to affect mitochondrial transport (Saxton & Hollenbeck, 2012), although, it is unlikely that the defects would be cell-wide. Furthermore, local changes at the level of the synapse would be difficult to observe in our current model and a closer look at synapse composition and active zone assembly might shed some light on this issue.

***Dynactin1a* loss-of-function does not affect cargo distribution or axonal transport**

We hypothesized that axonal transport defects could lead to the observed synapse instability and NMJ functional abnormalities either by impaired clearing activity of damaged organelles and vesicles, as well as detritus, by improper supply of new proteins or energy for synaptogenesis, or by altered signaling mechanisms. We selected general cargoes markers to investigate these defects: mitochondria for the energy component, early, late and recycling endosomes for the supply, signaling and clearance aspect.

We investigated axonal transport defects by live *in vivo* timelapse imaging of fluorophore-labeled cargoes, which revealed no noteworthy difference in the size, distribution, flux or transport metrics of mitochondria, early, late and recycling endosomal vesicles. These results are surprising as dynactin1 has been well studied in the context of axonal transport and was thought to be essential to the proper assembly of the dynactin complex, which is an essential activator and regulator of the dynein retrograde motor protein.

Synapse instability in *mok^{m632/-}* embryos is not caused by impaired trophic signaling

We then investigated a role for trophic signaling in the 6dpf growth defect by looking at filopodia dynamics, which informs us about the environment and the actin cytoskeleton health, and at the axonal transport of the low-affinity p75 receptor, responsible for signaling in response to neurotrophins (Charalampopoulos et al., 2012). We selected this receptor as it has been demonstrated that p75NTR, TrkB and BDNF share the same retrograde transport pathway that is controlled by the Rab5 and Rab7 GTPases (Bucci, Alifano, & Cogli, 2014). In addition, the p75 neurotrophin receptor has also been implicated in death/survival signaling and was found to promote autophagy in absence of trophic stimuli (Florez-McClure et al., 2004). We had not observed changes in the metrics of late endosomes/MVB transport, known to transport p75, but it is possible the effect of *dynactin1a* loss-of-function might only affect a sub-population of these vesicles to influence retrograde signaling.

We did not observe any difference in either the filopodial dynamics assay or the transport of p75-containing vesicles. These results suggest that the muscle is not compensating for the growth defect by overexpressing trophic factors, which could then stimulate synaptogenesis, a result confirmed by the quantitative RT-PCR showing no change in BDNF expression. They also suggest that the actin cytoskeleton is active and functional at all time points assayed (24hpf, 48hpf, 72hpf and 4dpf), and that the p75 receptor trafficking is not impaired, either in the particular dynamics of its transport or in the size of the vesicles in which it is transported.

Another explanation for both the growth defects seen at 6dpf and the synapse instability observed at 48hpf could be that the dynactin1-dependant retrograde signaling of a particular factor is necessary to stabilize synapses and that lack of dynactin1 leads to lower rates of synapse stabilization and smaller arbors, which require synapses to stabilize new branches (Meyer & Smith, 2006). This particular signaling could have gone unnoticed in our assay as we simply labeled endosomal vesicle without regard for what they contained.

Alternatively, the difference we observe here between 6dpf and 48hpf could be due to a different dependence on retrograde transport by the dynein-dynactin complex during active axon growth versus an established, albeit dynamic, NMJ (Lu & Je, 2003). This interpretation

has already been suggested in the fly model, where the overexpression of the *glued* truncated peptide of dynactin1 acts in a dominant-negative manner to disassemble the dynein-dynactin complex, but only leads to vesicle accumulation in distal synapses once the axon has stopped growing (Allen et al., 1999). As we can see from the filopodia dynamics analysis, the NMJ growth phase seems to be consistently high at 24hpf and 48hpf, then progressively slows down as connections are stabilized, where close to no activity is seen after 4dpf.

In the same way, the growth of mutant sensory axons in the *glued* fly model, similarly to the *cytoplasmic dynein light chain* fly mutant, has been shown to be affected, by producing cells with defective terminal arborisation, but with normal axon outreach. The suggested explanatory mechanisms implicated the stabilization of nascent synapses, which they hypothesized to be due to faulty retrograde signaling, or to local remodeling of the cytoskeleton (Murphey, Caruccio, Getzinger, Westgate, & Phillis, 1999). As dynactin1 is known to interact with the cytoskeleton via its CAP-Gly domain, we next investigated this interaction to explain the synapse instability.

One thing to note at this point is that both of the phenotypes of reports cited above are consequential to the overexpression of a dominant-negative form of dynactin1, which has been shown to disassemble the dynactin complex, and reported to have potential toxic aggregative effects. It is important to point out that due to the downregulation of *DCTN1* mRNA and lower expression of DCTN1 protein in the tissue of ALS patients, it was suggested that neurodegeneration in the pathogenic context might in fact be due to a loss of function of the protein (Kuźma-Kozakiewicz et al., 2013; F. Tanaka et al., 2012). This is therefore more in line with the approach we are taking in the present study, and consequentially, our results might not entirely reflect what has been published previously by studies using dominant-negative versions of dynactin1 or purified dynactin-dynein complexes which might be lacking some components present *in vivo*. In fact, no effect on neurite outgrowth was reported following the depletion of dynactin1 in mouse primary dorsal root ganglia neuron cultures (Moughamian & Holzbaur, 2012), suggesting that the effect observed upon loss of *dynactin1* function might vary across models, cell types, and even developmental stages.

Synapse instability in *mok*^{m632/-} embryos is not caused by impaired microtubule stability, dynamics or capture at synapses

To investigate the implication of the microtubule cytoskeleton in synapse instability, we first performed immunohistochemistry on *mok*^{m632/-} embryos at 48hpf and 6dpf to determine if microtubules displayed an altered stability. We did not see any difference in acetylation, a marker for stability, at either timepoint. This is consistent with previous reports that no changes in microtubule acetylation or axonal caliber were found in cell culture (COS7 and HEK293 cells) upon overexpression of either wild-type or mutant forms of dynactin1 (Stockmann et al., 2013), as well as our observation that axonal transport metrics, which would be disturbed by changes in acetylation, were unaffected. In addition, we also investigated microtubule growth dynamics, as revealed by EB3 comets forming when this +tip binding protein associates with microtubule during polymerization bouts, and did not observe any noteworthy difference that could explain the synapse instability. In addition, as comet length was maintained in our mutant, it suggests that dynactin1 does not act as an anti-catastrophe factor as was previously reported (Lazarus et al., 2013). The next step was to determine if the microtubule cytoskeleton had impaired capture at synapses, a process which has been shown to rely on dynein interaction with adhesion molecule NCAM180 (Perlson et al., 2013). We performed timelapse imaging of EB3 comets and quantified the proportion of comets terminating at synapses, which was also unchanged in our *mok*^{m632/-} embryos. Therefore, in our model, loss of dynactin1 function does not impair microtubule stability, dynamics, or capture at synapses.

The zebrafish neuromuscular junction formation relies on guidance cues, integrated by cell-surface molecules at the level of the growth cone, which responds in a dynamic manner during axon migration (Sato-Maeda, Tawarayama, Obinata, Kuwada, & Shoji, 2006). At this level, adhesion molecules like N-cadherin play a role in stabilizing the cell-cell interactions that arise during axonal growth and synapse formation as depletion of this factor leads to defective axon outgrowth and to the formation of abnormal or aberrant branches (Brusés, 2011). An interaction of dynactin1 with the membrane could thus be considered as the dynactin complex was already shown to be associated with membranes (Marjan et al., 2007), possibly via the interaction of subunits like p62, known to interact with the actin cytoskeleton (Garces et al., 1999). In addition, the loss of p62's interaction with AnkB was shown to lead to defective axonal elongation and stabilization without affecting microtubule dynamics or stability (Lorenzo et al., 2014). We investigated the presence of N-cadherin puncta, which are structures

typically located at the very center of NMJ synapses, and did not find any difference at this level in *mok^{m632/-}* embryos, either at 48hpf or 6dpf, where presynaptic synaptotamin2 appeared well distributed around the puncta, and apposed to a post-synaptic structure of AChR.

In summary, *dynactin1a* loss-of-function leads to a behavioral defect in 48hpf zebrafish embryo, which suggests NMJ fatiguing. The CaP primary motor neurons in those embryos initially display a normal morphology, with a typical number and size of putative synapses and a normal NMJ structure, but later on display a an overall smaller axonal arbor composed of fewer projections which also has fewer synapses, of smaller size, and NMJ structural defects, albeit without obvious signs of degeneration. Synapse instability is observed at 48hpf, which is thought to underlie the growth defects between the two timepoints, and causes NMJ functional deficits where paired-recordings of CaP motor neurons and fast-twitch muscle fibers reveal a higher failure rate in mutants, as well as asynchronous synaptic release. The synapse instability was not explained by obvious defects in axonal transport of mitochondria, early, late or recycling endosomes, all of which were also normally distributed throughout the cells. Trophic signaling also appeared to be normal, as no overexpression of trophic factor was detected by quantitative RT-PCR, and p75 trophic receptor transport was unaffected. The actin and microtubule cytoskeleton had proper stability and dynamics, and loss of dynactin1 did not affect dynein and NCAM180-mediated microtubule capture at synapses. We therefore report that loss of dynactin1 leads to motor neuron growth defects and synapse instability, which causes NMJ dysfunction and behavioral deficits, independently of its functions in axonal transport or microtubule dynamics regulation.

Possible mechanisms to explain synapse instability and growth defects in *mok^{m632/-}* embryos

The growth defect could be due to the dynein-dynactin complex interacting with the cytoskeleton in growth cones, where small fragments of microtubules are severed and reorganized to be moved into filopodia to form new branches, a process which requires dynein and could also be dynactin1 dependent (Baas et al., 2005). As a support for this last hypothesis, it was previously found that overexpression of dynactin1 in fibroblasts led to microtubule disorganization, an effect that was independent of the subunit's microtubule-binding activity (Quintyne et al., 1999).

NMJ synapses are initially assembled at sites where the muscle is prepatterned with AChR (Panzer et al., 2006), but it was suggested that synapses that are added after the initial migration and contact events might require different types of interaction or signaling events. It is possible that the synapse instability results from the reduced activity observed in motor neuron-muscle fiber paired-recordings, as activity is known to affect the size and organization of the presynaptic active zone. In addition, synapses within the same cell could have different properties, which could explain the variability of the effect we found at the physiological level. Indeed, as individual active zones within the same synapses have been reported to have variable properties in terms of evoked release probabilities, it is likely that this also extends to synapses within the same arbor. This variability relies on the active zone scaffolding, a process which is dynamic and influenced by activity (Petzoldt et al., 2016).

Something else to consider is that the instability we report here might be rab3-specific, and not visible by use of other presynaptic markers, like SV2, which only label synaptic vesicles. Rab3 is known to have a role in regulating active zone scaffolding, which requires membrane attachment, and this protein also contributes to synaptic vesicle docking (Petzoldt et al., 2016). Indeed, while their presence and distribution might be unaltered, it is possible that impaired active zone scaffolding could lead to ineffective coupling and recruitment of synaptic vesicles, or that it could affect calcium channel clustering. In our current *in vivo* model, we were not able to determine if the active zone scaffolding was impaired, but electron microscopy studies of the CaP NMJ might reveal some new information about the organization of the active zones and help determine the defects underlying synapse instability.

The dynactin complex without dynactin1

Taking everything into account, our results suggest that the dynactin1 subunit might not be essential for dynein-mediated axonal transport in our model. Indeed, based on our results and previous studies of the dynactin2 subunit, where a zebrafish mutant *ale oko* (X. Jing & Malicki, 2009) exhibited a more severe phenotype than our *mok^{m632/-}* embryos (also shown in Figure 37), we hypothesize that the dynactin complex is capable of performing its function as a dynein adaptor and regulator without the dynactin1 subunit. In addition, a redundancy in function of many adaptor proteins and interactors of dynein and even dynactin suggest that compensation mechanisms do occur. For instance, other proteins with coiled-coil domains have been reported to link cargoes to dynein directly like Hook proteins for early endosomes (Zhang, Qiu, Arst, Peñalva, & Xiang, 2014) and Rab11 family-interacting protein 3 (Rab11-FIP3) for

recycling endosomes (Horgan, Hanscom, Jolly, Futter, and McCaffrey, 2010; McKenney, Huynh, Tanenbaum, Bhabha, & Vale, 2014). While these interactions were shown to include the dynactin complex for processivity, the exact composition of the subunits necessary was not investigated.

In addition, many components of the dynein-dynactin have reported interactions with cargo that could be sufficient for recruitment in the context of axonal transport. For example, evidence for dynein binding directly to membrane, without the use of the dynactin complex, could indicate the recruitment of endosomal vesicles, which was shown to be independent of dynactin (Valetti et al., 1999) could occur via binding to subunits of the dynein motor (Marjan et al., 2007), or perhaps independent of dynactin1, via other dynactin subunits like dynamitin (Liu et al., 2015). Moreover, it was reported that the p25 subunit, located at the pointed end of the ARP1 filament and tethered via ARP11, is necessary for the recruitment and transport of early endosomes by the dynein-dynactin, but not otherwise necessary for the assembly of the dynactin complex (Zhang et al., 2011). Dynactin subunit p62 was also shown to be essential for axonal transport of endosomes, lysosomes, synaptic vesicles and mitochondria via its interaction with AnkB, which is necessary for the recruitment of cargo by binding to Phosphatidylinositol 3-phosphate (PI3P) (Lorenzo et al., 2014).

Another hypothesis could be that the exact composition of the dynactin complex would change in absence of the full-length dynactin1. Indeed, there have been reports of the dynamitin subunit interacting directly with the dynein motor domain (Marjan et al., 2007), and other adaptor proteins are known to interact with dynein and dynactin, for instance Lis1-NudEL is another regulatory factor of dynein activity, thought to antagonize the dynactin complex (Vallee, McKenney, & Ori-McKenney, 2012).

Lis1 (*PAFAH1B1*) itself is also a regulatory protein of dynein activity, which is found at dynamic microtubule +ends, localizing in distinct pools from dynactin. It was shown to be important for initiation of axonal transport, along with CLIP-170, and for maintenance of processivity after the recruitment of dynein-dynactin by end-binding proteins (EBs; discussed more in the cytoskeleton section) EB1 and EB3 for cargo such as mitochondria, early endosomes, late endosomes as well as TrkA, TrkB and APP-containing vesicles (Moughamian et al., 2013). It was suggested that Lis1 might promote recruitment of dynein-dynactin, with a direct interaction with dynein, at less dynamic areas of microtubules, explaining a conserved mid-axon flux in absence of dynactin1 or its CAP-Gly domain. In addition, normal Lis1

expression was found to be necessary for association of dynein with the dynactin complex, possibly via its interaction with dynein heavy chain or intermediate chain and dynamitin (Dix et al., 2013).

Furthermore, another regulatory protein, BicD2, has been reported to be essential for stabilization of the dynein-dynactin interaction by forming a stable tertiary complex called DDB (dynein-dynactin-BicD2) (McKenney et al., 2014), where the absence of BicD2 could essentially disassemble the dynein-dynactin complex, abolishing retrograde transport and leading to motor neuron degeneration in a mouse model (Teuling et al., 2008). The role of all these regulatory proteins is not fully understood and has not been investigated in studies examining the function of dynactin as a dynein regulator. It is possible they might all interplay *in vivo* as part of the biological redundancy processes.

Other roles for dynactin1 in ALS pathogenesis

Dynactin1 might also have other roles which we could not explore in this study, and which could explain our phenotype and possibly link this mechanism with what has been proposed for ALS pathogenesis. For instance, in the protein degradation pathway, which is essential for neuronal health and synapse function is known to be affected by loss of dynactin1.

In a *C. elegans* knockdown model for *DCTN1* showed motor neuron degeneration and motor defects and autophagosome accumulation was detected. It was also reported that the degenerating neurons had a higher number of autophagosomes which displayed an impaired movement (Ikenaka et al., 2013). These results suggest that the defects in transport of autophagosomes lead to motor neuron degeneration, which is in line with evidence for defective autophagy pathway in ALS (Cirulli et al., 2015).

Also of interest, misfolded proteins that fail to be degraded rapidly by the proteasome are dependent on the dynein-dynactin complex for the formation of aggresomes-large groupings of aggresomal proteins, essentially aggregates of aggregates-which are then transported to the microtubule organizing center at the centrosome, where recruitment of degradative machinery will begin (Garcia-Mata, Gao, & Sztul, 2002). As protein aggregates are a hallmark of ALS and many other neurodegenerative diseases, a possible loss of this function could lead to defects in clearance of misfolded proteins. Indeed, in support of this hypothesis, mice models of fALS with *SOD1* mutations revealed the dynein-dynactin complex was involved in mutant protein

inclusion formation (Ström et al., 2008). Furthermore, new evidence supports a direct role of dynactin1 in clearance of aggregates, thus this subunit could be playing a role in protein surveillance and neurodegenerative pathogenesis. Defects in this pathway was shown to cause misfolded proteins accumulation and result in apoptosis (Park et al., 2017).

On another note, the dynein-dynactin complex has been reported to be necessary for the retrograde transport of transcription factor NF- κ B to the nucleus, which is necessary for synaptic plasticity, learning and memory. The activity of this factor has also been noted to be dependent on intracellular calcium concentration (Mikenberg, Widera, Kaus, Kaltschmidt, & Kaltschmidt, 2007). In addition, ALS mice models overexpressing *TARDBP* have been reported to show accumulation of peripherin and a reduction of neurofilament levels, both of which were alleviated upon inhibition of NF- κ B (Millecamps & Julien, 2013). This defective signaling hypothesis could potentially tie in axonal transport with transcription defects and identify a sequence of events in ALS pathogenesis. Once again, as we visualized the transport of whole populations of endosomes, we might have missed a subtle effect affecting only endosomes carrying this particular cargo.

Dynactin1 as a risk factor in ALS

From our results, we cannot conclude on whether *DCTN1* is indeed causative or simply a risk factor of ALS. However one thing to keep in consideration is the role of normal aging and how it could affect the function of dynactin1, or vice versa, how a mutated and unstable dynactin1 might function in an aging system. Indeed, it has been reported that the interaction between dynein and dynactin decreases during normal aging, an effect possibly due to change in the activity of phosphatases, which are necessary, along with kinases, to regulate dynein binding to cargo by phosphorylation and dephosphorylation of intermediate and light chains (Blasier et al., 2014; Gibbs et al., 2015; Kimura, Imamura, Ono, & Terao, 2007).

At the level of the cytoskeleton, the C-terminal tail domains of both α - and β -tubulin are subject to various types of post-translational modifications, which are thought to regulate their interactions with microtubule-binding proteins. As motor proteins move along microtubules, these modifications could impact attachment or processivity. Indeed, it was reported that dynein is more processive on tyrosinated microtubules, where the modification is present on α -tubulin. This effect was reported to be mediated by dynactin1's CAP-Gly domain, which preferentially binds to tyrosinated microtubules (Peris et al., 2006), and only necessary for initial recruitment

(McKenney et al., 2016; Nirschl, Magiera, Lazarus, Janke, & Holzbaur, 2016). This is consistent with reports that stable microtubules are detyrosinated and acetylated, which reduces depolymerization, and that tyrosination is usually present at dynamic ends, where dynactin would be present (Dubey, Ratnakaran, & Koushika, 2015). Interestingly, tyrosination is a dynamic process and decreases during normal aging (Saha & Slepecky, 2000). This could act as a risk factor, which could affect dynactin1 function, where a mutated *dynactin1* might be slightly more unstable and less efficient, aging would exacerbate the defects by reducing its binding capacity for microtubules and lead to pathogenesis.

Overall, our results suggest a role for *dynactin1* in ALS pathogenesis. Indeed, we show that dynactin1 is necessary for synapse stability, a function independent of its role in regulating dynein activity, general axonal transport, or in its regulation of microtubule dynamics. We propose that the reported synapse instability leads to growth defects, independently of trophic signaling or gross defects in the cytoskeleton, and that it also causes NMJ electrophysiological abnormalities, leading to impaired locomotion. We conclude that this model, while presenting a different phenotype from what has been shown so far in terms of modeling ALS in zebrafish, could be used to study the role of *dynactin1* in disease pathogenesis, especially since the present study only scratched the surface of the possible mechanisms in which dynactin1 could be involved.

Conclusion and perspectives

As is common with scientific work, the results gathered over the course of this study raise more questions than they answer.

We have established that loss-of-function of *dynactin1* is sufficient to cause ALS-related defects in a zebrafish embryo. These defects are characterized by impaired locomotor activity, defective axonal growth, unstable synapses, and NMJ functional abnormalities. Surprisingly, we did not observe morphological defects at 48hpf, which is a common occurrence in zebrafish models of ALS. Dynactin1 has been widely studied in *in vitro* and *in silico* models and has a plethora of proposed functions. Based on these reports, we investigated possible mechanisms of action, which could explain the phenotype exhibited by our *mok^{m632-/-}* embryos. What we found was unexpected, as the observed defects were not explained by well-described functions of dynactin1, namely: interactions with the cytoskeleton, impaired trophic signaling, or alterations in the axonal transport directionality or metrics. We now suggest that the synapse instability is the cause of the growth defect, as well as the NMJ abnormalities and the behavioral phenotype, however we have no explanation as to what causes synapses to be unstable in the absence of dynactin1. At this point, we can only speculate on possible hypothesis that will guide future experiments.

As we observed defects that seemed to affect synapse stability in a very local manner, we now hypothesize that the effects presented here are due to the organization of the active zone itself. Indeed, the localization of dynactin1 at synaptic sites, as well as reported interactions with cytoskeletal and scaffolding proteins support this hypothesis. Electron microscopy studies could enlighten us as to the structure of the scaffolding present at this level. In addition, the functional defects in NMJ paired-recordings suggest that this impairment could be calcium-mediated and therefore it would be worth investigating mechanisms to buffer calcium, including synaptic calcium sensors, mitochondria, and autophagosomes.

Overall, we present here a novel model for ALS pathogenesis, which will require further study, but could be of great use as we untangle the molecular mechanisms that underlie NMJ loss, motor neuron retraction and death, and progressive paralysis typical of this tragic disease.

Materials and Methods

All reagents were obtained from Sigma-Aldrich unless otherwise noted.

I-Zebrafish husbandry and transgenic lines

The zebrafish lines were housed in the Curie Institute animal facility, raised and maintained at 28,5°C. Embryos were raised in egg medium containing methylene blue. All experiments were performed according to the French and European Union animal welfare guidelines, as well as the Curie Institute ethics protocol.

I.1- list of zebrafish lines

- Tg(*mnx1*:Gal4) (Zelenchuk & Brusés, 2011)
- Tg(*mok*^{*m632*}; *mnx1*:Gal4; UAS:GCaMP5G) (Akerboom et al., 2012)
- Tg(*cdh2*:Cdh2-GFP; *mnx1*:Gal4) (Revenu et al., 2014)
- Tg(*dync1h1*^{*mw20*}) (Insinna et al., 2010)
- Tg(*dctn2*^{*jj50*}) (Jing & Malicki, 2009)
- Tg(*dynactin1b*^{**253*}) (this study)

II-Microinjections

Embryos were injected at the zygote stage (1 cell) using a Picospritzer III pressure ejector and a glass capillary tube pulled with a Flaming-Brown puller as a needle. Injection mixes contained phenol red to judge injected volume and were set to 30-50ng/ul of construct DNA with or without added transposase mRNA (50ng/ul).

III-DNA extraction and genotyping

Genomic DNA of single embryos or from adult fin clips was extracted in total volumes of 5ul and 150ul respectively of a solution composed of a 1:10 ratio of proteinase K (0.17 mg/mL, Roche Diagnostics) in TE buffer (10mM Tris-HCl containing 1mM EDTA Na₂). The tissues were digested for one hour at 55°C, then the proteinase K was inactivated at 95°C for 15 minutes and the tubes were spun down to pellet the cellular debris.

III.1- *mok*^{m632} genotyping

To determine the presence of the *mok*^{m632} mutation, the template DNA was pipetted from the supernatant and amplified by PCR with Taq DNA Polymerase (5U/μl, LifeTechnologies) using the following primer set: forward CTG CTC CAC TGC TTT AAA GGC CAC, reverse GTG AGC GAG GCG CTG GCG GAC AG. The amplicon was subsequently digested with Hpyl88I (New England BioLabs), where the restriction site is destroyed in *mok*^{m623} mutants (one band at 162 base pairs), creating one band for wild-type embryos (two superimposed 81 bp fragments), and two bands for heterozygous embryos (one wild-type allele at 81 bp and one mutant allele at 161 bp).

III.2- *dynactin1b*^{*253} genotyping

To determine the presence of the insertion in our CRISPR mutant, the template DNA was amplified by PCR as previously using the following primer set: forward ACT CGG CTC TCT CTT CAG CC, reverse GCC CGA GGT CCA CAT GAT GCA AT. The amplicon was then ran on a 2% agarose gel to determine the presence of the insertion (expected product at 448bp, wild-type allele at 291bp).

IV-Molecular cloning

Our constructs rely on the bipartite GAL4/UAS system to target single CaP motor neurons in the embryonic zebrafish spinal cord. The GAL4 transcription activator is expressed under a specific promoter in a subset of primary motor neurons, and injection into the zygote of DNA constructs of our gene of interest following the UAS sequence is sufficient to induce binding of the transactivator to the UAS, and expression in a single-cell manner. In this study, we sometimes used a combination of different UAS sequences obtained from various sources (4 non-repeated UAS-hereafter, 4nrUAS, (Auer et al., 2015)) or multiple repeats of the same UAS sequence (10xUAS or 14xUAS) depending on the plasmids available and the method of cloning used to generate the construct of interest.

To obtain an efficient expression of our constructs, we made use of *Tol* transgenesis, which relies on a transposable element isolated from medaka fish. When DNA constructs are injected alongside *in vitro*-generated mRNA of the transposase, this allows for the generation

of genomic integration into cells, including germ cells, during development and can therefore be used to create stably-expressing zebrafish lines (Abe, Suster, & Kawakami, 2011).

IV.1-Gateway cloning

The Gateway cloning method relies on site-specific recombination properties of bacteriophage λ to integrate DNA into bacterial chromosomes. It requires the use of specific recombination sites (att sites), which are recognized by the λ integrase family, allowing for site-specific recombination reactions where DNA fragments flanked with these sites can be recombined into new vectors, also containing the recombination sites (Hartley, Temple, & Brasch, 2000).

We used the MultiSite Gateway Three-Fragment Vector Construction Kit (ThermoFisher Scientific), which works in a two-step process: cloning the genes of interest into entry vectors (BP reaction), then have been created in order to interact with each other in a specific way (att1 with att2 for example), which allows for the use of multiple entry vectors which will be recombined in order (5'-entry, middle-entry "pME", and 3'-entry) in the final LR reaction, while maintaining a proper reading frame. Many entry and destination vectors were made available to the public in the Tol2kit and will be referenced as such (Kwan et al., 2007). Molecular cloning to obtain the final constructs was done using standard restriction digestions and PCR protocols using the Phusion High-Fidelity DNA Polymerase (ThermoFischer Scientific).

We used two different destination vectors to generate the constructs used in this study: a simple destination vector containing an SV40 pA signal flanked by Tol2 inverted repeats (pDestTol2pA2, #394 from Tol2kit), and one containing an additional transgenesis marker *cmcl2:eGFP* (pDestTol2CG, #393 from Tol2kit) (Kwan et al., 2007).

4nrUAS-tagRFPCaax-pA-4nrUAS-eGFP-Rab5c-pA;cmcl2:eGFP; -Rab7-pA;cmcl2:eGFP; -Rab11a-pA;cmcl2:eGFP

These three constructs were cloned in parallel using the p5'-4nrUAS-tagRFPCaax-pA-4nrUAS vector, containing a membrane-bound (via Caax) tagRFP reporter under the expression of four non-repeated UAS sequences, which was previously cloned in our lab (Auer et al., 2015). We constructed fusion proteins by digesting out the *eGFP* sequence from a standard middle-entry vector (Tol2kit) and fusing it in a T4 ligation step with the *rab5c*, *rab7* and *rab11a*

sequences from the p3'E vectors kindly provided by Brian Link (Clark et al., 2011). The fusion proteins product were purified on gel and inserted into a middle-entry vector via restriction digest. The p5'E and the pME described above were combined with a standard p3'E vector containing the SV40 into the pDestTol2CG #393 destination vector via LR reaction to obtain *4nrUAS-tagRFPCaax-pA-4nrUAS-eGFP-Rab5c-pA*, *4nrUAS-tagRFPCaax-pA-4nrUAS-eGFP-Rab7-pA*, and *4nrUAS-tagRFPCaax-pA-4nrUAS-eGFP-Rab11a-pA*.

mnx1:lyn-GFP-pA

For this construct, we generated the p5'E plasmid by amplifying the promoter region of the *mnx1* gene and inserting it via a BP reaction. The middle entry plasmid was obtained by BP reaction from amplification of the *lyn-GFP* sequence of the *cldnb:lynGFP* plasmid (Donà et al., 2013) and the entry vectors were combined into pDestTol2pA2 #394 in a final LR reaction to obtain *mnx1:lyn-GFP-pA*.

pUAS-dendra2-rab3-pA

For this construct, we generated a fusion protein middle entry vector by fusing the *rab3* sequence from the pBHUAS-Rab3-YFP kindly provided by Michael Nonet, (Campbell et al., 2007) and the *dendra2* sequence from pDendra2-N1 kindly provided by Jean-René Huynh (Institut Curie, Paris) via fusion PCR. The middle entry vector was combined with a standard p5'UAS vector (Tol2kit) and a standard p3'SV40pA in a final LR reaction to obtain *pUAS-dendra2-rab3-pA*.

IV.2-Gibson assembly cloning

This type of cloning was developed by Dr Daniel Gibson and allows for recombination of multiple DNA fragments, independent of size or end compatibility. The DNA fragments are generated via standard PCR by primers generating an overlap of 20 to 40 bp between the fragments and recombined in a single-tube isothermal reaction by a combination of exonucleases, DNA polymerases and DNA ligases contained in a single master mix. The backbone vector can be opened by restriction digest or synthesized via PCR and the primers used to create overlap can include an added "spacer" sequence to introduce small tags or restriction sites between fragments (Gibson et al., 2009).

For cloning with this method, we used the pT1UciMP Toll destination vector previously described, which includes 14 repeats of the UAS sequence, followed by an Ebf1 minimal promoter and the carp β -actin initiator sequence, the *ubc* intron. The intron was shown to increase functional protein expression and was used in combination with the pou1 *afp* 3'UTR, also contained in the destination vector (Horstick et al., 2015). All fragments were cloned with Phusion High-Fidelity DNA Polymerase (ThermoFischer Scientific) and destination vectors were opened by restriction digest.

14xUAS:ubc-hDCTN1-eGFP-E2A-tagRFPCaax-pA

For cloning this construct, we used the pEGFP-C3 constructs of human *Dynactin1* kindly provided by Stefan Liebau (Stockmann et al., 2013) and amplified the *Dynactin1* sequence. We followed it by the *eGFP* sequence from a standard pME (Tol2kit) and an E2A linked *tagRFPCaax* sequence from the p5'-4nrUAS-tagRFPCaax-pA-4nrUAS vector described above (Auer et al., 2015). Using the NEBuilder HiFi DNA Assembly Cloning Kit (NEB) all of these sequences were inserted after the *ubc* intron of the pT1UciMP Toll destination vector opened by restriction digest with NcoI-HF (NEB) to obtain *14xUAS:ubc-hDCTN1-eGFP-E2A-tagRFPCaax-pA*.

14xUAS:ubc-ngfra-eGFP-E2A-tagRFPCaax-pA

For this construct, we cloned the cDNA sequence of the *ngfra* zebrafish gene (ENSDARG00000088708) coding for the p75 trophic receptor. The rest of the cloning was done exactly like the previous construct to obtain *14xUAS:ubc-ngfra-eGFP-E2A-tagRFPCaax-pA*.

IV.3-List of constructs used

- p4nrUAS:tagRFPCaax-pA-4nrUAS:PhbGFP-pA-Tol2;cmcl2:eGFP (Auer et al., 2015)
- 4nrUAS-tagRFPCaax-pA-4nrUAS-eGFP-Rab5c-pA;cmcl2:eGFP (this study)
- 4nrUAS-tagRFPCaax-pA-4nrUAS-eGFP-Rab7-pA;cmcl2:eGFP (this study)
- 4nrUAS-tagRFPCaax-pA-4nrUAS-eGFP-Rab11a-pA;cmcl2:eGFP (this study)
- *mnx1:lyn-GFP-pA* (this study)
- *14xUAS:ubc-hDCTN1-eGFP-E2A-tagRFPCaax-pA* (this study)

- 14xUAS:ubc-ngfra-eGFP-E2A-tagRFPcaax-pA (this study)
- pUAS-dendra2-rab3-pA (this study)
- 10xUAS:eb3-GFP-pA (Revenu et al., 2014)
- 10xUAS:eb3-GFP-E2A-tagRFP-rab3-pA (this study)

V-Touch-evoked escape response assay

The embryos were staged at 48hpf and dechorionated 30 minutes prior to the experiment. They were left to acclimate at room temperature during this time, then were placed one by one in the center of a 144mm petri dish containing egg medium. A refractory period of 30 seconds was allotted before the presentation of a stimulus. The escape response was elicited by a light brush on the tail of the embryo with a pair of blunt forceps and was recorded with an Olympus FE-5000 camera at 30Hz. The videos were analyzed in ImageJ using the Manual Tracking plugin (Fabrice Cordelières, Institut Curie-Orsay, France).

VI-Microscopy and image analysis

VI.1-Morphological images

Morphological images of embryos were acquired on a Leica MZ FLIII stereomicroscope (Leica) equipped with a Leica DFC310FX digital camera (Leica).

VI.2-Spinning disk confocal

Imaging was performed on a Roper confocal spinning disk head mounted on a Zeiss upright microscope, and acquisitions were done with a CoolSNAP HQ2 CDD camera (Photometrics, USA) through the MetaMorph software (Molecular Devices, USA). Embryos were anesthetized using 0.02% tricaine (MS-222, Sigma) diluted in egg water and embedded in 1% low melting-point agarose in a glass-bottom cell tissue culture dish (Fluorodish, World Precision Instruments, USA). Acquisitions were done using water immersion long working distance lenses, at 40x magnification (W DIC PL APO VIS-IR; 421462-9900) for z-stack images of the whole tectum and at 63x magnification (W PL APO VIS-IR (421480-9900) for single plane time-lapse imaging of linear axonal segments, and for filopodia imaging. Acquisitions were done using the Metamorph software (Molecular Devices) and resolution in z was set at 1µm for stacks. Images were assembled and analyzed in ImageJ (NIH). 6dpf z-

stacks taken in two frames were stitched together using the pairwise stitching function of the Stitching plugin (Preibisch, Saalfeld, & Tomancak, 2009).

VI.2.1-Time-lapse imaging

Live imaging of axonal transport was done using fusion proteins combined with a membrane reporter, described previously, expressed in the CaP primary motor neurons by use of the Tg(*mnx1*:GAL4) line. Time-lapse parameters were determined based on the speed of transport in the spinal cord and set at 1 seconds intervals for mitochondria (*4nrUAS:tagRFP**Caax-pA-4nrUAS:PhbGFP-pA-Tol2;cmcl2:eGFP*), for 10 minutes total duration, and set at 500ms for endosomes (*rab5c*, 7 and 11a), p75, and eb3 comets for 5 minutes total duration.

For filopodia dynamics timelapses, z-stacks were taken every 2 minutes for 10 minutes of total duration.

VI.2.2- Kymogram production and analysis

Time-lapse images were assembled and analyzed in ImageJ. Kymograms were extracted for each timelapse serie on linear axonal segments using the Kymograph Tool (Montpellier RIO Imaging, CNRS, France), where each pixels on the Y axis represents one timepoint projected against axonal length (X axis).

VI.2.3- Colocalization analysis

The colocalization was analyzed in ImageJ on z-stack projections acquired as described previously with a 40x objective using the JACoP plugin (Fabrice Cordelières & Susane Bolte, Institut Curie-Orsay, France).

VII-Whole-mount immunohistochemistry

Embryos were fixed in 4% paraformaldehyde diluted in PBS for 4h at room temperature. They were then rinsed multiple times in PBS containing 0,1% triton X-100 (PBST) then incubated with a solution of 1mg/ml of collagenase (from *Clostridium histolyticum*, Sigma) in PBS for 20 minutes (48hpf embryos) or 2h (6dpf embryos). The embryos were rinsed several times with PBST then blocked for 1h in a block solution containing 1% bovine serum albumin

(BSA), 2% normal goat serum, 1% DMSO and 0,1% triton X-100. The primary antibody was then added with fresh block solution according to the working dilutions listed below, with an incubation time of 2h at room temperature. After several washes in PBST, the secondary antibody was added in fresh block solution for an incubation of 2h at room temperature, then rinsed thoroughly. The embryos were then processed for imaging.

For labelling with conjugated α -bungarotoxin, the fixation step was done overnight and the block solution used was composed of 2% BSA, 0,5% triton X-100 in PBS. The incubation time for the conjugated α -bungarotoxin was 30 minutes at room temperature.

VII.1-List of antibodies

- Anti-synaptotagmin2 (znp1) from the (Developmental Studies Hybridoma Bank), monoclonal mouse IgG2a, used at 1:300.
- Conjugated α -bungarotoxin-AlexaFluor 594 (ThermoFischer Scientific), α -subunit of the nicotinic acetylcholine receptor (AChR) extracted from *Bungarus multicinctus* venom and conjugated with Alexa Fluor 594 used at 10ug/ml.
- Anti-acetylated tubulin clone 6-11-B-1 (Sigma) purified mouse monoclonal IgG antibody 1,5mg/ml used at 1:200.
- Anti-GFP (GeneTex, Euromedex) purified chicken polyclonal IgG antibody, 10mg/ml, used at 1:300.
- Goat anti-chicken Alexa Fluor 488 (Life Technologies) purified goat antibody, used at 1:1000
- Goat anti-mouse Alexa Fluor 488 (Life Technologies) purified goat antibody, used at 1:1000
- Goat anti-mouse Alexa Fluor 635 (Life Technologies) purified goat antibody, used at 1:1000

VIII-Quantitative RT-PCR

Total RNA was extracted from previously phenotyped 6dpf embryos using a standard TRIzol reagent protocol (ThermoFisher Scientific). cDNA was then synthesized using the retrotranscription SuperScript III First-Strand Synthesis system kit (ThermoFisher Scientific)

with the random hexamer primers. The qRT-PCR mix was prepared in technical triplicates with SYBR Green Master Mix (ThermoFisher Scientific) and run on an ABI PRISM 7900HT Real-Time PCR System (ThermoFisher Scientific) using *ef1a* and *rpl13a* as reference genes (Tang, Dodd, Lai, McNabb, & Love, 2007). The analysis was performed according to the deltaCT quantification method (Livak & Schmittgen, 2001).

VIII.1-List of primers

dctn1a_Fwd	TCGAAGCTGA TGATCCCGTG
dctn1a_Rev	TCCTGAGGGA GTGTGTGTGA
dctn1b-fwd	GCAAAGGAGG AGAAGAGAGG
dctn1b-rev	TGGAGAAGGC GATGGAC
P22P24_Fwd	CACAAATACA CATTCAACAG CAGGAC
P22P24_Rev	AGAGTTTCAT CCCACTGTGA AAAC TG
P25_Fwd	CTGTCCTTCC CCCAGAGACA
P25_Rev	TCTGGCTGAG AGGGAGGAAT
p50_Fwd	CCTCCAACGA GCCTGATGTT
p50_Rev	TAGCGCTGAC GTGTTTGTCT
ndel1b_Fwd	TACACCTGTG GGGAAGACCA
ndel1b_Rev	TCCTTGCTGC CTGATCCTTG
pafah1b1a_Fwd	CTTGTGCACC CTGGAGGAAA
pafah1b1a_Rev	GTACGGAGCA GTCTTGTGGA
pafah1b1b_Fwd	TGACACTGGT TGGCCATGAT
pafah1b1b_Rev	AGTGTTTCATG GGC ACTGAGG
bdnf_Fwd	CTTGAGGTGG AAGGGGAAGC G
bdnf_Rev	GTAACGGCGG CTCCAAAGGC
actr1.1-1_Fwd	GGGTCGGGAG TTATCAAGGC
actr1.1-1_Rev	CCGGTGCTCCTCTGCTTTAG
kif14_Fwd	CTCCAGCACA CCTCATGGAG
kif14_Rev	TCCCTGGAGC TGAAAGGTCT
rpl13a__Fwd	TCTGGAGGACTG TAAGAGGTTGC
rpl13a__Rev	AGACGCACAATC TTGAGAGCAG
ef1a_Fwd	CTGGAGGCCAGC TCAAACAT
ef1a_Rev	ATCAAGAAGAGT AGTACCGCTAGCATTAC

IX-Calcium imaging of fictive swimming (Kevin Fidelin, Claire Wyart laboratory)

GCaMP5G was paired with ventral nerve root (VNR) recordings to compare the profile of fictive swimming activity in mutant *mok^{m632}* embryos with wild type siblings at 4dpf. Larvae

were paralyzed by injection of 0.1-0.3 nL of 0.5mM α -Bungarotoxin (Tocris, UK), then embedded on their side in 1,5% low melting-point agarose in a glass-bottom dish filled with external solution ([NaCl]=134mM, [KCl]=2.9mM, [MgCl₂]=1.2mM, [HEPES]=10mM, [glucose]=10mM and [CaCl₂]=2.1mM; adjusted to pH 7.7-7.8 with NaOH) and placed under a 40X objective. The motor output is recorded at the level of the VNR upon stimulus (water puff to the otic vesicle) meant to elicit a fictive escape response. The GCaMP5G signal was visualized with a 488 λ laser in expressing cells of the spinal cord and recorded at 10Hz (Slidebook software). ROIs of interest were manually outlined and calcium signals were extracted online using a custom MATLAB script (Kevin Fidelin, Claire Wyart Laboratory, Paris). The VNR signals were recorded through a glass capillary filled with external solution positioned close to the intermyotomal junction and ventral relative to the axial musculature midline. Recordings were performed as previously described (Knafo et al., 2017).

X-Electrophysiology (Jeffrey M. Hubbard, Claire Wyart laboratory)

6 dpf zebrafish larvae were decapitated and pinned to a Sylgard-coated recording chamber (Sylgard 184, Dow Corning, Midland, MI, USA) through the notochord with electrolytically-sharpened tungsten pins. The skin was removed and the specimen was bathed briefly in a 10% formamide solution and subsequently washed in bath recording solution to eliminate spontaneous muscle twitching. The dura was exposed by suctioning away dorsal muscle fibers with a glass pipette to access motor neurons for paired recordings. Typically 3-7 segments of dorsal muscle were removed.

Recording electrodes were fashioned from capillary glass (1.5 mm O.D., 1.1 ID, WPI, Sarasota, FL, USA) with a horizontal puller (P1000, Sutter Instruments, Novato, CA). Electrode resistances were 6-12 M Ω for motor neuron recordings and 3-5 M Ω for muscle cell recordings. Positive pressure (65mm Hg) was applied to the recording electrode via a pneumatic transducer (Fluke Biomedical DPM1B, Everett, WA). Once the electrode was driven through the dura in order to approach the CaP motor neuron targeted for patch experiments, the positive pressure was reduced to 35mm Hg.

CaP motor neurons were chosen based on their large soma size and location within the spinal cord which was visualized in DIC using a Zeiss D1 upright microscope with a 40x water immersion objective (Carl Zeiss, Oberkochen, Germany). External bath recording solution contained the following (in mM), 134 NaCl, 2.9 KCl, 2.1 CaCl₂-H₂O, 1.2 MgCl₂, 10 Glucose,

10 HEPES with pH adjusted to 7.4, and osmolarity to 290 mOsm. Internal solution for muscle and motor neuron recordings contained the following (in mM), 115 K-Gluconate, 15 KCl, 2 MgCl₂, 0.5 EGTA, 4 Mg-ATP, 10 HEPES pH 7.2, 290 mOsm. Patch electrodes typically contained 40 μ M Alexa Fluor 647 hydrazide to confirm the identity of CaP motor neurons (Life Technologies Ltd., Paisley, UK).

Physiological recordings were made with an Axopatch 700B amplifier and digitized with a Digidata 1440A (Molecular Devices, Fremont, CA, USA). pClamp software was used to acquire electrophysiological data at a sampling rate of 50 kHz and low pass filtered at 2.2 kHz for the motor neuron recordings and postsynaptic muscle cell recordings were sampled at 1000 kHz and low pass filtered at 2.2 kHz. Data were analyzed with Clampfit (Molecular Devices, Fremont, CA, USA), Igor Pro 6.34 (WaveMetrics, Lake Oswego, OR), Excel 2010 (Microsoft, Redmond, WA, USA), and Matlab (Mathworks, Natick, MA, USA). For miniature EPC analysis, events were detected with MiniAnalysis (Synapsoft, Fort Lee, NJ, USA).

mEPC detection threshold was set to 30pA. For evoked EPC analysis in the paired recording configuration, EPC failures were analyzed during the full stimulus train (at 1 Hz, 10 Hz and 20 Hz) and only during the first second of stimulation at 100 Hz due to the subsequent onset of asynchronous release.

XI-CRISPR/Cas9-mediated knock-in of *dynactin1b*

The target site for guide RNA sequences (CCATGTAACGCTCTTTAGCT) was exon 5 of the sequence found for transcript *dctn1b*-202 of the gene *dynactin1b* (ENSDART00000169953.1) and exon 8 of transcript *dctn1b*-201 (ENSDART00000102411.4). We identified an allele with an insertion of 157 bp leading to a premature stop codon at position 253 a.a. of the wild-type protein. The founder was outcrossed to wild-type and subsequent generations were incrossed to generate a homozygous mutant line.

The guide RNAs were synthesized using the Megascript T7 transcription kit (Ambion) and were purified using the RNAeasy Mini Kit (Quiagen). The *Cas9* mRNA was transcribed using the mMessage mMachine T7 kit (Life Technologies), followed by a DNaseI polyA tailing reaction.

XII-Graph generation and statistical analysis

Data compilation and analysis was done using Excel (Microsoft, USA) and graph generations was done using GraphPad Prism version 6 for Windows (GraphPad Software, USA). Using GraphPad, Student's t-test was used for normally distributed data and Mann-Whitney U test was used for non-normally distributed data, when comparing mutants and wild-types. For comparison of multiple groups, SigmaPlot 11.0 integrated with SigmaStat 3.1 was used and a one-way ANOVA on ranks was performed, followed by Dunn's multiple comparison procedure (pairwise). The Z-test was used to compare population proportions. Significance, set at $p \leq 0,05$ (*), $p \leq 0,01$ (**), $p \leq 0,001$ (***)).

References

- Abascal, F., Tress, M. L., & Valencia, A. (2015). The evolutionary fate of alternatively spliced homologous exons after gene duplication. *Genome Biology and Evolution*, 7(6), 1392–1403. <http://doi.org/10.1093/gbe/evv076>
- Abe, G., Suster, M. L., & Kawakami, K. (2011). *Tol2-mediated transgenesis, gene trapping, enhancer trapping, and the Gal4-UAS system. Methods in cell biology* (Third Edit, Vol. 104). Elsevier Inc. <http://doi.org/10.1016/B978-0-12-374814-0.00002-1>
- Adler, J., & Parmryd, I. (2010). Quantifying colocalization by correlation: The Pearson correlation coefficient is superior to the Mander's overlap coefficient. *Cytometry Part A*, 77A(8), 733–742. <http://doi.org/10.1002/cyto.a.20896>
- Adler, J., & Parmryd, I. (2013). Colocalization analysis in fluorescence microscopy. *Methods in Molecular Biology (Clifton, N.J.)*, 931, 97–109. http://doi.org/10.1007/978-1-62703-056-4_5
- Akerboom, J., Chen, T.-W., Wardill, T. J., Tian, L., Marvin, J. S., Mutlu, S., ... Looger, L. L. (2012). Optimization of a GCaMP Calcium Indicator for Neural Activity Imaging. *The Journal of Neuroscience*, 32(40), 13819–13840. <http://doi.org/10.1523/JNEUROSCI.2601-12.2012>
- Akhmanova, A., & Hammer III, J. A. (2012). Linking molecular motors to membrane cargo. *Current Opinion in Cell Biology*, 22(4), 479–487. <http://doi.org/10.1016/j.ceb.2010.04.008>. Linking
- Allen, M. J., Shan, X., Caruccio, P., Froggett, S. J., Moffat, K. G., & Murphey, R. K. (1999). Targeted expression of truncated glued disrupts giant fiber synapse formation in *Drosophila*. *The Journal of Neuroscience : The Official Journal of the Society for Neuroscience*, 19(21), 9374–84. Retrieved from <http://www.ncbi.nlm.nih.gov/pubmed/10531442>
- Aren, Reiley, Zarei, S., Carr, K. L., Diaz, K., Guerra, O., Altamirano, P. F., ... Chinea, A. (2015). A comprehensive review of amyotrophic lateral sclerosis. *Surgical Neurology International*, 6, 171. <http://doi.org/10.4103/2152-7806.169561>
- Armstrong, G. A. B., & Drapeau, P. (2013). Calcium channel agonists protect against neuromuscular dysfunction in a genetic model of TDP-43 mutation in ALS. *The Journal of Neuroscience : The Official Journal of the Society for Neuroscience*, 33(4), 1741–52. <http://doi.org/10.1523/JNEUROSCI.4003-12.2013>
- Armstrong, G. A. B., & Drapeau, P. (2013). Loss and gain of FUS function impair neuromuscular synaptic transmission in a genetic model of ALS. *Human Molecular Genetics*. Retrieved from <http://hmg.oxfordjournals.org/content/early/2013/06/13/hmg.ddt278.short>
- Ashworth, R., Zimprich, F., & Bolsover, S. R. (2001). Buffering intracellular calcium disrupts motoneuron development in intact zebrafish embryos. *Developmental Brain Research*, 129(2), 169–179. [http://doi.org/10.1016/S0165-3806\(01\)00198-5](http://doi.org/10.1016/S0165-3806(01)00198-5)
- Askham, J. m., Vaughan, K. T., Goodson, H. V., & Morrison, E. E. (2002). Evidence That an Interaction between EB1 and p150Glued Is Required for the Formation and Maintenance of a Radial Microtubule Array Anchored at the Centrosome. *Molecular Biology of the Cell*, 13, 3627–3645. <http://doi.org/doi/10.1091/mbc.E02-01-0061>
- Atkin, J. D., Farg, M. a, Soo, K. Y., Walker, A. K., Halloran, M., Turner, B. J., ... Horne, M. K. (2013). Mutant SOD1 inhibits ER-Golgi transport in Amyotrophic Lateral Sclerosis. *Journal of Neurochemistry*. <http://doi.org/10.1111/jnc.12493>
- Auer, T. O., Xiao, T., Bercier, V., Gebhardt, C., Duroure, K., Concordet, J.-P., ... Del Bene, F. (2015). Deletion of a kinesin I motor unmask a mechanism of homeostatic branching

- control by neurotrophin-3. *eLife*, 4, 1–26. <http://doi.org/10.7554/eLife.05061>
- Ayloo, S., Lazarus, J. E., Dodda, A., Tokito, M., Ostap, E. M., & Holzbaur, E. L. F. (2014). Dynactin functions as both a dynamic tether and brake during dynein-driven motility. *Nature Communications*, 5, 4807. <http://doi.org/10.1038/ncomms5807>
- Baas, P. W., Karabay, A., & Qiang, L. (2005). Microtubules cut and run. *Trends in Cell Biology*, 15(10), 518–524. <http://doi.org/10.1016/j.tcb.2005.08.004>
- Baas, P. W., Nadar, C. V., & Myers, K. A. (2006). Axonal transport of microtubules: The long and short of it. *Traffic*, 7(5), 490–498. <http://doi.org/10.1111/j.1600-0854.2006.00392.x>
- Baas, P. W., Rao, A. N., Matamoros, A. J., & Leo, L. (2016). Stability properties of neuronal microtubules. *Cytoskeleton*, 73(9), 442–460. <http://doi.org/10.1002/cm.21286>
- Babin, P. J., Goizet, C., & Raldúa, D. (2014). Zebrafish models of human motor neuron diseases: Advantages and limitations. *Progress in Neurobiology*. <http://doi.org/10.1016/j.pneurobio.2014.03.001>
- Bearce, E. A., Erdogan, B., & Lowery, L. A. (2015). TIPsy tour guides: how microtubule plus-end tracking proteins (+TIPs) facilitate axon guidance. *Frontiers in Cellular Neuroscience*, 9(June), 1–12. <http://doi.org/10.3389/fncel.2015.00241>
- Berezuk, M. a., & Schroer, T. a. (2007). Dynactin enhances the processivity of kinesin-2. *Traffic*, 8(Table 1), 124–129. <http://doi.org/10.1111/j.1600-0854.2006.00517.x>
- Bisby, M. (1977). Retrograde axonal transport of endogenous protein : differences between motor and sensory axons. *Journal of Neurochemistry*, 28, 249–251.
- Blasier, K. R., Humsi, M. K., Ha, J., Ross, M. W., Smiley, W. R., Inamdar, N. a., ... Pfister, K. K. (2014). Live cell imaging reveals differential modifications to cytoplasmic dynein properties by phospho- and dephosphomimic mutations of the intermediate chain 2C S84. *Journal of Neuroscience Research*, 92(9), 1143–1154. <http://doi.org/10.1002/jnr.23388>
- Blokhuis, A. M., Groen, E. J. N., Koppers, M., van den Berg, L. H., & Pasterkamp, R. J. (2013). Protein aggregation in amyotrophic lateral sclerosis. *Acta Neuropathologica*, 125(6), 777–94. <http://doi.org/10.1007/s00401-013-1125-6>
- Bonanomi, D., & Pfaff, S. L. (2010). Motor axon pathfinding. *Cold Spring Harbor Perspectives in Biology*, 2(3), 1–19. <http://doi.org/10.1101/cshperspect.a001735>
- Brady, S. T., & Morfini, G. A. (2017). Regulation of motor proteins, axonal transport deficits and adult-onset neurodegenerative diseases. *Neurobiology of Disease*. <http://doi.org/10.1016/j.nbd.2017.04.010>
- Brusés, J. L. (2011). N-cadherin regulates primary motor neuron axon growth and branching during zebrafish embryonic development. *Journal of Comparative Neurology*, 519(9), 1797–1815. <http://doi.org/10.1002/cne.22602>
- Bucci, C., Alifano, P., & Cogli, L. (2014). The role of rab proteins in neuronal cells and in the trafficking of neurotrophin receptors. *Membranes*, 4(4), 642–77. <http://doi.org/10.3390/membranes4040642>
- Burkhardt, J. K., Echeverri, C. J., Nilsson, T., & Vallee, R. B. (1997). Overexpression of the dynamitin (p50) subunit of the dynactin complex disrupts dynein-dependent maintenance of membrane organelle distribution. *Journal of Cell Biology*, 139(2), 469–484. <http://doi.org/10.1083/jcb.139.2.469>
- Campbell, D. S., Stringham, S. A., Timm, A., Xiao, T., Law, M. Y., Baier, H., ... Chien, C. Bin. (2007). Slit1a Inhibits Retinal Ganglion Cell Arborization and Synaptogenesis via Robo2-Dependent and -Independent Pathways. *Neuron*, 55(2), 231–245. <http://doi.org/10.1016/j.neuron.2007.06.034>
- Carter, A. P., Diamant, A. G., & Urnavicius, L. (2016). How dynein and dynactin transport cargos: A structural perspective. *Current Opinion in Structural Biology*, 37, 62–70.

- <http://doi.org/10.1016/j.sbi.2015.12.003>
- Chang, L., Kreko, T., Davison, H., Cusmano, T., Wu, Y., Rothenfluh, A., & Eaton, B. a. (2013). Normal dynactin complex function during synapse growth in *Drosophila* requires membrane binding by Arfaptin. *Molecular Biology of the Cell*, *24*(11), 1749–64, S1–5. <http://doi.org/10.1091/mbc.E12-09-0697>
- Charalampopoulos, I., Vicario, A., Padiaditakis, I., Gravanis, A., Simi, A., & Ibáñez, C. F. (2012). Genetic Dissection of Neurotrophin Signaling through the p75 Neurotrophin Receptor. *Cell Reports*, *2*(6), 1563–1570. <http://doi.org/10.1016/j.celrep.2012.11.009>
- Cheong, F. K. Y., Feng, L., Sarkeshik, A., Yates, J. R., & Schroer, T. a. (2014). Dynactin integrity depends upon direct binding of dynamitin to Arp1. *Molecular Biology of the Cell*, *25*, 1–25. <http://doi.org/10.1091/mbc.E14-03-0842>
- Chevalier-Larsen, E., & Holzbaur, E. L. F. (2006). Axonal transport and neurodegenerative disease. *Biochimica et Biophysica Acta*, *1762*(11–12), 1094–108. <http://doi.org/10.1016/j.bbadis.2006.04.002>
- Chevalier-Larsen, E. S., Wallace, K. E., Pennise, C. R., & Holzbaur, E. L. F. (2008). Lysosomal proliferation and distal degeneration in motor neurons expressing the G59S mutation in the p150Glued subunit of dynactin. *Human Molecular Genetics*, *17*(13), 1946–55. <http://doi.org/10.1093/hmg/ddn092>
- Chowdhury, S., Ketcham, S. a, Schroer, T. a, & Lander, G. C. (2015). Structural organization of the dynein–dynactin complex bound to microtubules. *Nature Structural & Molecular Biology*, (March), 1–6. <http://doi.org/10.1038/nsmb.2996>
- Cirulli, E. T., Lasseigne, B. N., Petrovski, S., Sapp, P. C., Dion, P. A., Leblond, C. S., ... Goldstein, D. B. (2015). Exome sequencing in amyotrophic lateral sclerosis identifies risk genes and pathways. *Science*, *347*(6229), 1436–1441. <http://doi.org/10.1126/science.aaa3650>
- Ciura, S., Lattante, S., Le Ber, I., Latouche, M., Tostivint, H., Brice, A., & Kabashi, E. (2013). Loss of function of C9orf72 causes motor deficits in a zebrafish model of amyotrophic lateral sclerosis. *Annals of Neurology*, *74*(2), 180–7. <http://doi.org/10.1002/ana.23946>
- Clark, B., Winter, M., Cohen, A., & Link, B. (2011). Generation of Rab-based transgenic lines for in vivo studies of endosome biology in zebrafish. *Developmental Dynamics*, *240*(11), 2452–2465. <http://doi.org/10.1002/dvdy.22758>. Generation
- Cosker, K. E., Pazyra-Murphy, M. F., Fenstermacher, S. J., & Segal, R. a. (2013). Target-derived neurotrophins coordinate transcription and transport of Bclw to prevent axonal degeneration. *Annals of Internal Medicine*, *158*(6), 5195–5207. <http://doi.org/10.1523/JNEUROSCI.3862-12.2013>
- Crowder, M. E., Flynn, J. R., McNally, K. P., Cortes, D. B., Price, K. L., Kuehnert, P. a., ... McNally, F. J. (2015). Dynactin-dependent cortical dynein and spherical spindle shape correlate temporally with meiotic spindle rotation in *Caenorhabditis elegans*. *Molecular Biology of the Cell*, *26*(17), 3030–3046. <http://doi.org/10.1091/mbc.E15-05-0290>
- Culver–Hanlon, T. L., Lex, S. A., Stephens, A. D., Quintyne, N. J., & King, S. J. (2006). A microtubule-binding domain in dynactin increases dynein processivity by skating along microtubules. *Nature Cell Biology*, *8*(3), 264–270. <http://doi.org/10.1038/ncb1370>
- Deacon, S. W., Serpinskaya, A. S., Vaughan, P. S., Lopez Fanarraga, M., Vernos, I., Vaughan, K. T., & Gelfand, V. I. (2003). Dynactin is required for bidirectional organelle transport. *Journal of Cell Biology*, *160*(3), 297–301. <http://doi.org/10.1083/jcb.200210066>
- Dean, C., & Dresbach, T. (2006). Neuroligins and neuexins: Linking cell adhesion, synapse formation and cognitive function. *Trends in Neurosciences*, *29*(1), 21–29. <http://doi.org/10.1016/j.tins.2005.11.003>

- Del Bene, F., Wehman, A. M. A., Link, B. B. A., Baier, H., (2007). Regulation of neurogenesis by interkinetic nuclear migration through an apical-basal Notch gradient. *Cell*, 134(6), 1055–1065. <http://doi.org/10.1016/j.cell.2008.07.017>. Regulation
- De Vos, K. J., & Hafezparast, M. (2017). Neurobiology of axonal transport defects in motor neuron diseases: Opportunities for translational research? *Neurobiology of Disease*. <http://doi.org/10.1016/j.nbd.2017.02.004>
- Dent, E. W., & Kalil, K. (2001). Axon branching requires interactions between dynamic microtubules and actin filaments. *The Journal of Neuroscience : The Official Journal of the Society for Neuroscience*, 21(24), 9757–9769. <http://doi.org/10.1523/JNEUROSCI.2124-01.2001> [pii]
- Dix, C. I., Soundararajan, H. C., Dzhindzhev, N. S., Begum, F., Suter, B., Ohkura, H., ... Bullock, S. L. (2013). Lissencephaly-1 promotes the recruitment of dynein and dynactin to transported mRNAs. *The Journal of Cell Biology*, 202(3), 479–94. <http://doi.org/10.1083/jcb.201211052>
- Dixit, R., Levy, J. R., Tokito, M., Ligon, L. A., & Holzbaur, E. L. F. (2008). Regulation of dynactin through the differential expression of p150 Glued isoforms. *Journal of Biological Chemistry*, 283(48), 33611–33619. <http://doi.org/10.1074/jbc.M804840200>
- Doerre, G., & Malicki, J. (2001). A mutation of early photoreceptor development, mikre oko, reveals cell-cell interactions involved in the survival and differentiation of zebrafish photoreceptors. *The Journal of Neuroscience : The Official Journal of the Society for Neuroscience*, 21(17), 6745–57. Retrieved from <http://www.ncbi.nlm.nih.gov/pubmed/11517263>
- Donà, E., Barry, J. D., Valentin, G., Quirin, C., Khmelinskii, A., Kunze, A., ... Gilmour, D. (2013). Directional tissue migration through a self-generated chemokine gradient. *Nature*. <http://doi.org/10.1038/nature12635>
- Drerup, C. M., Herbert, A. L., Monk, K. R., & Nechiporuk, A. V. (2017). Regulation of mitochondria-dynactin interaction and mitochondrial retrograde transport in axons. *eLife*, 1–25. <http://doi.org/10.7554/eLife.22234>
- Dubey, J., Ratnakaran, N., & Koushika, S. P. (2015). Neurodegeneration and microtubule dynamics: death by a thousand cuts. *Frontiers in Cellular Neuroscience*, 1–15. <http://doi.org/10.3389/fncel.2015.00343>
- Duncan, J. E., & Goldstein, L. S. B. (2006). The genetics of axonal transport and axonal transport disorders. *PLoS Genetics*, 2(9), e124. <http://doi.org/10.1371/journal.pgen.0020124>
- Eaton, B. a, Fetter, R. D., & Davis, G. W. (2002). Dynactin is necessary for synapse stabilization. *Neuron*, 34(5), 729–41. Retrieved from <http://www.ncbi.nlm.nih.gov/pubmed/12062020>
- Echeverri, C. J., Paschal, B. M., Vaughan, K. T., & Vallee, R. B. (1996). Molecular characterization of the 50-kD subunit of dynactin reveals function for the complex in chromosome alignment and spindle organization during mitosis. *Journal of Cell Biology*, 132(4), 617–633. <http://doi.org/10.1083/jcb.132.4.617>
- Encalada, S. E., & Goldstein, L. S. B. (2014). Biophysical challenges to axonal transport: motor-cargo deficiencies and neurodegeneration. *Annual Review of Biophysics*, 43, 141–69. <http://doi.org/10.1146/annurev-biophys-051013-022746>
- Fejtova, A., Davydova, D., Bischof, F., Lazarevic, V., Altroch, W. D., Romorini, S., ... Gundelfinger, E. D. (2009). Dynein light chain regulates axonal trafficking and synaptic levels of Bassoon. *Journal of Cell Biology*, 185(2), 341–355. <http://doi.org/10.1083/jcb.200807155>
- Flanagan-Steet, H., Fox, M. A., Meyer, D., & Sanes, J. R. (2005). Neuromuscular synapses can form in vivo by incorporation of initially aneural postsynaptic specializations. *Development*, 132(20), 4471–4481. <http://doi.org/10.1242/dev.02044>

- Florez-McClure, M. L., Linseman, D. A., Chu, C. T., Barker, P. A., Bouchard, R. J., Le, S. S., ... Heidenreich, K. A. (2004). The p75 Neurotrophin Receptor Can Induce Autophagy and Death of Cerebellar Purkinje Neurons. *Journal of Neuroscience*, *24*(19), 4498–4509. <http://doi.org/10.1523/JNEUROSCI.5744-03.2004>
- Frey, D., Schneider, C., Xu, L., Borg, J., Spooren, W., & Caroni, P. (2000). Early and selective loss of neuromuscular synapse subtypes with low sprouting competence in motoneuron diseases. *The Journal of Neuroscience*, *20*(7), 2534–2542. Retrieved from <http://www.jneurosci.org/content/20/7/2534.short>
- Fu, M. meng, & Holzbaur, E. L. F. (2014). Integrated regulation of motor-driven organelle transport by scaffolding proteins. *Trends in Cell Biology*, *24*(10), 564–574. <http://doi.org/10.1016/j.tcb.2014.05.002>
- Garces, J. A., Clark, I. B., Meyer, D. I., & Vallee, R. B. (1999). Interaction of the p62 subunit of dynactin with Arp1 and the cortical actin cytoskeleton. *Current Biology*, *9*(24), 1497–1500. [http://doi.org/10.1016/S0960-9822\(00\)80122-0](http://doi.org/10.1016/S0960-9822(00)80122-0)
- Garcia-Mata, R., Gao, Y.-S., & Sztul, E. (2002). Hassles with taking out the garbage: aggravating aggresomes. *Traffic (Copenhagen, Denmark)*, *3*(6), 388–396. <http://doi.org/tra030602> [pii]
- Gibbs, K. L., Greensmith, L., & Schiavo, G. (2015). Regulation of Axonal Transport by Protein Kinases. *Trends in Biochemical Sciences*, *40*(10), 597–610. <http://doi.org/10.1016/j.tibs.2015.08.003>
- Gibson, D. G., Young, L., Chuang, R.-Y., Venter, J. C., Hutchison, C. A., & Smith, H. O. (2009). Enzymatic assembly of DNA molecules up to several hundred kilobases. *Nature Methods*, *6*(5), 343–345. <http://doi.org/10.1038/nmeth.1318>
- Graf, E. R., Daniels, R. W., Burgess, R. W., Schwarz, T. L., & DiAntonio, A. (2009). Rab3 Dynamically Controls Protein Composition at Active Zones. *Neuron*, *64*(5), 663–677. <http://doi.org/10.1016/j.neuron.2009.11.002>. Rab3
- Hafezparast, M., Klocke, R., Ruhrberg, C., Marquardt, A., Ahmad-Annuar, A., Bowen, S., ... Fisher, E. M. C. (2003). Mutations in dynein link motor neuron degeneration to defects in retrograde transport. *Science (New York, N.Y.)*, *300*(5620), 808–12. <http://doi.org/10.1126/science.1083129>
- Hartley, J. L., Temple, G. F., & Brasch, M. A. (2000). DNA Cloning Using In Vitro Site-Specific Recombination. *Genome Research*, *10*(11), 1788–1795. <http://doi.org/10.1101/gr.143000.that>
- Haucke, V., Neher, E., & Sigrist, S. J. (2011). Protein scaffolds in the coupling of synaptic exocytosis and endocytosis. *Nature Reviews Neuroscience*, *12*(3), 127–138. <http://doi.org/10.1038/nrn2948>
- Hendricks, A., Perlson, E., Ross, J., Schroeder III, H., Tokito, M., & Holzbaur, E. L. F. (2010). Motor coordination via a tug-of-war mechanism drives bidirectional vesicle transport. *Current Biology*, *20*(8), 697–702. <http://doi.org/10.1016/j.cub.2010.02.058>. Motor
- Heuston, E., Bronner, C. E., Kull, F. J., & Endow, S. A. (2010). A kinesin motor in a force-producing conformation. *BMC Structural Biology*, *10*(1), 19. <http://doi.org/10.1186/1472-6807-10-19>
- Hirokawa, N., Niwa, S., & Tanaka, Y. (2010). Molecular motors in neurons: transport mechanisms and roles in brain function, development, and disease. *Journal of Neuroscience*, *68*(4), 610–38. <http://doi.org/10.1016/j.neuron.2010.09.039>
- Horgan, C. P.; Hanscom, S. R.; Jolly, R. S.; Futter, C. E. and McCaffrey, M. W. (2010). Rab11-FIP3 links the Rab11 GTPase and cytoplasmic dynein to mediate transport to the endosomal-recycling compartment. *Journal of Cell Science*, *123*(Pt 2), 181–191. <http://doi.org/10.1242/jcs.052670>

- Horstick, E. J., Jordan, D. C., Bergeron, S. A., Tabor, K. M., Serpe, M., Feldman, B., & Burgess, H. A. (2015). Increased functional protein expression using nucleotide sequence features enriched in highly expressed genes in zebrafish. *Nucleic Acids Research*, *43*(7), e48. <http://doi.org/10.1093/nar/gkv035>
- Ikenaka, K., Kawai, K., Katsuno, M., Huang, Z., Jiang, Y.-M., Iguchi, Y., ... Sobue, G. (2013). Dnc-1/Dynactin 1 Knockdown Disrupts Transport of Autophagosomes and Induces Motor Neuron Degeneration. *PLoS One*, *8*(2), e54511. <http://doi.org/10.1371/journal.pone.0054511>
- Ilieva, H., Polymenidou, M., & Cleveland, D. W. (2009, December 14). Non-cell autonomous toxicity in neurodegenerative disorders: ALS and beyond. *Journal of Cell Biology*. <http://doi.org/10.1083/jcb.200908164>
- Insinna, C., Baye, L., Amsterdam, A., Besharse, J., & Link, B. (2010). Analysis of a zebrafish *dync1h1* mutant reveals multiple functions for cytoplasmic dynein 1 during retinal photoreceptor development. *Neural Development*, *12*(April). Retrieved from <http://scholar.google.com/scholar?hl=en&btnG=Search&q=intitle:Analysis+of+a+zebrafish+dync1h1+mutant+reveals+multiple+functions+for+cytoplasmic+dynein+1+during+r+etinal+photoreceptor+development#0>
- Jackson, H. E., & Ingham, P. W. (2013). Control of muscle fibre-type diversity during embryonic development: the zebrafish paradigm. *Mechanisms of Development*, *130*, 447–57. <http://doi.org/10.1016/j.mod.2013.06.001>
- Jaiswal, M. K. (2013). Calcium, mitochondria, and the pathogenesis of ALS: the good, the bad, and the ugly. *Frontiers in Cellular Neuroscience*. <http://doi.org/10.1124/mol.108.050831>
- James, P. a., & Talbot, K. (2006). The molecular genetics of non-ALS motor neuron diseases. *Biochimica et Biophysica Acta*, *1762*(11–12), 986–1000. <http://doi.org/10.1016/j.bbadis.2006.04.003>
- Janke, C., & Bulinski, J. C. (2011). Post-translational modifications: Post-translational regulation of the microtubule cytoskeleton: mechanisms and functions. *Nature Publishing Group*, *12*(12), 773–786. <http://doi.org/10.1038/nrm3227>
- Jin, M., Yamada, M., Arai, Y., Nagai, T., & Hirotsune, S. (2014). Arl3 and LC8 regulate dissociation of dynactin from dynein. *Nature Communications*, *5*, 5295. <http://doi.org/10.1038/ncomms6295>
- Jing, L., Lefebvre, J. L., Gordon, L. R., & Granato, M. (2009). Wnt signals organize synaptic prepattern and axon guidance through the zebrafish unplugged/MuSK receptor. *Neuron*, *61*(5), 721–33. <http://doi.org/10.1016/j.neuron.2008.12.025>
- Jing, X., & Malicki, J. (2009). Zebrafish *ale oko*, an essential determinant of sensory neuron survival and the polarity of retinal radial glia, encodes the p50 subunit of dynactin. *Development (Cambridge, England)*, *136*(17), 2955–64. <http://doi.org/10.1242/dev.037739>
- Johansson, M., Rocha, N., Zwart, W., Jordens, I., Janssen, L., Kuijl, C., ... Neefjes, J. (2007). Activation of endosomal dynein motors by stepwise assembly of Rab7-RILP-p150Glued, ORP1L, and the receptor β tail spectrin. *The Journal of Cell Biology*, *176*(4), 459–71. <http://doi.org/10.1083/jcb.200606077>
- Kabashi, E., Bercier, V., Lissouba, A., Liao, M., Brustein, E., Rouleau, G. A., & Drapeau, P. (2011). *Fus* and *tardbp* but not *sod1* interact in genetic models of amyotrophic lateral sclerosis. *PLoS Genetics*, *7*(8), 17–28. <http://doi.org/10.1371/journal.pgen.1002214>
- Kabashi, E., Lin, L., Tradewell, M. L., Dion, P. A., Bercier, V., Bourgouin, P., ... Drapeau, P. (2009). Gain and loss of function of ALS-related mutations of TARDBP (TDP-43) cause motor deficits in vivo. *Human Molecular Genetics*, *19*(4), 671–683. <http://doi.org/10.1093/hmg/ddp534>

- Kaesler, P. S., & Rgehr, W. G. (2014). Molecular Mechanisms for Synchronous, Asynchronous, and Spontaneous Neurotransmitter Release. *Annual Review of Physiology*, *76*, 333–363. <http://doi.org/10.1146/annurev-physiol-021113-170338>.Molecular
- Kardon, J., & Vale, R. (2009). Regulators of the cytoplasmic dynein motor. *Nature Reviews Molecular Cell Biology*, *10*(12), 854–865. <http://doi.org/10.1038/nrm2804>.DATABASES
- Katsuno, M., Adachi, H., Minamiyama, M., Waza, M., Tokui, K., Banno, H., ... Sobue, G. (2006). Reversible disruption of dynactin 1-mediated retrograde axonal transport in polyglutamine-induced motor neuron degeneration. *The Journal of Neuroscience: The Official Journal of the Society for Neuroscience*, *26*(47), 12106–17. <http://doi.org/10.1523/JNEUROSCI.3032-06.2006>
- Kim, H., Ling, S.-C. C., Rogers, G. C., Kural, C., Selvin, P. R., Rogers, S. L., & Gelfand, V. I. (2007). Microtubule binding by dynactin is required for microtubule organization but not cargo transport. *Journal of Cell Biology*, *176*(5), 641–651. <http://doi.org/10.1083/jcb.200608128>
- Kimura, N., Imamura, O., Ono, F., & Terao, K. (2007). Aging Attenuates Dynactin–Dynein Interaction: Down-Regulation of Dynein Causes Accumulation of Endogenous Tau and Amyloid Precursor Protein in Human Neuroblastoma Cells Nobuyuki. *Journal of Neuroscience Research*, *85*, 2909–2916. <http://doi.org/DOI: 10.1002/jnr.21408>
- Kishore, S., & Fetcho, J. R. (2015). Homeostatic regulation of dendritic dynamics in a motor map in vivo. *Nature Communications*, *7*(4), 389–400. <http://doi.org/10.1530/ERC-14-0411>.Persistent
- Knafo, S., Fidelin, K., Prendergast, A., Tseng, P. B., Dickey, C., Figueiredo, S. N., ... Wyart, C. (2017). Mechanosensory Neurons Control the Timing of Spinal Microcircuit Selection during Locomotion. *eLife*, *6*. <http://doi.org/doi: 10.7554/eLife.25260>
- Kuh, G. F., Stockmann, M., Meyer-Ohlendorf, M., Linta, L., Proepper, C., Ludolph, A. C., ... Liebau, S. (2012). Tubulin-binding cofactor B is a direct interaction partner of the dynactin subunit p150Glued. *Cell and Tissue Research*, *350*(1), 13–26. <http://doi.org/10.1007/s00441-012-1463-z>
- Kuźma-Kozakiewicz, M., Chudy, A., Kaźmierczak, B., Dziewulska, D., Usarek, E., & Barańczyk-Kuźma, A. (2013). Dynactin Deficiency in the CNS of Humans with Sporadic ALS and Mice with Genetically Determined Motor Neuron Degeneration. *Neurochemical Research*. <http://doi.org/10.1007/s11064-013-1160-7>
- Kwan, K. M., Fujimoto, E., Grabher, C., Mangum, B. D., Hardy, M. E., Campbell, D. S., ... Chien, C. Bin. (2007). The Tol2kit: A multisite gateway-based construction Kit for Tol2 transposon transgenesis constructs. *Developmental Dynamics*, *236*(11), 3088–3099. <http://doi.org/10.1002/dvdy.21343>
- Lai, C., Lin, X., Chandran, J., Shim, H., Yang, W.-J., & Cai, H. (2007). The G59S Mutation in p150glued Causes Dysfunction of Dynactin in Mice. *Journal of Neuroscience*, *27*(51), 13982–13990. <http://doi.org/10.1523/JNEUROSCI.4226-07.2007>
- Laird, F. M., Farah, M. H., Ackerley, S., Hoke, A., Maragakis, N., Rothstein, J. D., ... Wong, P. C. (2008). Motor neuron disease occurring in a mutant dynactin mouse model is characterized by defects in vesicular trafficking. *Journal of Neuroscience*, *28*(9), 1997–2005. <http://doi.org/10.1523/JNEUROSCI.4231-07.2008>
- LaMonte, B., Wallace, K., Holloway, B., Shelly, S., Ascano, J., Tokito, M., ... Holzbaur, E. L. F. (2002). Disruption of dynein/dynactin inhibits axonal transport in motor neurons causing late-onset progressive degeneration. *Neuron*, *34*, 715–727. Retrieved from <http://www.sciencedirect.com/science/article/pii/S0896627302006967>
- Lattante, S., De Calbiac, H., Le Ber, I., Brice, A., Ciura, S., & Kabashi, E. (2015). Sqstm1

- knock-down causes a locomotor phenotype ameliorated by rapamycin in a zebrafish model of ALS/FTLD. *Human Molecular Genetics*, 24(6), 1682–1690.
<http://doi.org/10.1093/hmg/ddu580>
- Lazarus, J. E., Moughamian, A. J., Tokito, M. K., & Holzbaur, E. L. F. (2013). Dynactin Subunit p150(Glued) Is a Neuron-Specific Anti-Catastrophe Factor. *PLoS Biology*, 11(7), e1001611. <http://doi.org/10.1371/journal.pbio.1001611>
- Leal, S. S., & Gomes, C. M. (2015). Calcium dysregulation links ALS defective proteins and motor neuron selective vulnerability. *Frontiers in Cellular Neuroscience*, 9(June), 1–6.
<http://doi.org/10.3389/fncel.2015.00225>
- Levy, J. R., Sumner, C. J., Caviston, J. P., Tokito, M. K., Ranganathan, S., Ligon, L. a, ... Holzbaur, E. L. F. (2006). A motor neuron disease-associated mutation in p150Glued perturbs dynactin function and induces protein aggregation. *The Journal of Cell Biology*, 172(5), 733–45. <http://doi.org/10.1083/jcb.200511068>
- Lipka, J., Kuijpers, M., Jaworski, J., & Hoogenraad, C. C. (2013). Mutations in cytoplasmic dynein and its regulators cause malformations of cortical development and neurodegenerative diseases. *Biochemical Society Transactions*, 41(6), 1605–1612.
<http://doi.org/10.1042/BST20130188>
- Liu, G., Sanghavi, P., Bollinger, K. E., Perry, L., Marshall, B., Roon, P., ... Gonsalvez, G. B. (2015). Efficient endocytic uptake and maturation in drosophila oocytes requires Dynamitin/p50. *Genetics*, 201(2), 631–649. <http://doi.org/10.1534/genetics.115.180018>
- Livak, K. J., & Schmittgen, T. D. (2001). Analysis of relative gene expression data using real-time quantitative PCR and the 2(-Delta Delta C(T)) Method. *Methods (San Diego, Calif.)*, 25(4), 402–8. <http://doi.org/10.1006/meth.2001.1262>
- Lloyd, T. E., Machamer, J., O'Hara, K., Kim, J. H., Collins, S. E., Wong, M. Y., ... Kolodkin, A. L. (2012). The p150(Glued) CAP-Gly domain regulates initiation of retrograde transport at synaptic termini. *Neuron*, 74(2), 344–60.
<http://doi.org/10.1016/j.neuron.2012.02.026>
- Lorenzo, D. N., Badea, A., Davis, J., Hostettler, J., He, J., Zhong, G., ... Bennett, V. (2014). A PIK3C3-Ankyrin-B-Dynactin pathway promotes axonal growth and multiorganelle transport. *The Journal of Cell Biology*, 207(6), 735–752.
<http://doi.org/10.1083/jcb.201407063>
- Lu, B., & Je, H. S. (2003). Neurotrophic regulation of the development and function of the neuromuscular synapses. *Journal of Neurocytology*, 32(5–8), 931–941.
<http://doi.org/10.1023/B:NEUR.0000020633.93430.db>
- Luo, G., Yi, J., Ma, C., Xiao, Y., Yi, F., Yu, T., & Zhou, J. (2013). Defective mitochondrial dynamics is an early event in skeletal muscle of an amyotrophic lateral sclerosis mouse model. *PloS One*, 8(12), e82112. <http://doi.org/10.1371/journal.pone.0082112>
- Maday, S., Twelvetrees, A. E., Moughamian, A. J., & Holzbaur, E. L. F. (2014). Axonal Transport: Cargo-Specific Mechanisms of Motility and Regulation. *Neuron*, 84(2), 292–309. <http://doi.org/10.1016/j.neuron.2014.10.019>
- Magrané, J., Cortez, C., Gan, W.-B., & Manfredi, G. (2014). Abnormal mitochondrial transport and morphology are common pathological denominators in SOD1 and TDP43 ALS mouse models. *Human Molecular Genetics*, 23(6), 1413–24.
<http://doi.org/10.1093/hmg/ddt528>
- Maier, B., Kirsch, M., Anderhub, S., Zentgraf, H., & Krämer, A. (2013). The novel actin/focal adhesion-associated protein MISP is involved in mitotic spindle positioning in human cells. *Cell Cycle*, 12(9), 1457–1471. <http://doi.org/10.4161/cc.24602>
- Malicki, J., Neuhauss, S. C. F., Schier, A. F., Solnica-krezel, L., Stemple, D. L., Stainier, D. Y. R., ... Driever, W. (1996). Mutations affecting development of the zebrafish retina. *Development (Cambridge, England)*, 123, 263–273. Retrieved from

- <http://dev.biologists.org/content/123/1/263.short>
- Marjan, H., Cavalli, V., Shah, S. B., Schimmelpfeng, K., Bruschi, R., Yang, G., ... Goldstein, L. S. B. (2007). Dynactin Is Required for Coordinated Bidirectional Motility, but Not for Dynein Membrane Attachment. *Molecular Biology of the Cell*, 18, 2081–2089.
- Matthews, V. B., Åström, M. B., Chan, M. H. S., Bruce, C. R., Krabbe, K. S., Prelovsek, O., ... Febbraio, M. A. (2009). Brain-derived neurotrophic factor is produced by skeletal muscle cells in response to contraction and enhances fat oxidation via activation of AMP-activated protein kinase. *Diabetologia*, 52(7), 1409–1418.
<http://doi.org/10.1007/s00125-009-1364-1>
- Matus, S., Valenzuela, V., Medinas, D. B., & Hetz, C. (2013). ER Dysfunction and Protein Folding Stress in ALS. *International Journal of Cell Biology*, 2013, 674751.
<http://doi.org/10.1155/2013/674751>
- McKenney, R. J., Huynh, W., Tanenbaum, M. E., Bhabha, G., & Vale, R. D. (2014). Activation of cytoplasmic dynein motility by dynactin-cargo adapter complexes. *Science*, 345(6194), 337–341.
- McKenney, R. J., Huynh, W., Tanenbaum, M. E., Bhabha, G., & Vale, R. D. (2014). Supplementary: Activation of cytoplasmic dynein motility by dynactin-cargo adapter complexes. *Science*, 345(6194), 337–341. <http://doi.org/10.1126/science.1254198>
- McKenney, R. J., Huynh, W., Vale, R. D., & Sirajuddin, M. (2016). Tyrosination of α -tubulin controls the initiation of processive dynein-dynactin motility. *The EMBO Journal*, 35(11), e201593071. <http://doi.org/10.15252/embj.201593071>
- Meyer, M. P., & Smith, S. J. (2006). Evidence from in vivo imaging that synaptogenesis guides the growth and branching of axonal arbors by two distinct mechanisms. *The Journal of Neuroscience*, 26(13), 3604–14. <http://doi.org/10.1523/JNEUROSCI.0223-06.2006>
- Mikenberg, I., Widera, D., Kaus, A., Kaltschmidt, B., & Kaltschmidt, C. (2007). Transcription factor NF- κ B is transported to the nucleus via cytoplasmic dynein/dynactin motor complex in hippocampal neurons. *PLoS ONE*, 2(7).
<http://doi.org/10.1371/journal.pone.0000589>
- Millecamps, S., & Julien, J.-P. (2013). Axonal transport deficits and neurodegenerative diseases. *Nature Reviews. Neuroscience*, 14(3), 161–76. <http://doi.org/10.1038/nrn3380>
- Mitchell, C. S., & Lee, R. H. (2012). Cargo distributions differentiate pathological axonal transport impairments. *Journal of Theoretical Biology*, 300, 277–291.
<http://doi.org/10.1016/j.jtbi.2012.01.019>
- Moloney, E. B., de Winter, F., & Verhaagen, J. (2014). ALS as a distal axonopathy: molecular mechanisms affecting neuromuscular junction stability in the presymptomatic stages of the disease. *Frontiers in Neuroscience*, 8(August), 252.
<http://doi.org/10.3389/fnins.2014.00252>
- Moore, J. K., Sept, D., & Cooper, J. a. (2009). Neurodegeneration mutations in dynactin impair dynein-dependent nuclear migration. *Proceedings of the National Academy of Sciences of the United States of America*, 106(13), 5147–52.
<http://doi.org/10.1073/pnas.0810828106>
- Moreno, R. L., & Ribera, A. B. (2009). Zebrafish motor neuron subtypes differ electrically prior to axonal outgrowth. *Journal of Neurophysiology*, 102(4), 2477–84.
<http://doi.org/10.1152/jn.00446.2009>
- Moughamian, A. J., & Holzbaur, E. L. F. (2012). Dynactin Is Required for Transport Initiation from the Distal Axon. *Neuron*, 74(2), 331–43.
<http://doi.org/10.1016/j.neuron.2012.02.025>
- Moughamian, A. J., Osborn, G. E., Lazarus, J. E., Maday, S., & Holzbaur, E. L. F. (2013). Ordered Recruitment of Dynactin to the Microtubule Plus-End is Required for Efficient

- Initiation of Retrograde Axonal Transport. *The Journal of Neuroscience : The Official Journal of the Society for Neuroscience*, 33(32), 13190–203.
<http://doi.org/10.1523/JNEUROSCI.0935-13.2013>
- Mühlemann, O., Eberle, A. B., Stalder, L., & Zamudio Orozco, R. (2008). Recognition and elimination of nonsense mRNA. *Biochimica et Biophysica Acta*, 1779(9), 538–49.
<http://doi.org/10.1016/j.bbagr.2008.06.012>
- Münch, C., Rosenbohm, A., Sperfeld, A. D., Uttner, I., Reske, S., Krause, B. J., ... Ludolph, A. C. (2005). Heterozygous R1101K mutation of the DCTN1 gene in a family with ALS and FTD. *Annals of Neurology*, 58(5), 777–780. <http://doi.org/10.1002/ana.20631>
- Münch, C., Sedlmeier, R., Meyer, T., Homberg, V., Sperfeld, A. D., Kurt, A., ... Ludolph, A. C. (2004). Point mutations of the p150 subunit of dynactin (DCTN1) gene in ALS. *Neurology*, 63(4), 724–6. Retrieved from <http://www.ncbi.nlm.nih.gov/pubmed/15326253>
- Murphey, R. K., Caruccio, P. C., Getzinger, M., Westgate, P. J., & Phillis, R. W. (1999). Dynein-dynactin function and sensory axon growth during Drosophila metamorphosis: A role for retrograde motors. *Developmental Biology*, 209(1), 86–97.
<http://doi.org/10.1006/dbio.1999.9217>
- Myers, P. Z. (1985). Spinal Motoneurons of the Larval Zebrafish. *The Journal of Comparative Neurology*, 236, 555–561.
- Myers, P. Z., Eisen, J. S., & Westerfield, M. (1986). Development and axonal outgrowth of identified motoneurons in the zebrafish. *Journal of Neuroscience*, 6(8), 2278–2289. Retrieved from <http://www.ncbi.nlm.nih.gov/pubmed/3746410>
- Nirschl, J. J., Magiera, Maria M., Lazarus, J. E., Janke, C., & Holzbaur, E. L. F. (2016). α -tubulin tyrosination and CLIP-170 phosphorylation regulate the initiation of dynein-driven transport in neurons. *Cell Reports*, 14(11), 1–30.
<http://doi.org/10.1016/j.bbamem.2015.02.010>
- Ohki, Y., Wenninger-Weinzierl, A., Hruscha, A., Asakawa, K., Kawakami, K., Haass, C., ... Schmid, B. (2017). Glycine-alanine dipeptide repeat protein contributes to toxicity in a zebrafish model of C9orf72 associated neurodegeneration. *Molecular Neurodegeneration*, 12(1), 6. <http://doi.org/10.1186/s13024-016-0146-8>
- Pang, Z. P., Melicoff, E., Padgett, D., Liu, Y., Teich, A. F., Dickey, B. F., ... Sudhof, T. C. (2006). Synaptotagmin-2 is essential for survival and contributes to Ca²⁺ triggering of neurotransmitter release in central and neuromuscular synapses. *J Neurosci*, 26(52), 13493–13504. <http://doi.org/10.1523/JNEUROSCI.3519-06.2006>
- Panzer, J. A., Song, Y., & Balice-Gordon, R. J. (2006). In vivo imaging of preferential motor axon outgrowth to and synaptogenesis at prepatterned acetylcholine receptor clusters in embryonic zebrafish skeletal muscle. *The Journal of Neuroscience : The Official Journal of the Society for Neuroscience*, 26(3), 934–947.
<http://doi.org/10.1523/JNEUROSCI.3656-05.2006>
- Paquet, D., Plucińska, G., & Misgeld, T. (2014). In vivo imaging of mitochondria in intact zebrafish larvae. *Methods in Enzymology*, 547, 151–64. <http://doi.org/10.1016/B978-0-12-801415-8.00009-6>
- Park, J., Park, Y., Ryu, I., Choi, M.-H., Lee, H. J., Oh, N., ... Kim, Y. K. (2017). Misfolded polypeptides are selectively recognized and transported toward aggresomes by a CED complex. *Nature Communications*, 8, 15730. <http://doi.org/10.1038/ncomms15730>
- Peris, L., Thery, M., Fauré, J., Saoudi, Y., Lafanechère, L., Chilton, J. K., ... Job, D. (2006). Tubulin tyrosination is a major factor affecting the recruitment of CAP-Gly proteins at microtubule plus ends. *Journal of Cell Biology*, 174(6), 839–849.
<http://doi.org/10.1083/jcb.200512058>
- Perlson, E., Hendricks, A. G., Lazarus, J. E., Ben-Yaakov, K., Gradus, T., Tokito, M., &

- Holzbaur, E. L. F. (2013). Dynein interacts with the neural cell adhesion molecule (NCAM180) to tether dynamic microtubules and maintain synaptic density in cortical neurons. *Journal of Biological Chemistry*, 288(39), 27812–27824. <http://doi.org/10.1074/jbc.M113.465088>
- Perlson, E., Jeong, G., Ross, J., Dixit, R., Wallace, K. E., Kalb, R. G., & Holzbaur, E. L. F. (2009). A Switch in Retrograde Signaling from Survival to Stress in Rapid Onset Neurodegeneration. *The Journal of Neuroscience*, 29(31), 9903–9917. <http://doi.org/10.1523/JNEUROSCI.0813-09.2009.A>
- Perlson, E., Maday, S., Fu, M.-M., Moughamian, A. J., & Holzbaur, E. L. F. (2010). Retrograde axonal transport: pathways to cell death? *Trends in Neurosciences*, 33(7), 335–44. <http://doi.org/10.1016/j.tins.2010.03.006>
- Petzoldt, A. G., Lu, J., & Sigrist, S. J. (2016). Mechanisms controlling assembly and plasticity of presynaptic active zone scaffolds. *Current Opinion in Neurobiology*, 39, 69–76. <http://doi.org/10.1016/j.conb.2016.04.009>
- Plucińska, G., Paquet, D., Hruscha, A., Godinho, L., Haass, C., Schmid, B., & Misgeld, T. (2012). In vivo imaging of disease-related mitochondrial dynamics in a vertebrate model system. *The Journal of Neuroscience : The Official Journal of the Society for Neuroscience*, 32(46), 16203–12. <http://doi.org/10.1523/JNEUROSCI.1327-12.2012>
- Preibisch, S., Saalfeld, S., & Tomancak, P. (2009). Globally optimal stitching of tiled 3D microscopic image acquisitions. *Bioinformatics*, 25(11), 1463–1465. <http://doi.org/10.1093/bioinformatics/btp184>
- Puls, I., Jonnakuty, C., LaMonte, B., Holzbaur, E. L. F., Tokito, M. K., Mann, E., ... Fischbeck, K. H. (2003). Mutant dynactin in motor neuron disease. *Nature Genetics*, 33(4), 455–6. <http://doi.org/10.1038/ng1123>
- Quintyne, N. J., Gill, S. R., Eckley, D. M., Crego, C. L., Compton, D. A., & Schroer, T. A. (1999). Dynactin is required for microtubule anchoring at centrosomes. *Journal of Cell Biology*, 147(2), 321–334. <http://doi.org/10.1083/jcb.147.2.321>
- Revenu, C., Streichan, S., Dona, E., Lecaudey, V., Hufnagel, L., & Gilmour, D. (2014). Quantitative cell polarity imaging defines leader-to-follower transitions during collective migration and the key role of microtubule-dependent adherens junction formation. *Development*, 141(6), 1282–1291. <http://doi.org/10.1242/dev.101675>
- Rizo, J., & Xu, J. (2015). The Synaptic Vesicle Release Machinery. *Annual Review of Biophysics*, 44(1), 339–367. <http://doi.org/10.1146/annurev-biophys-060414-034057>
- Saha, S., & Slepecky, N. B. (2000). Age-related changes in microtubules in the guinea pig organ of Corti. Tubulin isoform shifts with increasing age suggest changes in micromechanical properties of the sensory epithelium. *Cell and Tissue Research*, 300(1), 29–46. <http://doi.org/10.1007/s004410050045>
- Saint-Amant, L., & Drapeau, P. (1998). Time course of the development of motor behaviors in the zebrafish embryo. *J Neurobiol*, 37(4), 622–632. [http://doi.org/10.1002/\(SICI\)1097-4695\(199812\)37:4<622::AID-NEU10>3.0.CO;2-S](http://doi.org/10.1002/(SICI)1097-4695(199812)37:4<622::AID-NEU10>3.0.CO;2-S) [pii]
- Sandow, S. L., Heydon, K., Weible, M. W., Reynolds, A. J., Bartlett, S. E., & Hendry, I. A. (2000). Signalling organelle for retrograde axonal transport of internalized neurotrophins from the nerve terminal. *Immunology and Cell Biology*, 78(4), 430–435. <http://doi.org/10.1046/j.1440-1711.2000.00924.x>
- Sanes, J. R., & Lichtman, J. W. (1999). Development of the vertebrate neuromuscular junction. *Annual Review Neuroscience*, 22, 389–442.
- Sato-Maeda, M., Tawarayama, H., Obinata, M., Kuwada, J. Y., & Shoji, W. (2006). Sema3a1 guides spinal motor axons in a cell- and stage-specific manner in zebrafish. *Development (Cambridge, England)*, 133(5), 937–47. <http://doi.org/10.1242/dev.02268>

- Saxena, S., & Caroni, P. (2011). Selective Neuronal Vulnerability in Neurodegenerative Diseases: From Stressor Thresholds to Degeneration. *Neuron*. Elsevier Inc. <http://doi.org/10.1016/j.neuron.2011.06.031>
- Saxton, W. M., & Hollenbeck, P. J. (2012). The axonal transport of mitochondria. *Journal of Cell Science*, 125(Pt 9), 2095–104. <http://doi.org/10.1242/jcs.053850>
- Schluter, O. M., Schmitz, F., Jahn, R., Rosenmund, C., & Südhof, T. C. (2004). A Complete Genetic Analysis of Neuronal Rab3 Function. *Journal of Neuroscience*, 24(29), 6629–6637. <http://doi.org/10.1523/JNEUROSCI.1610-04.2004>
- Schmid, B., Hruscha, A., Hognl, S., Banzhaf-Strathmann, J., Strecker, K., van der Zee, J., ... Haass, C. (2013). Loss of ALS-associated TDP-43 in zebrafish causes muscle degeneration, vascular dysfunction, and reduced motor neuron axon outgrowth. *Proceedings of the National Academy of Sciences of the United States of America*, 110(13), 1–6. <http://doi.org/10.1073/pnas.1218311110>
- Schnapp, B. J., & Reese, T. S. (1989). Dynein is the motor for retrograde axonal transport of organelles. *Proceedings of the National Academy of Sciences of the United States of America*, 86(5), 1548–1552. <http://doi.org/10.1073/pnas.86.5.1548>
- Schroer, T. A. (2004). DYNAMACTIN. *Annual Review of Cell and Developmental Biology*, 20(1), 759–779. <http://doi.org/10.1146/annurev.cellbio.20.012103.094623>
- Shaw, P. J. (2005). Molecular and cellular pathways of neurodegeneration in motor neuron disease. *Journal of Neurology, Neurosurgery & Psychiatry*, 76(8), 1046–1057. <http://doi.org/10.1136/jnnp.2004.048652>
- Sleigh, J. N., Burgess, R. W., Gillingater, T. H., & Cader, M. Z. (2014). Morphological analysis of neuromuscular junction development and degeneration in rodent lumbrical muscles. *Journal of Neuroscience Methods*, 1–7. <http://doi.org/10.1016/j.jneumeth.2014.02.005>
- Smith, R. B., Machamer, J. B., Kim, N. C., Hays, T. S., & Marques, G. (2012). Relay of retrograde synaptogenic signals through axonal transport of BMP receptors. *Journal of Cell Science*, 125(16), 3752–3764. <http://doi.org/10.1242/jcs.094292>
- Song, Y., & Brady, S. T. (2015). Posttranslational Modifications of Tubulin: Pathways to Functional Diversity of Microtubules. *Trends in Cell Biology*, 25(3), 125–136. <http://doi.org/10.1016/j.immuni.2010.12.017>. Two-stage
- Soo, K. Y., Farg, M., & Atkin, J. D. (2011, January). Molecular motor proteins and amyotrophic lateral sclerosis. *International Journal of Molecular Sciences*. <http://doi.org/10.3390/ijms12129057>
- Sorbara, C. D., Wagner, N. E., Ladwig, A., Nikić, I., Merkler, D., Kleele, T., ... Kerschensteiner, M. (2014). Pervasive Axonal Transport Deficits in Multiple Sclerosis Models. *Neuron*, 1–8. <http://doi.org/10.1016/j.neuron.2014.11.006>
- Stockmann, M., Meyer-Ohlendorf, M., Achberger, K., Putz, S., Demestre, M., Yin, H., ... Liebau, S. (2013). The dynactin p150 subunit: cell biology studies of sequence changes found in ALS/MND and Parkinsonian syndromes. *Journal of Neural Transmission (Vienna, Austria : 1996)*, 120(5), 785–98. <http://doi.org/10.1007/s00702-012-0910-z>
- Ström, A. L., Shi, P., Zhang, F., Gal, J., Kilty, R., Hayward, L. J., & Zhu, H. (2008). Interaction of amyotrophic lateral sclerosis (ALS)-related mutant copper-zinc superoxide dismutase with the dynein-dynactin complex contributes to inclusion formation. *Journal of Biological Chemistry*, 283(33), 22795–22805. <http://doi.org/10.1074/jbc.M800276200>
- Sztal, T. E., Ruparelia, A. A., Williams, C., & Bryson-Richardson, R. J. (2016). Using Touch-evoked Response and Locomotion Assays to Assess Muscle Performance and Function in Zebrafish. *Journal of Visualized Experiments*, (116), 1–6. <http://doi.org/10.3791/54431>
- Tanaka, F., Ikenaka, K., Yamamoto, M., & Sobue, G. (2012). Neuropathology and omics in

- motor neuron diseases. *Neuropathology*, 32(4), 458–462. <http://doi.org/10.1111/j.1440-1789.2011.01281.x>
- Tanaka, M., Miyoshi, J., Ishizaki, H., Togawa, A., Ohnishi, K., Endo, K., ... Takai, Y. (2001). Role of Rab3 GDP/GTP exchange protein in synaptic vesicle trafficking at the mouse neuromuscular junction. *Molecular Biology of the Cell*, 12(5), 1421–1430. <http://doi.org/10.1091/mbc.12.5.1421>
- Tang, R., Dodd, A., Lai, D., McNabb, W. C., & Love, D. R. (2007). Validation of zebrafish (*Danio rerio*) reference genes for quantitative real-time RT-PCR normalization. *Acta Biochimica et Biophysica Sinica*, 39(5), 384–390. <http://doi.org/10.1111/j.1745-7270.2007.00283.x>
- Teuling, E., van Dis, V., Wulf, P. S., Haasdijk, E. D., Akhmanova, A., Hoogenraad, C. C., & Jaarsma, D. (2008). A novel mouse model with impaired dynein/dynactin function develops amyotrophic lateral sclerosis (ALS)-like features in motor neurons and improves lifespan in SOD1-ALS mice. *Human Molecular Genetics*, 17(18), 2849–2862. <http://doi.org/10.1093/hmg/ddn182>
- Therrien, M., Dion, P. A., & Rouleau, G. A. (2016). ALS: Recent Developments from Genetics Studies. *Current Neurology and Neuroscience Reports*, 16(6). <http://doi.org/10.1007/s11910-016-0658-1>
- Tokito, M. K., Howland, D. S., Lee, V. M., & Holzbaur, E. L. F. (1996). Functionally distinct isoforms of dynactin are expressed in human neurons. *Molecular Biology of the Cell*, 7(8), 1167–80. Retrieved from <http://www.pubmedcentral.nih.gov/articlerender.fcgi?artid=275970&tool=pmcentrez&rendertype=abstract>
- Tripathy, S. K., Weil, S. J., Chen, C., Anand, P., Vallee, R. B., & Gross, S. P. (2014). Autoregulatory mechanism for dynactin control of processive and diffusive dynein transport. *Nature Cell Biology*, (October). <http://doi.org/10.1038/ncb3063>
- Tsujikawa, M., Omori, Y., Biyanwila, J., & Malicki, J. (2007). Mechanism of positioning the cell nucleus in vertebrate photoreceptors. *Proceedings of the National Academy of Sciences of the United States of America*, 104(37), 14819–24. <http://doi.org/10.1073/pnas.0700178104>
- Urnavicius, L., Zhang, K., Diamant, A. G., Motz, C., Schlager, M. A., Yu, M., ... Carter, A. P. (2015). The structure of the dynactin complex and its interaction with dynein. *Science*, 347(6229), 1441–1446. <http://doi.org/10.1126/science.aaa4080>
- Vaccaro, A., Patten, S. a, Aggad, D., Julien, C., Maios, C., Kabashi, E., ... Parker, J. A. (2013). Pharmacological reduction of ER stress protects against TDP-43 neuronal toxicity in vivo. *Neurobiology of Disease*, 55, 64–75. <http://doi.org/10.1016/j.nbd.2013.03.015>
- Valetti, C., Wetzell, D. M., Schrader, M., Hasbani, M. J., Gill, S. R., Kreis, T. E., & Schroer, T. A. (1999). Role of dynactin in endocytic traffic: effects of dynamitin overexpression and colocalization with CLIP-170. *Molecular Biology of ...*, 10(December), 4107–4120. Retrieved from <http://www.molbiolcell.org/content/10/12/4107.short>
- Vallee, R. B., McKenney, R. J., & Ori-McKenney, K. M. (2012). Multiple modes of cytoplasmic dynein regulation. *Nature Cell Biology*, 14(3), 224–30. <http://doi.org/10.1038/ncb2420>
- Van Damme, P., Robberecht, W., & Van Den Bosch, L. (2017). Modelling amyotrophic lateral sclerosis: progress and possibilities. *Disease Models & Mechanisms*, 10(5), 537–549. <http://doi.org/10.1242/dmm.029058>
- Vaughan, K. T., Tynan, S. H., Faulkner, N. E., Echeverri, C. J., & Vallee, R. B. (1999). Colocalization of cytoplasmic dynein with dynactin and CLIP-170 at microtubule distal ends. *Journal of Cell Science*, 112 (Pt 1), 1437–47. Retrieved from

- <http://www.ncbi.nlm.nih.gov/pubmed/10212138>
- Vaughan, K. T., & Vauee, R. B. (1995). Cytoplasmic Dynein Binds Dynactin through a Direct Interaction between the Intermediate Chains and p150. *The Journal of Cell Biology*, 131(6), 1507–1516.
- Vaughan, P. S., Miura, P., Henderson, M., Byrne, B., & Vaughan, K. T. (2002). A role for regulated binding of p150(Glued) to microtubule plus ends in organelle transport. *Journal of Cell Biology*, 158(2), 305–319. <http://doi.org/10.1083/jcb.200201029>
- Vilariño-Güell, C., Wider, C., Soto-Ortolaza, A. I., Cobb, S. A., Kachergus, J. M., Keeling, B. H., ... Farrer, M. J. (2009). Characterization of DCTN1 genetic variability in neurodegeneration. *Neurology*, 72(23), 2024–2028. <http://doi.org/10.1212/WNL.0b013e3181a92c4c>
- Villarin, J. M., McCurdy, E. P., Martínez, J. C., & Hengst, U. (2016). Local synthesis of dynein cofactors matches retrograde transport to acutely changing demands. *Nature Communications*, 7, 13865. <http://doi.org/10.1038/ncomms13865>
- Wadsworth, P., & Lee, W. L. (2013). Microtubule motors: Doin' it without dynactin. *Current Biology*, 23(13), R563-5. <http://doi.org/10.1016/j.cub.2013.05.026>
- Wandinger-Ness, A., & Zerial, M. (2014). Rab Proteins and the Compartmentalization of the Endosomal System. *Cold Spring Harbor Perspectives in Biology*, 6(11), a022616. <http://doi.org/10.1101/cshperspect.a022616>
- Wang, M., Wen, H., & Brehm, P. (2008). Function of neuromuscular synapses in the zebrafish choline-acetyltransferase mutant bajan. *Journal of Neurophysiology*, 100(4), 1995–2004. <http://doi.org/10.1152/jn.90517.2008>
- Wang, W., Li, L., Lin, W.-L., Dickson, D. W., Petrucelli, L., Zhang, T., & Wang, X. (2013). The ALS disease associated mutant TDP-43 impairs mitochondrial dynamics and function in motor neurons. *Human Molecular Genetics*, 1–14. <http://doi.org/10.1093/hmg/ddt319>
- Waterman-Storer, C. M., Karki, S., & Holzbaur, E. L. F. (1995). The p150Glued component of the dynactin complex binds to both microtubules and the actin-related protein centractin (Arp-1). *Proceedings of the National Academy of Sciences of the United States of America*, 92(5), 1634–8. Retrieved from <http://www.pubmedcentral.nih.gov/articlerender.fcgi?artid=42574&tool=pmcentrez&rendertype=abstract>
- Weber, T., & Köster, R. (2013). Genetic Tools for Multicolor Imaging in zebrafish larvae. *Methods (San Diego, Calif.)*, (July). <http://doi.org/10.1016/j.ymeth.2013.07.028>
- Wijesekera, L. C., & Leigh, P. N. (2009). Amyotrophic lateral sclerosis. *Orphanet Journal of Rare Diseases*, 4, 3. <http://doi.org/10.1186/1750-1172-4-3>
- Yogev, S., Cooper, R., Fetter, R., Horowitz, M., & Shen, K. (2016). Microtubule Organization Determines Axonal Transport Dynamics. *Neuron*, 92(2), 449–460. <http://doi.org/10.1016/j.neuron.2016.09.036>
- Zelenchuk, T. a, & Brusés, J. L. (2011). In vivo labeling of zebrafish motor neurons using an mnx1 enhancer and Gal4/UAS. *Genesis (New York, N.Y. : 2000)*, 49(7), 546–54. <http://doi.org/10.1002/dvg.20766>
- Zhang, J., Qiu, R., Arst, H. N., Peñalva, M. a, & Xiang, X. (2014). HookA is a novel dynein-early endosome linker critical for cargo movement in vivo. *The Journal of Cell Biology*, 204(6), 1009–26. <http://doi.org/10.1083/jcb.201308009>
- Zhang, J., Yao, X., Fischer, L., Abenza, J. F., Peñalva, M. A., & Xiang, X. (2011). The p25 subunit of the dynactin complex is required for dynein-early endosome interaction. *Journal of Cell Biology*, 193(7), 1245–1255. <http://doi.org/10.1083/jcb.201011022>

Annex

Annex 1-Research article: Deletion of a kinesin I motor unmasks a mechanism of homeostatic branching control by neurotrophin-3. Auer, Xiao, Bercier et al, eLife, 2015

During the course of my PhD, I developed the axonal transport assay presented here in the context of another project, which focused on the characterization of a zebrafish line, mutant for kinesin1 (*kif5aa*) with regard to the development of retinal ganglion cells of the optic tectum. We uncovered an activity-dependent homeostatic mechanism regulating the growth of these cells via neurotrophins-3.

My role in this project was to develop and perform axonal transport assay in the zebrafish tectum for the cargo presented previously, as well as for synaptophysin-GFP (not used in the present study). We also investigated a phenotype at the level of the spinal cord CaP (KIF5A is causative of hereditary spastic paraplegia, another disease leading to paralysis) but another lab published similar result before we completed the analysis (see **Unique function of Kinesin Kif5A in localization of mitochondria in axons**. Campbell PD, Shen K, Sapio MR, Glenn TD, Talbot WS, Marlow FL. J Neurosci. 2014).

Axonal transport assay in live embryos is a technique that was not yet used in the lab, and as axonal transport is a very new research interest at the Del Bene lab, many of the tools had to be created and gleaned from kind researchers willing to share both their knowledge and their constructs with us. In this annex you will find the eLife article where part of the results gathered for this initial project were published. As it was used in the development and validation of the live axonal transport assay, we reference this work in the thesis text.

Deletion of a kinesin I motor unmasks a mechanism of homeostatic branching control by neurotrophin-3

Thomas O Auer^{1,2,3,4*†}, Tong Xiao^{5,6†}, Valerie Bercier^{1,2,3}, Christoph Gebhardt^{1,2,3}, Karine Duroure^{1,2,3}, Jean-Paul Concordet⁷, Claire Wyart⁸, Maximiliano Suster^{9,10}, Koichi Kawakami¹⁰, Joachim Wittbrodt⁴, Herwig Baier^{5,11}, Filippo Del Bene^{1,2,3*}

¹Institut Curie, Centre de Recherche, Paris, France; ²CNRS UMR 3215, Paris, France; ³INSERM U934, Paris, France; ⁴Centre for Organismal Studies, University of Heidelberg, Heidelberg, Germany; ⁵Department of Physiology, University of California San Francisco, San Francisco, United States; ⁶Department of Chemistry, University of California, Berkeley, Berkeley, United States; ⁷Museum National d'Histoire naturelle, Inserm U 1154, CNRS, UMR 7196, Museum National d'Histoire Naturelle, Paris, France; ⁸Institut du Cerveau et de la Moelle épinière, ICM, Inserm U 1127, CNRS, UMR 7225, Sorbonne Universités, UPMC University Paris 6, Paris, France; ⁹Neural Circuits and Behaviour Group, Uni Research AS High Technology Centre, Bergen, Norway; ¹⁰Division of Molecular and Developmental Biology, National Institute of Genetics, Shizuoka, Japan; ¹¹Department Genes–Circuits–Behavior, Max Planck Institute of Neurobiology, Center for Integrated Protein Science Munich (CIPSM), Martinsried, Germany

À

RESEARCH ARTICLE

*For correspondence: thomas.auer@curie.fr (TOA); filippo.delbene@curie.fr (FDB)

†These authors contributed equally to this work

Competing interests: The authors declare that no competing interests exist.


Funding: See page 21

Received: 06 October 2014

Accepted: 18 May 2015

Published: 15 June 2015

Reviewing editor: Graeme W Davis, University of California, San Francisco, United States

 Copyright Auer et al. This article is distributed under the terms of the [Creative Commons Attribution License](https://creativecommons.org/licenses/by/4.0/), which permits unrestricted use and redistribution provided that the original author and source are credited.

Abstract Development and function of highly polarized cells such as neurons depend on microtubule-associated intracellular transport, but little is known about contributions of specific molecular motors to the establishment of synaptic connections. In this study, we investigated the function of the Kinesin I heavy chain Kif5aa during retinotectal circuit formation in zebrafish. Targeted disruption of Kif5aa does not affect retinal ganglion cell differentiation, and retinal axons reach their topographically correct targets in the tectum, albeit with a delay. In vivo dynamic imaging showed that anterograde transport of mitochondria is impaired, as is synaptic transmission. Strikingly, disruption of presynaptic activity elicits upregulation of Neurotrophin-3 (Ntf3) in postsynaptic tectal cells. This in turn promotes exuberant branching of retinal axons by signaling through the TrkC receptor (Ntrk3). Thus, our study has uncovered an activity-dependent, retrograde signaling pathway that homeostatically controls axonal branching.

DOI: [10.7554/eLife.05061.001](https://doi.org/10.7554/eLife.05061.001)

Introduction

Intracellular transport is an essential process in cell growth, maintenance, and inter- and intracellular signaling. This is especially apparent in highly polarized cells like neurons that are composed of complex dendrites and a long axon responsible for impulse propagation. Most of the proteins, mRNAs, and organelles required for cellular growth and function are produced in the cell body and must, therefore, be moved down the axon to the synaptic terminals. Microtubules serve as main longitudinal cytoskeletal tracks in axons, and it is well established that microtubule stabilization is a landmark of early axonal development that is sufficient to induce axon formation in vivo. Besides, microtubule stabilization alone can even lead to the transformation of mature dendrites into axons in

eLife digest Different regions of a neuron have distinct structures and roles. For example, each neuron has a cable-like structure called the axon that extends out of the body of the cell and carries electrical signals away from the cell body. To pass these messages on to neighboring cells, branches on the axon form connections called synapses with other neurons.

The axon lacks most of the cellular machinery needed to make proteins and other molecules that the cell needs to work correctly. Therefore, neurons must transport these materials from the cell body—where they are produced—down to the end of the axon. Specialized proteins called molecular motors carry this cargo down the axon along ‘tracks’ composed of filaments called microtubules. Auer, Xiao et al. have now used genetic techniques to disrupt the gene that encodes an important molecular motor, called Kif5A, in developing zebrafish larvae. The effects of this manipulation on the development of the zebrafish’s visual system were then examined.

When zebrafish are a few days old, neurons in the retina—the structure at the back of the eye that responds to light—extend axons into a region of the brain called the tectum. The formation of synapses between cells in the retina and the tectum provides a pathway that enables information to travel from the eye to the brain. Auer, Xiao et al. found that in larvae that lack Kif5A, axons from the retina enter the brain about a day later than they do in normal larvae. However, when these mutant axons arrive, they produce large numbers of branches, each with the potential to form multiple synapses with cells in the tectum. However, none of the resulting synapses appear to respond to visual stimuli, which is consistent with the fact that Kif5A mutant larvae are blind.

Experiments to identify what triggers the excessive branching of retinal axons revealed that the mutant fish had elevated levels of a growth-promoting protein called neurotrophin-3 in cells in the tectum. This increased production of neurotrophin-3 was also observed when neuronal activity was blocked, for example by toxins. The lack of neuronal activity in retinal axons therefore seems to increase the production of neurotrophin-3, which in turn stimulates axonal branching. Future experiments could investigate the molecular signal that drives this increased production of neurotrophin-3, and how this is regulated during normal neuronal development.

DOI: [10.7554/eLife.05061.002](https://doi.org/10.7554/eLife.05061.002)

differentiated neurons (Gomis-Ruth et al., 2008; Witte and Bradke, 2008; Witte et al., 2008). Along the axonal microtubule cytoskeleton molecular motors of the kinesin and dynein superfamily act as main transport molecules (Hirokawa, 1998; Karki and Holzbaur, 1999; Vale, 2003). Although it is well established that anterograde molecular motors are essential for synapse generation and function (Okada et al., 1995), little is known about their exact role in neural circuit establishment in vivo.

Of the kinesin superfamily, which comprises 45 members in mammals (Miki et al., 2001) and many more in zebrafish, the kinesin I subclass plays an especially prominent role in neuronal function. The kinesin motors mediate the plus end directed transport of cargo proteins along microtubules and are composed of two identical heavy chains and two identical light chains (Hirokawa et al., 2010). In the mammalian genome, three kinesin I heavy chain genes are present: Kif5A, Kif5B, and Kif5C. While Kif5B is ubiquitously expressed, Kif5A and Kif5C are neuron-specific (Xia et al., 1998). Their cargoes include voltage-gated potassium channels, AMPA receptor GluR2, GABAA receptors, sodium channels, neurofilaments, and mitochondria (Rivera et al., 2007; Uchida et al., 2009; Twelvetrees et al., 2010; Karle et al., 2012; Su et al., 2013; Barry et al., 2014). In humans, Kif5A mutations have been implicated in a heterogenous group of neurodegenerative disorders, including a form of Hereditary Spastic Paraplegia characterized by slowly progressive lower limb paralysis (Goldstein, 2001) and Charcot Marie Tooth Type 2, a peripheral axonal neuropathy (Crimella et al., 2012).

In this study, we have taken a combined genetic, molecular biological, and in vivo imaging approach in developing zebrafish larvae to investigate the role of anterograde intracellular transport in the development of connections between retina and tectum. By TALEN-mediated gene disruption, we generated a kif5aa loss-of-function allele and could show that kif5aa mutant fish display a de-synchronisation of retinal axon and tectal growth. A delay in tectal innervation by mutant retinal ganglion cell (RGC) axons is followed by a period of exuberant branching, resulting in enlarged axonal arbors. GCaMP imaging revealed that kif5aa mutant RGCs do not transmit signals from the retina to their postsynaptic partner cells. Utilizing two additional zebrafish mutant lines with defects in RGC

formation or function, *lakritz* (Kay et al., 2001) and *blumenkohl* (Smear et al., 2007), or specific silencing of RGCs by expression of botulinum toxin light chain B (BoTxLCB), we show that in all four cases the reduction of presynaptic activity leads to increased expression of neurotrophic factor 3 (Ntf3). The overabundance of this neurotrophin causes excessive branching by RGC axons. Thus, a defect in *Kif5aa*-mediated axonal transport has unmasked a homeostatic mechanism that adjusts axon arbor growth to levels of synaptic activity and depends on Ntf3 signaling.

Results

Generation of *Kif5aa* loss-of-function alleles by TALEN mediated gene targeting

To investigate the role of axonal transport in visual-system development, we generated a series of insertion and deletion (indel) mutations in the open reading frame (ORF) of the zebrafish anterograde motor protein *Kif5aa* by targeted gene disruption using transcription activator like nucleases (TALENs). Subsequently, we isolated two alleles with a 10 base pair (bp) and 13 bp deletion, respectively (Figure 1A), both resulting in a frameshift in the ORF from amino acid (aa) 122 onwards. This frameshift leads to a premature stop codon at position 162 of 1033aa (*kif5aa*^{*162}) of the wild-type full-length protein (Figure 1A). In situ hybridization showed a strong expression of *kif5aa* in RGCs. In contrast, *kif5aa* mutant mRNA is dramatically down regulated in embryos starting from 24 hours post fertilization (hpf) onwards, probably by nonsense-mediated decay (Figure 1B). By quantitative reverse transcription PCR (qRT-PCR) (Figure 1C), we could see a 47% decrease of *kif5aa* transcript levels in mutant embryos compared to controls. Both alleles were not complementing each other, and the mutant phenotype co-segregated with the TALEN-induced mutation over three consecutive generations. This indicates that the genomic targeting was specific and argues for the absence of off-target effects of the TALEN pair used.

Kif5aa mutant embryos lack visual responses and die at a larval stage

In a clutch of 5 day post-fertilization (dpf) zebrafish larvae, derived from a cross of two heterozygous carriers of the *kif5aa*^{*162} allele, 25% of the larvae exhibited a dark coloration in comparison to their wild-type siblings (Figure 1D), indicating that the mutation is recessive, completely penetrant and results in a failure to adapt to a light background by melanosome re-distribution. This phenotype is frequently observed in visually defective mutants, specifically in those with RGC impairments (Neuhauss et al., 1999; Muto et al., 2005). For example, the *lakritz* (Kay et al., 2001) and the *blumenkohl* (Smear et al., 2007) mutations affect both vision and are darkly pigmented (Figure 1—figure supplement 1A). The former represents a mutation in the basic helix-loop-helix transcription factor atonal homolog 7 (*atoh7*), which is required for RGC fate specification (Kay et al., 2001). Loss of *Atoh7* in zebrafish leads to a complete absence of RGCs in the retina and consequently no functional connections between the retina and other brain areas are established. Nevertheless, as *Atoh7* is solely expressed in the retina, no further developmental defects are described and *lakritz* mutant fish develop normally apart from their complete blindness (Kay et al., 2001). *Blumenkohl* mutants fail to produce a functional vesicular glutamate transporter, *vglut2a*, the main vesicular glutamate transporter expressed in zebrafish RGCs. The lack of functional *Vglut2a* leads to reduced synaptic transmission between the retina and the optic tectum. Furthermore, it was described that RGC axons consequently develop increased axonal arbors and show aberrant branching upon innervation of the optic tectum (Figure 1—figure supplement 1A,C).

To test visual system function in *kif5aa* mutant larvae, we employed the optokinetic response (OKR) to a moving grating as a sensitive and quantifiable indicator of visual functions in zebrafish (Brockerhoff et al., 1995). We found that the OKR was absent in *kif5aa* mutants ($n = 6$), while it was present in all wild-type fish examined ($n = 6$) (Figure 1—figure supplement 1D). This suggests that the disruption of *kif5aa* causes blindness. Unlike *lakritz* and *blumenkohl*, which are viable, *kif5aa* mutants fail to inflate their swim bladder (Figure 1E) and die around 10 days post fertilization (dpf).

As a dynamic interaction between actin- and tubulin-based motility controls melanosome transport within melanocytes (Evans et al., 2014), we wanted to rule out the possibility that the dark pigmentation is caused by a melanophore-autonomous defect. *Kif5aa* mutant embryos were treated with norepinephrin resulting in aggregation of melanosomes and consecutive re-expansion upon washing out of the drug ([Wagle et al., 2011], Figure 1—figure supplement 1B). Similar results were

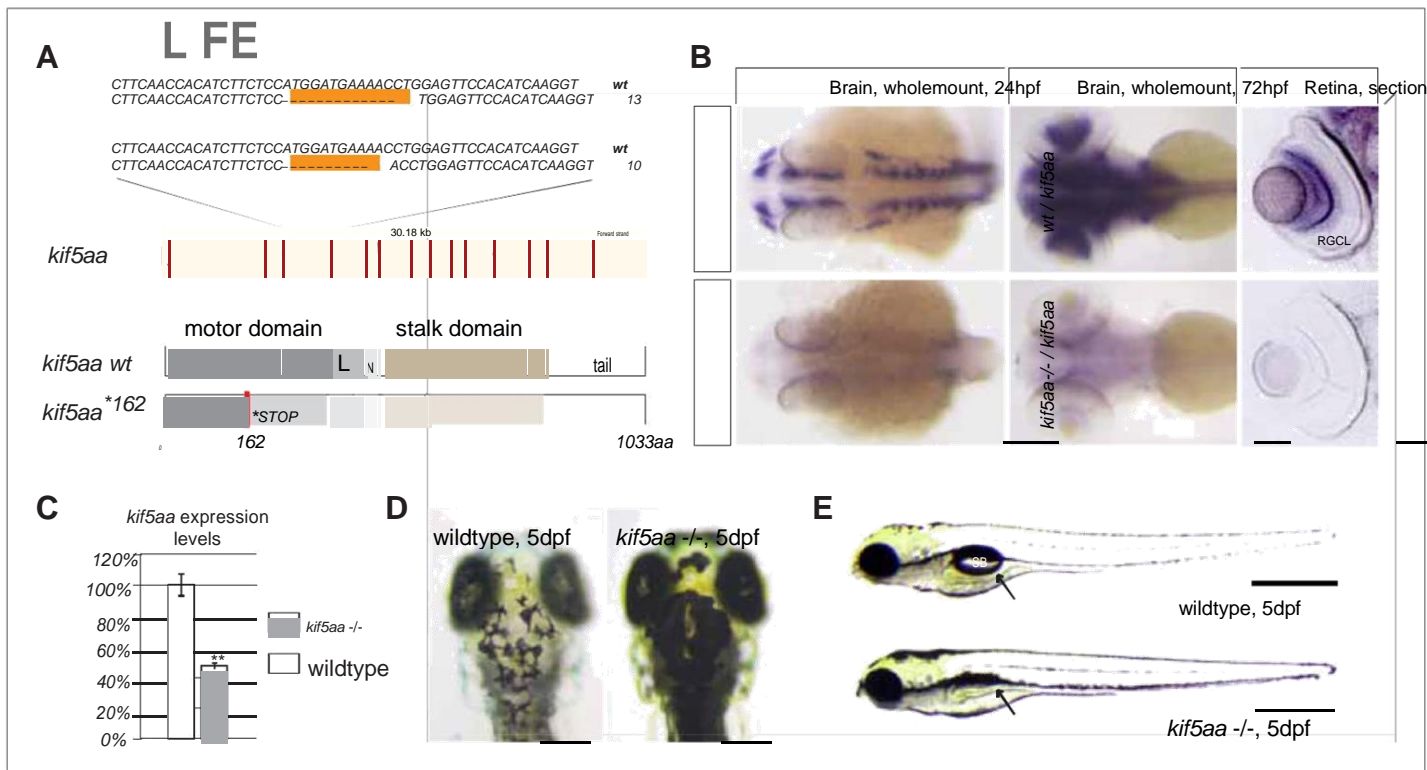


Figure 1. Generation of loss-of-function alleles of the anterograde motor protein Kif5aa. (A) Employing TALENs targeting exon4 of the *kif5aa* open reading frame, we generated two loss-of-function alleles with a 10 bp and 13 bp deletion, respectively. These result in a frameshift at amino acid 122 and a premature stop codon after 162 of 1033aas within the motor domain of Kif5aa. L = linker region, N = neck region. (B) In situ hybridization shows a substantial downregulation of *kif5aa* mRNA in 24 hpf and 72 hpf old embryos. Scale bars (from left to right) = 150 μ m, 100 μ m, 50 μ m. RGCL = Retinal Ganglion Cell layer. (C) Quantitative reverse transcription PCR confirms that only 47% of wild-type *kif5aa* mRNA expression levels are reached in homozygote mutant embryos at 4 dpf ($p < 0.01$). (D) Kif5aa mutant embryos show expanded melanosomes within their melanocytes and appear dark compared to wild-type embryos. Scale bars = 200 μ m. (E) They fail to inflate their swim bladder and die 10 days post fertilization. Scale bars = 400 μ m. Arrow: pointing at the respective location of the swim bladder. SB = swim bladder.

DOI: [10.7554/eLife.05061.003](https://doi.org/10.7554/eLife.05061.003)

The following figure supplement is available for figure 1:

Figure supplement 1. Melanosomes transport is not abolished in *kif5aa* mutants but they show no optokinetic response. DOI: [10.7554/eLife.05061.004](https://doi.org/10.7554/eLife.05061.004)

obtained for *lakritz* and *blumenkohl* (Figure 1—figure supplement 1A). This indicates that melanosome transport inside melanocytes in both antero- and retrograde direction is not affected in *kif5aa* mutant embryos.

Patterning of the retina, formation of the optic chiasm, and retinotopic mapping appear normal in *kif5aa* mutant embryos

To examine if visual system defects were caused by retinal neurogenesis or patterning defects during development, we compared the expression of known marker genes between wild-type and *kif5aa* deficient embryos. In mutant embryos, we could not observe alterations neither in the onset of retinal neurogenesis (characterized by sonic hedgehog expression [Shkumatava et al., 2004]) nor in the later specification of RGCs or other retinal cell types (Figure 2—figure supplement 1). Choroid fissure and optic stalk formation, as well as rostral-caudal patterning, were normal as revealed by the expression of *pax2.1* and *tag-1*, respectively. Further, cell type specific marker analysis revealed that all major retinal cell types were present and the layering of the retina was not affected in *kif5aa* mutant retinæ (Figure 2—figure supplement 1).

As retinal morphology and cellular composition were not altered by the loss of *kif5aa* function, we decided to analyze the outgrowth of RGC axons from the retina and their retinotopic mapping onto

the optic tectum. To this purpose, we introduced the transgenic line Tg(pou4f3:mGFP) (Xiao et al., 2005), which labels a subpopulation of RGCs, into the *kif5aa*^{*162} mutant background and imaged optic nerve outgrowth and optic chiasm formation at 48 hpf. No misrouting of RGCs to the ipsilateral side could be observed, and the optic chiasm was correctly established at the right developmental time (Figure 2A). To confirm that pathfinding was unaffected, we used Zn5 antibody staining to bulk-label outgrowing RGC axons (Fashena and Westerfield, 1999) (Figure 2A). Axon tracing at later stages of development, following injection of the two lipophilic dyes DiO and Dil (Baier et al., 1996) into opposite quadrants of the contralateral eye, revealed that the retinotectal projection was correctly patterned in mutant embryos (Figure 2B) and no misrouting to the ipsilateral hemisphere occurred.

Axons enter the tectum with a delay, reminiscent of the previously identified vertigo mutant

To gain deeper insights into the phenotype of single RGCs, we made use of the Tg(BGUG) transgenic line (Xiao and Baier, 2007). The BGUG (Brn3C [also known as pou4f3]:Gal4; UAS:mGFP) transgene marks RGCs projecting to the SO (stratum opticum) and SFGS (stratum fibrosum et griseum superficiale) layers of the optic tectum. Probably due to position-effect variegation of the transgene, a stochastic subset of one to ten RGCs per retina is labeled with membrane-bound GFP, which allows the imaging of RGC trajectories in the living or fixed fish brain. By *in vivo* imaging, we thus followed the growth behavior of single RGC axons over consecutive days. To guarantee comparability between RGC axons, we analyzed only RGC axons growing into the SFGS layer of the optic tectum at a central

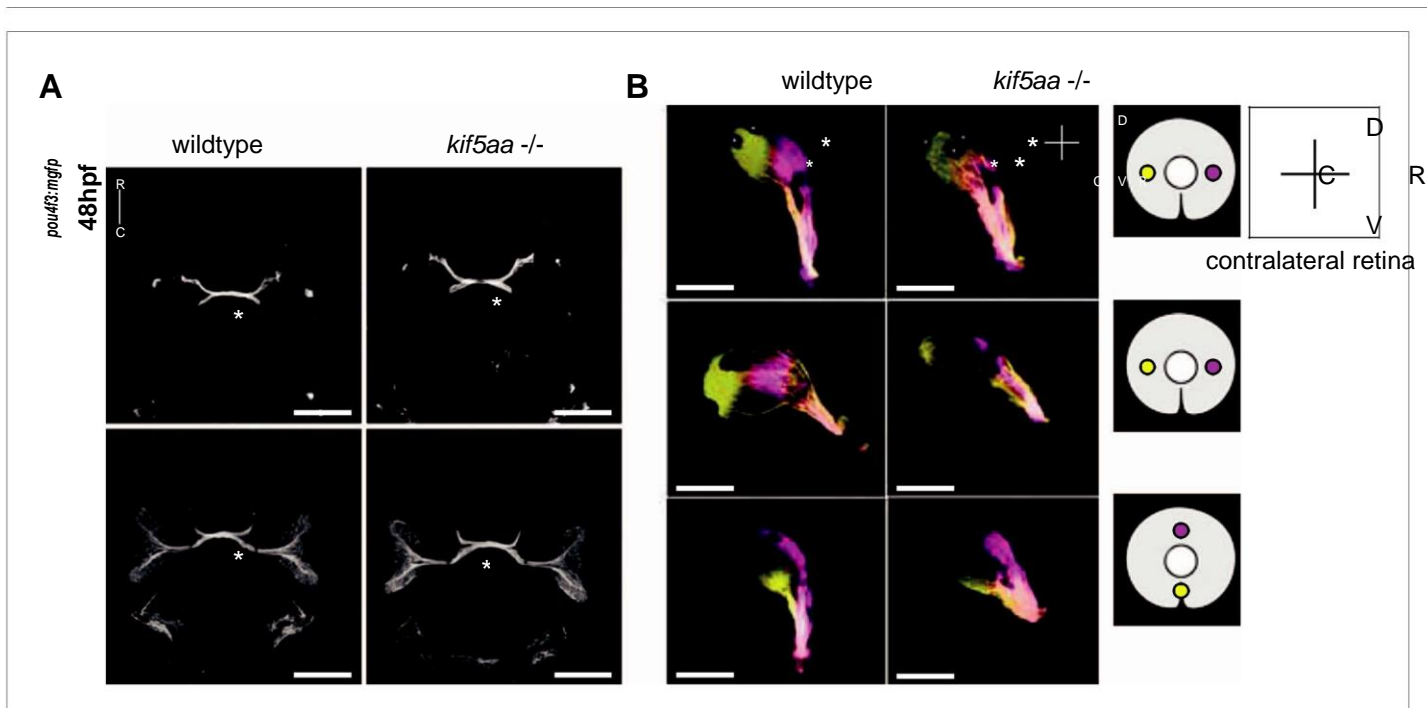


Figure 2. Outgrowth of the optic nerve and retinotopic mapping is normal in *kif5aa* mutants. (A) Confocal imaging of the Tg(pou4f3:mGFP) transgene, labeling a subpopulation of Retinal Ganglion Cells (RGCs) with membrane bound GFP, at 48 hpf reveals that outgrowth of the optic nerve formed by RGC axons from the retina is not affected by the *kif5aa* mutation. Immunostaining against the Zn5 antigen (DM- GRASP/neuroilin present within the visual system only on RGCs [Laessing and Stuermer, 1996; Fashena and Westerfield, 1999]) confirms that optic chiasm formation is normal (marked with an asterisk). No pathfinding errors occur at this level of axonal growth. Scale bars = 200 μ m. Embryos facing upwards. R = rostral, C = caudal. (B) Injections of the lipophilic dyes Dil and DiO in different quadrants of the contralateral retina (depicted in the right panel) show that retinotopic mapping to the optic tectum is performed in the correct manner. Asterisks = pigment cells in the skin. D = dorsal, V = ventral, R = rostral, C = caudal. No misrouting of RGC axons to the ipsilateral tectum was observed (data not shown). Scale bars = 150 μ m.

DOI: [10.7554/eLife.05061.005](https://doi.org/10.7554/eLife.05061.005)

The following figure supplement is available for figure 2:

Figure supplement 1. Patterning of the mutant retina and neurogenesis is not affected in mutants.

DOI: [10.7554/eLife.05061.006](https://doi.org/10.7554/eLife.05061.006)

position on the rostral-caudal axis. While wild-type axons reach the tectal neuropil at 72 hpf and start forming a complex axonal arbor, axons of *kif5aa* mutant RGCs showed a delayed ingrowth into the target tissue (Figure 3A). This phenotype was confirmed by analyzing a larger RGC population, which was labeled by Dil injections into quadrants of the contralateral retina (Figure 3A).

A strikingly similar phenotype was reported in a previously published forward genetic screen for defects in the visual system in the *vertigo*^{S1614} mutant without further in-depth characterization of this mutant line nor identification of the causal gene (Xiao et al., 2005). Our genetic linkage analysis confirmed that the ethylnitrosourea-induced mutation of the *vertigo*^{S1614} allele is located at linkage group 9 of the zebrafish genome (Figure 3—figure supplement 1). Utilizing the newly generated *kif5aa*^{*162} allele we could confirm by complementation crosses that *vertigo*^{S1614} represents a loss-of-function allele of *kif5aa*. Although sequencing of the genome has not identified a telltale mutation of *kif5aa* coding sequence or its flanking regulatory regions in *vertigo* mutants, judging by its penetrance and expressivity, we expect the *kif5aa*^{S1614} mutation to be a strong hypomorph or null allele. Furthermore, our analysis did not reveal any phenotypic difference between the different alleles and for our subsequent analysis we used *kif5aa*^{*162}.

Axons of *kif5aa* mutants exhibit increased filopodial extensions and branch excessively

Wild-type axons continually expand their arbors during lifelong growth of the tectum. After 5 dpf, however, branching activity noticeably subsides, and axons maintain their complexity over the following days (Meyer and Smith, 2006) (Figure 3B). This phase of relative stability coincides with the consolidation of synaptic connections with tectal dendrites in the neuropil region (Nevin et al., 2010). In *kif5aa* mutant axons, the observed delay of ingrowth into the tectum is followed by a period of highly active growth of the axonal arbor after 5 dpf, at a stage when wild-type axons are comparatively stable. We investigated the underlying branching dynamics by multi-day single axon imaging. Between 5 and 7 dpf, mutant axons added branches at about double the wild-type rate (Figure 3B,C). Mutant axons also showed markedly increased numbers of active filopodia either being retracted or newly formed at any time point analyzed, as observed in 10 min timelapse movies (Figure 3B,D). Together, these findings suggest that, perhaps counterintuitively, absence of the motor protein Kif5aa stimulates growth of the axon arbor and maintains high filopodia activity.

Calcium imaging reveals the disruption of presynaptic activity in *kif5aa* mutant RGCs

The loss of optokinetic response of *kif5aa* mutants raises the question on which level of the visual pathway the visual information processing is perturbed. To understand this better, we used genetically encoded Ca^{2+} sensors that were differentially expressed in two different neuronal types of the visual system, namely in RGCs and tectal periventricular neurons (PVNs) (Del Bene et al., 2010; Nikolaou et al., 2012; Hunter et al., 2013). First, we probed the overall activity of the larva's visual system from 5 to 7 dpf in response to defined visual stimuli by using the Tg(HuC:GCaMP5G) transgenic line, in which among other neuron types, all RGCs and PVNs are labeled (Ahrens et al., 2013) (Figure 4B, left). We did observe clear stimulus-evoked Ca^{2+} transients in the wild-type PVN layer and the tectal neuropil (the later contains both PVNs dendritic and RGC axonal arbors) in response to a bar (Nikolaou et al., 2012) moving in a caudal-to-rostral direction (Figure 4C, Video 1) across the larva's visual field. This response was almost completely absent in *kif5aa* mutants at 5 dpf (Figure 4C, Figure 4—figure supplement 1, Video 2). In addition, also no response was detected in older larvae (7 dpf), arguing against a delayed onset of activity in mutants, as could have been speculated based on the observed developmental delay of RGC ingrowth (Figure 3). Besides bars running caudal-to-rostrally, we also tested bar stimuli running in the opposite direction, bars moving in different orientations of 45° steps across the visual field as well as looming stimuli. In neither of these, *kif5aa* mutants showed a response comparable to their wild-type siblings at any developmental stage between 5 dpf and 7 dpf (data not shown). We next investigated whether this loss of Ca^{2+} responses in the tectum was due to a presynaptic defect in RGC axons. For this, the same stimulation paradigms were employed in compound transgenic fish carrying Tg(Isl2b:Gal4) and Tg(UAS:GCaMP3), which express the Ca^{2+} sensor GCaMP3 in all or nearly all RGCs (Ben Fredj et al., 2010; Warp et al., 2012). Mutant RGC axons in the tectal neuropil remained unresponsive to

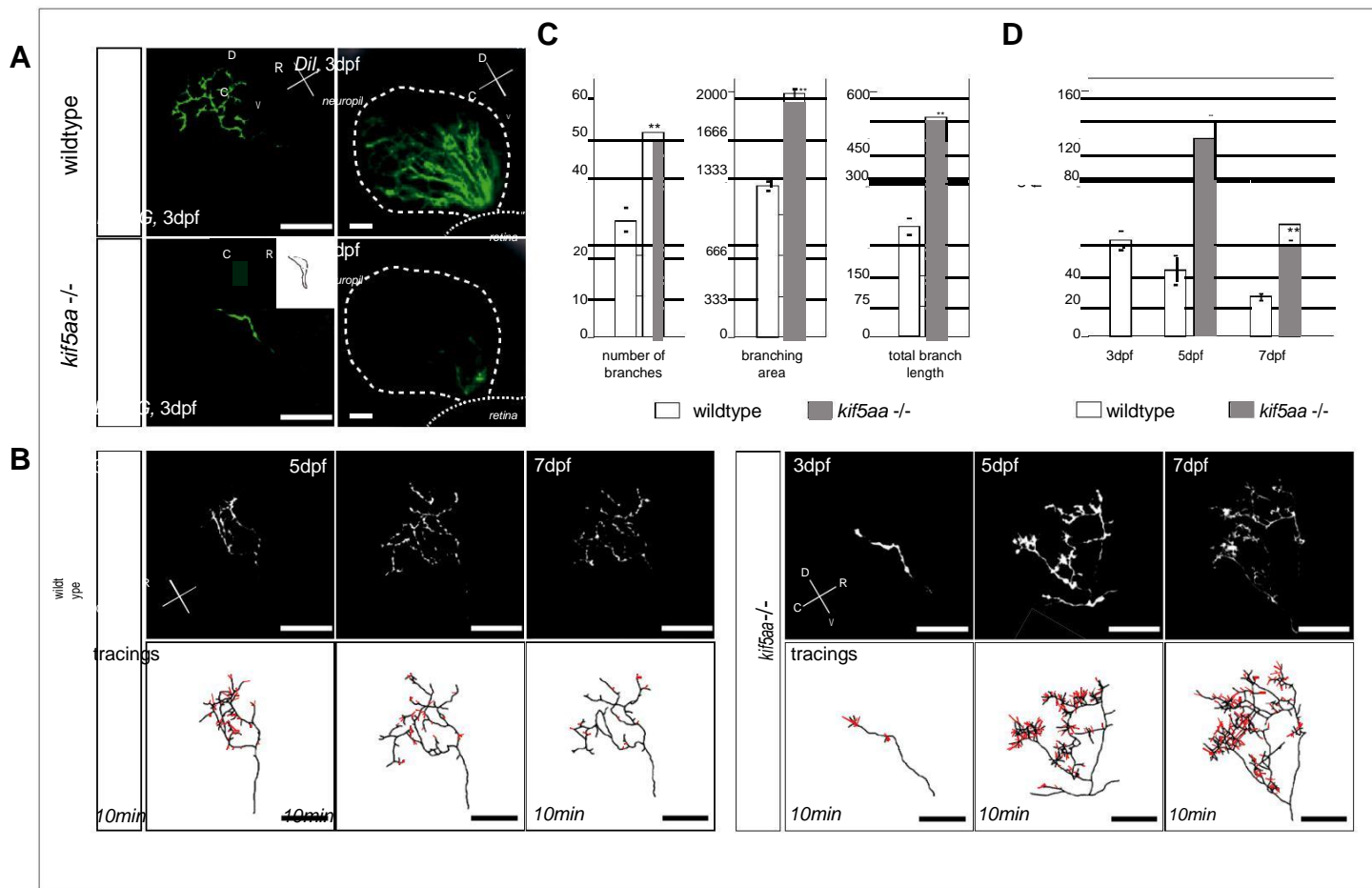


Figure 3. RGC axons in *kif5aa* mutants show a delayed ingrowth into the optic tectum and grow larger arbors at later stages. (A) Single membrane-GFP expressing RGC axons from the Tg(BGUG) transgene (left panel) and Dil injections into the contralateral retina of 3 dpf old wild-type and *kif5aa* mutant embryos (right panel) illustrate the delay of tectal innervation in mutants. Scale bars = 20 μm. The schematic in the lower left panel illustrates the perspective chosen for image acquisition (indicated by an arrow). D = dorsal, V = ventral, R = rostral, C = caudal. (B) Upper panel, left: Axonal arbor of a single wild-type RGC at 3, 5, and 7 dpf. Lower panel, left: Tracings of an axonal arbor at time point zero. In red: Overlay of filopodia formed and retracted within 10 min (1 frame/2 min). Scale bars = 20 μm. Upper panel, right: Axonal arbor of a single *kif5aa* mutant RGC axonal arbor at 3, 5, and 7 dpf. Lower panel, right: Tracing of an axonal arbor at time point zero. In red: Overlay of filopodia formed and retracted within 10 min (1 frame/2 min). Scale bars = 20 μm. (C) *Kif5aa* mutant RGC axons grow significantly more branches, cover a larger area of the optic tectum with their arbors (in μm²) and grow longer arbors (in μm) than wild-type cells at 7 dpf ($n = 10$, $p < 0.01$). Scale bars = 20 μm. For quantification, only branches stable within 10 min of image acquisition were selected. (D) Quantification of filopodia numbers formed and retracted within 10 min per cell at 3, 5, and 7 dpf. While wild-type RGC arbors form most filopodia at 3 dpf and reduce this rate constantly until 7 dpf, *kif5aa* mutant RGC axons grow almost three times more filopodia at 5 dpf ($n = 4$, $p < 0.01$). At 7 dpf, the rate is still more as double as high as for their wild-type counterparts ($n = 4$, $p < 0.01$). DOI: 10.7554/eLife.05061.007

The following figure supplement is available for figure 3:

Figure supplement 1. Mapping of the *vertigo*^{S1614} locus by genetic linkage analysis. DOI: 10.7554/eLife.05061.008

visual stimulation, whereas wild-type axons were robustly activated (Figure 4D). These data provide an explanation for the behavioral blindness of *kif5aa* mutant larvae and indicate that the *Kif5aa* motor is required for proper synaptic transmission from RGC axon terminals to tectal dendrites.

Kif5aa mutant RGCs form presynaptic sites but are depleted of mitochondria

As loss of synaptic activity in RGCs might be caused by a failure in synapse formation, we monitored synapse distribution and transport of synaptic vesicles in RGC axons *in vivo*. For this experiment, we

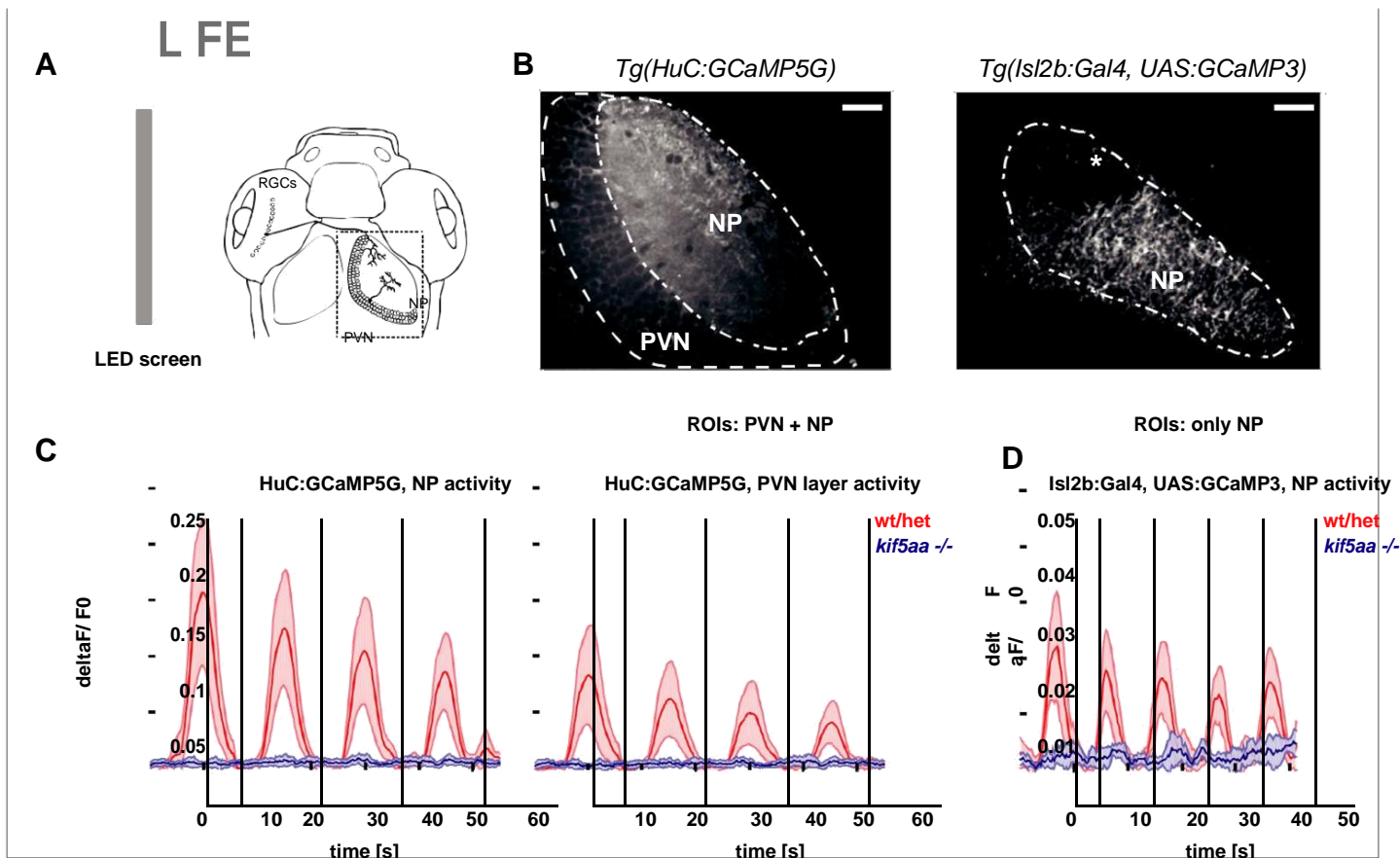


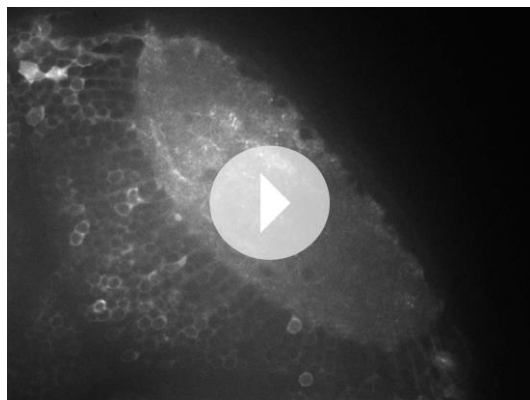
Figure 4. *Kif5aa* mutant larvae show no activity in RGCs and no synaptic transmission to tectal cells. (A) 5–7 dpf larvae were visually stimulated by bars on an LED screen running in caudal-to-rostral direction across the larva's visual field. Wild-type and *kif5aa* mutant larvae expressing genetically encoded calcium indicators (GCaMPs) in different subsets of neurons of the visual system were confocally imaged in the tectum contralaterally to the stimulated eye (dashed box inset). RGCs = Retinal Ganglion Cells, PVNs = periventricular neurons, NP = neuropil. (B) The activity of visual system neurons in response to visual stimuli is shown as normalized GCaMP fluorescence intensity changes ($\Delta F/F_0$) over time. GCaMP intensity was averaged over manually determined regions of interest (ROIs) that corresponded to well-distinguishable anatomical regions in the larval tectum, the neuropil (NP) and the periventricular cell bodies area (PVNs). In *Tg(HuC:GCaMP5)* fish (left), GCaMP5 is expressed pan-neuronally, that is, in both neuropil and PVNs, whereas in *Tg(Isl2b:Gal4) × Tg(UAS:GCaMP3)* fish (right), it is expressed in all RGCs and their processes. Scale bars = 20 μm . Asterisk = pigment cell in the skin. (C) Averaged $\Delta F/F_0$ ratio over time in response to a moving bar visual stimulation (black vertical line denotes the time point of the stimulus onset) in fish with pan-neuronal GCaMP5G expression. Four sequential rounds of stimulus presentation and the time-courses of Ca^{2+} -transients in the neuropil ROIs (left panel) and periventricular cell bodies ROIs (right panel) of wild-type/heterozygous (red curve) and *kif5aa* mutant larvae (blue curve) ($n = 7$ each) are shown. Activity in the visual system of *kif5aa* mutants was almost absent between 5 and 7 dpf compared to wild-type larvae. Light red and blue zones indicate the 95% confidence intervals around the averaged $\Delta F/F_0$ curves for each region of interest (NP and PVN), respectively. (D) Averaged $\Delta F/F_0$ ratio over time in response to a moving bar visual stimulation (black vertical line denotes stimulus onset) in fish with GCaMP3 expression in RGC axons. Five sequential rounds of stimulus presentation and time-courses of Ca^{2+} -transients in the neuropil of wild-type/heterozygous (red curve) and *kif5aa* mutant larvae (blue) ($n = 9$ each). RGC arbor activity in *kif5aa* mutants was strongly diminished. Light red and blue zones indicate the 95% confidence intervals around the averaged $\Delta F/F_0$ curves for the neuropil region of interest (NP).

DOI: [10.7554/eLife.05061.009](https://doi.org/10.7554/eLife.05061.009)

The following figure supplement is available for figure 4:

Figure supplement 1. Regression-based analysis of wild-type/heterozygous vs *kif5aa*^{-/-} *Tg(HuC:GCaMP5G)* mutants to a visual stimulus. DOI: [10.7554/eLife.05061.010](https://doi.org/10.7554/eLife.05061.010)

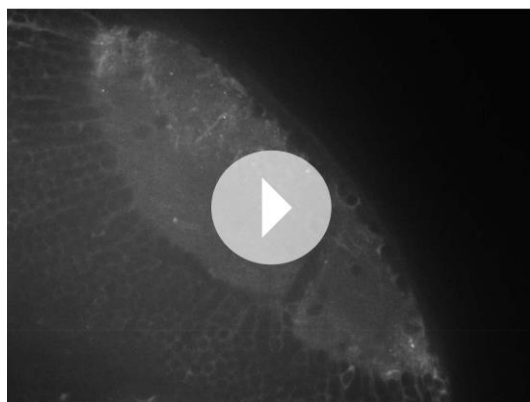
made use of a Synaptophysin-GFP (Syn-GFP) fusion construct, a marker for stable presynaptic sites as well as for motile Synaptophysin-containing clusters (Meyer and Smith, 2006). When co-expressed with a membrane-localized red fluorescent protein (RFPCaax) in single RGCs in wild-type or *kif5aa* mutant embryos (Figure 5A), we observed no difference in distribution of stable presynaptic clusters at 5 and 7 dpf by in vivo imaging (Figure 5B). This indicates that the formation of stable presynaptic clusters is not affected by the loss of *Kif5aa*. Quantification of Synaptophysin-containing vesicle



Video 1. In vivo timelapse imaging of the optic tectum in a Tg(HuC:GCaMP5G) transgenic 5 dpf wild-type fish. A wild-type larva was stimulated with a visual bar running from caudal to rostral through the visual field of the contralateral eye to the imaged optic tectum. Stimulus onset is indicated by a white circle in the top right corner of the image sequence. The movie is accelerated to a framerate of 40 frames/s.

DOI: [10.7554/eLife.05061.011](https://doi.org/10.7554/eLife.05061.011)

chondria within the axon of mutant RGCs compared to wild-type cells (Figure 5C). This is consistent with previous reports showing that mitochondria are transported by Kif5a in other experimental systems (Macaskill et al., 2009; Karle et al., 2012; Chen and Sheng, 2013). We confirmed this result by quantification of the area covered by mitochondria per neuropil area in electron micrographs of transverse section of the tectal neuropil (Figure 5D). At 6 dpf, mutants show a significant depletion of mitochondria from their branched axons (Figure 5E). To test if this mitochondria depletion from the distal axon of RGCs is caused by transport defects of this known cargo of Kif5a, we quantified the



Video 2. In vivo timelapse imaging of the optic tectum in Tg(HuC:GCaMP5G) transgenic 5 dpf kif5aa mutant embryos. A kif5aa mutant larva was stimulated with

a visual bar running from caudal to rostral through the visual field of the contralateral eye to the imaged optic tectum. Stimulus onset is indicated by a white circle in the top right corner of the image sequence. The movie is accelerated to a framerate of 40 frames/s.

DOI: [10.7554/eLife.05061.012](https://doi.org/10.7554/eLife.05061.012)

movements in axonal segments (Figure 5—figure supplement 1, Video 3) did not show a difference in either anterograde or retrograde transport upon loss of kif5aa at 4, 5, and 7 dpf. This is consistent with previous studies showing that Synaptophysin containing vesicles are not transported by Kinesin I (Karle et al., 2012) and furthermore argues against a general loss of vesicle movement in kif5aa mutant RGCs. To distinguish between different sized clusters, we divided vesicles into small (<0.4 μm) and middle-sized to large clusters (>0.4 μm) as defined previously for RGC axons in zebrafish (Meyer and Smith, 2006). Using these different categories, we detected a higher fraction of small, motile clusters in kif5aa mutant cells at 4 and 5 dpf, but not at 7 dpf, most probably reflecting their highly active growth behavior at that stage of development (Figure 5—figure supplement 1C).

In vivo imaging of labeled mitochondria (mitoGFP) and membranes (RFPCaax) in single RGCs in contrast showed a reduction of mito-

transport dynamics of mitochondria within RGC axonal segments (Figure 5—figure supplement 2, Video 4). We did not detect a difference in overall amount of mobile vs stable mitochondria. In mutant cells, though, mitochondria were transported significantly more often in a retro-grade direction than in an anterograde direction (Figure 5—figure supplement 2D). This bias explains the depletion of mitochondria from the tips of kif5aa mutant RGCs. Mitochondria are preferentially localized at active synapses (Oba-shi and Okabe, 2013) and are found in close proximity to stable Synaptophysin-containing clusters in RGC arbors (Figure 5—figure supplement 2A). By co-labeling mitochondria and presynaptic clusters in the same cells in vivo we showed that approximately 40% stable pre-synaptic sites are associated with mitochondria in wild-type and blu-/- RGC axons (Figure 5—figure supplement 2B). We extended and confirmed these data observing mitochondria distribution and presynaptic densities in trigeminal ganglion cell axons (TGCs) (Figure 5—figure supplement 2A,B). In contrast to wild-type cells, in TGCs in kif5aa-/- we observed a marked

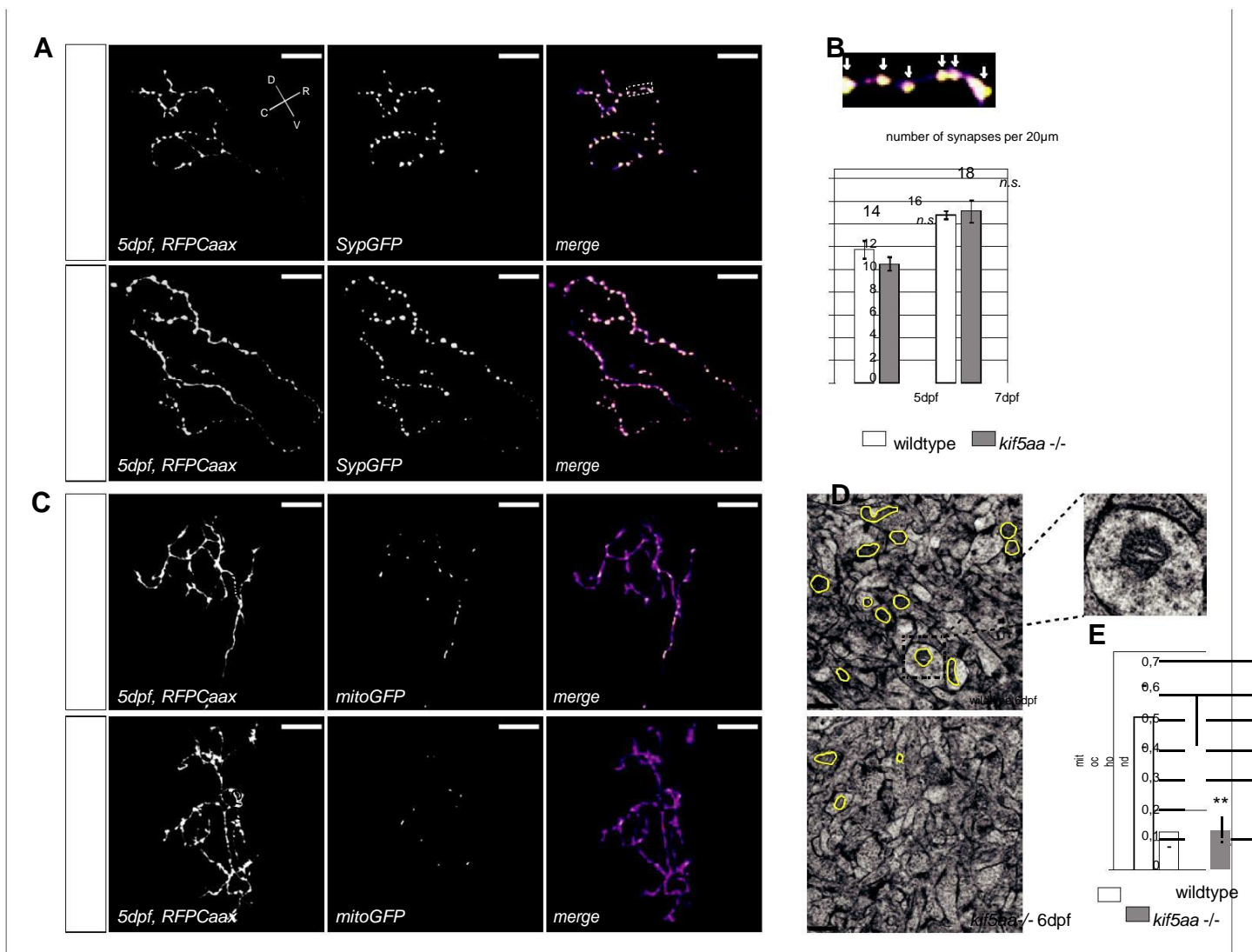


Figure 5. Kif5aa mutant RGC arbors show the same density of presynaptic sites but are depleted of mitochondria. (A) In vivo imaging shows the distribution of presynaptic sites marked by Synaptophysin-GFP (SypGFP) in single kif5aa mutant and wild-type RGC arbors expressing membrane localized RFP (RFPCaax). Upper panel: wild-type cell arbor, lower panel: kif5aa mutant cell arbor. Scale bars = 20 μ m. D = dorsal, V = ventral, R = rostral, C = caudal. (B) Upper panel: Zoom in to an axonal segment indicated in the right panel of (A). Stable presynaptic clusters of SypGFP larger than 0.4 μ m were defined as synapses (white arrows in the upper panel) and synapse density in axonal segments of wild-type and mutant cell arbors does not show a significant difference at 5 and 7 dpf (lower panel). (C) Distribution of mitochondria (labeled by mitoGFP) in single mutant and wild-type RGC arbors expressing membrane localized RFP (RFPCaax) in vivo. Upper panel: wild-type cell arbor, lower panel: kif5aa mutant cell arbor. Mutants RGC cell arbors show substantially less mitochondria. Scale bars = 20 μ m. (D) Transmission electron micrograph of a transvers section of the neuropil containing RGC axonal arbors. Upper panel: wild-type neuropil, lower panel: kif5aa mutant neuropil. In yellow circles: mitochondria. Left panel: Zoom in into a single axonal segment containing a mitochondrion. The kif5aa mutant neuropil contains less mitochondria. Scale bar = 500 nm. (E) Quantification of mitochondria area per neuropil area comparing wild-type and mutant tecta at 6 dpf. Mutant cells contain significantly less mitochondria than wild-type cells ($p < 0.01$).

DOI: [10.7554/eLife.05061.013](https://doi.org/10.7554/eLife.05061.013)

The following figure supplements are available for figure 5:

Figure supplement 1. Analysis of transport dynamics of synaptic vesicles in wild-type and kif5aa mutant cells during visual system development. DOI: [10.7554/eLife.05061.014](https://doi.org/10.7554/eLife.05061.014)

Figure supplement 2. Analysis of mitochondria localization and transport dynamics in wildtype and kif5aa mutant RGC arbors. DOI: [10.7554/eLife.05061.015](https://doi.org/10.7554/eLife.05061.015)

Figure supplement 3. Retinal Ganglion Cells show a normal mitochondria distribution in blumenkohl mutants. DOI: [10.7554/eLife.05061.016](https://doi.org/10.7554/eLife.05061.016)



Video 3. In vivo timelapse imaging of Synaptophysin-GFP containing clusters in RGC axonal segments. Representative RGC axonal segment in a 5 dpf old wild-type larva. SypGFP labels synaptic clusters of different sizes that were grouped in small and middle-sized plus large vesicles. Compare Figure 5—figure supplements 1A,B for grouping and kymogram analysis. DOI: [10.7554/eLife.05061.017](https://doi.org/10.7554/eLife.05061.017)

mitochondria, however, results in a depletion of these organelles from synaptic terminals.

Lack of synaptic input leads to an increased production of neurotrophic factor 3 (Ntf3) in the tectum

We aimed to identify the signal responsible for the observed increased growth of RGC arbors in *kif5aa* mutant tecta. As it was previously shown in the optic tectum of *X. laevis* that Brain-Derived Neurotrophic Factor (BDNF) can promote axonal arborization (Cohen-Cory and Fraser, 1995), we decided to measure the expression levels of this neurotrophic factor in *kif5aa* mutant embryos. In parallel, we performed quantitative reverse transcription PCR of other known members of the neurotrophic factor family, namely neurotrophin 3 (*ntf3*), neurotrophin 4 (*ntf4*), neurotrophin 7 (*ntf7*), and nerve growth factor (*ngf*) present in the zebrafish genome (Heinrich and Lum, 2000). Comparing 4 dpf old homozygous *kif5aa* mutants to their siblings, we detected a significant upregulation of *ntf3* in mutants to up to 160% of its normal expression level in wild-type embryos, while the levels of *bdnf*, *ngf*, *ntf4*, and *ntf7* were not significantly altered (Figure 6A). By in situ hybridization with an *ntf3* antisense probe, we could furthermore see an increased staining intensity in mutant tecta compared to their siblings (Figure 6B).

For further validation of these results, we performed Western blotting analysis using an antibody targeting the human orthologue of Ntf3. This antibody recognizes the zebrafish Ntf3 protein. We could demonstrate cross-reactivity by overexpressing a construct carrying the zebrafish *ntf3* cDNA followed by an E2A sequence allowing multicistronic expression (Szymczak et al., 2004) of *ntf3* and a RFP reporter gene from the same cDNA (Figure 6C). This experiment showed that *kif5aa* mutant embryos produced significantly more Ntf3 protein than their siblings.

To see if Ntf3 upregulation was a common feature in mutants with defective retinotectal synaptic transmission, we investigated *lakritz* mutants, which lack all RGCs and *blumenkohl*, in which RGCs show impaired glutamate secretion into the synaptic cleft. Ntf3 protein was increased in the tecta of all three mutant lines in which presynaptic input to the tectum was abolished or highly reduced (Figure 6D). To directly test the causality link between the lack of presynaptic input and upregulation of Ntf3 in the optic tectum, we silenced the neuronal activity of RGCs by expressing a UAS:BoTxLCB-



Video 4. In vivo timelapse imaging of mitochondria in RGC axonal segments. Representative RGC axonal segment in a 5 dpf old wild-type larva. Compare Figure 5—figure supplement 2B for kymogram analysis of mitochondria movements. DOI: [10.7554/eLife.05061.018](https://doi.org/10.7554/eLife.05061.018)

decrease of presynaptic densities located in close proximity of mitochondria. This observation is consistent with a recent study in zebrafish reporting a reduced number of mitochondria in periph-

eral cutaneous axon arbors in *kif5aa* mutant zebrafish embryos (Campbell et al., 2014) without affecting the distribution of presynaptic densities.

Taken together, these experiments show that *kif5aa* mutant RGCs form presynaptic sites at the same density as wild-type cells and transport Synaptophysin-containing clusters at the same rate and direction as wild-type. A detectable reduction in the relative anterograde transport of

GFP construct in *Islet2b:Gal4* zebrafish larvae. BoTx has been shown to specifically block synaptic vesicle release (Brunger et al., 2008) and its injection has been used successfully in zebrafish embryos to silence neuronal activity (Nevin et al., 2008). Similar to what previously observed in *kif5aa*, *lak*, and *blu* mutants, silencing of RGCs via BoTx expression leads to melanosomes expansion and failure to adapt to a light back-ground (Figure 6—figure supplement 1A). Both, via qRT-PCR and Western blotting analysis we detected an upregulation of Ntf3 in these trans-genic animals showing that, like in the previously described mutants, lack of RGCs presynaptic activity per se is sufficient to cause Ntf3

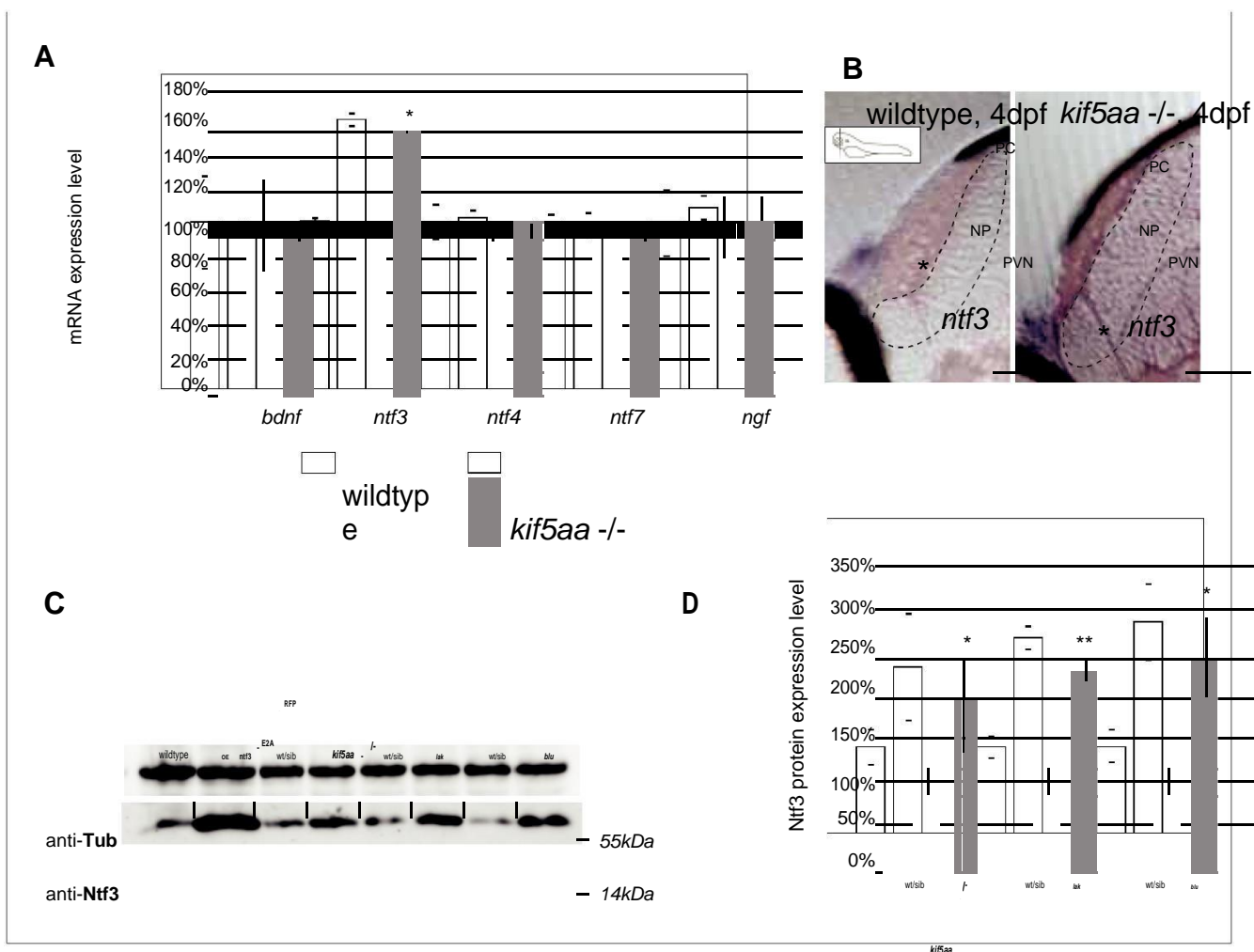


Figure 6. Expression of the neurotrophic factor neurotrophin 3 in visually impaired mutants. (A) Relative expression levels of *bdnf*, *ntf3*, *ntf4*, *ntf7*, and *ngf* in 4 dpf old wild-type and *kif5aa* mutant embryos. *ntf3* is upregulated to 160% of wild-type expression levels ($p < 0.05$) while all other neurotrophic factors show the same expression levels between wild-type and mutant embryos. (B) Transversal sections through the tectum after in situ hybridization with an *ntf3* specific antisense probe detect higher expression levels of *ntf3* in tecta of *kif5aa*. Scale bars = 25 μ m. PC = pigment cell, NP = neuropil, PVN = periventricular neurons. Asterisk = strong *ntf3* signal in the otic vesicle. (C) Confirmation of Ntf3 overexpression by Western blotting in 4 dpf old embryos. To show the specificity of the antibody, we generated a Ntf3 overexpression construct (UAS:*ntf3*-E2A-RFP). The two visually impaired mutant lines *lakritz* and *blumenkohl* also show a substantial upregulation of *ntf3* expression levels. (D) Quantification of Ntf3 protein expression levels based on Western blotting data in wild-type and visually impaired mutant embryos. All three mutant lines show a substantial upregulation of Ntf3 protein levels.

DOI: 10.7554/eLife.05061.019

The following figure supplement is available for figure 6:

Figure supplement 1. Silencing of all Retinal Ganglion Cells by BoTx expression leads to Ntf3 upregulation.

DOI: 10.7554/eLife.05061.020

overexpression (Figure 6—figure supplement 1B,C). These results strongly suggest that lack of presynaptic activity and subsequent overexpression of Ntf3 in the tectum trigger the increased size of axonal branches of RGCs in *kif5aa*, *blumenkohl*, and *lakritz* mutants (see Figure 2, [Smear et al., 2007; Gosse et al., 2008]).

Neurotrophic factor 3 signaling acts on RGC axonal branching

To further test this hypothesis, we designed an experiment to interfere with Ntf3 signaling in RGCs. We generated a kinase-dead, GFP-tagged, dominant-negative version of the zebrafish *ntrk3a* gene orthologous to the gene encoding the TrkC receptor in mammals (*ntrk3adN*-GFP) (Parada et al., 1992). A similar approach was previously shown to efficiently block Ntf3 function in mammalian cells (Tsoulfas et al., 1996; Lin et al., 2000). In zebrafish two TrkC paralogues, *ntrk3a* and *ntrk3b* exist,

which are both expressed in RGCs (Figure 7A). We decided to generate our dominant-negative construct based on the *ntrk3a* coding sequence, which shows a higher degree of conservation (based on amino acid identity and sequence similarity) to the rat TrkC receptor (Martin et al., 1998). Both receptors are predicted to bind to Ntf3 based on binding motif analysis (Martin et al., 1998). Upon overexpression of the truncated *ntrk3adN*-GFP construct in single wild-type RGCs by mosaic DNA expression, we observed a substantial reduction of axon branch length and number of branches at 5 dpf (Figure 7B,E), consistent with a role of Ntrk3 as a branch-promoting receptor.

In addition, *ntrk3adN*-GFP overexpression in single *kif5aa*^{-/-} and *blu*^{-/-} RGCs could abolish the axonal overgrowth normally observed in these mutants as measured by total branch length (Smear et al., 2007) and even reduce the number of branches compared to wild-type cells (Figure 7E).

To analyze the consequence of Ntf3 overexpression, we injected an UAS:Ntf3-E2A-RFP construct into the Tg(gSA2AzGFF49A) (Muto et al., 2013) transgenic line, driving the expression of the transgene in tectal neurons and glia cells from 2 dpf onwards. Thereby, we generated larvae specifically overexpressing Ntf3 in the optic tectum just before innervation by RGC axons. Analyzing the morphology of single RGCs marked by membrane-bound eGFP and growing under these conditions, we confirmed that these cells formed larger axonal arbors than wild-type cells (Figure 7C,E) at 5 and 7 dpf. Taken together, these results strongly support the hypothesis that Ntf3 signaling is a signal promoting RGC arbor growth and branching and that Ntf3 upregulation is responsible for axonal arbor overgrowth when RGC presynaptic activity is impaired.

We next decided to test if the observed increased formation and retraction of filopodia in the axons of *kif5aa* mutant RGCs was directly caused by Ntf3 upregulation. Therefore, we analyzed filopodia dynamics via time-lapse imaging both in *blu*^{-/-} RGCs and in axons growing when Ntf3 was overexpressed in the tectum via our transgenic construct. In both experimental conditions we did not observe any increase in the filopodia dynamics or RGC axons (Figure 7—figure supplement 1A–C), excluding the possibility that Ntf3 overexpression has a direct effect on this process. In addition, we observed that the distribution of mitochondria was not significantly altered in *blu*^{-/-} RGC axons nor was the association with stable presynaptic sites (Figure 5—figure supplements 2B, 3). Together these data suggest that Ntf3 upregulation does not per se affect mitochondria localization.

Axons of wild-type RGCs transplanted into *kif5aa* mutant tecta show excessive branching

For the dissection of cell-autonomous vs non-cell autonomous effects of the loss of *kif5aa*, we generated mutant/wild-type chimeric embryos by blastomere transplantations at the 1000-cell stage (Gosse et al., 2008). Donor RGCs were derived from a Tg(Pou3f4:Gal4) × Tg(UAS:RFP) cross and visualized by the expression of a fluorescent membrane-targeted RFP. When cells were transplanted in low numbers from a transgenic donor into a host embryo, we could image single donor derived and fluorescently labeled RGCs, within a host environment. First, we could observe that the delayed ingrowth of *kif5aa* mutant RGC axons in the tectal neuropil is a cell-autonomous effect (Figure 8—figure supplement 1). When growing in a wild-type environment, *kif5aa* mutant RGC axons invade the tectal neuropil 1 day later (4 dpf) than wild-type cells. Second, in contrast to what we observed in mutant larvae, arbor size was not increased at 5 or 7 dpf in mutant RGC axons that grow into a wild-type tectum (Figure 8A,B). Mutant RGC arbors are significantly smaller, similar to those that overexpress *ntrk3adN*-eGFP (see Figure 7B). Wild-type cells growing in a *kif5aa* mutant background show the opposite behavior. No stalling at 3 dpf was detected (Figure 8—figure supplement 1) and, at 5 and 7 dpf, they established a significantly increased axonal arbor (Figure 8A, B). To further demonstrate that the axonal arbor overgrowth observed both in *kif5aa*^{-/-} and *blu*^{-/-} was due to a common molecular mechanism, we transplanted single *kif5aa*^{-/-} RFP labeled RGC into a *blu* mutant host. In these conditions, *kif5aa* mutant RGC axonal arbors were significantly larger than when transplanted into a wild-type host (Figure 8—figure supplement 2).

Taken together, these experiments support a homeostatic mechanism by which tectum-secreted Ntf3 directly promotes the growth of innervating RGC axons. Lack of retinal synaptic activity results in upregulation of Ntf3 and, consequently, in an enlargement of RGC axonal arbors.

Discussion

Here, we report for the first time the role of the anterograde transport motor Kif5aa in the larval development of the zebrafish visual system. The loss-of-function *kif5aa* allele that we generated

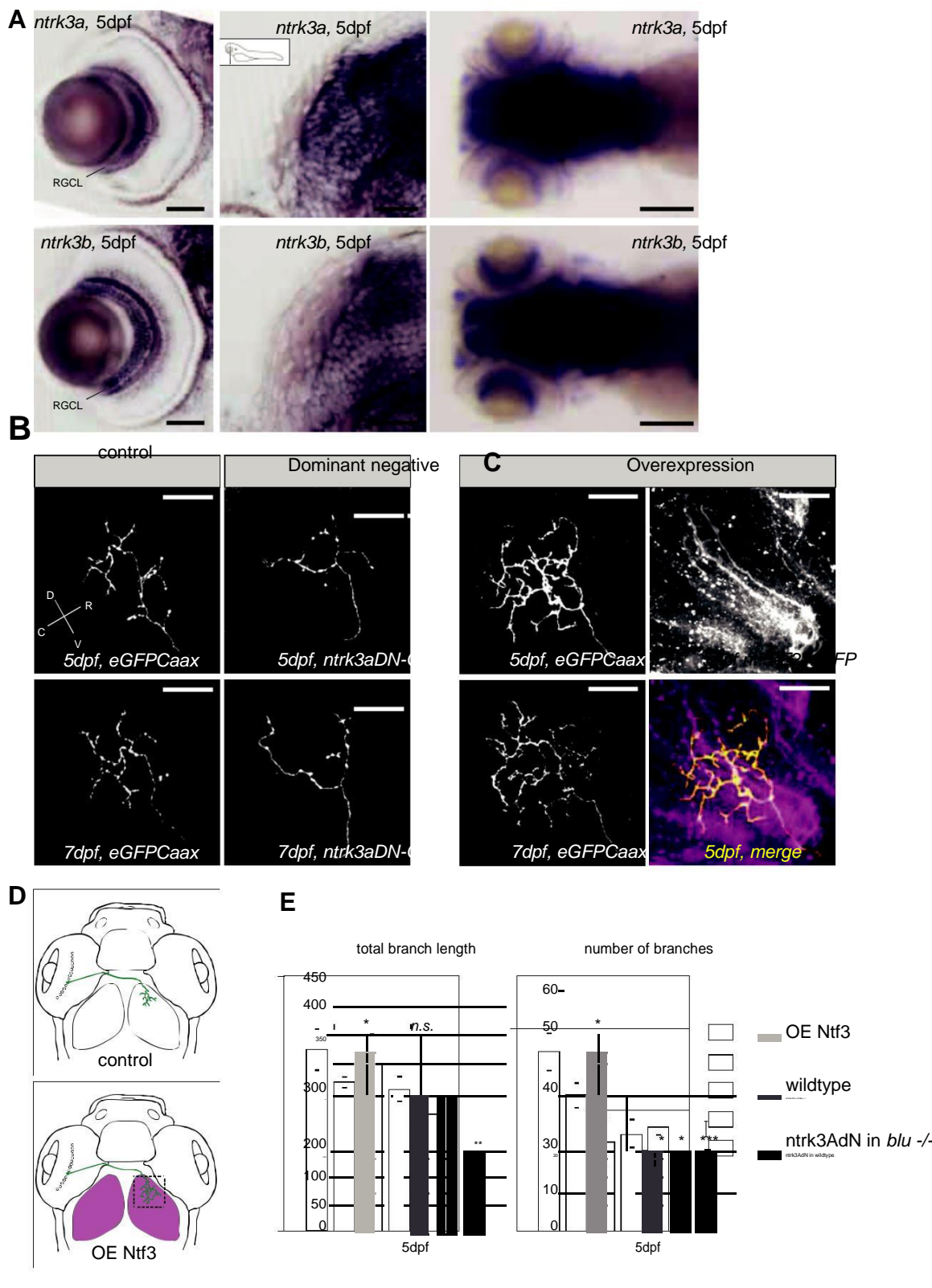


Figure 7. Neurotrophin 3 signaling alters axonal branch size in RGCs. (A) In situ hybridization with *ntrk3a* and *ntrk3b* specific antisense probes shows expression of both paralogues in broad parts of the nervous system in 5 dpf larvae. Both receptors are strongly expressed in RGCs. RGCL = Retinal Ganglion Cell Layer. Scale bars (from left to right) = 50 μ m, 50 μ m, 150 μ m. (B) Representative pictures of single RGC axons at 5 (upper) and 7 dpf (lower) Figure 7. continued on next page

Figure 7. Continued

panel). Control RGC cells express a membrane bound eGFP (control; left panel). To render cells unresponsive to the TrkC pathway, single RGCs express a dominant negative, kinase dead and eGFP-tagged form of the neurotrophic factor receptor *ntrk3a* (*ntrk3adN-GFP*) (dominant negative, right panel). Consequently, RGCs grow smaller arbors with less branches. (C) To investigate the effect of Ntf3 on RGC axonal growth, we monitored single eGFP positive RGCs while growing into a tectum overexpressing Ntf3 (overexpression) at 5 (upper left panel) and 7 dpf (lower left panel). Overexpression of Ntf3 was driven by an UAS:*ntf3-E2A-RFP* construct in the Tg(*gSA2AzGFF49A*) (Muto et al., 2013) transgenic line in tectal glial cells and periventricular neurons from 2 dpf onwards. By employing a 2A sequence between the *ntf3* and the RFP open reading frame, both proteins were produced from the same construct. Thereby Ntf3 overexpressing cells were marked by RFP expression (right upper panel) and we analyzed the arbors of single eGFP^{Caax} positive RGCs at 5 (upper left panel) and 7 dpf (lower left panel) growing in RFP expressing optic tecta. RGCs grow more complex arbors with more branches when invading into the Ntf3 overexpressing tectal environment compared to control RGCs (A, left panel). Lower left panel = merge of *ntf3-E2A-RFP* expressing tectal cells and an eGFP^{Caax} expressing RGC axon. Scale bars = 20 μ m. D = dorsal, V = ventral, R = rostral, C = caudal. (D) Schematics illustrating the approach for analysis of single RGC arbors. While in control and dominant negative expression experiments, single RGCs were labeled (upper panel), in the Ntf3 overexpression situation, single membrane bound eGFP (eGFP^{Caax}) labeled RGCs were growing into a tectum overexpressing Ntf3 (labeled by RFP expression, shown in magenta, lower panel). (E) Quantification of total branch length and number of branches at 5 dpf in single RGC arbors upon overexpression of the dominant negative *ntrk3adN-GFP* construct in single RGCs or overexpression of Ntf3 in tectal cells. *Ntrk3adN-GFP* expressing wild-type cells are significantly smaller and grow fewer branches at 5 dpf ($p < 0.001$). In both, *kif5aa* and *blumenkohl* mutant embryos, expression of *ntrk3adN-GFP* in single RGCs inhibits the overgrowth of the axonal arbor that is normally observed. The branch length is not different to the length in wild-type cells. Ntf3 overexpression in the tectum leads to increased axonal branch length and increased branch number in wild-type RGCs ($p < 0.05$) ($n = 8, 23, 7, 8, 26$). DOI: [10.7554/eLife.05061.021](https://doi.org/10.7554/eLife.05061.021)

The following figure supplement is available for figure 7:

Figure supplement 1. *Blumenkohl* mutant RGC arbors and RGC arbors growing into a Ntf3 overexpressing tectum do not show increased filopodia dynamics.

DOI: [10.7554/eLife.05061.022](https://doi.org/10.7554/eLife.05061.022)

disrupts the open reading frame after 122 of 1033aa within the motor domain of the protein and results in mRNA degradation likely by nonsense-mediated decay. We therefore expect that no functional Kif5aa protein is produced.

Disruption of Kif5aa created a complex and dynamically changing retinotectal phenotype. At 3 to 4 dpf, RGC axons devoid of Kif5aa grew more slowly and reached their targets in the tectum with a delay of about 24 hr. Mutant retinotectal synapses did not transmit signals to tectal cells, but were apparently silent, resulting in a complete loss of visual responses. Both the stalled growth and the synaptic transmission defects were likely a direct consequence of the absence of Kif5aa. Some of the known cargoes of mammalian Kif5a are required for normal axon outgrowth (Karle et al., 2012; Chen and Sheng, 2013; Schwarz, 2013; Sheng, 2014). In the zebrafish *kif5aa* mutant, mitochondria are significantly depleted from distal RGC axon terminals, as shown by *in vivo* imaging and transmission electron microscopy, suggesting that these organelles are Kif5a cargoes as in mammals. Furthermore, a recent report showed that Kif5aa has a similar role in the posterior lateral line nerve and peripheral cutaneous axonal arbors (Campbell et al., 2014). Mitochondrial ATP production is required for synapse assembly (Lee and Peng, 2008), the generation of action potentials (Attwell and Laughlin, 2001) and synaptic transmission (Verstreken et al., 2005). In addition, synaptic mitochondria maintain and regulate neurotransmission by buffering Ca^{2+} (Medler and Gleason, 2002; David and Barrett, 2003). This deficit can therefore explain the impairment in transmitter release at the presynaptic terminals without, however, excluding the possibility that the impaired transport of other cargoes is also involved.

Interestingly, outgrowth of axons from the retina was not affected by loss of Kif5aa. Only after crossing the optic chiasm, at the entrance to the tectum, did RGC axons stall. Reduced axonal growth is caused by loss of kinesin-1 in other experimental systems or other axonal transport motors like Dynein/Dynactin (Ferreira et al., 1992; Ahmad et al., 2006; Abe et al., 2008; Karle et al., 2012; Prokop, 2013), but often the deficit is evident from the start. Early functions of kinesin I heavy chains are probably carried out by other members of this gene family in zebrafish, such as *kif5ab*, *kif5b* or *kif5c*. All isoforms homodimerize and may carry distinct sets of cargoes (DeBoer et al., 2008). In mammalian neurons, KIF5C likely contributes to axon specification (Jacobson et al., 2006). Similarly, the *Drosophila* KIF5 homolog kinesin heavy chain (KHC) drives axon initiation and transiently maintains axonal growth (Lu et al., 2013). The zebrafish Kif5c orthologue is therefore the prime candidate to carry out this early kinesin motor function for RGCs.

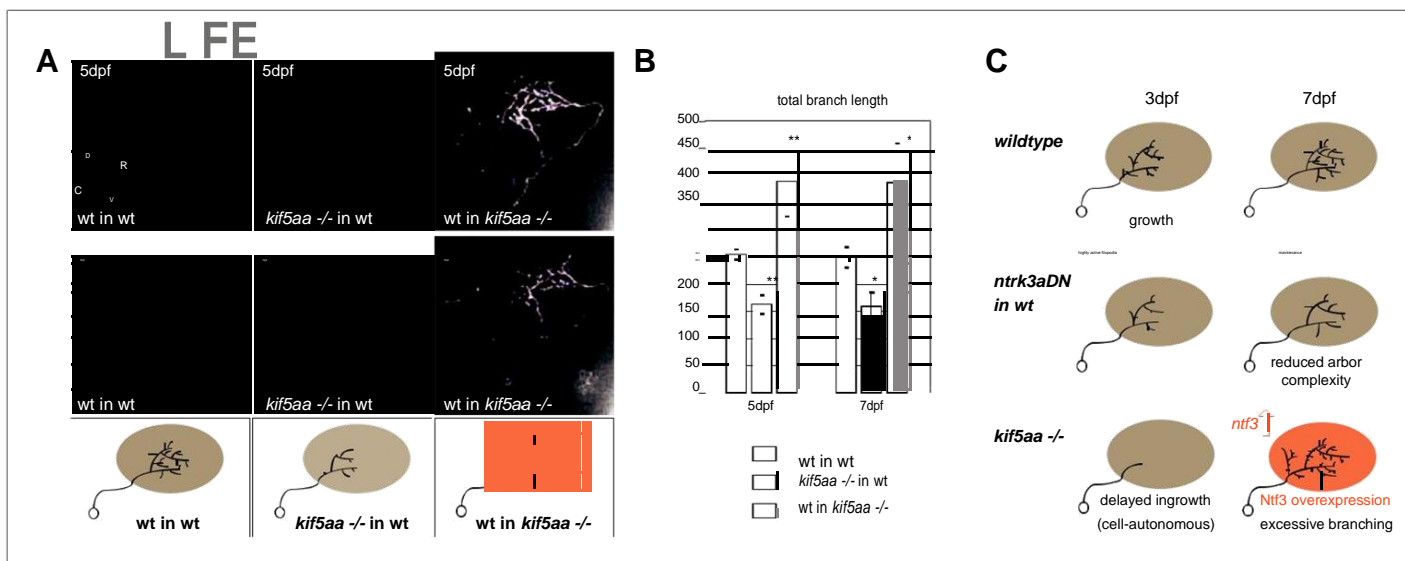


Figure 8. Transplantations confirm the growth promoting-effect in *kif5aa* mutant tecta. (A) Representative pictures of single in vivo imaged RGC axons after blastula stage transplantations from wild-type donors into a wild-type tectum (left panel), from *kif5aa* mutants into a wild-type tectum (middle panel) or from a wild-type donor into a *kif5aa* mutant tectum (right panel). The same cell was analyzed at 5 dpf (upper panel) and 7 dpf (middle panel). Scale bars = 20 μ m. Schematics of RGC arbor complexity and size in the lower panel. In orange: *Ntf3* overexpressing *kif5aa* mutant tectum. D = dorsal, V = ventral, R = rostral, C = caudal. (B) Quantification of total branch length of transplanted RGC axons at 5 and 7 dpf. *kif5aa* mutant cell arbors are significantly smaller than wild-type cell arbors when growing into a wild-type tectum ($p < 0.01$). Wild-type cells built larger arbors when growing into a *kif5aa* mutant tectum ($p < 0.05$) (5 dpf: $n = 14, 35, 6$; 7 dpf: $n = 14, 19, 5$). (C) Schematic illustrating growth behavior of RGC axons in wildtype (upper panel) and *kif5aa* mutant tecta (lower panel) and upon loss of TrkC signaling (middle panel). Wild-type RGCs start to grow into the wild-type neuropil at 3 dpf. They grow highly active filopodial protrusions and start to form complex axonal arbors. At 5 dpf they reach their final size and maintain their branch shape at 7 dpf. When TrkC signaling is blocked by overexpression of a dominant negative receptor (*ntrk3adN*-GFP), wild-type cells show a substantially reduced arbor complexity (middle panel). *Kif5aa* mutant RGC arbors show a delay of ingrowth into the tectal neuropil. This is followed by a period of highly active growth with abundant filopodia formation. This results in highly complex arbors at 7 dpf. The delay of RGC growth is cell autonomous (Figure 8—figure supplement 1). The lack of retinal input leads to an upregulation of *ntf3* expression by tectal cells and constitutes a growth-promoting environment.

DOI: [10.7554/eLife.05061.023](https://doi.org/10.7554/eLife.05061.023)

The following figure supplements are available for figure 8:

Figure supplement 1. Phenotype of transplanted RGC arbors at early stages of development.

DOI: [10.7554/eLife.05061.024](https://doi.org/10.7554/eLife.05061.024)

Figure supplement 2. Transplantation of *kif5aa* mutant RGCs into a blumenkohl mutant acceptor leads to an increased growth compared to transplantation into a wild-type acceptor.

DOI: [10.7554/eLife.05061.025](https://doi.org/10.7554/eLife.05061.025)

Synapse assembly (as assayed by transport and distribution of Synaptophysin-containing clusters) was not detectably affected by the *kif5aa* mutation, in agreement with previous experiments in mouse KO cells (Xia et al., 2003). The observed higher percentage of mobile vesicles likely reflects the highly active growth at days 4 and 5, as it was previously shown in RGCs that synaptic puncta stability increases with axon maturation (Meyer and Smith, 2006). Filopodial activity was previously described as a sign of immature, silent axons before the onset of presynaptic activity (Ben Fredj et al., 2010). This is in line with the observed failure of *kif5aa* mutant axons to transmit neuronal signals.

As a secondary, non-cell autonomous consequence of *kif5aa* disruption, we observed that *Ntf3* was upregulated by the tectum. Overexpression of *Ntf3* in wild-type tectum and blockade of its receptor *Ntrk3* (TrkC) in RGCs demonstrated that this neurotrophin is both sufficient and necessary to alter branch dynamics in RGC axon arbors. Classical work in the optic tectum of *Xenopus laevis* showed that overexposure to BDNF leads to enlarged and more complex axonal arbors (Marshak et al., 2007). Here, we identified the related *Ntf3* as the intrinsic, growth-promoting signal for RGC axons in zebrafish.

Ntf3 upregulation was observed not only in *kif5aa* mutant larvae but also in two other previously characterized mutant lines, blumenkohl and lakritz, and when directly silencing RGCs via BoTx expression. In all cases, this upregulation was correlated with RGC absence or dysfunction. In lakritz

zebrafish larvae, RGCs are absent; the functional connection between the retina and the tectum thus is eliminated (Kay et al., 2001). In blumenkohl, transmitter release is diminished (Smear et al., 2007). Similar to our results with kif5aa, blumenkohl RGC axons show an increased arbor size and complexity (Smear et al., 2007). The same retrograde signal may underlie the enlargement of retinal arbors following treatment with MK-801, a blocker of glutamate receptors of the NMDA-subtype (Schmidt et al., 2004), or in macho mutants, in which RGCs fail to generate action potentials (Gnuegge et al., 2001). In the case of lakritz, when single wild-type RGCs were transplanted into a lakritz host, their solitary axons formed larger and more complex arbors (Gosse et al., 2008). This result is reminiscent of the phenotype of wild-type RGCs growing in a kif5aa mutant larva, that is, when they are surrounded by inactive axons. Interestingly, Ntf3 upregulation alone as observed in blu mutants or in overexpression experiments had no significant effect on mitochondria distribution and short-lived filopodia dynamic. This suggests that these phenotypes are specific to kif5aa^{-/-} RGCs and probably caused by direct axonal trafficking defects, and that they are not due to impaired synaptic activity.

Together, these data suggest a model in which a deficit in presynaptic activity enhances the production and release of Ntf3 by tectal neurons. Tectum-derived Ntf3, in turn, retrogradely stimulates axonal branching and, thus, the addition of presynaptic terminals (Figure 7C). Such a signal could be the core motif of a compensatory pathway that is triggered when synaptic drive deviates from some homeostatic setpoint (Davis and Bezprozvanny, 2001; Burrone and Murthy, 2003). Our analysis of a mutation in a motor protein has thus unmasked a potentially general structural plasticity mechanism that together with the well-known competition-based and Hebbian mechanisms shapes the retinotectal projection and determines the final axonal arbor size (Ruthazer et al., 2003; Ruthazer and Cline, 2004; Hua et al., 2005; Uesaka et al., 2006; Schwartz et al., 2009, 2011; Ben Fredj et al., 2010; Munz et al., 2014).

Materials and methods

Ethics statements

All fish are housed in the fish facility of our laboratory, which was built according to the local animal welfare standards. All animal procedures were performed in accordance with French and European Union animal welfare guidelines.

Fish lines

The following transgenic fish lines were used or generated: Tg(UAS:RFP, cry:eGFP) (Auer et al., 2014), Tg(UAS:SypGFP) (Meyer and Smith, 2006), Tg(HuC:GCaMP5) (Ahrens et al., 2013), Tg(BGUG) (Xiao and Baier, 2007), Tg(Pou3f4:Gal4) (Xiao and Baier, 2007), Tg(gSA2AzGFF49A) (Muto et al., 2013), Tg(Shh:eGFP) (Neumann and Nusslein-Volhard, 2000), Tg(pou4f3:mGFP) (Xiao et al., 2005), Tg(Isl2b:Gal4, cmlc2:eGFP), Tg(UAS:BoTxLCB-GFP) (see 'Materials and methods'). TALENs used to generate the kif5aa loss-of-function alleles were described previously (Auer et al., 2014). All mutant and transgenic lines used in this study are described in Supplementary file 1.

Genotyping of the kif5aa^{*162} mutant alleles

For genotyping the following primers were used (5' to 3'): kif5aa_geno_fwd: GTTCACAGATTGTGATGTCTGTG, kif5aa_geno_rev: TGGAGGATGGAGAAATGATGACA. After PCR amplification from genomic DNA the 400 bp long amplicon was digested with NcoI. The wild-type allele is digested into two fragments of 240 bp and 160 bp length, respectively. The mutant alleles are not digested and show a band at 387 bp or 390 bp.

Molecular cloning

The pIsl2b:Gal4, cmlc2:eGFP construct was generated by a Gateway reaction (MultiSite Gateway Three-Fragment Vector Construction Kit, ThermoFisher Scientific, Waltham, MA) using the p5E-Isl2b (Ben Fredj et al., 2010), pME-Gal4, p3E-pA and the pDest-Tol2;cmlc2:eGFP (Kwan et al., 2007) vectors. We generated a p5E-4nrUAS vector with four non repetitive UAS sequences by digestion of the 4Xnr UAS:GFP vector (Akitake et al., 2011) and insertion of the 4nrUAS fragment into the p5E-10UAS vector (Kwan et al., 2007) after HindIII and AelI digestion. To obtain constructs with multiple UAS sequences, we generated a p5E-4nrUAS-tagRFPCaax-pA-4nrUAS vector. The tagRFPCaax sequence was amplified with primers listed in Supplementary file 2 and inserted into the pME-MCS vector (Kwan et al., 2007) after BamHI/NotI digestion resulting in pME-tagRFPCaax. After a Gateway

reaction (MultiSite Gateway Three-Fragment Vector Construction Kit) using the p5E-4nrUAS, pME-tagRFPcaax, p3E-pA, and the pDest-Tol2; cmcl2:eGFP (Kwan et al., 2007) vectors, the p4nrUAS: tagRFPcaax-pA-Tol2;cmcl2:eGFP vector was digested with *StuI* and *SnaBI*. The 4nrUAS:tagRFPcaax-pA fragment was subsequently inserted into the *StuI* digested and dephosphorylated p5E-4nrUAS vector to create a p5E-4nrUAS-tagRFPcaax-pA-4nrUAS vector. We generated a pME-SypGFP vector by digestion of 5x UAS:SypGFP (Meyer and Smith, 2006) with *EcoRI* and *NotI* and insertion into the pME-MCS plasmid. To obtain the p4nrUAS:tagRFPcaax-pA-4nrUAS:SypGFP-pA-Tol2;cmcl2:eGFP vector we performed a Gateway reaction using p5E-4nrUAS-tagRFPcaax-pA-4nrUAS, pME-SypGFP, p3E-pA and pDest-Tol2;cmcl2:eGFP. We generated a pME-PhbGFP and a pME-Phbmcherry vector by digestion of pClontecN1-PhbGFP and pClontecN1-Phbmcherry (a kind gift from Christian Wunder) (Rajalingam et al., 2005) with *EcoRI* and *NotI* and insertion into pME-MCS. To obtain the p4nrUAS: tagRFPcaax-pA-4nrUAS:PhbGFP-pA-Tol2;cmcl2:eGFP vector we performed a Gateway reaction using p5E-4nrUAS-tagRFPcaax-pA-4nrUAS, pME-PhbGFP, p3E-pA and pDest-Tol2;cmcl2:eGFP. We generated a p5E-4nrUAS-SypGFP-pA-4nrUAS vector by performing a Gateway reaction using p5E-4nrUAS, pME-SypGFP, p3E-pA and pDest-Tol2; cmcl2:eGFP. The resulting p4nrUAS:SypGFP-pA-Tol2;cmcl2:eGFP vector was digested with *StuI* and *SnaBI* to create a p5E-4nrUAS-SypGFP-pA-4nrUAS vector after insertion into the *StuI* digested and dephosphorylated p5E-4nrUAS vector fragment. To create a p4nrUAS:SypGFP-pA-4nrUAS:Phbmcherry-pA-Tol2;cmcl2:eGFP plasmid we performed a Gateway reaction using p5E-4nrUAS-SypGFP-pA-4nrUAS, pME-Phbmcherry, p3E-pA and pDest-Tol2;cmcl2:eGFP. To create a *ntf3_E2A_tagRFP* expression construct we amplified *ntf3_E2A* from wild-type zebrafish cDNA (3 dpf) and fused it to a tagRFP fragment. Primers used are listed in Supplementary file 2. After digestion and insertion into the pME-MCS vector with *HindIII* and *NotI*, we performed a Gateway reaction using p5E-10UAS (Kwan et al., 2007), pME-*ntf3_E2A_tagRFP*, p3E-pA and pDest-Tol2; cmcl2:eGFP to generate p10UAS-*ntf3_E2A_tagRFP*-pA-tol2, cmcl2:eGFP. To create a dominant negative *ntrk3A* expression construct, we amplified a truncated fragment of *ntrk3A* from wild-type zebrafish cDNA (3 dpf) and fused it to the eGFP open reading frame. Primers used are listed in Supplementary file 2. After digestion and insertion into the pME-MCS vector with *HindIII* and *NotI* we performed a Gateway reaction using p5E-10UAS, pME-*ntrk3AdNeGFP*, p3E-pA and pDest-Tol2; cmcl2:eGFP to generate p10UAS:*ntrk3AdNeGFP*-pA-Tol2; cmcl2:eGFP. To create a *pIsl2b:eGFPcaax* construct, we performed a Gateway reaction using p5E-*Isl2b*, pME-eGFPcaax (Kwan et al., 2007), p3E-pA and pDest-Tol2; cmcl2:eGFP. To generate a UAS: *BoTxBLC-GFP* construct, a codon-optimized cDNA encoding botulinum toxin light chain B serotype (Kurazono et al., 1992; Whelan et al., 1992) was fused in frame with GFP and cloned downstream of the 5x UAS sequence using gateway recombination (Asakawa and Kawakami, 2008). Microinjection of the pT2UAS:*BoTxBLC-GFP* plasmid (50 ng/μl) was based on standard protocols with *Tol2* mRNA (25 ng/μl). Over 50 founders were screened for the presence of a functional transgene using a combination of behavioral assays (touch-evoked swimming, escape response) and the level of expression of the *BoTxBLC-GFP* fusion protein (Suster et al., in preparation).

Genetic linkage mapping of the vertigo mutation

The genomic locus of the *vertigo*^{S1614} allele (*vert*) was determined using a PCR based simple sequence length polymorphisms (SSLPs) marker strategy. *vert* carriers in the TL genomic background (in which the mutagenesis was carried out) were crossed to the WIK genomic background to generate mapping crosses. From 1800 meioses the two SSLP markers, *fj61a10* and *tsub1g3*, located 0.1 cM apart were identified to flank the *vert* locus. Both markers are placed on Contig 963 of the Sanger center BAC sequencing project built by two overlapped BACs with sequencing information and four genes, one of which is *kif5aa*, are predicted between the two mapping markers.

Immunohistochemistry and in situ hybridization

Retinal sections of 5 dpf old embryos and whole mount embryos were stained using standard protocols (Kay et al., 2001). The full list of primary and secondary antibodies is given below. Whole-mount in situ hybridization was performed according to standard protocols (Di Donato et al., 2013). *Kif5aa*, *ntrk3a*, *ntrk3b*, and *ntf3* specific sense and antisense probes were amplified by PCR from cDNA and cloned into the pCRII-topo vector (ThermoFisher Scientific). All primers used are reported in Supplementary file 2. The tag-1 probe was synthesized from a 3.1 kb tag1 cDNA clone

(Warren et al., 1999) and the pax2.1 probe was synthesized using the complete pax2.1 cDNA (Krauss et al., 1991). Probes were hydrolyzed to 200 bp fragments prior to use.

Antibodies

The following primary antibodies were used in the course of this study: anti-Parvalbumine (EMD Millipore, Billerica, MA, MAB1572, 1:500), anti-eGFP (Genetex, GXT13970, 1:500), anti-PKC (Santa Cruz Biotechnology, Santa Cruz, CA, sc-209, 1:500), anti-humanNT3 (ThermoFisher Scientific, PA1-18385, 1:500), anti-alpha-tubulin (Genetex, Irvine, CA, GTX11304, 1:5000). The following secondary antibodies were used in the course of this study: anti-mouse-Alexa635 (ThermoFisher Scientific, A31574, 1:250), anti-rabbit-Alexa546 (ThermoFisher Scientific, A11081, 1:250), anti-chicken-Alexa488 (ThermoFisher Scientific, A11039, 1:250), anti-Rabbit IgG, HRP conjugated (Promega, W4011, 1:2000), anti-mouse IgG, HRP conjugated (Promega, Madison, WI, W4021, 1:2000).

Optokinetic response

The behavioral test for the optokinetic response was performed as described previously (Muto et al., 2005).

Single cell labeling and filopodia analysis

The morphology of single RGCs was analyzed using the Tg(BGUG), *kif5aa*^{162+/-} transgenic line and single cells were imaged over consecutive days. To quantify filopodia dynamics, imaging was performed for 10 min at a rate of 1 frame/2 min. All branches not extending within this imaging period were assigned as stable branches and used for quantification of branch number and length. All branches extended or retracted within this imaging period were defined as filopodia. Single cell labeling to analyze synapse and mitochondria distribution was achieved by injection of 1 nl of naked plasmid DNA (25 ng/μl) into 1 cell stage embryos of the Tg(1sl2b:Gal4, *cmcl2:eGFP*), *kif5aa*^{162+/-} transgenic line. The following constructs were used: p4nrUAS:tagRFPCaax-pA-4nrUAS:PhBGFP-pA-Tol2; p4nrUAS: tagRFPCaax-pA-4nrUAS:SypGFP-pA-Tol2;*cmcl2:eGFP*; p4nrUAS:SypGFP-pA-4nrUAS:PhBmcherry-pA-Tol2;*cmcl2:eGFP*. To generate single RGCs expressing the dominant negative *ntrk3a* receptor, we injected 1 nl of naked p10UAS:*ntrk3aDN-eGFP-pA-Tol2;cmcl2:eGFP* plasmid DNA into 1 cell stage embryos of the Tg(Pou3f4:Gal4), *nacre+/-* transgenic line. To generate single eGFP expressing RGCs growing into a *ntf3* overexpressing tectum, we performed injections of 0.1 ng/μl *1sl2b:eGFPCaax* plasmid DNA, 15 ng/μl p10UAS:*ntf3-E2A-tagRFP-pA-tol2, cmcl2:eGFP* plasmid DNA and 50 ng/μl Tol2 transposase mRNA into 1 cell stage embryos of the Tg(*gSA2AzGFF49A*) (Muto et al., 2013) transgenic line. In control injections, no p10UAS:*ntf3-E2A-tagRFP-pA-tol2, cmcl2:eGFP* plasmid DNA was injected.

Confocal microscopy

Imaging was performed on a Roper confocal spinning disk head mounted on a Zeiss upright microscope, and acquisitions were done with a CoolSNAP HQ2 CDD camera (Photometrics, USA) through the MetaMorph software (Molecular Devices, Sunnyvale, CA). Embryos were anaesthetized using 0.02% tricaine (MS-222, Sigma-Aldrich, Saint Louis, MO) diluted in egg water and embedded in 1% low melting-point agarose in glass-bottom cell tissue culture dish (Fluorodish, World Precision Instruments, Sarasota, FL). Acquisitions were done using water immersion long working distance lenses, at 40x magnification (W DIC PL APO VIS-IR; 421462-9900) for z-stack images of the whole tectum and at 63x magnification (W PL APO VIS-IR; 421480-9900) for single plane time-lapse imaging of linear axonal segments. Images were assembled and analyzed in ImageJ (NIH). Z-stack images were manual edited to remove skin autofluorescence.

Time-lapse imaging, kymogram production and analysis

Time-lapse parameters were determined similar to previous studies (Moughamian et al., 2013; Niwa et al., 2013) based on the speed of transport in the tectum and set at 5 s intervals for 15 min (SypGFP) and 20 min (mitoGFP) total duration. Time-lapse images were assembled and analyzed in ImageJ to determine the percentage of moving vs stable particles, as well as distribution/density and size of the organelles. Kymograms were extracted for each linear segment using the kymogram tool (Montpellier RIO Imaging, CNRS, France). Extraction of small structures of the kymograms was done using the rotational watershed algorithm of the KymoMaker program (Chiba et al., 2014) and trace detection was done manually in ImageJ.

Calcium imaging

5- to 7-day-old nacre (*mitfa*^{-/-}) or TL larvae were taken from a cross of *kif5aa*^{*162+/-} Tg(HuC:GCaMP5G) or Tg(Isl2b:Gal4), Tg(UAS:GCaMP3) transgenic fish. They were immobilized in 2% low melting point agarose and mounted with the dorsal side up on a plexiglas platform. The platform was then placed in a custom-made chamber and immersed in E3 solution without methylene blue. The agarose around the eyes was cut away with a scalpel to allow for an unhindered view for the larvae. The larvae faced with one eye towards a glass cover slip in the chamber wall at a distance between 8 and 10 mm. Directly behind this glass cover slip and outside the chamber, a monochromatic OLED array (800 × 600 px, 13 × 9 mm, eMagin) for visual stimulus presentation covering approximately 70° by 50° of the larva's visual field was positioned. A colored filter (Kodak Wratten No. 32) was placed between glass cover slip and OLED to block green light emitted from the OLED thus allowing for simultaneous imaging and visual stimulation. Visual stimuli were synchronized to the acquisition and consisted of single black bars on a white background (or the inverse) running along the caudal rostral axis. The long axis of the bar was orthogonal to the direction of motion. Each bar was approximately 7° in width and moved at 16°/s. Visual stimuli were generated and controlled by custom scripts written in Matlab (MathWorks, for details see Source code 1) using the Psychophysics Toolbox extensions (Brainard, 1997; Pelli, 1997). Confocal imaging of visually-evoked calcium responses in the tectum contralateral to the eye receiving the visual stimulus was performed using an upright microscope (Roper/Zeiss, Germany) equipped with a Spinning Disk head (CSU-X1, Yokogawa, Japan) and a 40x/1.0 NA water-immersion objective (Zeiss). Time-series streams of 5 min duration were acquired at 4 Hz with 0.323 × 0.323 μm spatial resolution (620 × 520 pixels). GCaMP3 or GCaMP5G were excited by a 491 nm laser and emitted light was bandpass-filtered (HQ 525/50). Images were taken with a CCD camera (CoolSnap HQ2 Photometrics, Tucson, AZ). We did not observe any differences in larvae from 5 dpf to 7 dpf. Therefore, the data sets were combined for analysis. Occasionally, a visual response at the onset of the laser illumination or the power-on of the OLED was observed that quickly returned to baseline, probably due to habituation of the fish. Therefore, we excluded the first few seconds from acquisition analysis. Each stimulus epoch was presented for 4.4 s to every animal with an inter-epoch interval of 5.6 or 10.6 s to allow for the GCaMP signal to return to baseline values. After the experiment, fish were genotyped. Confocal time-series were pre-processed by correcting for motion with a translation algorithm (Fiji [Schindelin et al., 2012]). For each acquisition, ROIs for Neuropil and PVNs, respectively, were determined manually. Then the averaged ROI based time-series were smoothed by a low pass filter and the baseline signal was calculated by calculating the minimum in a time interval of 10 s before stimulus onset. The smoothed fluorescence signal and the baseline fluorescence were then used to calculate normalized signal intensity changes (% F / F₀). To identify pixels that were response locked to the stimulus, we performed linear regression on the Calcium evoked time-series (Miri et al., 2011). For this, we convolved the stimulus time-series with an exponentially decaying kernel with half-decay times for GCaMP5G (667 ms) (Akerboom et al., 2012) or GCaMP3 (597 ms) (Tian et al., 2009). This predicted fluorescence trace for the bar stimulus was then compared with the measured calcium traces for each pixel using Pearson correlation.

Transmission electron microscopy

6 dpf larvae were anaesthetized in 0.004% Tricaine in E3 solution and then fixed in 2% glutaraldehyde in 0.1 M phosphate buffer, pH 7.2. Tails were severed to increase permeability of fixation. Four drops of 4% OsO₄ were added to 1 ml of glutaraldehyde fixative, and samples were soaked for 15 min. After three washes in 0.1 M phosphate buffer, samples were stored in 2% glutaraldehyde solution. Prior to embedding, samples were washed three times with 0.1 M phosphate buffer for 2 min and dehydrated with graded acetone: 35% acetone, 50% acetone, 75% acetone, 80% acetone, 95% acetone, and 100% acetone (three times) for 10 min per solution while shaking. Samples were infiltrated with Epon resin/acetone mixtures: Epon resin: acetone (1:3), Epon resin: acetone (1:1) and Epon resin: acetone (3:1) followed by pure Epon resin containing the accelerant BDMA (three washes). Finally, embedded samples were cured in a vacuum oven and sectioned with a RMC MT6000 Microtome to 70 nm slices. Images were acquired with an FEI Tecnai 12 Transmission electron microscope.

Quantitative RT-PCR

Total RNA was prepared from 4 or 5 dpf embryos with TRIzol reagent (ThermoFisher Scientific) and TURBO DNA-free reagents (ThermoFisher Scientific). RNA (1 μg) was retrotranscribed using random

primers and the SuperScript III First-Strand Synthesis system (ThermoFisher Scientific). For q-RT-PCR, the SYBR Green PCR Master Mix (ThermoFisher Scientific) was used according to the manufacturers protocol and the PCR reaction was performed on an ABI PRISM 7900HT instrument. Ef1a and RPL13a were used as reference genes as reported previously (Tang et al., 2007). All assays were performed in triplicate using 11.25 ng of cDNA per reaction. The mean values of triplicate experiments were calculated according to the deltaCT quantification method.

Western blotting

Western blot analysis of embryo extracts was performed using standard techniques. Briefly, about 25 5 dpf larvae were homogenized in lysis buffer (20 μ l/embryo) containing: 10 mM HEPES, 300 mM KCl, 5 mM MgCl₂, 0.45% Triton, 0.05% Tween, Protease inhibitor-EDTA (Mini Complete, Roche, Switzerland). Protein extracts (about 20 μ g/lane) were separated by SDS-PAGE and subsequently blotted onto a PVDF membrane. Secondary antibody couples with Horseradish peroxidase (1:2000) were used to detect the anti-NTF3 (1:500) and anti-alpha-Tubulin (1:5000) primary antibodies (see Antibody section above for details), and revealed using ECL Western Blotting Detection Reagents (GE Healthcare Life Sciences, Pittsburgh, PA). Western blot quantification was performed using a chemiluminescence digital imaging system (ImageQuant Las-4000 Mini, GE Healthcare Life Sciences) and analyzed using ImageJ software.

Acknowledgements

We want to thank F Engert for the Tg(HuC:GCaMP5) transgenic line and C Nueslein-Vollhard for the Tg(shh:eGFP) transgenic line. Furthermore, we are grateful to M Meyer for sharing the 5xUAS:SypGFP construct and C Wunder for sharing the PhB:eGFP and PhB:mcherry constructs. We thank Manuela Portoso for helpful advice with the Western Blot analysis and all members of the Del Bene lab for fruitful discussions. We thank the Developmental Biology Curie imaging facility (PICT-IBISA@BDD, Paris, France, UMR3215/U934) member of the France-BioImaging national research infrastructure for their help and advice with confocal microscopy. The Del Bene laboratory 'Neural Circuits Development' is part of the Laboratoire d'Excellence (LABEX)

entitled DEEP (ANR-11-LABX-0044), and of the Ecole des Neurosciences de Paris Ile-de-France network. TOA was supported by a Boehringer Ingelheim Fonds Ph.D. fellowship and VB by an FRSQ and CIHR Doctoral Award and is enrolled in the ENP Graduate Program. CG was supported by a FRM postdoctoral fellowship. This work has been supported by an ATIP/AVENIR program starting grant (FDB), ERC-StG #311159 (FDB), ANR-II-INBS-0014 (JPC), CNRS, INSERM and Institut Curie core funding.

Additional information

Funding

Funder	Grant reference	Author
ATIP/Avenir starting grant CNRS/INSERM	Starting Grant	Filippo Del Bene
European Research Council (ERC)	ERC-StG#311159	Filippo Del Bene
Boehringer Ingelheim Fonds	Graduate Student Fellowship	Thomas O Auer
Fonds de Recherche du Quebec - Sante'	Graduate Student Fellowship	Valerie Bercier
Fondation pour la Recherche Medicale'	Postdoctoral Fellowship	Christoph Gebhardt
National Funding Agency for Research (ANR)	ANR-II-INBS-0014	Jean-Paul Concordet


The funders had no role in study design, data collection and interpretation, or the decision to submit the work for publication.

Author contributions

TOA, Conception and design, Acquisition of data, Analysis and interpretation of data, Drafting or revising the article; TX, Conception and design, Acquisition of data, Analysis and interpretation of data; VB, CG, KD, Acquisition of data, Analysis and interpretation of data; J-PC, MS, KK, Drafting or revising the article, Contributed unpublished essential data or reagents; CW, Conception and design, Contributed unpublished essential data or reagents; JW, Conception and design, Drafting or revising the article; HB, FDB, Conception and design, Analysis and interpretation of data, Drafting or revising the article

Author ORCIDs

Joachim Wittbrodt,  <http://orcid.org/0000-0001-8550-7377>

Filippo Del Bene,  <http://orcid.org/0000-0001-8551-2846>

Ethics

Animal experimentation: All fish are housed in the fish facility of our laboratory, which was built according to the local animal welfare standards. All animal procedures were performed in accordance with French and European Union animal welfare guidelines.

Additional files

Supplementary files

■ Supplementary file 1. Description of zebrafish mutant and transgenic lines used in this study.
DOI: [10.7554/eLife.05061.026](https://doi.org/10.7554/eLife.05061.026)

■ Supplementary file 2. Primers used in this study.
DOI: [10.7554/eLife.05061.027](https://doi.org/10.7554/eLife.05061.027)

■ Source code 1. Source code for moving bar stimulus.
DOI: [10.7554/eLife.05061.028](https://doi.org/10.7554/eLife.05061.028)

References

- Abe TK, Honda T, Takei K, Mikoshiba K, Hoffman-Kim D, Jay DG, Kuwano R. 2008. Dynactin is essential for growth cone advance. *Biochemical and Biophysical Research Communications* 372:418–422. doi: [10.1016/j.bbrc.2008.05.008](https://doi.org/10.1016/j.bbrc.2008.05.008).
- Ahmad FJ, He Y, Myers KA, Hasaka TP, Francis F, Black MM, Baas PW. 2006. Effects of dynactin disruption and dynein depletion on axonal microtubules. *Traffic* 7:524–537. doi: [10.1111/j.1600-0854.2006.00403.x](https://doi.org/10.1111/j.1600-0854.2006.00403.x).
- Ahrens MB, Huang KH, Narayan S, Mensh BD, Engert F. 2013. Two-photon calcium imaging during fictive navigation in virtual environments. *Frontiers in Neural Circuits* 7:104. doi: [10.3389/fncir.2013.00104](https://doi.org/10.3389/fncir.2013.00104).
- Akerboom J, Chen TW, Wardill TJ, Tian L, Marvin JS, Mutlu S, Calderon NC, Esposti F, Borghuis BG, Sun XR, Gordus A, Orger MB, Portugues R, Engert F, Mackli JJ, Filosa A, Aggarwal A, Kerr RA, Takagi R, Kracun S, Shigetomi E, Khakh BS, Baier H, Lagnado L, Wang SS, Bargmann CI, Kimmel BE, Jayaraman V, Svoboda K, Kim DS, Schreiner ER, Looger LL. 2012. Optimization of a GCaMP calcium indicator for neural activity imaging. *The Journal of Neuroscience* 32:13819–13840. doi: [10.1523/JNEUROSCI.2601-12.2012](https://doi.org/10.1523/JNEUROSCI.2601-12.2012).
- Akitake CM, Macurak M, Halpern ME, Goll MG. 2011. Transgenerational analysis of transcriptional silencing in zebrafish. *Developmental Biology* 352:191–201. doi: [10.1016/j.ydbio.2011.01.002](https://doi.org/10.1016/j.ydbio.2011.01.002).
- Asakawa K, Kawakami K. 2008. Targeted gene expression by the Gal4-UAS system in zebrafish. *Development, Growth & Differentiation* 50:391–399. doi: [10.1111/j.1440-169X.2008.01044.x](https://doi.org/10.1111/j.1440-169X.2008.01044.x).
- Attwell D, Laughlin SB. 2001. An energy budget for signaling in the grey matter of the brain. *Journal of Cerebral Blood Flow and Metabolism* 21:1133–1145. doi: [10.1097/00004647-200110000-00001](https://doi.org/10.1097/00004647-200110000-00001).
- Auer TO, Duroure K, De Cian A, Concordet JP, Del Bene F. 2014. Highly efficient CRISPR/Cas9-mediated knock-in in zebrafish by homology-independent DNA repair. *Genome Research* 24:142–153. doi: [10.1101/gr.161638.113](https://doi.org/10.1101/gr.161638.113).
- Baier H, Klostermann S, Trowe T, Karlstrom RO, Nusslein-Volhard C, Bonhoeffer F. 1996. Genetic dissection of the retinotectal projection. *Development* 123:415–425.
- Barry J, Gu Y, Jukkola P, O'Neill B, Gu H, Mohler PJ, Rajamani KT, Gu C. 2014. Ankyrin-G directly binds to kinesin-1 to transport voltage-gated Na⁺ channels into axons. *Developmental Cell* 28:117–131. doi: [10.1016/j.devcel.2013.11.023](https://doi.org/10.1016/j.devcel.2013.11.023).
- Ben Fredj N, Hammond S, Otsuna H, Chien CB, Burrone J, Meyer MP. 2010. Synaptic activity and activity-dependent competition regulates axon arbor maturation, growth arrest, and territory in the retinotectal projection. *The Journal of Neuroscience* 30:10939–10951. doi: [10.1523/JNEUROSCI.1556-10.2010](https://doi.org/10.1523/JNEUROSCI.1556-10.2010).
- Brainard DH. 1997. The psychophysics toolbox. *Spatial Vision* 10:433–436. doi: [10.1163/156856897X00357](https://doi.org/10.1163/156856897X00357).
- Brockerhoff SE, Hurley JB, Janssen-Bienhold U, Neuhauss SC, Driever W, Dowling JE. 1995. A behavioral screen for isolating zebrafish mutants with visual system defects. *Proceedings of the National Academy of Sciences of USA* 92:10545–10549. doi: [10.1073/pnas.92.23.10545](https://doi.org/10.1073/pnas.92.23.10545).

- Brunger AT, Jin R, Breidenbach MA. 2008. Highly specific interactions between botulinum neurotoxins and synaptic vesicle proteins. *Cellular and Molecular Life Sciences* 65:2296–2306. doi: [10.1007/s00018-008-8088-0](https://doi.org/10.1007/s00018-008-8088-0).
- Burrone J, Murthy VN. 2003. Synaptic gain control and homeostasis. *Current Opinion in Neurobiology* 13:560–567. doi: [10.1016/j.conb.2003.09.007](https://doi.org/10.1016/j.conb.2003.09.007).
- Campbell PD, Shen K, Sapio MR, Glenn TD, Talbot WS, Marlow FL. 2014. Unique function of Kinesin Kif5A in localization of mitochondria in axons. *The Journal of Neuroscience* 34:14717–14732. doi: [10.1523/JNEUROSCI.2770-14.2014](https://doi.org/10.1523/JNEUROSCI.2770-14.2014).
- Chen Y, Sheng ZH. 2013. Kinesin-1-syntrophin coupling mediates activity-dependent regulation of axonal mitochondrial transport. *The Journal of Cell Biology* 202:351–364. doi: [10.1083/jcb.201302040](https://doi.org/10.1083/jcb.201302040).
- Chiba K, Shimada Y, Kinjo M, Suzuki T, Uchida S. 2014. Simple and direct assembly of kymographs from movies using KYMOMAKER. *Traffic* 15:1–11. doi: [10.1111/tra.12127](https://doi.org/10.1111/tra.12127).
- Cohen-Cory S, Fraser SE. 1995. Effects of brain-derived neurotrophic factor on optic axon branching and remodelling in vivo. *Nature* 378:192–196. doi: [10.1038/378192a0](https://doi.org/10.1038/378192a0).
- Crimella C, Baschiroto C, Arnoldi A, Tonelli A, Tenderini E, Airoidi G, Martinuzzi A, Trabacca A, Losito L, Scarlato M, Benedetti S, Scarpini E, Spinicci G, Bresolin N, Bassi MT. 2012. Mutations in the motor and stalk domains of KIF5A in spastic paraplegia type 10 and in axonal Charcot-Marie-Tooth type 2. *Clinical Genetics* 82:157–164. doi: [10.1111/j.1399-0004.2011.01717.x](https://doi.org/10.1111/j.1399-0004.2011.01717.x).
- David G, Barrett EF. 2003. Mitochondrial Ca²⁺ uptake prevents desynchronization of quantal release and minimizes depletion during repetitive stimulation of mouse motor nerve terminals. *The Journal of Physiology* 548:425–438. doi: [10.1113/jphysiol.2002.035196](https://doi.org/10.1113/jphysiol.2002.035196).
- Davis GW, Bezprozvanny I. 2001. Maintaining the stability of neural function: a homeostatic hypothesis. *Annual Review of Physiology* 63:847–869. doi: [10.1146/annurev.physiol.63.1.847](https://doi.org/10.1146/annurev.physiol.63.1.847).
- DeBoer SR, You Y, Szodorai A, Kaminska A, Pignio G, Nwabuisi E, Wang B, Estrada-Hernandez T, Kins S, Brady ST, Morfini G. 2008. Conventional kinesin holoenzymes are composed of heavy and light chain homodimers. *Biochemistry* 47:4535–4543. doi: [10.1021/bi702445j](https://doi.org/10.1021/bi702445j).
- Del Bene F, Wyart C, Robles E, Tran A, Looger L, Scott EK, Isacoff EY, Baier H. 2010. Filtering of visual information in the tectum by an identified neural circuit. *Science* 330:669–673. doi: [10.1126/science.1192949](https://doi.org/10.1126/science.1192949).
- Di Donato V, Auer TO, Duroure K, Del Bene F. 2013. Characterization of the calcium binding protein family in zebrafish. *PLOS ONE* 8:e53299. doi: [10.1371/journal.pone.0053299](https://doi.org/10.1371/journal.pone.0053299).
- Evans RD, Robinson C, Briggs DA, Tooth DJ, Ramalho JS, Cantero M, Montoliu L, Patel S, Sviderskaya EV, Hume AN. 2014. Myosin-va and dynamic actin oppose microtubules to drive long-range organelle transport. *Current Biology* 24:1743–1750. doi: [10.1016/j.cub.2014.06.019](https://doi.org/10.1016/j.cub.2014.06.019).
- Fashena D, Westerfield M. 1999. Secondary motoneuron axons localize DM-GRASP on their fasciculated segments. *The Journal of Comparative Neurology* 406:415–424. doi: [10.1002/\(SICI\)1096-9861\(19990412\)406:3<415::AID-CNE9>3.0.CO;2-2](https://doi.org/10.1002/(SICI)1096-9861(19990412)406:3<415::AID-CNE9>3.0.CO;2-2).
- Ferreira A, Niclas J, Vale RD, Banker G, Kosik KS. 1992. Suppression of kinesin expression in cultured hippocampal neurons using antisense oligonucleotides. *The Journal of Cell Biology* 117:595–606. doi: [10.1083/jcb.117.3.595](https://doi.org/10.1083/jcb.117.3.595).
- Gnuegge L, Schmid S, Neuhauss SC. 2001. Analysis of the activity-deprived zebrafish mutant macho reveals an essential requirement of neuronal activity for the development of a fine-grained visuotopic map. *The Journal of Neuroscience* 21:3542–3548.
- Godinho L, Mumm JS, Williams PR, Schroeter EH, Koerber A, Park SW, Leach SD, Wong RO. 2005. Targeting of amacrine cell neurites to appropriate synaptic laminae in the developing zebrafish retina. *Development* 132: 5069–5079. doi: [10.1242/dev.02075](https://doi.org/10.1242/dev.02075).
- Goldstein LS. 2001. Kinesin molecular motors: transport pathways, receptors, and human disease. *Proceedings of the National Academy of Sciences of USA* 98:6999–7003. doi: [10.1073/pnas.111145298](https://doi.org/10.1073/pnas.111145298).
- Gomis-Ruth S, Wierenga CJ, Bradke F. 2008. Plasticity of polarization: changing dendrites into axons in neurons integrated in neuronal circuits. *Current Biology* 18:992–1000. doi: [10.1016/j.cub.2008.06.026](https://doi.org/10.1016/j.cub.2008.06.026).
- Gosse NJ, Nevin LM, Baier H. 2008. Retinotopic order in the absence of axon competition. *Nature* 452:892–895. doi: [10.1038/nature06816](https://doi.org/10.1038/nature06816).
- Heinrich G, Lum T. 2000. Fish neurotrophins and Trk receptors. *International Journal of Developmental Neuroscience* 18:1–27. doi: [10.1016/S0736-5748\(99\)00071-4](https://doi.org/10.1016/S0736-5748(99)00071-4).
- Hirokawa N. 1998. Kinesin and dynein superfamily proteins and the mechanism of organelle transport. *Science* 279:519–526. doi: [10.1126/science.279.5350.519](https://doi.org/10.1126/science.279.5350.519).
- Hirokawa N, Niwa S, Tanaka Y. 2010. Molecular motors in neurons: transport mechanisms and roles in brain function, development, and disease. *Neuron* 68:610–638. doi: [10.1016/j.neuron.2010.09.039](https://doi.org/10.1016/j.neuron.2010.09.039).
- Hua JY, Smear MC, Baier H, Smith SJ. 2005. Regulation of axon growth in vivo by activity-based competition. *Nature* 434:1022–1026. doi: [10.1038/nature03409](https://doi.org/10.1038/nature03409).
- Hunter PR, Lowe AS, Thompson ID, Meyer MP. 2013. Emergent properties of the optic tectum revealed by population analysis of direction and orientation selectivity. *The Journal of Neuroscience* 33:13940–13945. doi: [10.1523/JNEUROSCI.1493-13.2013](https://doi.org/10.1523/JNEUROSCI.1493-13.2013).
- Jacobson C, Schnapp B, Banker GA. 2006. A change in the selective translocation of the Kinesin-1 motor domain marks the initial specification of the axon. *Neuron* 49:797–804. doi: [10.1016/j.neuron.2006.02.005](https://doi.org/10.1016/j.neuron.2006.02.005).
- Karki S, Holzbaur EL. 1999. Cytoplasmic dynein and dynactin in cell division and intracellular transport. *Current Opinion in Cell Biology* 11:45–53. doi: [10.1016/S0955-0674\(99\)80006-4](https://doi.org/10.1016/S0955-0674(99)80006-4).
- Karle KN, Mockel D, Reid E, Schols L. 2012. Axonal transport deficit in a KIF5A(-/-) mouse model. *Neurogenetics* 13:169–179. doi: [10.1007/s10048-012-0324-y](https://doi.org/10.1007/s10048-012-0324-y).

- Kay JN, Finger-Baier KC, Roeser T, Staub W, Baier H. 2001. Retinal ganglion cell genesis requires lakritz, a zebrafish atonal homolog. *Neuron* 30:725–736. doi: [10.1016/S0896-6273\(01\)00312-9](https://doi.org/10.1016/S0896-6273(01)00312-9).
- Krauss S, Johansen T, Korzh V, Fjose A. 1991. Expression of the zebrafish paired box gene pax[zf-b] during early neurogenesis. *Development* 113:1193–1206.
- Kurazono H, Mochida S, Binz T, Eisel U, Quanz M, Grebenstein O, Wernars K, Poulain B, Tauc L, Niemann H. 1992. Minimal essential domains specifying toxicity of the light chains of tetanus toxin and botulinum neurotoxin type A. *The Journal of Biological Chemistry* 267:14721–14729.
- Kwan KM, Fujimoto E, Grabher C, Mangum BD, Hardy ME, Campbell DS, Parant JM, Yost HJ, Kanki JP, Chien CB. 2007. The Tol2kit: a multisite gateway-based construction kit for Tol2 transposon transgenesis constructs. *Developmental Dynamics* 236:3088–3099. doi: [10.1002/dvdy.21343](https://doi.org/10.1002/dvdy.21343).
- Laessing U, Stuermer CA. 1996. Spatiotemporal pattern of retinal ganglion cell differentiation revealed by the expression of neurodin in embryonic zebrafish. *Journal of Neurobiology* 29:65–74. doi: [10.1002/\(SICI\)1097-4695\(199601\)29:1<65::AID-NEU5>3.0.CO;2-5](https://doi.org/10.1002/(SICI)1097-4695(199601)29:1<65::AID-NEU5>3.0.CO;2-5).
- Lang DM, Warren JT Jr, Klisa C, Stuermer CA. 2001. Topographic restriction of TAG-1 expression in the developing retinotectal pathway and target dependent reexpression during axon regeneration. *Molecular and Cellular Neurosciences* 17:398–414. doi: [10.1006/mcne.2000.0936](https://doi.org/10.1006/mcne.2000.0936).
- Lee CW, Peng HB. 2008. The function of mitochondria in presynaptic development at the neuromuscular junction. *Molecular Biology of the Cell* 19:150–158. doi: [10.1091/mbc.E07-05-0515](https://doi.org/10.1091/mbc.E07-05-0515).
- Lin MI, Das I, Schwartz GM, Tsoulfas P, Mikawa T, Hempstead BL. 2000. Trk C receptor signaling regulates cardiac myocyte proliferation during early heart development in vivo. *Developmental Biology* 226:180–191. doi: [10.1006/dbio.2000.9850](https://doi.org/10.1006/dbio.2000.9850).
- Lu W, Fox P, Lakonishok M, Davidson MW, Gelfand VI. 2013. Initial neurite outgrowth in *Drosophila* neurons is driven by kinesin-powered microtubule sliding. *Current Biology* 23:1018–1023. doi: [10.1016/j.cub.2013.04.050](https://doi.org/10.1016/j.cub.2013.04.050).
- Macaskill AF, Rinholm JE, Twelvetrees AE, Arancibia-Carcamo IL, Muir J, Fransson A, Aspenstrom P, Attwell D, Kittler JT. 2009. Miro1 is a calcium sensor for glutamate receptor-dependent localization of mitochondria at synapses. *Neuron* 61:541–555. doi: [10.1016/j.neuron.2009.01.030](https://doi.org/10.1016/j.neuron.2009.01.030).
- Marshak S, Nikolakopoulou AM, Dirks R, Martens GJ, Cohen-Cory S. 2007. Cell-autonomous TrkB signaling in presynaptic retinal ganglion cells mediates axon arbor growth and synapse maturation during the establishment of retinotectal synaptic connectivity. *The Journal of Neuroscience* 27:2444–2456. doi: [10.1523/JNEUROSCI.4434-06.2007](https://doi.org/10.1523/JNEUROSCI.4434-06.2007).
- Martin SC, Sandell JH, Heinrich G. 1998. Zebrafish TrkC1 and TrkC2 receptors define two different cell populations in the nervous system during the period of axonogenesis. *Developmental Biology* 195:114–130. doi: [10.1006/dbio.1997.8839](https://doi.org/10.1006/dbio.1997.8839).
- Medler K, Gleason EL. 2002. Mitochondrial Ca(2+) buffering regulates synaptic transmission between retinal amacrine cells. *Journal of Neurophysiology* 87:1426–1439.
- Meyer MP, Smith SJ. 2006. Evidence from in vivo imaging that synaptogenesis guides the growth and branching of axonal arbors by two distinct mechanisms. *The Journal of Neuroscience* 26:3604–3614. doi: [10.1523/JNEUROSCI.0223-06.2006](https://doi.org/10.1523/JNEUROSCI.0223-06.2006).
- Miki H, Setou M, Kaneshiro K, Hirokawa N. 2001. All kinesin superfamily protein, KIF, genes in mouse and human. *Proceedings of the National Academy of Sciences of USA* 98:7004–7011. doi: [10.1073/pnas.111145398](https://doi.org/10.1073/pnas.111145398).
- Miri A, Daie K, Burdine RD, Aksay E, Tank DW. 2011. Regression-based identification of behavior-encoding neurons during large-scale optical imaging of neural activity at cellular resolution. *Journal of Neurophysiology* 105:964–980. doi: [10.1152/jn.00702.2010](https://doi.org/10.1152/jn.00702.2010).
- Moughamian AJ, Osborn GE, Lazarus JE, Maday S, Holzbaur EL. 2013. Ordered recruitment of dynactin to the microtubule plus-end is required for efficient initiation of retrograde axonal transport. *The Journal of Neuroscience* 33:13190–13203. doi: [10.1523/JNEUROSCI.0935-13.2013](https://doi.org/10.1523/JNEUROSCI.0935-13.2013).
- Munz M, Gobert D, Schohl A, Poquerusse J, Podgorski K, Spratt P, Ruthazer ES. 2014. Rapid Hebbian axonal remodeling mediated by visual stimulation. *Science* 344:904–909. doi: [10.1126/science.1251593](https://doi.org/10.1126/science.1251593).
- Muto A, Ohkura M, Abe G, Nakai J, Kawakami K. 2013. Real-time visualization of neuronal activity during perception. *Current Biology* 23:307–311. doi: [10.1016/j.cub.2012.12.040](https://doi.org/10.1016/j.cub.2012.12.040).
- Muto A, Orger MB, Wehman AM, Smear MC, Kay JN, Page-McCaw PS, Gahtan E, Xiao T, Nevin LM, Gosse NJ, Staub W, Finger-Baier K, Baier H. 2005. Forward genetic analysis of visual behavior in zebrafish. *PLOS Genetics* 1: e66. doi: [10.1371/journal.pgen.0010066](https://doi.org/10.1371/journal.pgen.0010066).
- Neuhauss SC, Biehmaier O, Seeliger MW, Das T, Kohler K, Harris WA, Baier H. 1999. Genetic disorders of vision revealed by a behavioral screen of 400 essential loci in zebrafish. *The Journal of Neuroscience* 19:8603–8615.
- Neumann CJ, Nusslein-Volhard C. 2000. Patterning of the zebrafish retina by a wave of sonic hedgehog activity. *Science* 289:2137–2139. doi: [10.1126/science.289.5487.2137](https://doi.org/10.1126/science.289.5487.2137).
- Nevin LM, Robles E, Baier H, Scott EK. 2010. Focusing on optic tectum circuitry through the lens of genetics. *BMC Biology* 8:126. doi: [10.1186/1741-7007-8-126](https://doi.org/10.1186/1741-7007-8-126).
- Nevin LM, Taylor MR, Baier H. 2008. Hardwiring of fine synaptic layers in the zebrafish visual pathway. *Neural Development* 3:36. doi: [10.1186/1749-8104-3-36](https://doi.org/10.1186/1749-8104-3-36).
- Nikolaou N, Lowe AS, Walker AS, Abbas F, Hunter PR, Thompson ID, Meyer MP. 2012. Parametric functional maps of visual inputs to the tectum. *Neuron* 76:317–324. doi: [10.1016/j.neuron.2012.08.040](https://doi.org/10.1016/j.neuron.2012.08.040).
- Niwa S, Takahashi H, Hirokawa N. 2013. β -Tubulin mutations that cause severe neuropathies disrupt axonal transport. *The EMBO Journal* 32:1352–1364. doi: [10.1038/emboj.2013.59](https://doi.org/10.1038/emboj.2013.59).
- Obashi K, Okabe S. 2013. Regulation of mitochondrial dynamics and distribution by synapse position and neuronal activity in the axon. *The European Journal of Neuroscience* 38:2350–2363. doi: [10.1111/ejn.12263](https://doi.org/10.1111/ejn.12263).

- Okada Y, Yamazaki H, Sekine-Aizawa Y, Hirokawa N. 1995. The neuron-specific kinesin superfamily protein KIF1A is a unique monomeric motor for anterograde axonal transport of synaptic vesicle precursors. *Cell* 81:769–780. doi: [10.1016/0092-8674\(95\)90538-3](https://doi.org/10.1016/0092-8674(95)90538-3).
- Parada LF, Tsoulfas P, Tessarollo L, Blair J, Reid SW, Soppet D. 1992. The Trk family of tyrosine kinases: receptors for NGF-related neurotrophins. *Cold Spring Harbor Symposia on Quantitative Biology* 57:43–51. doi: [10.1101/SQB.1992.057.01.006](https://doi.org/10.1101/SQB.1992.057.01.006).
- Pelli DG. 1997. The VideoToolbox software for visual psychophysics: transforming numbers into movies. *Spatial Vision* 10:437–442. doi: [10.1163/156856897X00366](https://doi.org/10.1163/156856897X00366).
- Prokop A. 2013. The intricate relationship between microtubules and their associated motor proteins during axon growth and maintenance. *Neural Development* 8:17. doi: [10.1186/1749-8104-8-17](https://doi.org/10.1186/1749-8104-8-17).
- Puschel AW, Westerfield M, Dressler GR. 1992. Comparative analysis of Pax-2 protein distributions during neurulation in mice and zebrafish. *Mechanisms of Development* 38:197–208.
- Rajalingam K, Wunder C, Brinkmann V, Churin Y, Hekman M, Sievers C, Rapp UR, Rudel T. 2005. Prohibitin is required for Ras-induced Raf-MEK-ERK activation and epithelial cell migration. *Nature Cell Biology* 7:837–843. doi: [10.1038/ncb1283](https://doi.org/10.1038/ncb1283).
- Rivera J, Chu PJ, Lewis TL Jr, Arnold DB. 2007. The role of Kif5B in axonal localization of Kv1 K(+) channels. *The European Journal of Neuroscience* 25:136–146. doi: [10.1111/j.1460-9568.2006.05277.x](https://doi.org/10.1111/j.1460-9568.2006.05277.x).
- Ruthazer ES, Akerman CJ, Cline HT. 2003. Control of axon branch dynamics by correlated activity in vivo. *Science* 301:66–70. doi: [10.1126/science.1082545](https://doi.org/10.1126/science.1082545).
- Ruthazer ES, Cline HT. 2004. Insights into activity-dependent map formation from the retinotectal system: a middle-of-the-brain perspective. *Journal of Neurobiology* 59:134–146. doi: [10.1002/neu.10344](https://doi.org/10.1002/neu.10344).
- Schindelin J, Arganda-Carreras I, Frise E, Kaynig V, Longair M, Pietzsch T, Preibisch S, Rueden C, Saalfeld S, Schmid B, Tinevez JY, White DJ, Hartenstein V, Eliceiri K, Tomancak P, Cardona A. 2012. Fiji: an open-source platform for biological-image analysis. *Nature Methods* 9:676–682. doi: [10.1038/nmeth.2019](https://doi.org/10.1038/nmeth.2019).
- Schmidt JT, Fleming MR, Leu B. 2004. Presynaptic protein kinase C controls maturation and branch dynamics of developing retinotectal arbors: possible role in activity-driven sharpening. *Journal of Neurobiology* 58:328–340. doi: [10.1002/neu.10286](https://doi.org/10.1002/neu.10286).
- Schwartz N, Schohl A, Ruthazer ES. 2011. Activity-dependent transcription of BDNF enhances visual acuity during development. *Neuron* 70:455–467. doi: [10.1016/j.neuron.2011.02.055](https://doi.org/10.1016/j.neuron.2011.02.055).
- Schwartz N, Schohl A, Ruthazer ES. 2009. Neural activity regulates synaptic properties and dendritic structure in vivo through calcineurin/NFAT signaling. *Neuron* 62:655–669. doi: [10.1016/j.neuron.2009.05.007](https://doi.org/10.1016/j.neuron.2009.05.007).
- Schwarz TL. 2013. Mitochondrial trafficking in neurons. *Cold Spring Harbor Perspectives in Biology* 5:a011304. doi: [10.1101/cshperspect.a011304](https://doi.org/10.1101/cshperspect.a011304).
- Sheng ZH. 2014. Mitochondrial trafficking and anchoring in neurons: new insight and implications. *The Journal of Cell Biology* 204:1087–1098. doi: [10.1083/jcb.201312123](https://doi.org/10.1083/jcb.201312123).
- Shkumatava A, Fischer S, Muller F, Strahle U, Neumann CJ. 2004. Sonic hedgehog, secreted by amacrine cells, acts as a short-range signal to direct differentiation and lamination in the zebrafish retina. *Development* 131: 3849–3858. doi: [10.1242/dev.01247](https://doi.org/10.1242/dev.01247).
- Smear MC, Tao HW, Staub W, Orger MB, Gosse NJ, Liu Y, Takahashi K, Poo MM, Baier H. 2007. Vesicular glutamate transport at a central synapse limits the acuity of visual perception in zebrafish. *Neuron* 53:65–77. doi: [10.1016/j.neuron.2006.12.013](https://doi.org/10.1016/j.neuron.2006.12.013).
- Su YY, Ye M, Li L, Liu C, Pan J, Liu WW, Jiang Y, Jiang XY, Zhang X, Shu Y, Bao L. 2013. KIF5B promotes the forward transport and axonal function of the voltage-gated sodium channel Nav1.8. *The Journal of Neuroscience* 33:17884–17896. doi: [10.1523/JNEUROSCI.0539-13.2013](https://doi.org/10.1523/JNEUROSCI.0539-13.2013).
- Szymczak AL, Workman CJ, Wang Y, Vignali KM, Dilioglou S, Vanin EF, Vignali DA. 2004. Correction of multi-gene deficiency in vivo using a single 'self-cleaving' 2A peptide-based retroviral vector. *Nature Biotechnology* 22: 589–594. doi: [10.1038/nbt957](https://doi.org/10.1038/nbt957).
- Tang R, Dodd A, Lai D, McNabb WC, Love DR. 2007. Validation of zebrafish (*Danio rerio*) reference genes for quantitative real-time RT-PCR normalization. *Acta Biochimica et Biophysica Sinica* 39:384–390. doi: [10.1111/j.1745-7270.2007.00283.x](https://doi.org/10.1111/j.1745-7270.2007.00283.x).
- Tian L, Hires SA, Mao T, Huber D, Chiappe ME, Chalasani SH, Petreanu L, Akerboom J, McKinney SA, Schreier ER, Bargmann CI, Jayaraman V, Svoboda K, Looger LL. 2009. Imaging neural activity in worms, flies and mice with improved GCaMP calcium indicators. *Nature Methods* 6:875–881. doi: [10.1038/nmeth.1398](https://doi.org/10.1038/nmeth.1398).
- Tsoulfas P, Stephens RM, Kaplan DR, Parada LF. 1996. TrkC isoforms with inserts in the kinase domain show impaired signaling responses. *The Journal of Biological Chemistry* 271:5691–5697. doi: [10.1074/jbc.271.10.5691](https://doi.org/10.1074/jbc.271.10.5691).
- Twelvetrees AE, Yuen EY, Arancibia-Carcamo IL, MacAskill AF, Rostaing P, Lumb MJ, Humbert S, Triller A, Saudou F, Yan Z, Kittler JT. 2010. Delivery of GABAARs to synapses is mediated by HAP1-KIF5 and disrupted by mutant huntingtin. *Neuron* 65:53–65. doi: [10.1016/j.neuron.2009.12.007](https://doi.org/10.1016/j.neuron.2009.12.007).
- Uchida A, Alami NH, Brown A. 2009. Tight functional coupling of kinesin-1A and dynein motors in the bidirectional transport of neurofilaments. *Molecular Biology of the Cell* 20:4997–5006. doi: [10.1091/mbc.E09-04-0304](https://doi.org/10.1091/mbc.E09-04-0304).
- Uesaka N, Ruthazer ES, Yamamoto N. 2006. The role of neural activity in cortical axon branching. *The Neuroscientist* 12:102–106. doi: [10.1177/1073858405281673](https://doi.org/10.1177/1073858405281673).
- Vale RD. 2003. The molecular motor toolbox for intracellular transport. *Cell* 112:467–480. doi: [10.1016/S0092-8674\(03\)00111-9](https://doi.org/10.1016/S0092-8674(03)00111-9).
- Verstreken P, Ly CV, Venken KJ, Koh TW, Zhou Y, Bellen HJ. 2005. Synaptic mitochondria are critical for mobilization of reserve pool vesicles at *Drosophila* neuromuscular junctions. *Neuron* 47:365–378. doi: [10.1016/j.neuron.2005.06.018](https://doi.org/10.1016/j.neuron.2005.06.018).

- Wagle M, Mathur P, Guo S. 2011. Corticotropin-releasing factor critical for zebrafish camouflage behavior is regulated by light and sensitive to ethanol. *The Journal of Neuroscience* 31:214–224. doi: [10.1523/JNEUROSCI.3339-10.2011](https://doi.org/10.1523/JNEUROSCI.3339-10.2011).
- Warp E, Agarwal G, Wyart C, Friedmann D, Oldfield CS, Conner A, Del Bene F, Arrenberg AB, Baier H, Isacoff EY. 2012. Emergence of patterned activity in the developing zebrafish spinal cord. *Current Biology* 22:93–102. doi: [10.1016/j.cub.2011.12.002](https://doi.org/10.1016/j.cub.2011.12.002).
- Warren JT Jr, Chandrasekhar A, Kanki JP, Rangarajan R, Furley AJ, Kuwada JY. 1999. Molecular cloning and developmental expression of a zebrafish axonal glycoprotein similar to TAG-1. *Mechanisms of Development* 80: 197–201. doi: [10.1016/S0925-4773\(98\)00215-9](https://doi.org/10.1016/S0925-4773(98)00215-9).
- Whelan SM, Elmore MJ, Bodsworth NJ, Brehm JK, Atkinson T, Minton NP. 1992. Molecular cloning of the clostridium botulinum structural gene encoding the type B neurotoxin and determination of its entire nucleotide sequence. *Applied and Environmental Microbiology* 58:2345–2354.
- Witte H, Bradke F. 2008. The role of the cytoskeleton during neuronal polarization. *Current Opinion in Neurobiology* 18:479–487. doi: [10.1016/j.conb.2008.09.019](https://doi.org/10.1016/j.conb.2008.09.019).
- Witte H, Neukirchen D, Bradke F. 2008. Microtubule stabilization specifies initial neuronal polarization. *The Journal of Cell Biology* 180:619–632. doi: [10.1083/jcb.200707042](https://doi.org/10.1083/jcb.200707042).
- Xia Ch, Rahman A, Yang Z, Goldstein LS. 1998. Chromosomal localization reveals three kinesin heavy chain genes in mouse. *Genomics* 52:209–213. doi: [10.1006/geno.1998.5427](https://doi.org/10.1006/geno.1998.5427).
- Xia CH, Roberts EA, Her LS, Liu X, Williams DS, Cleveland DW, Goldstein LS. 2003. Abnormal neurofilament transport caused by targeted disruption of neuronal kinesin heavy chain KIF5A. *The Journal of Cell Biology* 161: 55–66. doi: [10.1083/jcb.200301026](https://doi.org/10.1083/jcb.200301026).
- Xiao T, Baier H. 2007. Lamina-specific axonal projections in the zebrafish tectum require the type IV collagen dragnet. *Nature Neuroscience* 10:1529–1537. doi: [10.1038/nn2002](https://doi.org/10.1038/nn2002).
- Xiao T, Roeser T, Staub W, Baier H. 2005. A GFP-based genetic screen reveals mutations that disrupt the architecture of the zebrafish retinotectal projection. *Development* 132:2955–2967. doi: [10.1242/dev.01861](https://doi.org/10.1242/dev.01861).

Table of figures

Figure 1: Pathophysiological mechanisms proposed to underlie ALS motor neuron degeneration. The mechanisms shown here include 1- changes in transport of mRNAs and RNA-binding proteins in the cytosol and nucleus, 2-impaired RNA metabolism due to mislocalization of RNA-binding proteins, formation of stress granules, aggregate formation, 3-impaired proteostasis overloading the proteasome with reduced autophagy lead to protein aggregate accumulation, 4-impaired DNA repair, 5-mitochondrial dysfunction and oxidative stress caused by disruption of the organelle's normal function, and the accumulation of ROS, 6-glia implication, degeneration and dysfunction leading to reduced support of neurons, 7-neuroinflammation caused by activated astrocytes and microglia, 8-perturbed axonal transport due to disorganization of the cytoskeleton, 9-impaired vesicular transport, 10-escitotoxicity caused by impaired EAAT2 function. (Adapted from Van Damme, Robberecht, & Van Den Bosch, 2017)..... 2

Figure 2: Axonal transport and its molecular motors. A) Representation of axonal transport in a motor neuron, where a very long axon separates the site of protein synthesis, the soma, from the synapse. This highlights the dependence of those neurons on a functional process, both for signaling between the growing synapse and the cell body, the supply of proteins and organelle for growth, but also for the removal of detritus for degradation. B) Schematic illustration of the anterograde dynein-dynactin motor complex and the retrograde kinesin complex on a microtubule track. The dynactin complex is an adaptor complex that binds the motor complex of dynein to regulate its activity. The dynactin1 subunit is represented here as a dimer, demonstrating its binding capacity for dynein and the dynactin complex-black stripes, and with microtubules-blue circles. C) Protein structure with identified structural domains of the dynein motor complex. A reconstruction of the complex shows how the heavy motor chains are assembled with the intermediate and light chains, forming the tail that binds the motor complex to the dynactin complex. (Adapted from Carter, Diamant, & Urnavicius, 2016; Duncan & Goldstein, 2006; Maday, Twelvetrees, Moughamian, & Holzbaur, 2014)..... 8

Figure 3: Schematic representation of the dynactin complex. A) The dynactin complex is composed of 11 subunits that are assembled into three structural domains: the projecting arm domain (dynamitin/p50, dynactin1, and p22/24), the arp rod domain (Arp1, CapZ and β -actin), and the pointed end domain (Arp11, p62, p25 and p27). Many of the subunits in this complex are known to interfere with other proteins (identified in blue boxes), which could regulate the assembly or function of the complex. B) Protein domains of the dynactin1 subunit with identified functional domains. This gene produces two isoforms, including a shorter 135kDa isoform lacking the microtubule-binding CAP-Gly domain. The functional domains of dynactin1 gives the subunit an arm-like shape, which allows interaction with other subunits of the complex, as well as the dynein motor and microtubules. (Adapted from Kardon & Vale, 2009; Sorbara et al., 2014; Urnavicius et al., 2015) 9

Figure 4: The neuronal cytoskeleton during development. A) Neurons have a very complex and dynamic microtubule cytoskeleton that is subject to many types of post-translational modifications regulating its dynamics and interactions. These modifications vary according to location in the cell, as well as throughout the life of the neuron. B) The growth cone is an interface between microtubules and actin, where different types of cytoskeletal structures participate in forming the dynamic growth cone. Stable acetylated microtubules form the axon, whereas unstable tyrosinated microtubules are present in the growth cone. At the growth cone, filopodial actin is necessary for sensing of environmental factors that will

guide the axon during migration. Interaction between the two cytoskeletons is essential for axon branching. C) +tip proteins are located at the fast-growing end of microtubules, at the level of the growth cone where they play a role in coupling between the microtubules and the actin cytoskeleton for outgrowth and guidance. (Adapted from Bearce et al., 2015; Dent & Kalil, 2001; Song & Brady, 2015) 14

Figure 5: The synapse organization and function. A) The synapse is site dense with protein, organized in specialized domains called active zones, where the synaptic release machinery is localized adjacent to calcium channels. At these sites, synaptic vesicles fuse with the membrane to release neurotransmitters into the synaptic cleft and need to cycle back to the ready, releasable pool. They do so via the clathrin-dependent endocytosis, which then takes them to be refilled in the recycling pool before moving back to the ready pool. B) The neuromuscular junction is a special synaptic connection, where a motor neuron is innervating a muscle fiber. The presynaptic site is apposed to acetylcholine receptors organized in end plates, which are located a short distance away from the active zones, across the synaptic cleft. C) Adhesion molecules have a very important role at the synapse, as they organize the active zone proteins and fusion machinery to efficiently recruit the synaptic vesicle and produce a flow of neurotransmitters. They are also involved in trans-synaptic connectivity, which allows proper alignment of pre- and postsynaptic sites. (Adapted from Dean & Dresbach, 2006; Haucke, Neher, & Sigrist, 2011; Drachman, 1978) 17

Figure 6: The embryonic zebrafish spinal cord, its primary motor neurons, and their innervation pattern on the ventral musculature. A) 48hpf embryonic zebrafish are already able to produce complex swimming behavior and rely on their spinal cord motor neurons to do so. B) One somatic segment (delineated in red in A) contains various types of primary motor neurons, with different morphologies, cell body position and innervation patterns, which are repeated on each side of the embryo, and at each somite along the trunk and tail. The primary motor neurons can be visualized and studied by using a transgenic line where GAL4 is placed under the expression of a specific enhancer called *mnx1* (shown here in combination with a UAS-driven membrane-bound fluorophore). The caudal primary-CaP-motor neuron we use in this study (at 24hpf, red arrow, at 48hpf, blue arrow). C) The CaPs innervate ventral fast-twitch muscle fibers, located in deeper levels below the slow-twitch muscle layer. (Adapted from Ashworth, Zimprich, & Bolsover, 2001; Babin, Goizet, & Raldúa, 2014) 22

Figure 7: Zebrafish paralogs for *dynactin1*. The zebrafish genome has been duplicated along evolution and now contains two copies of the *dynactin1* gene. These paralogs, *dynactin1a* and *dynactin1b*, are both predicted to produce full-sized protein transcripts, while *dynactin1b* could also lead to a shorter transcript lacking the CAP-Gly domain in N-terminus. These two transcripts are depicted here, along with the full-sized transcript produced from *dynactin1a*, with their identified functional domains (graphics from ENSEMBL, ZV10 assembly of the zebrafish genome). 25

Figure 8: General morphology of the *mok^{m632}* embryos at 6dpf. A) Wild-type sibling and B) *mok^{m632/-}* embryo at 6dpf, side view and dorsal view, close-up showing a dorsal view of the head, with visible “bug eye” phenotype due to the loss of the photoreceptor layer in the *mok^{m632/-}* embryo. Pigmentation is more visible in *mok^{m632/-}* embryos (B), as a result of background adaptation in these blind fish. 29

Figure 9: Behavioral analysis at 48hpf by touch-evoked escape response assay. A) Superimposed traces of escape episodes for ten wild-type sibling embryos and for B) ten *mok^{m632/-}* embryos. C) Average swim duration ($p \leq 0,01$), D) average swim distance ($p \leq 0,05$), and E) maximum instant speed of evoked escape responses. All data shown as average +/-SD, where one symbol represents one escape done by one embryo ($n \geq 30$) 30

Figure 10: Axonal morphology of CaPs at 48hpf. A) Confocal z-stack projection of a single CaP cell, visualized by expression of *mnx1:lynGFP*, with tracing of the axonal arbor done with NeuronJ (ImageJ) for a wild-type sibling embryo at 48hpf and for a B) *mok^{m632/-}* embryo. C) Quantification of the axonal arbor size, by total cell length, D) total number of projection, and E) analysis of complexity by comparing the total length of projection grouped by type (branch order). All data presented as average +/- SD; (n=9, 9) 31

Figure 11: Axonal morphology of CaPs at 6dpf. A) Confocal z-stack projection of a single CaP cell, visualized by expression of *mnx1:lynGFP*, with tracing of the axonal arbor done with NeuronJ (ImageJ) for a wild-type sibling embryo at 48hpf and for a B) *mok^{m632/-}* embryo. C) Quantification of the axonal arbor size, by total cell length ($p \leq 0,05$), D) total number of projection ($p \leq 0,05$), and E) analysis of complexity by comparing the total length of projection grouped by type (branch order). All data presented as average +/- SD; (n=11, 14)..... 32

Figure 12: Integrity of the NMJ structure by double immunohistochemistry at 48hpf and 6dpf. Integrity of the NMJ is determined by the coverage and colocalization of the pre- and postsynaptic components of the synapse, which are respectively labeled by anti-synaptotagmin2 (Alexa488; in green) and Alexa594 conjugated α -bungarotoxin (in red). The colocalization is visualized in yellow in merged images of the two channels. Representative z-stack projection of a double labeled NMJ for wild-type and *mok^{m632/-}* embryo A) 48hpf and D) 6dpf. Each channel shown separately in B) for 48hpf and E) for 6dpf. The colocalization was quantified in C) and F) using Pearson's coefficient in combination with the overlap coefficient, and Mander's coefficients are also presented. All data shown as average +/- SD, ($p \leq 0,01$, $p \leq 0,001$) (48hpf n=12, 14; 6dpf n=11, 19) 35

Figure 13: Quantitative RT-PCR of dynein and dynactin components and interactors for 6dpf *mok^{m632/-}* embryos. Ratio is expressed in fold change over wild-type siblings expression. ($p \leq 0,05$) (N=3, n=50 embryos) 36

Figure 14: Axonal morphology of 6dpf cells overexpressing the human wild-type Dynactin1-eGFP. Confocal z-stack projection showing the membrane reporter, the tracing of the arbor and the signal from hDCTN1-eGFP in heatmap. Close-up showing synapse accumulation for A) a wild-type embryo and B) a *mok^{m632/-}* embryo. Quantification of the tracings for C) total number of projection ($p \leq 0,01$), D) total cell length ($p \leq 0,01$), and E) average projection length. F) Double immunohistochemistry was done to confirm accumulation of hDCTN1-eGFP (in cyan) at synaptic sites by labeling of post-synaptic receptors with Alexa594 conjugated α -bungarotoxin (in magenta; colocalization is white). All data shown as average +/- SD (n=19,13) 38

Figure 15: Axonal morphology of 48hpf cells overexpressing the human wild-type Dynactin1-eGFP. Confocal z-stack projection showing the membrane reporter, the tracing of the arbor and the signal from hDCTN1-eGFP in heatmap. Close-up showing synapse accumulation for A) a wild-type embryo and B) a *mok^{m632/-}* embryo. Quantification of the tracings for C) total number of projection, D) total cell length, and E) average projection. F) Comparison of total cell length with wild-type cells labeled with *mnx1:lynGFP* from Figure 10 to show no effect on growth. All data shown as average +/- SD (n=8,14) 39

Figure 16: Quantification of putative synapse of CaP arbors at 48hpf and at 6dpf. Putative synapses were visualized by single-cell expression of UAS:rab3-dendra2 in A) 48hpf embryos and B) 6dpf embryos. Quantification of the puncta observed for C/F) number (n.s./ $p \leq 0,05$), D/G) average area (n.s./ $p \leq 0,01$), and E/H) total area covered by of putative synapses (n.s./ $p \leq 0,01$) in arbors of 48hpf/6dpf embryos. All data shown as average +/- SD (n=26,20/n=17,15)..... 40

Figure 17: Putative synapse stability assay in 48hpf CaP arbors. Putative synapses were visualized as previously by single-cell expression of UAS:rab3-dendra2 in 48hpf embryos. A)

Z-stacks of cell arbors were acquired initially and B) 3h later to compare numbers of synapses lost and added during this time. Quantification was done by particle analysis, and presented as fold-change for each cell with regard to B) number ($p \leq 0,01$), C) mean area, and D) total area of putative synapses ($p \leq 0,01$). All data shown as average \pm SD (n=11,7)..... 42

Figure 18: GCaMP analysis of spinal cord primary motor neuron recruitment during a fictive evoked response. A) Schematic of the acquisition setup, where for each larva, five water jet stimuli were presented to elicit fictive escape responses. B) Confocal capture of the GCaMP5 signal in the spinal cord, at baseline and after stimulus, with regions of interest drawn in red. C) Calcium signals from dorsally located primary motor neurons D) with extracted maximum DF/F amplitude signal for each cell, where data is presented as mean DF/F signal per fish and per stimuli. (n embryos/n cells=6/63, 8/44) 43

Figure 19: Quantification of spontaneous synaptic release by mEPC measurement at 6dpf. A) Number of spontaneous releases of quanta, where the kinetics were quantified in terms of a B) average amplitude, frequency and quantal content, and in terms of the C) decay constant, and D) rise time. (n=17, 6)..... 44

Figure 20: Paired-recordings of CaP motor neurons and fast-twitch muscle fiber. Paired recordings were obtained by injecting current into the cell body of CaPs and recording the response at the level of the muscle fiber it innervates. A) Dye-filled CaP (green) and its paired dye-filled muscle fiber (red). Mutant embryos display higher rates of failures in response to stimulation, B) example trace shown here for a frequency of 1Hz, failures labeled with asterisks. Mutants also display higher frequency of asynchronous release (out-of synch peaks). C) The failure frequency is plotted here as a relation of stimulation frequency, data presented as mean with confidence interval, showing significance ($p \leq 0,05$). 46

Figure 21: Cargo distribution in live CaP cells at 48hpf. Cargo was visualized *in vivo* by co-expression of a membrane reporter (tagRFP-Caax, in red) and a cargo-specific tagged protein (in this case, eGFP-rab7, green). A) Examples of z-stack projections for late endosomes/MVB for 48hpf wild-type and *mok*^{m632/-} embryos. The quantification for cargo distribution was done by separating the axonal compartment from the arbor (determined by first branching point). The distribution from cell body metric is done in the axon and represents the average distance, based on the center of mass of each cargo, in order to determine if there is distal accumulation. B) Quantification for mitochondria, C) early endosomes (rab5c), D) late endosomes/MVB (rab7) and E) recycling endosomes (rab11a). All data shown as average \pm SD. (B n=7,6; C n=5,7; D n=7,9; E n=10,9)..... 49

Figure 22: Live *in vivo* axonal transport of cargo in 48hpf CaPs. Timelapse imaging was performed by spinning disk confocal microscopy on single-plane linear segments of the mid-axon in CaP cells. By convention, the axonal segment is presented with the cell body oriented to the left, and the arbor to the right, where cargo moving to the right would be going in the anterograde direction. The timelapse image sequence (first timepoint shown here) is used to generate a kymogram, which is a 2D representation of movement, where the axonal segment length in μm is in the X axis, and time is in the Y axis, where each pixel represents one timepoint of the timelapse sequence. Kymograms are shown here with labeled traces for retrograde (magenta) and anterograde runs (cyan), which were used for quantification of transport metrics. A) Example for analysis of mitochondria, imaged every 1s for 10 minutes (1s/10min) B) Example analysis for early endosomes, imaged every 500ms for 5 minutes (500ms/5min). 52

Figure 23: Axonal transport metrics for mitochondria at 48hpf. A) Directionality ratio chart for mitochondrial movement, where stable mitochondria were labeled as “immobile” (black), non-mobile but unstable mitochondria were labeled as “oscillating” (grey), retrograde-directed mobile mitochondria as “retrograde” (magenta) and anterograde-directed mobile mitochondria as “anterograde” (cyan). B) Area flux was determined for both direction

(number of moving mitochondria per minute, per 20 μm) and density (number of mitochondria per 20 μm) as well as coverage (ratio of area) was measured. Individual runs are defined as unbroken linear segments of movement, and were used to extract metrics for the C) retrograde direction and the D) anterograde direction for average run speed ($\mu\text{m/s}$), average run length (μm) and average run duration (s). All data averaged by kymogram and presented as average \pm -SEM. ($p \leq 0,05$) (n retro/ n antero = 5/20, 8/19)..... 53

Figure 24: Axonal transport metrics for early endosomes at 48hpf. A) Directionality ratio chart for endosome movement, where stable vesicles were labeled as “immobile” (black), non-mobile but unstable vesicles were labeled as “oscillating” (grey), retrograde-directed mobile vesicles as “retrograde” (magenta) and anterograde-directed mobile vesicles as “anterograde” (cyan). B) Area flux was determined for both direction (number of moving vesicles per minute, per 20 μm) and density (number of vesicles per 20 μm) was measured. Individual runs are defined as unbroken linear segments of movement, and were used to extract metrics for the C) retrograde direction and the D) anterograde direction for average run speed ($\mu\text{m/s}$), average run length (μm) and average run duration (s). All data averaged by kymogram and presented as average \pm -SEM. (n=18,17)..... 54

Figure 25: Axonal transport metrics for late endosomes/MVB at 48hpf. A) Directionality ratio chart for late endosome/MVB movement, where stable vesicles were labeled as “immobile” (black), non-mobile but unstable vesicles were labeled as “oscillating” (grey), retrograde-directed mobile vesicles as “retrograde” (magenta) and anterograde-directed mobile vesicles as “anterograde” (cyan). B) Area flux was determined for both direction (number of moving vesicles per minute, per 20 μm) and density (number of vesicles per 20 μm) was measured. Individual runs are defined as unbroken linear segments of movement, and were used to extract metrics for the C) retrograde direction and the D) anterograde direction for average run speed ($\mu\text{m/s}$), average run length (μm) and average run duration (s). All data averaged by kymogram and presented as average \pm -SEM. (n=27,30)..... 55

Figure 26: Axonal transport metrics for recycling endosomes at 48hpf. A) Directionality ratio chart for late recycling movement, where stable vesicles were labeled as “immobile” (black), non-mobile but unstable vesicles were labeled as “oscillating” (grey), retrograde-directed mobile vesicles as “retrograde” (magenta) and anterograde-directed mobile vesicles as “anterograde” (cyan). B) Area flux was determined for both direction (number of moving vesicles per minute, per 20 μm) and density (number of vesicles per 20 μm) was measured. Individual runs are defined as unbroken linear segments of movement, and were used to extract metrics for the C) retrograde direction and the D) anterograde direction for average run speed ($\mu\text{m/s}$), average run length (μm) and average run duration (s). All data averaged by kymogram and presented as average \pm -SEM. (n=18,19)..... 56

Figure 27: Proof of principle, axonal transport metrics for recycling endosomes at 6dpf. A) Representative kymograms used for analysis, where retrograde-directed mobile vesicle runs (magenta) and anterograde-directed mobile vesicles runs (cyan) are labeled. Individual runs are defined as unbroken linear segments of movement, and were used to extract metrics for the B) retrograde direction and the C) anterograde direction for average run speed ($\mu\text{m/s}$) (n.s., $p \leq 0,05$), average run length (μm) (n.s., $p \leq 0,01$) and average run duration (s). All data averaged by kymogram and presented as average \pm -SEM. (n=14, 12) 58

Figure 28: Filopodia dynamics at 24hpf, 48hpf, 72hpf and 4dpf. Filopodial dynamics were acquired by timelapse imaging, where a confocal z-stack of the axonal arbor was acquired every two minutes for a total of ten minutes (2/10minutes). A)The z-stack projections were then used to compare the growth and retraction of filopodia between the 6 timepoints, the sum of which is reported here as total unstable filopodia, with regard to total length, number and average length of unstable filopodia per cell arbor, at B) 24hpf, C) 48hpf, C) 72hpf and D)

4dpf. Data presented as average +/- SEM. ($p \leq 0,05$) (B n=10,5; C n=8,10, D n=8,8, E n=6,10) 60

Figure 29: Axonal transport metrics for p75 receptor-containing vesicles. Directionality ratio chart for p75-containing vesicle movement, where stable vesicles were labeled as “immobile” (black), non-mobile but unstable vesicles were labeled as “oscillating” (grey), retrograde-directed mobile vesicles as “retrograde” (magenta) and anterograde-directed mobile vesicles as “anterograde” (cyan). B) Area flux was determined for both direction (number of moving vesicles per minute, per 20 μm) and density (number of vesicles per 20 μm) was measured. Individual runs are defined as unbroken linear segments of movement, and were used to extract metrics for the C) retrograde direction and the D) anterograde direction for average run speed ($\mu\text{m}/\text{s}$), average run length (μm) and average run duration (s). All data averaged by kymogram and presented as average +/-SEM. (n=10,9)..... 62

Figure 30: Immunohistochemistry against acetylated tubulin in 48hpf and 6dpf embryos. Acetylated tubulin is a marker for stable microtubule, a modification that is site and developmental stage specific. We performed whole-mount immunohistochemistry to visualize microtubule acetylation in A) 48hpf CaPs and in B) 6dpf ventral roots. Close-up boxes show axonal caliber and distribution of microtubule acetylation. 63

Figure 31: Microtubule growth dynamics by EB3-GFP comet assay. Microtubules are dynamic structures that constantly undergo growth and retraction of their protofilaments by tubulin subunit polymerization. In the arbor, the fast-growing +ends are located at the synapse, where end-binding proteins like EB3 associate with the microtubule during growth episodes, where they form runs called “comets”. We visualized and quantified these comets by timelapse confocal imaging and quantified the metrics of their runs. Representative z-stack projections and timelapse stills with kymograms at A) 48hpf and B) 6dpf, shown here for mutant embryos. Quantification of comet distance, time and speed of runs, as well as comet area flux at C) 48hpf and D) 6dpf. Data presented as average +/- SEM. ($p \leq 0,01$) (A/C n=24, 22; B/D n=22,20)..... 65

Figure 32: Dynein-mediated EB3-GFP comet capture at synapses. We visualized and quantified the microtubule growth comets (eb3-GFP in green) simultaneously with putative synapses labeled by rab3-tagRFP (red) by timelapse confocal imaging and quantified the metrics of their runs. A) Representative z-stack projections and timelapse stills with kymograms at 48hpf shown here for a mutant embryo. Quantification of ratio of comets terminating at synapses, with control for comet density, and synapse density at B) 48hpf and C) 6dpf. Data presented as average +/- SEM. (B n=15, 28; C n=8,12) 67

Figure 33: N-Cadherin-GFP at the synapse. Whole-mount immunohistochemistry was performed in 48hpf Tg(cdh2:Cdh2-GFP; mokm632; mnx1:Gal4) embryos showing N-Cadherin-GFP (antiGFP, 488 in green) located at the center of a NMJ synapse, which was co-labeled by synaptotagmin2 (red) showing the presynaptic site and conjugated α -bungarotoxin showing the postsynaptic site (blue). Z-stacks of ventral somatic segment for wild-type and mutant embryos, with boxes showing close-up of the synaptic structure. 68

Figure 34: Axonal morphology at 6dpf for homozygous *dynactin1b*^{*235}, and double homozygous *dynactin1b*^{*235}; *mok*^{m632/-}, compared with *mok*^{m632/-} embryos. Confocal z-stack projection of a single CaP cell, visualized by expression of mnx1:lynGFP, with tracing of the axonal arbor done with NeuronJ (ImageJ) for A) wild-type sibling embryo (black) at 48hpf, for B) homozygous *dynactin1b*^{*235} (blue) and for C) double homozygous *dynactin1b*^{*235}; *mok*^{m632/-} embryo (violet). Quantification of the axonal arbor size, by D) total projection number, E) total cell length, and F) average length of projection, compared with *mok*^{m632/-} embryo data (red) compiled in Figure11. All data presented as average +/- SD. ($p \leq 0,05$) (A n=16, B n=14, C n=13)..... 70

Figure 35: Proof of principle for maintained axonal transport in full *dynactin1* mutant embryos at 48hpf. A) Timelapse still and kymogram for recycling endosome axonal transport in double homozygous *dynactin1b*^{*253/*253}; *mok*^{m632-/-} embryos. B) Quantification of retrograde and anterograde runs compared with *mok*^{m632-/-} embryos metrics presented in Figure 26. Double homozygous mutant data presented as average of runs from one kymogram compared with average +/-SEM for *mok*^{m632-/-} data. 72

Figure 36: Axonal morphology of 6dpf CaPs in homozygous *dctn2*^{ij50}, *dync1h1*^{mw20} mutant embryos, as well as in CaPs expressing the dominant-negative CC1 fragment (4nrUAS:zfCC1-E2A-tagRFPCaax-pA) compared to *mok*^{m632-/-} embryos. Confocal z-stack projections of single CaP cells, visualized by expression of *mnx1:lynGFP*, for a A) *mok*^{m632-/-} embryo, B) *dctn2*^{ij50-/-} embryo, C) *dync1h1*^{mw20-/-} embryo, and D) a wild-type embryo overexpressing the CC1 fragment of dynactin1, resulting in disassembly of the dynactin complex. 73

List of tables

Table 1: Mutations identified in *DCTN1* in the context of ALS or MND. Many pathogenic mutations have been reported within *DCTN1*, this table displays the reports of cases where patients were diagnosed as having either ALS or MND. The clinical presentation is included, as is the inheritance, when the data was available. 19

Résumé :

La sclérose latérale amyotrophique (SLA) est une pathologie neurodégénérative progressive se déclarant vers 50-60 ans. Elle est majoritairement de nature sporadique son incidence est estimée à 1 : 1000. La SLA mène à une paralysie progressive et entraîne généralement à la mort des patients de 2 à 5 ans suivant le diagnostic aux suite d'une fonte musculaire importante liée à la perte des neurones moteurs. Au cours des années, plusieurs mutations ont été identifiées autant chez les patients atteints de SLA sporadique que de SLA familiale. Ces mutations interfèrent avec la fonction de gènes variés, tels que DCTN1, codant pour la protéine dynactine1, sous-unité du complexe multimoléculaire dynactine. Ce complexe sert d'adaptateur au moteur moléculaire dynéine, chargé du transport axonal rétrograde, où sa fonction permettrait de régir l'activité du complexe moteur et sa capacité à lier divers cargos. Nous avons donc entrepris la caractérisation d'une lignée de poissons zèbre mutants pour dynactin1a (nommés mikre okom632, mokm632), plus particulière en terme du développement d'un type de neurone moteur primaire (les CaPs), afin de déterminer l'effet de la perte de fonction de ce gène sur l'axonogenèse, la formation et la stabilisation de la jonction neuromusculaire, sur le comportement de l'embryon, ainsi que sur le transport axonal.

Nous suggérons que dynactin1 favorise la stabilité synaptique, où une perte de fonction de ce gène entraîne des défauts de croissance, des anomalies électrophysiologiques et un comportement anormal. Ce rôle semble être indépendant des fonctions connues de régulateur du moteur dynéine, de son implication dans le transport axonal ou de son action sur la dynamique des microtubules. Cette étude vise donc à élucider des mécanismes moléculaires clés impliqués dans l'étiologie sous-jacent à la SLA, en révélant le rôle de la dynactine1 dans le développement et l'entretien fonctionnel de la jonction neuromusculaire.

Mots clés : Poisson zèbre, neurones moteurs, jonction neuromusculaire, SLA, Sclérose Latérale Amyotrophique, dynactine, dynéine, transport axonal

Dynactin1 mutations associated with amyotrophic lateral sclerosis and their effect on axonal transport and neuromuscular junction formation.

Abstract :

Amyotrophic lateral sclerosis (ALS) is an adult-onset neurodegenerative disease, which is mainly sporadic in nature. This progressive pathology has an estimated incidence of 1:1000 and generally leads to death within 2-5 years of diagnosis due to muscle wasting and severe motor neuron loss. Over the last years, mutations have been identified in both sporadic and familial ALS patients, interfering with the function of many genes, including DCTN1, which encodes for a subunit of the motor protein complex subunit dynactin. The dynactin complex serves as an adaptor for the dynein motor complex, responsible for retrograde axonal transport, and it is believed to regulate dynein activity and the binding capacity for cargos. We set out to characterize a mutant zebrafish line for dynactin1a (named mikre okom632, mokm632), looking specifically at caudal primary motor neurons (CaPs), with regard to axonal development, formation and stability of the neuromuscular junction (NMJ) and the behavioral phenotype produced in embryos, as well as axonal transport metrics.

We suggest a role for dynactin1 in synapse stability, where the loss-of-function of this gene leads to growth defects, electrophysiological abnormalities and behavioral deficits. This role appears to be independent of its known function as a regulator of dynein, its implication in axonal transport, or its regulation of microtubule dynamics. With this study, we hope to elucidate key molecular mechanisms in ALS etiology by revealing the role of dynactin1 in NMJ development and maintenance.

Keywords : Zebrafish, motor neurons, neuromuscular junction, ALS, Amyotrophic Lateral Sclerosis, dynactin, dynein, axonal transport